Abatement of toluene through storage-regeneration sequential process : application of thermal and plasma assisted catalytic regeneration

Shilpa Sonar

Joint Doctoral Ph.D.

For the obtention of the degrees of

Doctor of Engineering delivered by
Ghent University, Doctoral school of (BioScience) Engineering

AND

Doctor of "Molécules et Matière Condensée" delivered by
Lille University, Doctoral school of Sciences of matter, radiation and environment, Sciences and technologies

Presented by
SONAR Shilpa

17 December 2021

Abatement of Toluene through Storage-Regeneration Sequential Process: Application of Thermal and Plasma Assisted Catalytic Regeneration

---

Thesis supervision :

***Nathalie DE GEYTER**, Professor, Ghent University*	*Co-director*
***Axel LÖFBERG**, CNRS Research Director, Lille University*	*Co-director*
***Jean-Marc GIRAUDON**, Associate Professor, Lille University*	*Advisor for Lille University*

Jury members:

***Pascal GRANGER**, Professor, Lille University*	*Chair*
***Filip DE TURCK,** Professor, Ghent University*	*Co-Chair*
***Guy DE WEIRELD**, Professor, Mons University*	*Reviewer*
***Patrick DA COSTA**, Professor, Sorbonne University*	*Reviewer*
***Pascal VAN DER VOORT**, Professor, Ghent University*	*Examiner*
***Antoine ROUSSEAU**, CNRS Research Director, Ecole Polytechnique*	*Examiner*

THESE EN COTUTELLE

Pour Obtenir le grade de

Docteur en « Ingénierie » délivré par
Université de Gand, École doctorale d'ingénierie (BioScience)

ET

Docteur en « Molécules et Matière Condensée » délivré par
Université Lille, Ecole Doctorale Sciences de la Matière, du Rayonnement et de l'environnement, Sciences et Technologies

Présentée par
SONAR Shilpa

17 Décembre 2021

Dépollution du toluène par un procédé séquentiel stockage-régénération : application de la régénération catalytique activée par voie thermique et par plasma

---

Encadrement de la thèse:

***Nathalie DE GEYTER**, Professeur, Université de Gand*	*Co-directeur*
***Axel LÖFBERG**, Directeur de Recherches CNRS, Université de Lille*	*Co-directeur*
***Jean-Marc GIRAUDON**, Maître de Conférences, Université de Lille*	*Co-encadrant pour l'Université de Lille*

Membres de Jury:

***Pascal GRANGER**, Professeur, Université de Lille*	*Président*
***Filip DE TURCK,** Professeur, Université de Gand*	*Co- Président*
***Guy DE WEIRELD**, Professeur, Université de Mons*	*Rapporteur*
***Patrick DA COSTA**, Professeur, Sorbonne Université*	*Rapporteur*
***Pascal VAN DER VOORT**, Professeur, Université de Gand*	*Examinateur*
***Antoine ROUSSEAU**, Directeur de Recherches CNRS, École Polytechnique*	*Examinateur*

This research was supported by a grant from “INTERREGV DepollutAir”, “GoTtoS3” and “Union Européenne Europese Unie”.

Summary

Extensive research undergoes a paradigm shift in the field of air purification from pollutants such as volatile organic compounds (VOCs). VOCs are toxic organic compounds with low boiling point responsible for damage to the human health and to the environment. VOCs are emitted from a wide range of sources, including both outdoor sources (industrial processes and transportation) and indoor sources (household products, such as construction materials, consumer products, furniture, combustion byproducts and cooking). Because of their harmful characteristics, the emissions of VOCs into atmospheric environment are limited by strict regulations. Current abatement technologies being investigated include absorption, adsorption, condensation and membrane separation methods which are suitable for medium and high concentration VOCs (≥ 2500 ppm). Destruction technologies include combustion, non-thermal plasma, biological and catalytic oxidation methods. These are suitable for VOCs that are difficult to recover or to reuse. Adsorption is a cost effective and simple technique. Its main limitations are the need for periodic regeneration of the used adsorbent, the disposal of spent adsorbents and the processing of the adsorbed VOCs. On the other hand, catalytic oxidation is an efficient method due to its easy feasibility, low cost and relatively low temperature of operation. But, due to the incomplete decomposition of VOC, the generation of secondary by products can occur.

Non-thermal plasma (NTP), which can be produced by electrical discharge at room temperature and atmospheric pressure, draws increasing interest in the field of abatement of various pollutants. Non-thermal plasma is a weakly ionized state consisting of a cocktail of various reactive species produced at low temperatures; therefore, it can convert air contaminants at near room temperature. However, NTP has disadvantages such as the formation of unwanted toxic by-products, low energy efficiency, and incomplete oxidation of VOCs. Plasma can be coupled with catalysis to achieve low-temperature operation and higher efficiency. In such plasma-catalyst hybrid process, plasma discharge can contribute to the activation of the catalyst at lower temperature than catalysis alone and to the improvement of selectivity towards desired products. This can be achieved either by generating plasma in the catalyst (In-Plasma Catalysis, IPC), or by placing the plasma reactor and the catalytic reactor in series (Post-Plasma Catalysis, PPC). The plasma discharge produces reactive and energetic species in the gas phase. In IPC, short-lived species such as electrons, ions, excited-state atoms and radicals can directly interact with the

catalyst. On the other hand, only long- lived species such as O_3 can affect the catalyst in PPC. IPC and PPC are continuous processes in which plasma needs to be permanently ignited thus leading to high energy consumption.

To overcome drawbacks of individual abatement technologies, an innovative "storage-regeneration" hybrid processes is investigated. It is based on sequential adsorption-thermal catalytic oxidation (ATC) and sequential adsorption-plasma catalysis (APC) using toluene as model VOC compound. These processes are divided into two steps: the "storage step" where gaseous toluene is adsorbed on the surface of material at room temperature followed by the "oxidation step" where the adsorbed toluene species are catalytically converted into CO_2 and H_2O in thermal (ATC) or plasma (APC) environments. The steps are repeated cyclically allowing to regenerate the material without using an external system. Sequential and cyclic operation would help to reduce the operating costs by controlling the regeneration/discharge step duration with respect to the adsorption/storage step. In this work, the abatement of toluene in both ATC and APC systems is studied and compared.

Chapter 1 provides an overview of the VOCs and their sources. The effect of air quality on environment and human health is summarized and illustrated in more detail for toluene. The different removal technologies are also described. The combination of technologies is introduced and the concept of sequential adsorption-thermal catalysis and sequential adsorption-plasma catalysis is explained. An overview of the literature dealing with APC is given and the effect of different parameters on APC is summarized. Various potential materials for ATC or APC such as Hopcalite, Ceria-NR and UiO-66-SO_3H are described and a survey of the literature on catalytic oxidation of toluene is done. All experimental procedures, comprehensive synthesis protocols of different material, and the conditions of various characterization techniques are presented in Chapter 2.

In Chapter 3, the study of toluene abatement by ATC using a commercial Hopcalite, Ceria-NR and UiO-66-SO_3H is presented. First, the properties of these materials for conventional catalytic oxidation of toluene are presented. Hopcalite appears as an outstanding candidate due to the presence of mesopore, easy cycling between Cu and Mn different oxidation states. Breakthrough adsorption study done over Hopcalite with different initial toluene concentration (50-500 ppm) show that, at low concentration, toluene molecule disperses well on the surface of

material. As a result, the amount of irreversible adsorbed toluene is high. This study allows to determine the total adsorption capacities of individual materials but in real process, the concentration of toluene at the outlet of the system need to below and acceptable range. Therefore, the concept of "useful adsorption capacity" is introduced. Consequently, the adsorption properties of materials are given considering a maximum threshold of 10 ppm toluene in the exhaust flow. Subsequent oxidation of toluene performed with in inert atmosphere and in presence of $He:O_2$ atmosphere allow to assess the redox properties of the materials. The highest adsorption capacity is found for UiO-66-SO_3H due to the high surface area, but this material shows low oxidation properties. Hopcalite stands as the best candidate as CO_2 yield reaches to 92.3 %. These results indicate that limiting the amount of toluene to "useful capacity" leads to significant improvement in CO_2 yield and overall abatement efficiency.

The powder morphology and lack of synergy effect in Ceria-NR and UiO-66-SO_3H does not allow to generate stable plasma. Thus, only Hopcalite is studied in APC as described in Chapter 5. Different experimental variables such as duration of the storage step and plasma discharge power are considered. The energy cost rapidly decreases with an increase in the storage time as well as the efficiency of the APC process in terms of energy yields. Hence, limiting the amount of toluene adsorbed through a short adsorption time allows best performances in terms of CO_2 selectivity and yield, but clearly also induces the least energy efficiency and the highest energy cost. An optimum power of the plasma can be observed in terms of CO_2 selectivity and energy consumption for a power of 46 W. The cyclic sequential adsorption-plasma catalysis process show that the performances are not affected by repeated plasma treatment and this is also evidenced by several characterization techniques.

To further improve the efficiency of the oxidation step, the catalytic activity can be enhanced by impregnating active phase such as silver. The properties for toluene abatement of these on silver impregnated Hopcalite materials are examined for both ATC in Chapter 4 and APC in Chapter 6. In both processes, improvements in the CO_2 selectivity and CO_2 yield are obtained at very low silver loading with an optimum at 0.5 wt.% Ag for ATC and 2 wt.% Ag for APC, while the 0.5 wt.% Ag results to be the best in term of energy yield in APC. These results demonstrate the positive effect of silver addition but also reveal that highly active species can also contribute

to the desorption of unreacted toluene due to the heat generated on the surface of the materials by the combustion reaction.

Results for both processes, ATC and APC, are compared and discussed in Chapter 7. In both cases a good balance of adsorption capacity and catalytic activity is required. This feature is of particular importance considering that the processes are intrinsically dynamic systems and rely on unsteady state behavior. Moreover, the energy cost of APC is in the range of acceptable level ($11.6\ \mathrm{kWh \cdot m^{-3}}$). With further optimization of different experimental parameters, it can be upscaled in cost-effective manner. Both ATC and APC allow to reach toluene abatement efficiency and conversion to CO_2 above 95 % on first run and 75 % on stabilized materials.

This study shows that both ATC and APC could be a promising energy-efficient toluene abatement processes and opens the path for further development and scale-up.

Samenvatting

Er wordt momenteel uitgebreid onderzoek verricht op het vlak van luchtzuivering tegen verontreinigende stoffen zoals vluchtige organische stoffen (VOS). VOS zijn toxische organische verbindingen met een laag kookpunt die schade kunnen brengen aan de menselijke gezondheid en aan het milieu. VOS worden uitgestoten door een breed scala van bronnen, zowel buitenshuis (industriële processen en vervoer) als binnenshuis (huishoudelijke producten, zoals bouwmaterialen, consumptiegoederen, meubilair, verbrandingsbijproducten en koken). Wegens hun schadelijke eigenschappen wordt de uitstoot van VOS in de atmosfeer door strenge voorschriften beperkt. Tot de huidige onderzochte bestrijdingstechnologieën behoren absorptie, adsorptie, condensatie en membraanscheidingsmethoden die geschikt zijn voor de verwijdering van VOS in middelhoge en hoge concentraties (≥ 2500 ppm). Tot de vernietigingstechnologieën behoren verbranding, niet-thermische plasma's, biologische en katalytische oxidatiemethoden. Deze zijn geschikt voor VOS die moeilijk terug te winnen of te hergebruiken zijn. Adsorptie is een goedkope en eenvoudige techniek. De voornaamste beperkingen zijn de noodzaak van periodieke regeneratie van het gebruikte adsorbens, de verwijdering van de gebruikte adsorbentia en de verwerking van de geadsorbeerde VOS. Anderzijds is katalytische oxidatie een efficiënte methode omdat ze gemakkelijk uitvoerbaar is, weinig kost en bij een relatief lage temperatuur werkt. Maar door de onvolledige afbraak van VOS kunnen er secundaire nevenproducten ontstaan.

Niet-thermisch plasma (NTP), dat kan worden geproduceerd door elektrische ontlading bij kamertemperatuur en atmosferische druk, krijgt steeds meer belangstelling op het gebied van de bestrijding van verschillende verontreinigende stoffen. Niet-thermisch plasma is een zwak geïoniseerde toestand die bestaat uit een cocktail van verschillende reactieve species die bij lage temperaturen worden geproduceerd. Hierdoor kan het de luchtverontreinigende stoffen omzetten bij kamertemperatuur. NTP heeft echter nadelen, zoals de vorming van ongewenste toxische bijproducten, een laag energierendement en een onvolledige oxidatie van VOS. Plasma wordt daarom gekoppeld aan katalyse om een werking bij lage temperatuur en een hogere efficiëntie te bereiken. In een dergelijk hybride plasma-katalysator proces kan plasmaontlading bijdragen tot de activering van de katalysator bij een lagere temperatuur en tot de verbetering van de selectiviteit. Dit kan worden bereikt door het plasma in de katalysator te genereren (In-Plasma Catalysis, IPC), of door de plasmareactor en de katalytische reactor in serie te plaatsen (Post-Plasma Catalysis,

PPC). De plasmaontlading produceert reactieve en energetische stoffen in de gasfase. Bij IPC kunnen kortlevende soorten zoals elektronen, ionen, aangeslagen atomen en radicalen rechtstreeks met de katalysator reageren. Bij PPC daarentegen kunnen alleen langlevende stoffen zoals O_3 de katalysator beïnvloeden. IPC en PPC zijn continue processen waarbij het plasma permanent moet worden ontstoken, hetgeen leidt tot een hoog energieverbruik.

Om de nadelen van afzonderlijke emissiebeperkingstechnologieën op te vangen, wordt een innovatief "opslag-regeneratie"-hybride proces onderzocht. Het is gebaseerd op sequentiële adsorptie-thermische katalytische oxidatie (ATC) en sequentiële adsorptie-plasmakatalyse (APC) met tolueen als model-VOS-verbinding. Deze processen worden opgedeeld in twee stappen: de "opslagstap" waarbij gasvormig tolueen aan het oppervlak van het materiaal wordt geadsorbeerd bij kamertemperatuur, gevolgd door de "oxidatiestap" waarbij de geadsorbeerde tolueen-soorten katalytisch worden omgezet in CO_2 en H_2O in een thermische (ATC) of plasma (APC) omgeving. De stappen worden cyclisch herhaald zodat het materiaal kan worden geregenereerd zonder gebruik te maken van een extern systeem. Deze sequentiële en cyclische werking zou helpen om de exploitatiekosten te verlagen door de duur van de regeneratie-/ontladingsstap te regelen ten opzichte van de adsorptie-/opslagstap. In dit werk wordt de reductie van tolueen in zowel ATC- als APC-systemen bestudeerd en vergeleken.

In Hoofdstuk 1 wordt een overzicht gegeven van de VOS en hun bronnen. De invloed van tolueen op het milieu en de menselijke gezondheid wordt aangehaald en de verschillende verwijderingstechnologieën worden beschreven. De combinatie van technologieën wordt geïntroduceerd en het concept van sequentiële adsorptie-thermische katalyse en sequentiële adsorptie-plasmakatalyse wordt toegelicht. Er wordt een overzicht gegeven van de literatuur op het gebied van APC en het effect van verschillende parameters op APC wordt besproken. Verschillende potentiële materialen voor ATC of APC zoals Hopcaliet, Ceria-NR en UiO-66-SO_3H worden beschreven en er wordt een overzicht gegeven van de literatuur over katalytische oxidatie van tolueen. Alle experimentele procedures, de syntheseprotocollen van de verschillende materialen, en de verschillende karakteriseringstechnieken worden gepresenteerd in hoofdstuk 2.

In hoofdstuk 3 wordt de tolueen reductie door ATC met behulp van een commercieel Hopcaliet, Ceria-NR en UiO-66-SO_3H materiaal gepresenteerd. Eerst worden de eigenschappen van deze materialen voor conventionele katalytische oxidatie van tolueen gepresenteerd. Hopcaliet

blijkt een uitstekende kandidaat te zijn door de aanwezigheid van mesoporiën, en door het gemakkelijk kunnen wisselen tussen de verschillende oxidatietoestanden van Cu en Mn. De doorbraak adsorptie curves op Hopcalite met verschillende initiële tolueenconcentraties (50-500 ppm) tonen aan dat, bij lage concentratie, de tolueenmoleculen goed dispergeren op het oppervlak van het materiaal. Als gevolg hiervan is de hoeveelheid irreversibel geadsorbeerd tolueen hoog. Deze studie maakt het mogelijk om de totale adsorptiecapaciteit van ieder materiaal te bepalen, maar in het echte proces moet de concentratie tolueen aan de uitgang van het systeem onder een aanvaardbaar bereik liggen. Daarom wordt het begrip "nuttige adsorptiecapaciteit" geïntroduceerd. Bijgevolg worden de adsorptie-eigenschappen van de materialen gegeven uitgaande van een maximumdrempel van 10 ppm tolueen in de uitlaatgasstroom. De daaropvolgende oxidatie van tolueen, uitgevoerd in een inerte atmosfeer en in de aanwezigheid van een He:O_2-atmosfeer, maakt het mogelijk de redoxeigenschappen van de materialen te beoordelen. Het UiO-66-SO_3H materiaal bezit de hoogste adsorptiecapaciteit vanwege het grote oppervlak, maar dit materiaal vertoont lage oxidatie-eigenschappen. Hopcaliet is de beste kandidaat omdat de CO_2-opbrengst 92.3 % bedraagt. Deze resultaten geven aan dat het beperken van de hoeveelheid tolueen tot "nuttige capaciteit" leidt tot een aanzienlijke verbetering van het CO_2 -rendement en de algehele reductie-efficiëntie.

De poedermorfologie en het gebrek aan een synergie-effect in Ceria-NR en UiO-66-SO_3H laat niet toe om een stabiel plasma te genereren. Daarom wordt alleen Hopcaliet bestudeerd in APC, zoals beschreven in hoofdstuk 5. Verschillende experimentele parameters, zoals de duur van de opslagstap en het ontladingsvermogen van het plasma, worden onderzocht. De energiekosten nemen snel af met een toename van de opslagtijd, evenals de efficiëntie van het APC-proces in functie van energieopbrengst. Een beperking van de hoeveelheid geadsorbeerd tolueen door een korte adsorptietijd levert dus de beste prestaties op het vlak van CO_2-selectiviteit en -opbrengst, maar leidt duidelijk ook tot de laagste energie-efficiëntie en de hoogste energiekosten. Een optimaal vermogen van het plasma kan worden waargenomen in functie van de CO_2-selectiviteit en energieverbruik voor een vermogen van 46 W. Het cyclische sequentiële adsorptie-plasmakatalyse proces toont aan dat de prestaties niet worden beïnvloed door een herhaalde plasmabehandeling en dit wordt ook aangetoond door de verschillende analyse technieken.

Om de efficiëntie van de oxidatiestap verder te optimaliseren, kan de katalytische activiteit worden verhoogd door de impregnatie van een actieve fase zoals zilver. De eigenschappen voor

tolueen reductie van deze op zilver geïmpregneerde Hopcalite materialen worden onderzocht voor zowel ATC in hoofdstuk 4 en APC in hoofdstuk 6. In beide processen wordt een verhoging in de CO_2 selectiviteit en CO_2 opbrengst verkregen bij een zeer lage zilverbelasting met een optimum bij 0.5 wt.% Ag voor ATC en 2 wt.% Ag voor APC, terwijl de 0.5 wt.% Ag het beste blijkt te zijn in functie van energieopbrengst in APC. Deze resultaten tonen het positieve effect van zilvertoevoeging, maar laten ook zien dat zeer actieve species kunnen bijdragen aan de desorptie van niet-gereageerd tolueen door de warmte die aan het oppervlak van de materialen wordt opgewekt door de verbrandingsreactie.

De resultaten voor beide processen, ATC en APC, worden vergeleken en besproken in hoofdstuk 7. In beide gevallen is een goed evenwicht tussen adsorptiecapaciteit en katalytische activiteit vereist. Deze eigenschap is van bijzonder belang aangezien de processen intrinsiek dynamische systemen zijn en afhankelijk zijn van onstabiel gedrag. Bovendien liggen de energiekosten van APC in het aanvaardbare bereik (11.6 $kWh.m^{-3}$). Een verdere optimalisatie van de verschillende experimentele parameters kunnen opschaling toelaten. Zowel met ATC als met APC kan tolueen gereduceerd worden en kunnen conversies > 95 % voor CO_2 worden bereikt tijdens de eerste cyclus en 75 % bij gestabiliseerde materialen.

Deze studie toont aan dat zowel ATC als APC veelbelovende energie-efficiënte tolueen reductieprocessen kunnen zijn dewelke de weg openen naar verdere ontwikkeling en opschaling.

Résumé

Le toluène est un composé organique volatil (COV) toxique présent dans les environnements intérieurs et extérieurs. La dépollution du toluène se fait généralement par adsorption ou oxydation catalytique. Dans ce dernier cas, le toluène est converti en CO_2 et H_2O, mais des espèces toxiques peuvent s'accumuler sur les catalyseurs, provoquant leur empoisonnement, leur désactivation et leur frittage. Pour surmonter ces inconvénients, nous proposons des procédés hybrides innovants de "stockage-régénération". Il s'agit de procédés séquentiels basés l'adsorption suivie de l'oxydation catalytique activée soit thermiquement (ATC) ou par un plasma (APC). Ces procédés sont divisés en deux étapes : "L'étape de stockage où le toluène gazeux est adsorbé sur la surface du matériau et l'étape d'oxydation où le toluène adsorbé est converti catalytiquement en CO_2 et H_2O dans un environnement thermique ou plasma. Le processus ATC a été testé sur de l'hopcalite commerciale (CuMnOx), de la Cérine-NR et de l'UiO-66-SO_3H. L'hopcalite se distingue des autres par sa grande capacité d'adsorption "utile" et ses propriétés redox, permettant une activité et une sélectivité en CO_2 élevées dans l'oxydation du toluène. Dans le procédé APC, la morphologie de la poudre et le manque d'effet de synergie dans la Cérine-NR et l'UiO-66-SO_3H ne permettent pas de générer un plasma stable. Ainsi, seule l'Hopcalite a été étudiée de manière approfondie en APC. Il est observé que l'activité d'oxydation du toluène adsorbé est significativement affectée par les variables du procédé. La stabilité du matériau a été étudiée dans les deux cas au moyen de différentes techniques de caractérisation et il a été confirmé que les matériaux Hopcalite sont très stables. L'activité catalytique a été améliorée par l'imprégnation d'une phase active telle que l'argent, ce qui a conduit à une augmentation de la sélectivité et du rendement en CO_2 avec une charge d'argent très faible, tant dans l'ATC que dans l'APC. Un examen approfondi du matériau a révélé qu'un bon équilibre entre la capacité d'adsorption et l'activité catalytique (Cu^{2+},$^{3+}$ et Mn^{3+},$^{4+}$) est nécessaire. De plus, le coût énergétique de l'APC se situe dans une fourchette acceptable (11.6 kWh-m^{-3}), ce qui signifie qu'avec une optimisation supplémentaire des différents paramètres expérimentaux, il peut être facilement mis à l'échelle de manière rentable. L'ATC et l'APC permettent tous deux d'atteindre une efficacité de réduction du toluène et de conversion en CO_2 supérieure à 95 % au premier passage et à 75 % pour les matériaux stabilisés. Ces résultats montrent que les deux procédés ATC et APC pourraient être des procédés prometteurs de réduction

du toluène, efficaces sur le plan énergétique, et ouvrent la voie à de nouveaux développements et à une mise à l'échelle.

Acknowledgement

This thesis would not have been complete without the support and encouragement of my supervisors, family members, colleagues, and friends. I am honored to acknowledge all those people who contributed in many ways to make this journey memorable and an unforgettable experience for me.

I would like to thank the Interreg project 'Depollutair' for funding my research. I am grateful to the University of Lille, Unite de Catalyse et Chimie du Solide (UCCS), and University of Ghent, Department of Applied Physics, Faculty of Engineering and Architecture for providing the great research platform for my Ph.D.

I would like to express my heartfelt and sincere gratitude to my guide Prof. Axel LÖFBERG. I sincerely thank you for keeping your door always open for discussions which assisted me to acquire the skills and knowledge of this field. His expertise is invaluable in formulating the research questions and methodology. His deep knowledge of the subject and technical aspect helped me to understand the topic in depth. His immense support, guidance helped me during my research journey and in writing of thesis.

I wish to extend my gratitude to my supervisor Prof. Nathalie DE GEYTER for giving me an opportunity to be a part of RUPT and for providing me valuable inputs especially for plasma study. I am grateful for your guidance and efforts you put in my professional growth as a Ph.D. student, and in writing thesis.

I am deeply indebted to Dr. Jean-Marc GIRAUDON for all his help, discussion, advice, continuous support, patience, providing constructive criticisms and mainly your insightful feedback pushed me to sharpen my thinking. You played a critical role in improving the quality of work, being a researcher. I am surely gonna miss our endless discussion.

I would like to thank Prof. Jean-Francois LAMONIER and Prof. Rino MORENT for all of their scientific discussions, inputs and for the guidance during my research. I appreciate all of the technical staff members who have always been willing to lend a hand in completing my characterization studies. I would like to acknowledge the support and advice from the administration staff and secretory staff.

I would like to thank the members of the examination committee for reviewing my thesis and providing the valuable suggestions to improve it. I would like to thank Prof. Patrick DA COSTA for his time to provide me an extensive feedback and valuable comments. I would to thank Prof. Guy DE WEIRELD for a detailed report and valuable discussion. I would like to thank Prof. Antoine ROUSSEAU for his challenging questions and different point of views which allowed me to look at my work in different perspectives. I would like to thank Prof. Pascal Van Der Voort for all of his questions, and comment on the reaction scheme which helped to improve the quality of this research. I would like to extend my gratitude to Prof. Pascal GRANGER and Prof. Filip De Turck for chairing the examination committee.

My sincere thanks to the colleagues and friends, for maintaining enjoyable working atmosphere, for a cherished time spent together in the laboratory, at coffee-breaks and in social settings.

Finally, my personal gratitude towards my beloved family. I would have not come to this point without their encouragement, unconditional support, care and blessings. I would like to pay high regards to my parents, for allowing me to achieve my goal. To my sister and brother-in-law, thank you for your constant support, love, for being beside me through the thick and thin in my life. My deepest gratitude to my nephews.

List of Publications

International journal publications with peer review

1. **Sonar, Shilpa**; Giraudon, Jean-Marc, Kaliya Perumal Veerapandian, Savita; Lamonier, Jean-François; Morent, Rino; Löfberg, Axel ; De Geyter, Nathalie. *Adsorption followed by plasma assisted catalytic conversion of toluene into CO_2 on Hopcalite in an air stream*, ***Catalysts***, 2021, 11(7), 845. IF:4.146.

2. Kaliya Perumal Veerapandian, Savita; Giraudon, Jean-Marc; De Geyter, Nathalie; Onyshchenko, Yuliia; Krishnaraj, Chidharth; **Sonar, Shilpa**; Löfberg, Axel; Leus, Karen; Van Der Voort, Pascal; Lamonier, Jean-François; Morent, Rino. *Regeneration of Hopcalite used for the adsorption plasma catalytic removal of toluene by non-thermal plasma*, ***Journal of Hazardous Materials,*** 2021, 402(1), 123877. IF:10.588.

3. **Sonar, Shilpa**; Giraudon, Jean-Marc, Kaliya Perumal Veerapandian, Savita; Bitar, Rim; Leus, Karen; Van Der Voort, Pascal; Lamonier, Jean-François; Morent, Rino; De Geyter, Nathalie; Löfberg, Axel. *Abatement of toluene using a sequential adsorption-catalytic oxidation process: Comparative study of potential adsorbed/catalytic materials*, ***Catalysts***, 2020, 10(7), 761. IF:4.146.

Conferences participation

1. Societe Chimique de France (SCF, 2021), Nantes, France, Virtual Conference, *Oral presentation*.

2. Second International Conference On Advances in Plasma Science and Technology (ICAPST, 2021), Coimbatore, India, Virtual Conference, *Oral presentation*.

3. Plasma Processing and Technology International Conference (PlasmaTECH, 2021), Paris, France, Virtual Conference, *Poster presentation*.

4. French Conference On Catalysis, (FCcat, 2019), Fréjus, France, *Poster presentation*.

5. Conference On Cold Plasma Sources and Applications (COPSA, 2019), Ypres, Belgium, *attended*.

6. 4th International Conference on Advanced Complex Inorganic Nanomaterials (ACIN, 2018), Namur, Belgium, *attended*.

7. 7th North-European workshop for the treatment of VOCs, Namur, Belgium (2018), *attended*.

Table of Contents

Chapter 1

Introduction and bibliography

Chapter 1 Introduction and Bibliography

1.1 Air pollution

Air pollution is defined as all destructive effects of any sources which contribute to the pollution of the atmosphere and/or deterioration of the ecosystem. Air pollution is caused by both human interventions and/or natural phenomena. It is made up of many kinds of pollutants including materials in solid, liquid, and gas phases. There are two types of air pollution such as indoor and outdoor. People spend from 80 % to 90 % of their lifetimes in indoor environment, which may have important effects on human health and work efficiency. It is necessary to measure and estimate indoor pollution to improve air quality. From this point of view, several organizations such as the World health organization (WHO), the United States Environmental Protection Agency (USEPA) and the French Indoor Air Quality Observatory (OAQI) have established a list of priority indoor air pollutants based on the ubiquity, concentration and toxic effects of the involved substances.

The outdoor pollution is of two type primary and secondary pollutants. Primary pollutants which include: sulphur oxides, nitrogen oxides and carbon oxides. Secondary air pollutants which include gaseous ozone formed from nitrogen oxides, hydrocarbons and particulate sulphate. The main sources of outdoor air pollution are combustion of fossil fuels, industrial processes, waste incineration and natural processes. According global burden of disease project outdoor air pollution has identified as one of the top five risk factors worldwide with approximately 4 million deaths attributable to air pollution in 2016, especially in low- and middle income countries (LMICs) [1].

As air pollution is becoming more and more serious issue, enormous efforts have been made to investigate the abatement of harmful pollutants. Several chemicals are produced from various sources and some of them have been restricted under legal control. Among the harmful chemical pollutants that depreciate the air quality, **volatile organic compounds** (VOCs), which have boiling points in the rage of 50 ~ 260 °C, should be treated. Principally, harmful volatile chemicals need to be removed from the sources before they are spread in the air.

1.2 Volatile organic compounds (VOCs)

VOCs are organic compounds with a vapour pressure over 10.3 Pa at 293.15 K and a pressure of 101.325 kPa [2,3]. They are released into the atmosphere and contribute directly to the air pollution or indirectly through the greenhouse effect and as precursors of the stratospheric ozone. VOCs can have natural and anthropogenic sources. Industries such as chemical and pharmaceutical plants, petroleum refineries, automobile manufacturers, food processors, printers, insulating materials, solvents and cleaning products contribute significantly to anthropogenic part. According to world health organisation (WHO), VOCs can be divided into very volatile organic compounds (VVOCs), VOCs, semi volatile organic compounds (SVOCs) and particulate organic matters (POMs) on the bases of boiling point. The VOCs are classified into various groups e.g. hydrocarbons such as alkanes and aromatics, oxygenated VOCs such as esters, and aldehydes and at times as VOCs containing nitrogen and sulfur. The meticulous classification of common VOCs is displayed in Figure 1.1.

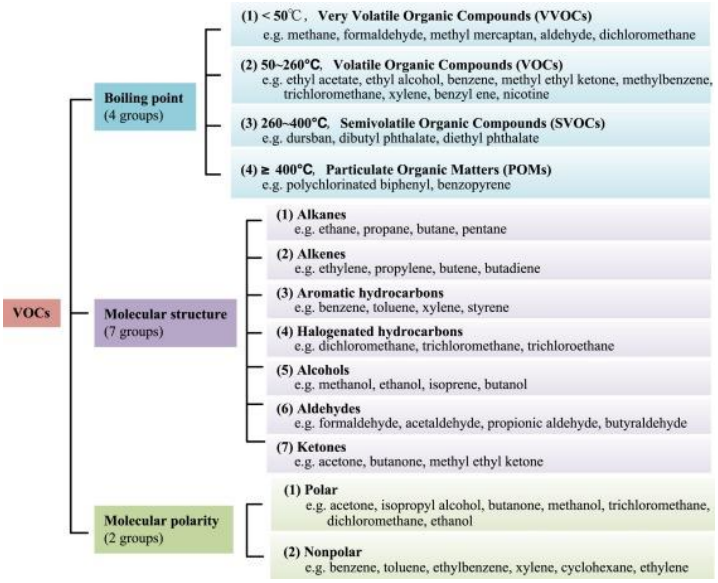

Figure 1.1. *The classification of different VOCs* [4].

Therefore, it is necessary to reduce the VOC emission due to their harmful nature. Different legislations have been adopted which are more and more stringent. Nowadays, although the VOC emissions, as the main pollutants, have significantly decreased due to such tightening legislation as shown in Figure 1.2, these efforts should be pursued.

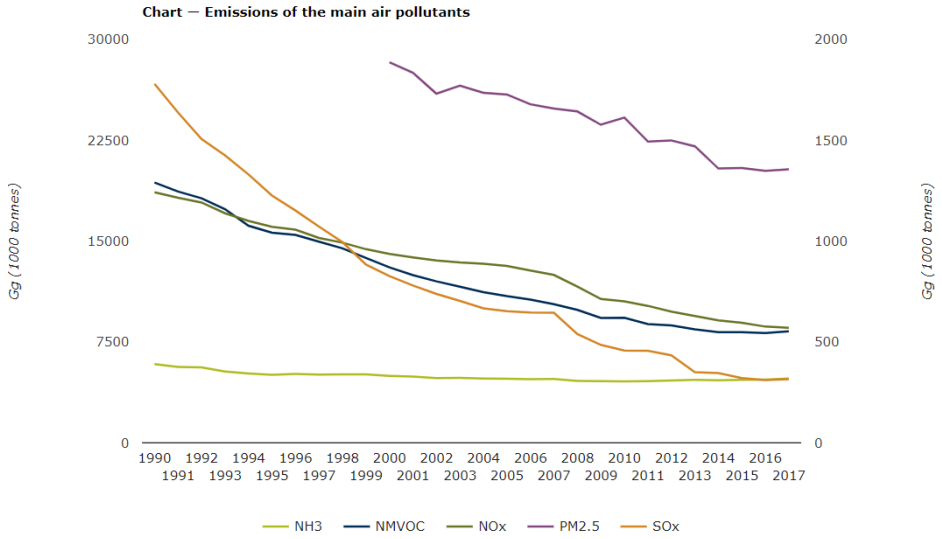

Figure 1.2. *Trends in emissions of air pollutants in the Europe (Source: European Environment agency).*

Considering the emission of the main air pollutants in Europe, the emission reduction commitments for 2020 and 2030 have been set under the NECD (National Emission Ceilings Directive) and for 2020 under the revised Gothenburg Protocol (Figure 1.3). While the original protocol sets national emission ceilings for 2010 for each pollutant, the revised protocol specifies emission reduction commitments in terms of percentage reductions from base 2005 to 2020. Thus, between 2005 and 2020 the EU member states must jointly cut their emissions of volatile organic compounds by 28 % and particles by 22.

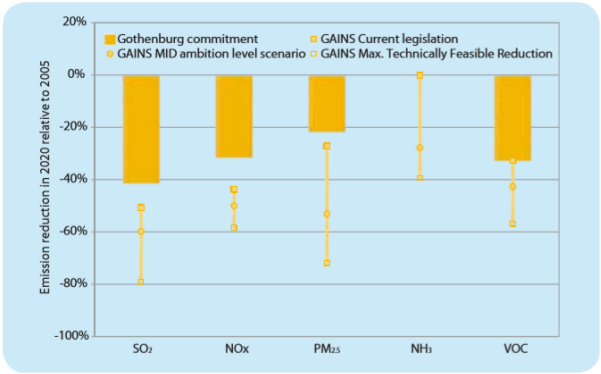

Figure 1.3. *Changes in European emissions in 2020 relative to 2005. The commitments of the revised Gothenburg Protocol are indicated by the bars, while the lines indicate the ranges between the 'current legislation' and the 'maximum technically feasible reduction' cases estimated by the GAINS model. (Source: AirClim Air pollution and Climate Secretariat).*

The VOCs emissions are regulated by different techniques [5] which can be divided into two main groups such as the recovery and destructive methods. The adsorption, absorption, condensation and membrane separation are included in the recovery methods while destruction methods involve incineration, photocatalytic oxidation, ozone catalytic oxidation, plasma catalysis and biological degradation. However, all these techniques seem to be unfavourable for the treatment of large air feedings at relatively low VOC concentration (< 100 ppmv). The advantages and disadvantages of those VOCs treatment technologies are ted in Table 1.1.

Table 1.1. *Comparison of different VOCs treatment technologies (Adapted from* [4]*).*

Treatment technologies	**Principles**	**Temp. °C**	**Conc. ppm**	**Efficiency %**	**Contaminant products**	**Advantages, Costs**	**Disadvantages**	**Ref.**
Destruction Technologies								
Thermal/ catalytic oxidation	Catalysts are used to reduce the temperature of complete oxidation of VOCs	300-820	20-1000	90-98	CO, NOx	Simple and easy, complete treatment, high efficiency, High	Catalyst poisoning, non-recyclable	[6,7]
Photocatalytic oxidation	Catalysts procedure free radicals with strong oxidizing ability under the radiation of light	<90	<500	100	Strong oxidant OH. radicals	Fast and efficient, low energy consumption, High	Low concentration, secondary pollution	[8,9]
Biofiltration	Oxidation occurs under the action of microorganisms	<50	<5000	60-95	Acetaldehyde, Propanol, Acetone	Simple, low cost Security Simple operation, Low	Slow reaction, big equipment, high pressure drop	[10,11]
Plasma catalysis	Plasma is produced under strong electric field, which bombards organic compounds and destroys their chemical structure, thus degrading	<80	<500	74-81	Formic acid, Carboxylic acid, NO_x,O_3	Low energy consumption, wide scope of application, High	Low concentration, incomplete treatment	[12,13]
Recovery Technologies								
Absorption	Dissolve VOCs in water or chemical solvents	Low	500-15000	90-98	Spent solvent	Simple process recycled, Low/moderate	Limited absorption capacity	[13,14]
Adsorption	Use porous materials as adsorbents	0-60	700-10000	80-97	Spent	Cost-effectiveness, flexible operation, low energy consumption, moderate	Poor thermal stability, poor blockage, limited adsorption capacity	[13,15]
Condensation	VOC is cooled to liquid at low temperature	<700	>5000	70-85	-	High concentration, High	High investment cost, high operating cost	[13,16]
Membrane separation	The separation, purification and concentration of differed VOCs are realized by selective separation of membrane	0-45	2000-50000	90-95	Clogged membrane	High efficiency, high recovery efficiency, Moderate/High	High investment cost	[13,17]

1.3 The treatment techniques for VOC removal

The efficiency of the different techniques for VOC abatement is under the dependence of the flow rate and of the concentrations as shown in Figure 1.4 [Source: Waterleau company - Belgium].

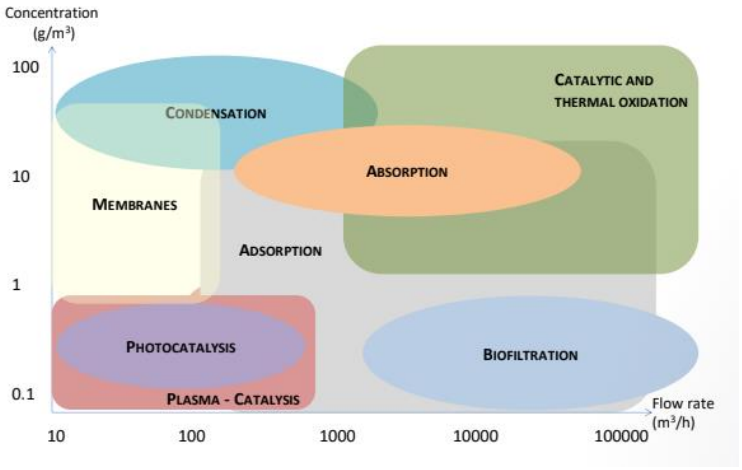

Figure 1.4. *Different techniques for recovery / emission control of VOC (Source: Waterleau).*

1.3.1 Adsorption

Adsorption [5,6] is a widely used technique for the removal of VOCs due to its high efficiency, low cost, and convenient operation. In adsorption process spontaneous accumulation of a gas or vapour (adsorbate) takes place at the solid surface (adsorbent or substrate) as compared to the bulk phase. The adsorption process is generally classified as either physisorption (physical adsorption) or chemisorption (chemical adsorption). **In physisorption** the forces involved are intermolecular forces (van der Waals forces). Therefore, the support can be easily recovered by either calcination, solvent exchange and sonication. **Chemisorption** (or chemical adsorption) is adsorption in which the forces involved are valence forces of the same kind as those operating in the formation of chemical compounds. Thus, chemical adsorption may not be fully reversible, and could require high energy for regeneration. Consequently, the regeneration of the support is a key step in that type of process.

Regeneration is defined as the process followed by adsorption to remove the organic vapours from the adsorbent either by raising the temperature or decreasing pressure or other driving force such as vacuum.

The following parameters were taken into account to assess the regeneration performances of spent adsorbents:

Adsorption capacity (Q): The adsorption capacity (Q) is defined as the amount of VOC adsorbed per unit of mass of adsorbent, once equilibrium has been reached.

Regeneration Efficiency (R.E.) The regeneration efficiency is computed as:

$$R.E = \frac{Q_i}{Q_o} * 100 \qquad (1.1)$$

Where Q_i is the adsorption capacity of the regenerated adsorbent and Q_o is the adsorption capacity of the fresh adsorbent.

The most generally encountered family of adsorbents reported in the literature for VOC removal are activated carbon [4,5,18], zeolites [5,19], alumina [20], metal oxides [21], MOFs [5,22,23]. The porosity [5], pore geometry [24,25] and adsorption sites [26,27] play vital for the removal efficiency. In any case, the used supports need to be replaced regularly to prevent VOC escape after saturation.

1.3.2 Catalytic oxidation

Catalytic oxidation [6,28,29] is the well-known, most effective and economically feasible methods for concentration higher than 1000 ppmv because it can be operate at relatively low temperatures (250–500 °C) and minimize the secondary hazardous air pollutants [6]. The catalytic oxidation at low temperature is helpful for the reduction of the fuel consumption, especially for the large volumes of VOC contaminated air. This process is mainly focused on the complete oxidation of the VOCs rather than transferring it to other products [30–33]. One of the main challenges of catalytic destruction of VOCs is the selection of the proper catalysts from a large number of available catalysts. Due to their wide variety and nature of the range of mixtures of VOCs, it is most often difficult to identify the best possible catalysts. Primarily, the catalyst has to allow ignition temperatures as low as possible. Moreover, it has to be very active, due to the low concentration of VOCs and the large volumes to be treated, and also highly selective in the sense

that only CO_2 and H_2O should be produced. Finally, the catalyst has to withstand the reaction conditions over long periods of operation, i.e. has to be thermally and mechanically stable. There are two classes of catalysts: noble metal and transition metal oxides. Transition metal oxides are cheap but show generally low catalytic activity. Comparatively, noble metals are very active but also very expensive. To avoid such expensive catalysts, the research mostly focuses on the design of cost effective environmentally friendly transition metal oxides [34] as a catalyst and as a support.

1.3.3 Plasma the fourth state of matter

Plasma the fourth state of matter, is an ionized form of gas consisting of free electrons and ions. On the bases of electron (Te) and ion temperature (Ti), plasmas are classified in high and low temperature plasmas. In high temperature plasma ($Ti \approx Te \geq 107$ K, known as hot plasma), the plasma particles (electrons, ions and neutral species) have the same temperature as a result subjected to high gas pressure. Low temperature plasma is divided into two sub category i.e. thermal and non-thermal plasma. In thermal plasma, charged and neutral particles (electrons and protons) have the same temperature in an atom and for non-thermal plasma, the energy is provided to the electrons resulting that the temperature of electrons and ions are different. Therefore, it is characterised as non-equilibrium plasma. Aforementioned, the energetic electrons are responsible for the propagation of reactions in non-thermal plasma (NTP), resulting in dissociation of molecules and generation of reactive species. The energetic electrons can degrade the molecules present in the gas environment and convert them to different transitional products [35] and finally convert these into carbon dioxide (CO_2) and carbon monoxide (CO) [36].

Over the past few decades, NTP has been extensively studied as a processing method in the field of VOC abatement as it can work at atmospheric pressure and ambient temperature. Typically, NTP can be generated by passing gases through electric fields and the generated energy is transferred to the electrons which become highly energetic (kinetic energy in the range between 1-25 eV). These electrons can generate highly reactive oxidizing radicals, neutral particles, ions and UV photons. In turn these active species can then react with the VOC molecules and oxidise them into less harmful molecules such as CO_2. In spite of that, NTP alone system failed at some extents due to the incomplete oxidation of the VOCs, poor energy efficiency and formation of the

unwanted by-products which may be more toxic than the initial pollutant. To overcome these drawbacks researchers, turn to the conception of hybrid systems resulting from the association of another processing method to NTP. Such processing methods can be catalysis [37,38], photocatalysis [39] or adsorption [40]. Since the two last decades, NTP/catalysis and NTP/adsorbent [29] has been considered as attractive hybrid systems allowing to a better energy efficiency and minimizing the undesired by-products formed during the VOC degradation reaction. Recently the combination of adsorption and NTP/catalysis [29] appear to be an efficient low cost processing technique for VOC removal with low energy consumption. However, there is a need today for the improvement of the energy efficiency and CO_2 selectivity for industrial application.

1.3.4 Sequential Adsorption-Thermal Catalytic oxidation (ATC) process

Instead of individual continuous technologies, sequential processes combining several technologies have been proposed for abatement of VOCs such as adsorption+photocatalysis [41], adsorption+plasma catalysis, photocatalysis+plasma, adsorption+catalysis and so on. For instance, storage regeneration processes have been proposed and investigated to eliminate low-concentration indoor VOCs such as formaldehyde and benzene [42]. The sequential method implies two steps: (i) first, the VOC is adsorbed on a material and (ii) then a regeneration of the material through VOC oxidation into CO_2 and H_2O is performed. A key issue in this approach is the design of adsorbent/catalytic materials which should possess balanced properties between storage and regeneration. The bifunctional materials used for the storage of VOCs should thus not only possess high and selective VOC storage capacity, but also be easily regenerated without any release of the VOCs or generation of secondary pollutants. To that order, thermal regeneration [42], non-thermal plasma oxidation [12,43], or ozone enabled regeneration [43,44] have been assessed as regeneration methods.

Regarding adsorption/catalytic regeneration, Guillemot et. al. reported on a double adsorbent/catalyst bed for the removal of tetrachloroethylene (PCE) and methyl ethyl ketone (MEK) in a moist gas stream. The VOCs were physically adsorbed on an appropriate adsorbent (zeolites) at room temperature. After that, the VOCs were desorbed from the adsorbent and catalytically oxidized by supported catalysts (Pt, Ag, etc.) at elevated temperature. It appeared that

the adsorbent-catalyst couple remains efficient for MEK transformation during several successive adsorption/oxidation cycles [45].

In the present study, the sequential adsorption-thermal catalytic (ATC) process is proposed for the abatement of toluene as VOC. The implementation of such process requires to identify proper materials that exhibit both sufficient adsorption capacity and good catalytic performances. This can be approached by different ways, for example by adding catalytic functions to well-known adsorbents or by developing the adsorption properties of known catalytic materials.

1.3.5 Plasma catalysis

Plasma catalysis is a heterogeneous process governed by gas-surface interactions. Two plasma catalysis configurations exist as shown in Figure 1.5 based on the relative position of the catalytic reactor with respect to that of the NTP: in-plasma catalysis (IPC, catalyst incorporated in the NTP reactor) and post-plasma catalysis (PPC, catalyst placed downstream the NTP reactor) [46,47]. Plasma-catalysis allows to get the advantages of the two techniques taken separately without *a priori* the disadvantages. Higher VOC removal efficiency and lower unwanted by-products are generally reported for these processing systems. The enhancement of the performances in terms of VOC abatement has been explained through the possibility of synergetic effects between the catalyst and the NTP [48–52].

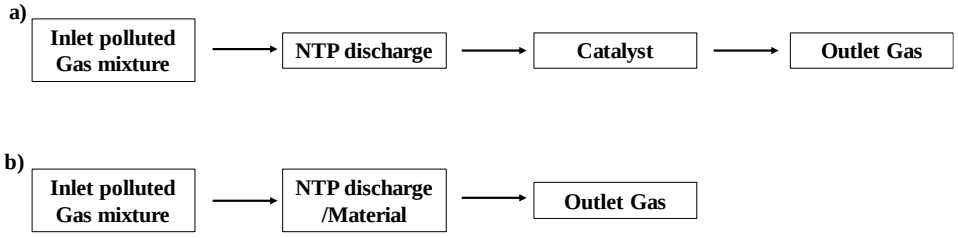

Figure 1.5. *Schematic representation of (a) PPC and (b) IPC used for VOC treatments.*

In these 2 configurations the NTP function continuously which can be a setback in terms of energy cost.

1.3.6 Sequential adsorption plasma catalytic oxidation system (APC)

To overcome the continuous functioning state of the NTP, further optimization of these hybrid systems is still necessary to evolve to a competitive air purification technology. In 1999, an innovative approach, which allows to increase the energy yield of the process was reported by Ogata et. al. [53,54]. A sequential treatment involving adsorption followed by NTP/catalyst oxidation was proposed. Through this new technique, it is expected to treat waste streams over a wide range of VOC concentrations. APC is divided into two steps: an adsorption step followed by an oxidation step. Firstly, the porous material is exposed to the VOC polluted stream. After saturation of the material, the VOC polluted flow is diverted to another similar packed bed reactor while at the same time the adsorbed VOC related species are oxidised simultaneously by the NTP and the catalyst following a cyclic operation as shown in Figure 1.6. The conversion of the VOC is expected to occur mainly through surface oxidation reactions between the adsorbed VOC/intermediates related species and the catalyst assisted by plasma generated reactive oxygen species. The material used in this type of process can be a composite material including an adsorbent and a catalyst but rather a porous bulk oxide catalyst or a supported active phase (noble metal, Transition metal oxide) are currently used.

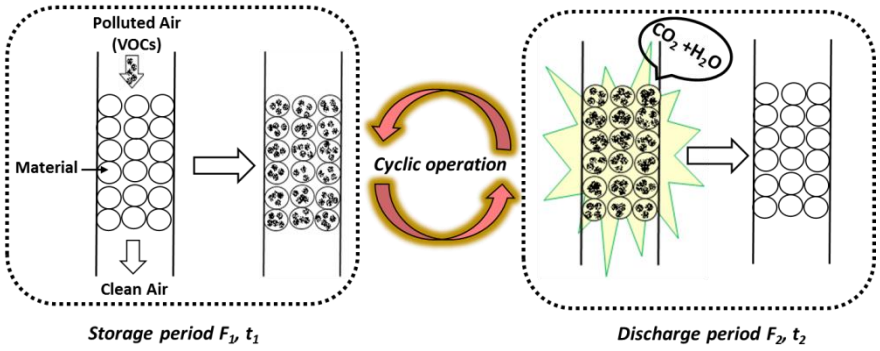

Figure 1.6. *Schematic diagram of the APC system.*

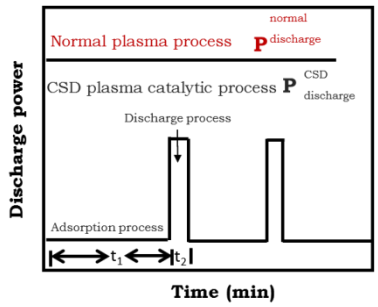

Figure 1.7. *Schematic diagram of the adsorption period (t_1) and plasma discharge period (t_2) APC system.*

The parameter which takes into account the energetic assessment in an APC process is the energy cost EC ($kWh.m^{-3}$) which is calculated according to the following equation [12]:

$$EC = \frac{P_{discharge}}{F_1} \times \frac{t_2}{t_1} \qquad (1.2)$$

Where F_1 is the flow rate ($m^3.h^{-1}$) during the storage period and t_1, t_2 are the storage and discharge period (h), respectively (see Figure 1.7). Hence the low energy cost is lowest for a long-time storage t_1 coupled with a short discharge period t_2. Many works focus on the feasibility and optimization of the duration of the sequential intervals. Optimization of t_1 implies to get first a comprehensive view of the adsorption properties of the material under study, namely the adsorption capacity and its affinity toward the targeted VOC in the absence and presence of water. Second, the impact of the regeneration mode in terms of energy density input, nature of the carrier gas) during t_2 has to be deeply investigated. Furthermore, the efficiency of the process has to be validate through the determination of the CO_2 yield, carbon balance, the determination of possible intermediates during the t_2 period.

Considering the regeneration by NTP, only the influence of process parameters such as the flow rate, temperature, discharge power, O_2 content, relative humidity, number of cycles have been investigated in the literature.

In the present study, the sequential adsorption-plasma catalytic (APC) process is investigated for the abatement of toluene and compared to thermally activated catalysis (ATC).

1.4 Toluene as a VOC model

Toluene is one of the BTEX (benzene, toluene, ethylbenzene, and xylenes) which, also known as methylbenzene is a clear, water-insoluble liquid with the typical smell of paint thinners, redolent of the sweet smell of the related compounds benzene. Toluene is an aromatic hydrocarbon which is widely used as an industrial feedstock as a solvent and reagent (coatings, gym, dyes and medicines etc.). It is the main component in the gasoline. The physical and chemical properties of Toluene are listed in Table 1.2.

Toluene is an aromatic hydrocarbon in electrophilic substitution [55]. The methyl group which is attached to the benzene ring possess a high electron-releasing property compare to the H atom in the same position. This property helps to have sulfation, halogenation and chlorination reaction. Comparison between methyl and phenyl group, methyl group is easily oxidising [56]. Toluene has plenty of industrial and commercial application such as it is the main precursor for the synthesis of the toluene diisocyanate (TDI), xylene, benzene. Toluene is also well known as an octane booster in gasoline fuels. Furthermore, Toluene is used as a solvent due to its properties, such as high solvency, low flammability and high stability. Commercially, it is present in nail polish remover, glues, paint thinner and disinfectants. Day to day toluene global demand has increased is expected to reach above USD 31.8 billion in 2021 [57]. The toluene worldwide production is expected to reach 19.6 million tons in 2020 [57]. Latest study reveals that annual global production of toluene is reported as 540 thousand tons per year and associated price being US $ 1265 per ton [58,59].

Table 1.2. *Physical and chemical properties of Toluene.*

Property	Value
Compound	Toluene
Formula	C_7H_8
Mol.Wt ($g.mol^{-1}$)	92.14
Description	Colorless liquid, sweet, pungent, benzene like
Density ($g.mL^{-1}$) @ 20 °C	0.87
Melting Point (°C)	- 95
Boiling Point (°C)	110.6
ΔG ($kJ.mol^{-1}$)	114.09
ΔH ($kJ.mol^{-1}$)	12
ΔH ($kJ.mol^{-1}$) @ 25 °C	- 3909.8
Kinetic Diameter (PM)	525
Solubility in water ($g.L^{-1}$)@ 20°C	0.52
Vapor Pressure (kPa))@ 20 °C	2.8
Magnetic susceptibility (X) ($cm^3.mol^{-1}$)	$-66.10.10^{-6}$
Refractive index (n_D) @ 20 °C	1.497
Viscosity @ 20 °C	0.590 cP
Dipole moment (D)	0.36
IDLH (PPM)	500

Moreover,~ 86 % of toluene produced is released into the troposphere and then too biosphere (primarily in the troposphere) due to its properties such as high volatility and low solubility in water. Emission of the toluene to the atmosphere is possible due to manmade activities such as industrial processes (33 %), toluene production (2 %) and inadvertent sources (65 %). On the bases of the atmospheric oxidation, the toluene half-life is 12.8 h which contributes in the photochemical-smog which is noticeable. The presence of toluene in the air is hazardous for the ecosystem. Toluene is one of the VOC molecules responsible for the indoor environmental pollution. The report entitled "toxicological profile for toluene" published in 2000 conducted by U.S. department of health and human services presents the health effects of toluene [60]. As shown in Table 1.3, there are three main exposure routes for human: inhalation, oral and dermal.

Table 1.3. Existing information on health effects of toluene (black dot: existing data); adapted from reference [60].

Health Effects	Oral	Dermal
Death	•	
Intermediate		
Acute	•	•
Chronic		
Immunologic/Lyphoretic		
Neurologic		
Cancer		
Reproductive		
Developmental		
Genotoxic		•

The high hazard profile of toluene is highlighted as it covered all the possible health effects listed in Table 1.3. For example, in Virginia, it was reported that 39 deaths were attributed to inhalant abuse from 1987 to 1996, and Hobara et. al. [61] estimated 1 h of exposure to 1800-2000 ppm toluene may be fatal to humans via inhalation. Regarding oral route, only cases of death and acute effect have been reported. Concerning the dermal route, it has been found that exposure of toluene caused the acute effect and genotoxic effect. Due to the adverse effects on human health, WHO (Word Health Organization) has published guideline for the toluene exposure limit. European Union has followed the instruction of WHO: The lowest-observed-adverse-effect level on the central nervous system (CNS) from occupational studies, is approximately 332 $mg.m^{-3}$ (88 ppmv) and the limit of occupational exposure for 8h of work is 188 $mg.m^{-3}$ (46 ppmv) in European Union (EU).

1.5 Plasma catalytic decomposition of toluene by APC process

This section investigates the previous works using APC system for toluene abatement in polluted exhausts. On purpose, Table 1.4 compiles the most relevant experimental parameters and the corresponding results. In terms of results, for each reference, the maximum removal efficiency (η_{Tol}) is given along with the corresponding specific energy density (SIE), i.e. the energy deposited per unit volume of process gas, the CO_2 selectivity, the carbon balance (CB) and the EC values are listed.

Table 1.4. Overview of published papers on toluene removal using APC.

Adsorption					Regeneration/NTP oxidation								
Plasma reactor	**Catalyst/Support/Bulk**	**Toluene concentration (ppmv)**	**Carrier gas and flow rate (mL/min)**	**Amount of toluene with t_1, ,µmol, µmol/.g^{-1}**	**Carrier gas and flow rate (mL.min^{-1})**	**Pdis (W) SIE (J/L)**	**Time (min)** t_1	t_2	**Removal efficiency (%)**	**CO_2 Selectivity (%)**	**Carbon balance (%)**	**EC (kWh/m^3)**	**Ref.**
DBD	**A**g (5 wt%)-HY	100	Dry air 300	-	Dry air 300	3.5 W	225	225	100	100	100	0.099	[62]
	HY								80	80	80		
	Hβ								80	40	60		
	HZSM-5								100	40	60		
	5A								40	10	20		
DBD	Ag (1 wt%) Mn (5 wt%)/SBA-15	21	Dry air 100	15.75 (0.1 g)	Dry air 100	317 J L^{-1}	72	65	100		78	47.7 kJ.h^{-1}.m^3	[63]
	Ag (1 wt%)/SBA-15			13.5 (0.1					-		-		
	Mn (5 wt%)/SBA-15			g) 9.6					-		-		
	SBA-15			(0.1 g)					100		50		
				10.7 (0.1 g)									
DBD	13 X	150	Dry air 400	570	Dry air 100	20 W	-		94	~ 80	~ 25	0.76	[64]
	Co/13X			510			270	62	92.7	~ 90	~ 81.4		
	Ce/13X			301					96.7	~ 83	~ 60		
	Mg/13X			252					97.2	~ 83	~ 63		
	Cu/13X			270					96.3	~ 90	~ 65		
	Co (1-15 wt%)/13X			233-510					-	~ 90	-		
DBD	γ -Al_2O_3	3.75	N_2 2500	13835	O_2 2500	88 W	190	60				0.18	[65]
DBD	H-ZSM-5	1000	Air 200		Air 50	1.5-2.5 W	120	18 0		80.8	86.5		[66]
	2 wt% Fe/H-ZSM-5									83.9	100		
	5 wt% Fe/H-ZSM-5									84.6	100.8		
	2 wt% Fe/Beta									81.9	83.9		
	5 wt% Fe/Beta									85.5	82.3		

Table 1.4. *Overview of published papers on toluene removal using APC. (Continued).*

Adsorption					Regeneration/NTP oxidation								
Plasma reactor	**Catalyst/Support/Bulk**	**Toluene concentration (ppmv)**	**Carrier gas and flow rate (mL/min)**	**Amount of toluene with t_1, ,µmol, µmol/.g^{-1}**	**Carrier gas and flow rate (mL.min^{-1})**	**Pdis (W) SIE (J/L)**	**Time (min)** t_1	t_2	**Removal efficiency (%)**	**CO_2 Selectivity (%)**	**Carbon balance (%)**	**EC (kWh/m^3)**	**Ref.**
DBD	13 X	150					Closed discharge						
	5A		Air 400		Air 400		282	60	~97	2	7	0.17	[67]
	Al_2O_3						30	60	97	40	45	0.41	
							21	60	99	38	39	0.29	
							Ventilation Discharge						
			Air 400		Air 100		282	60	98	20	25		
							30	60	95	20	25		
							21	60	98	15	18		
DBD	γ -Al_2O_3		Air 600	0.35	O_2 600	20 W	90	90	~ 92				[68]
	Ag (2.5 wt%)-MnOx (2.5 wt%)/ γ -Al_2O_3								~ 95				
	Ag (2.5 wt%)-MnOx (1 wt%)-CoOx (1 wt %)/ γ -Al_2O_3								~ 98				
DBD	γ -Al_2O_3	435.98	Air 2000	0.71	Air 2000		30	120	~ 75				[69]
	H-ZSM-5								~ 60				
	1 γ -Al_2O_3:1 H-ZSM-5								~ 87				
	2 γ -Al_2O_3:1 H-ZSM-5								~ 62				
	1 γ -Al_2O_3:2 H-ZSM-5								~ 90				
	1 γ -Al_2O_3:3 H-ZSM-5								~ 85				
DBD	γ -Al_2O_3	435.98	Air 2000	0.71	Air 2000		38	120		95	~ 65	0.52	[70]
	Ag-Mn-C/γ -Al_2O_3						58	120		95	~ 82	0.34	
	Ag-Mn (F)/γ -Al_2O_3						70	120		-	~ 90	0.285	
	Ag (F)-Mn/γ -Al_2O_3						70	120		-	~ 70	0.34	

Table 1.4. *Overview of published papers on toluene removal using APC. (Continued).*

Adsorption							Regeneration/NTP oxidation						
Plasma reactor	**Catalyst/Support/Bulk**	**Toluene concentration (ppmv)**	**Carrier gas and flow rate (mL/min)**	**Amount of toluene with t_1, ,µmol, µmol/.g^{-1}**	**Carrier gas and flow rate (mL.min^{-1})**	**Pdis (W) SIE (J/L)**	**Time (min)** t_1	t_2	**Removal efficiency (%)**	**CO_2 Selectivity (%)**	**Carbon balance (%)**	**EC (kWh/m^3)**	**Ref.**
DBD	Ag (1 wt%)/H-ZSM-5 Mn (3 wt%)/H-ZSM-5 Ce (3 wt%)/H-ZSM-5 Ag (1 wt%)- Mn (3 wt%)/H-ZSM-5 Ce (3 wt%)- Mn (3 wt%)/H-ZSM-5	3±0.1	Air 3000, RH 40±5%	0.3 0.22 0.21 0.27 0.21	Air 3000	2.4 W	480	120		~ 63.8 ~ 69.7 ~ 56.5 ~ 93.5 ~ 70.5	~ 99.8 ~ 99.7 ~ 99.4 ~ 99.9 ~ 99.7	0.03	[71]
DBD	CPM-5 MIL-53 MIL-101	1	Air 3000, RH 0,30%		Air 3000	RH 0 142.2J.L^{-1} RH 30 132.2J.L^{-1}							[72]
DBD	γ -Al_2O_3 CrOx/ γ -Al_2O_3 MIL-101	106	Air 100		Air 100	720.0 J.L^{-1}	20	110	- 100	- 70	- 93.5	6.6×10^{-5}	[73]
DBD	SBA-15 Ni-SBA-15	50	Air 100	15.1 13.5	Air 100		480	120	53.6 71.8				[43]
DBD	SBA-15 2 % Ni-SBA 5 % Ni-SBA 8 % Ni-SBA 10 % Ni-SBA	50	Air 100, RH 40%		Air 100		-	60			~ 53 ~ 60 ~ 69 ~ 58 ~ 56		[74]
DBD	ZSM-5 Ni/ZSM-5 Ca- Ni/ZSM-5	100	Diluent gas (20% O_2/N_2) 100	445.0 318.0 261.55	Diluent gas (20% O_2/N_2) 100		-	60	~ 57.0 ~ 78.0 90.2	39.1 58.8 70.7	51.0 83.3 83.3		[75]
DBD	Ag/ZSM-5	150	Air, 1000	133.9	Pure air, 1000		20	60	100	100	100	0.193 kJ.µmol^{-1}	[76]
DBD	ZSM-5 Ag/ZSM-5 Ce/ZSM-5 Fe/ZSM-5 Mn/ZSM-5	150	Air, 1000	~ 2600 ~ 3200 ~ 1500 ~ 1700 ~ 2250	Pure air, 1000		450 520 270 330 370		~ 85 ~ 95 ~ 75 ~ 50 ~ 55	~ 88 ~ 95 ~ 88 ~ 85 ~ 88	100 100 100 100 100		[76]
DBD	Hopcalite	500±10	Dry air, 200		Dry air, 200	44	300	60	100	86	90	0.74	[77]

1.5.1 Nature of reactor

NTP can be generated by various reactors (Figure 1.8) for VOCs removal. Each reactor has different characteristic such as:

- *Type of discharge*: (DC or pulsed) corona discharge, surface discharge, dielectric barrier discharge, ferro-electric packed bed discharge, microwave, gliding arc discharge, electron beam, etc..
- *Type of power supply*: AC, DC, pulse, microwave, RF, . . .
- *Other characteristics*: electrode configuration, voltage level, polarity, gas composition, . . .

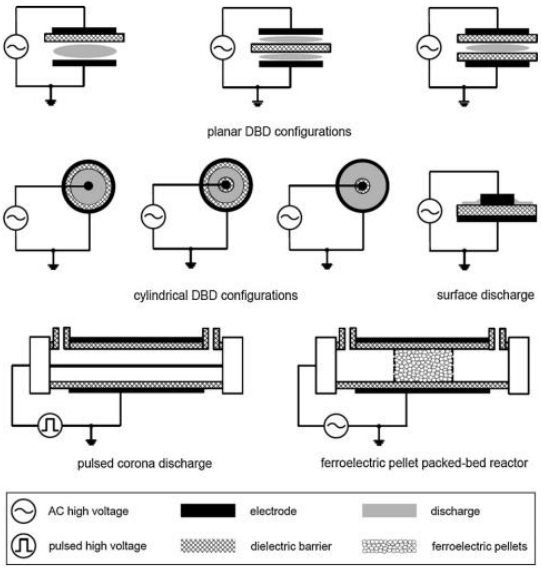

Figure 1.8. *Illustrations of various NTP reactor configurations.*

Among all DBD, plasma for abatements of VOCs have paid great attention due to its several characteristic. DBD, also known as barrier discharge which has following advantages such as:

1) A bulk homogenized volume plasma can be produced with the durable plasma area which ensures the gas to be treated uniformly.
2) DBD is more adequate and compared to other plasma techniques it utilized low energy [78].

DBDs are characterized by the presence of one or more insulating layers in the current path between metal electrodes in addition to the discharge space. The main advantage of DBD is due

to the formation of non-equilibrium plasma conditions which can be provided in a much simpler way than with other alternatives. DBDs have the advantage to have much easier up-scaling [79] and simpler power supply unit. The most interesting property of DBDs is that in most gases at about atmospheric pressure breakdown is initiated in a large number of independent current filaments or microdischarges. At the dielectric surface a microdischarge channel spreads into a surface discharge covering a region much larger than the original channel diameter. In dielectric-barrier discharges the conditions in the microdischarges can be optimized to produce sufficient free radicals for the intended destruction reaction and avoid concentrations where radical-radical reassociation or annihilation reactions become important.

It is well known that the number of microdischarges per period will rise with increasing permittivity. The dielectric constants (ε_r) of typical metal oxides and ferroelectric materials are given in Table 1.5 and show a very large range of values. High dielectric constants are obtained with ferroelectric ceramics but their use as a barrier is difficult, since they tend to fracture when supplying a high current pulse due to their modest dielectric strengths.

Table 1.5. Relative dielectric constants of typical metal oxides and ferroelectric materials [80].

Composition	Dielectric constant
SiO_2	3.9
Al_2O_3	9
ZrO_2	29
HfO_2	25
$HfSiO_4$	11
Ta_2O_5	26
La_2O_3	30
$LaAlO_3$	30
Nb_2O_3	35
TiO_2	30-40 (Anatase), 80-100 (Rutile)
$BaTiO_3$	1700
$SrTiO_3$	2000
$Pb(Zr,Ti)O_3$, $(Pb,La)(Zr,Ti)O_3$	2500
$CaCu_3Ti_4O_{12}$	80000

1.5.2 Properties of Materials

In the APC process, the VOCs are first stored in a material (adsorption stage), and then oxidized by plasma (plasma catalytic stage). As already pointed out, the energy consumption can be lowered by lengthening the adsorption period and/or shortening the discharge time. Therefore, the material of choice for this system requires not only humidity tolerance (resistance to water

adsorption in humid air) and excellent adsorption ability but also has to possess good plasma catalytic performances for total oxidation of toluene.

Recently, various materials have been developed for removing toluene from gas streams mainly at much higher concentration levels (e.g. hundreds of ppm) than those observed in actual indoor environments (hundreds of ppb to several ppm).

Most materials consist of an active component dispersed on a support. In order to improve these catalysts, the main focus has been to test different active components on the removal of toluene in terms of adsorption capacity, decomposition efficiency, carbon balance, and CO_2 selectivity. Different types of Supports such as γ-Al_2O_3, 13X, HZSM-5, SBA-15 and recently Metal organic frameworks (MOFs) have been used in the APC process and have been shown to enhance the oxidation of toluene.

Y. Mok and D. Kim have investigated the oxidation of toluene in an NTP reactor packed with γ-Al_2O_3 pellets as an adsorbent material [65]. A typical sequence is represented in Figure 1.9.

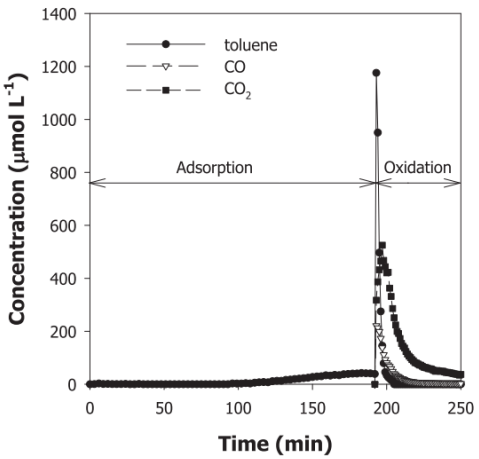

Figure 1.9. *Concentrations of toluene, CO and CO_2 at the outlet of the DBD reactor during the adsorption and NTP oxidation (molar flow rate of toluene during the adsorption step: 102 mmol min^{-1}; flow rate of pure oxygen during the oxidation step: 2.5 L min^{-1}; discharge power: 88 W).*

Experiments were conducted with a toluene molar flow rate of 102 $mmol.min^{-1}$. In the early stage of the NTP oxidation, the concentrations of CO and CO_2 formed from the oxidation of the adsorbed toluene abruptly increased, and then gradually decreased. The time required to oxidize the adsorbed toluene was shorter when the discharge power P was higher. By this method, the gaseous toluene was effectively treated with reasonable electrical energy consumption. The presence of the

dielectric beads consisting of γ-Al_2O_3 pellets in the discharge zone essentially decreases the breakdown voltage due to significant non uniformities of the electric field and local overvoltage, particularly around the contact points between the beads. Hence this process was found to be very effective for the treatment of dilute gaseous toluene.

Due to their excellent characteristics, zeolite based media show high removal efficiency for most VOCs. However, the relatively small pore sizes of these materials limit the application of zeolites for removal of large VOCs. On purpose 13X zeolite exhibited better adsorption of toluene compared with Al_2O_3 and 5Å molecular sieve. HZSM-5 possesses both high toluene adsorption capacity and good hydrophobicity. Furthermore, HZSM-5 was found to be the most promising zeolite support for VOC catalytic decomposition due to its characteristic pore system and high hydrothermal stability as compared to mordenite and beta (Table 1.6) [81].

With that respect various types of zeolites (5A, HZSM-5, Hβ, HY) were chosen as materials to remove toluene under NTP conditions [62].

Table 1.6. Composition and pore diameters of the zeolites used.

Type	FWI[a]	Pore diameter(Å)	Si/Al
5A	LTA	5	2
HZSM-5	MFI	5.5	25
Hβ	BEA	6.6	25
HY	FAU	7.4	5.3

[a] Framework type

The results showed that all the zeolites, with or without toluene adsorption abilities, significantly enhanced the toluene removal efficiency in the plasma discharge zone. Moreover, the carbon balance and CO_2 selectivity showed the same tendency of HY > Hβ (HZSM-5) > 5A, which was basically consistent with toluene adsorption ability, while being opposite to the ozone emission.

Santa Barbara Amorphous-15 (SBA-15) is a highly stable amorphous mesoporous silica sieve developed by researchers at the University of California at Santa Barbara. SBA-15 and its modified have attracted more and more attention as a promising material in chemical engineering and environmental science because of the large surface area, large pore size and high stability [82,83].

The mesopore-silica with uniform hexagonal pores and regular pore channels exhibits unique structure properties which lead to excellent toluene adsorption and desorption performances [84,85].

MOFs constitute a new class of porous materials exhibiting excellent specifications, such as exceptionally large surface area, high gas adsorption, substantial storage capacity, and extra-high porosity [73]. It is recognized that the uniform crystal size and size distribution of MOFs [73] facilitate mass transport phenomena, including adsorption of target compounds, diffusion into pores, and desorption of the products, providing a favorable condition for catalyzing a reaction [73].

MOFs also have an abundant amount of metal content (20–40 wt.%) in the form of metal nods, with free and exchangeable active sites [73]. The presence of these metal sites induces heterogeneous catalytic properties in MOFs [73]. The above-mentioned specifications of MOFs suggest that these materials can be excellent candidates as DFA/Cs (dual functional adsorbent/catalyst) for the removal of VOCs in a NTP-catalytic reactor.

Table 1.7. Comparison of maximum adsorption capacities toward toluene of ZSM-5 and some other adsorbents reported in the literature.

Adsorbent	**Temperature (K)**	**Maximum adsorption capacity**		**References**
		mmol.g^{-1}	**(*10^3 mmol.m^{-2})**	
ZSM-5	298	0.93	3.01	[86]
Na-ZSM-5	473	0.92	2.5	[87]
HMOR(Si/Al=10)	473	1.07	2.2	[87]
NaY	303	~2.3	-	[88]
EA95	298	1.7	3.4	[89]
CVD80	298	1.6	2.6	[89]
MCM-41	298	4.98	3.3	[90]
S-MCM	298	2.49	2	[90]
MOF-177	298	6.06	2	[91]
MCM-48	300.15	1.08-3.45	2.3-2.2	[92]
Silica-Alumina	300	0.085	0.13	[93]
DAY zeolite	298	~1.8	2.5	[94]
	318	~1.5	2.1	
Na-Y/H-Y/USY/ZSM-5	298	~2-2.5 or 3-4	3.3-4.1	[95]

EA95 and CVD80 refer to single-wall carbon nanotubes manufactured by electric arc and the HiPco by chemical vapour deposition; DAY zeolite represents a dealuminated Y-zeolite.

As a way of comparison, Table 1.7 lists the maximum toluene adsorption capacities on ZSM-5 [86] and from literature references, using different adsorbents under similar conditions. As can be seen, the adsorption capacity of ZSM-5 toward toluene was in excellent agreement with the

observed values using other porous adsorbents such as NaZSM-5, HMOR, NaY and some activated carbons EA95, CVD80.

However, a systematic analysis of these different supports on the catalytic performance has not been yet performed. Different supports may have different BET surface areas which may play an important role in the adsorption process. Moreover, each support has a different dielectric constant which will affect the discharge character of the catalyst as well as affect the kind and number of active species.

Sequential adsorption plasma oxidation system was used to remove toluene from simulated dry air using-Al_2O_3, HZSM-5, a mixture of the two adsorbents under atmospheric pressure and room temperature [69]. After 120 min of plasma oxidation, γ-Al_2O_3 had a better CB (∼75 %) than HZSM-5, but the CO_2 yield of γ-Al_2O_3 was only ∼ 50 %; and there was some desorption of toluene when-Al_2O_3 was used. When a mixture of HZSM-5 and γ-Al_2O_3 with a mass ratio of ½ was used, the carbon balance was up to 90 % and 82 % of this was CO_2. Moreover, the mixed supports produced less O_3 and N_2O by-products compared to γ-Al_2O_3. However Organic intermediates or toluene remaining on the surface of the supports are responsible for the deactivation of the supports.

Cu/13X, Co/13X, Ce/13X and Mg/13X catalysts were prepared by an impregnation method [64]. 13X zeolite exhibited excellent toluene adsorption capacity but weak catalytic performance. The adsorption capacity was reduced and catalytic ability significantly improved by loading active compounds on 13X zeolite. The active compound blocked the pores and reduced the specific surface area of 13X but it decomposed ozone to produce more atomic oxygen species, resulting in decreased adsorption capacity but enhanced catalytic performance. Co/13X catalyst exhibited good toluene adsorption capacity by π-complexation formation between Co^{3+} and toluene molecules. Co_3O_4, which was a P-type semiconductor, had excellent oxygen adsorption capacity and converted oxygen into O^- and O_2^- easily, presenting active centers for toluene adsorption and plasma catalysis.

It has been reported that Ag-based catalysts show excellent adsorption ability for toluene [71]. Previous work [68,96] showed that AgO_x catalysts have better CO_2 selectivity than MnO_x catalysts in the plasma catalytic oxidation of adsorbed toluene. Fan et. al. [97] reported that MnO_x

species showed good performance in the plasma catalytic oxidation of toluene and were able to suppress the production of by-products. Wang et. al. [71] reported that Mn and Ag-based bimetallic catalysts have better performance than monometallic Mn or Ag-based catalysts. Furthermore, the bimetallic catalysts had a relatively high adsorption capacity compared to the monometallic analogues. For a supported bimetallic catalyst, it is well known that the impregnation sequence of the active component might affect the existing state or dispersion of the active component. On purpose, the effects of altering the Ag and Mn impregnation sequence on the synthesis of Ag-Mn/γ-Al_2O_3 materials were tested in an adsorption-plasma catalytic process of toluene removal [70]. The results show that when Mn was impregnated first (Ag-Mn(F)/ γ-Al_2O_3), the catalyst had longer breakthrough time, less emission of toluene, better carbon balance and better CO_x yield compared to the co-impregnated catalyst Ag-Mn-C/γ-Al_2O_3, the catalyst with Ag impregnated first Ag(F)-Mn/γ-Al_2O_3 and bare γ-Al_2O_3.

In recent years, many researchers have explored the application of M-Mn catalysts in catalytic combustion of VOCs [71], among which the Ag-Mn [71] and Ce-Mn [71] catalysts were intensively investigated. These studies showed that the addition of Ag could significantly promotes the reducibility of the manganese oxides [71], the formation of abundant active lattice oxygen [71] and thus the catalytic activity; the addition of Ce often leads to structural stabilization of the manganese catalysts and greater specific surface areas [71]. In order to look for a synergetic effect Ag/HZSM-5, Mn/HZSM-5, Ce/HZSM-5 were prepared by impregnation as well as the bimetallic Ag-Mn/HZSM-5, Ce-Mn/HZSM-5 catalysts and compared by both their adsorption capacity and catalytic oxidation performance of adsorbed toluene with the help of air-plasma [71]. The drawing conclusions are the following : The addition of Ag increases the adsorption capacity of HZSM-5 by the π interaction between the aromatic ring of toluene and Ag which is not encountered with Mn and Ce. Additionally, the combination of Ag and Mn supported on HZSM-5 promotes the complete oxidation of the adsorbed toluene. Although the Ag-Mn/HZSM-5 catalyst suffers from deactivation due to the accumulation of organic intermediates on the catalyst surface, calcination appears as an efficient method to restore activity.

Moreover, Xu.et.al. [75] studied effect of Ca modification on the Ni/ZSM-5 for efficient toluene oxidation. The catalysts were prepared by impregnation method. Sequential adsorption plasma catalysis was studied for 100 ppm of toluene in diluent gas (20 % O_2/N_2). ZSM-5 had the

highest adsorption capacity than other catalysts. But, Ca-Ni/ZSM-5 showed the best potential for toluene conversion (90.2 %) and CO_2 selectivity (70.7 %). The addition of Ca helps in coke removal, through its effect of valence band of catalyst.

Additionally, Yu et.al. [76] studied effect of position of the catalyst as well as operation mode. The catalysts were synthesized by wet impregnation method. 5 % of metal (Ag, Ce, Mn, Fe) impregnated on ZSM-5. Among all Ag/ZSM-5 had highest adsorption capacity due to the availability of empty s orbital and formation of π-complex. Among different operation mode SIPC standing outstanding approach. In which Ag/ZSM-5 showed the mineralization rate 96 % and CO_2 selectivity 98 %.

Metals (Ag, Mn and AgMn) loaded SBA-15 catalysts were prepared by an impregnation method [63]. Two types of plasma catalytic system, including continuously introduced and adsorption-discharge plasma system, were studied for abatement of 21 ppm of toluene in dry air. AgMn/SBA-15 had the highest breakthrough capacity among the four catalysts. The activities of the fresh catalysts for the toluene conversion and carbon balance in both catalytic systems decreased in the following order: AgMn/SBA-15 > Ag/SBA-15 > Mn/SBA-15 > SBA-15, which was consistent with the ozone decomposition activities. Compared to traditional continuously introduced plasma system, the adsorption-discharge plasma system slightly increased toluene conversion and significantly improved the carbon balance. The different performances encountered for the two processes were mainly due to the formation of carbonaceous intermediates.

Ni-SBA catalyst was also applied to investigate the catalytic decomposition performance of toluene in adsorption–discharge non-thermal plasma system [43] as the Ni-based catalysts are active in ozone decomposition and inhibit carbon deposition. The main results showed that pure SBA had longer breakthrough time and higher adsorption capacity than Ni-SBA, while Ni-SBA catalyst exhibited eminent properties in toluene mineralization rate and CO_2 yield. Moreover, the adsorption amount of toluene over Ni-SBA increased after plasma treatment due to the decrease of metal oxide particle size and enhancement of dispersion that may be beneficial for toluene adsorption and catalytic stability.

The experimental results showed that the incorporation of Ni into the ordered hexagonal mesopores of SBA afforded a remarkable enhancement in the catalytic activity and CO_2 selectivity. However, the presence of the metal oxide lowered the specific surface area and

decreased the adsorbed amount of toluene. In situ FTIR was used to explore catalysts adsorption process, and revealed that incorporation of Ni resulted in partial oxidation of toluene over Ni-SBA. The catalysts, after several adsorption-plasma process cycles, were characterized by XRD and TEM techniques. The results indicated that the plasma treatment tended to decrease the size of the metal oxides and increase their dispersion in the support surface and influence the adsorption and catalytic performance. In addition, GC-MS spectra were used to analyze the by-products and speculate the reason of catalysts deactivation.

Furthermore, Xu et.al. [74] did extendable study on impregnated Ni (2-10 %)-SBA-15 to evaluate towards different relative humidities of air (RH). The experimental result showed that 5 % Ni-SBA-15 sample exhibited higher toluene mineralization (71.8 %) than other samples. But different RH had a negative impact on toluene degradation due to different adsorption capacities and blocking of active sites on the catalysis surfaces. Interestingly, humidity decreased the yield of CO and increased in the production of CO_2 due to enhanced oxidation of both CO and other intermediates during the reaction. This study may provide new sights for plasma catalysis removal of industrial VOCs at medium and high RH.

The studies about the investigation of the potentialities of MOFs as DFA/Cs for the removal of toluene in a APC process are very scare [72,73]. In a first study [72], the adsorption and oxidation abilities of MIL-101, MIL-53 (MIL: Materials of Institute Lavoisier) and CPM-5 (CPM: Crystalline Porous Material), were studied for the removal of one 1 ppmv toluene in a DBD plasma-catalytic reactor in dry (RH = 0 %) and humid (RH = 30 %) air. As the MIL-101 possesses the highest adsorption capacity in dry air, MIL-53 capacity surpasses those of MIL-101 and CPM-5 at 30 % RH. Otherwise, it is found a high toluene removal efficiency (≈ 90 %) for all MOFs in dry air which decreases at 30 % RH. Furthermore, in the course of the NTP-oxidation reaction different organic compounds and ozone are detected as by-products. Finally, no significant change occurs in terms of MOF structure.

In the second study [73], the catalytic performance of MIL-101, a type of chromium-based metal-organic frameworks (MOFs), was assessed and compared to those of Cr_2O_3/γ-Al_2O_3 and γ-Al_2O_3 in a DBD reactor considering a toluene (106 ppmv) contaminated air flue gas. The MIL-101 exhibited a significantly high toluene conversion, which was 20 % and 35 % higher than Cr_2O_3/γ-Al_2O_3 and γ-Al_2O_3, respectively, all other things being equal, as well as higher carbon balance and CO_2 selectivity. The analysis of by-products on the surfaces of the catalysts before

and after reaction demonstrated that MIL-101 had better resistance towards by-products accumulation compared to Cr_2O_3/γ-Al_2O_3 and γ-Al_2O_3. The loading of MnO_x on MIL-101 further promoted its catalytic performance.

To sum up, these two studies show that MIL-101 exhibits attractive catalytic properties in APC process for the decomposition of toluene.

1.5.3 Effect of the generation of the surface species

The presence of the heterogeneous catalyst changes the physical characteristics of the discharge which will be affected to chemical activities. Toluene passing through the reactor towards the plasma discharge zone where catalyst/adsorbent bed present. In which toluene can be trapped on catalyst/adsorbent bed surface either by physisorption or chemisorption or by both. Physisorption is nothing but the due to the van der waals forces and chemisorption is nothing but the reaction which helps to generate the new type electronic/ionic/covalent bonds which is irreversible in nature i.e. active sites are consumed [98]. For example, Huang et.al. [62] reported different zeolites such as 5A (Pore diameter 5 Å), HZSM-5 (Pore diameter 5.5 Å), Hβ (Pore diameter 6.6 Å), HY (Pore diameter 7.4 Å) and Ag/HY for 100 ppm toluene adsorption-plasma catalysis system. Results indicate that HY shows high adsorption capacity among all due to presence of the surface acidic characteristic; it may be due to the lower Si/Al ratio as compare to other zeolites. Comparatively, Ag/HY possess good adsorption capacity than HY because presence of Ag metal possessed vacant s orbital and electron availability for the formation of the π-complexation which helps for the increase the adsorption capacity of the catalyst.

1.5.4 Effect of plasma on performance

In adsorption-plasma catalysis study, plasma could be switch on the only for the certain time of the period on the toluene saturated catalyst surface to prompt oxidative desorption of the VOCs which leads to regeneration of the catalyst. The plasma discharge helps for the desorption of the toluene degradation. Kim et. al. [99] explained that there are two type of the discharge: 1) Partial discharge which contains the countless contact points of catalysts [100]. The partial discharge is come into sight when the voltage reaches to the plasma set value. The partial discharge is possible due to the electric field augmentation which happens by the dielectric constants of the packing material [100]. 2) The another discharge is the surface streamers. Wu et. al. [73] found the microdischarge and the combination of the partial discharge and surface streamer. They

observed the change in the voltage and current which indicates that the interaction between plasma and catalyst. In this catalyst can be activated due to active species which are generate in the microdischarge zone which further helps to decompose the toluene by sequential manner.

The plasma may also affect the catalyst properties and as compare to the thermal catalysis plasma catalysis has been shown the high adsorption at the catalyst surface. There is not clear explanation has been found so far. The adsorption probability is essential for the all the surface mechanisms. The adsorption probability at the catalyst surface is rise with surface area of the catalyst. The plasma give rise to the formation of smaller nanoparticles, leading to the high dispersion and hence a large total surface area.

The breakdown voltage is reduced by the packing material, thus the increasing energy efficiency. The presence of catalyst changes the physical and chemical properties of plasma.

1.5.5 Effect of the relative humidity

Relative humidity is a key factor for the synergy of plasma-catalysis and energy efficiency of plasma processing. The presence of water decomposed into ·OH which has a strong oxidation power over different active species such as oxygen atoms, metastable nitrogen molecules and atoms. The presence of water influenced the characteristic of DBD. The presence of water overlap on the surface of dielectric, as a result surface resistance reduced and increased the dielectric capacitance, which leads to decline of total transferred discharge. In packed DBD, the presence of water may poison the catalyst or block the active sites. Therefore, the resistance of water study should be considered when choosing a catalyst.

In sequential study, the presence of the highly concentrated humidity may overlap the active site of the catalyst and decreases the formation of the O_3 and oxygen species which play crucial role for the oxidation of the toluene [101]. The presence of the humidity helps to decrease the formation of CO and have the good selectivity towards the CO_2 . Huang et. al. [102] found the combination of the TiO_2 or MnO_x and optimum water vapour helps for the high CO_2 selectivity and carbon balance. Fan et. al.[97] exemplified the effect of different humidity range on the removal of the mixture of the VOCs such as BTX (Benzene, Toluene and Xylene) by using MnO_x/Al_2O_3 (5 wt. % Mn). The decomposition of BTX was inhibited by the presence of relative humidity and ozone. Wu et.al. [103] examined the Ni based different support for the removal of the toluene in dry air and in humidity. They have found the complete removal of the toluene in dry

air condition but in presence of the relative humidity they observed a negative effect of water on the decomposition of the water due to presence of the water cluster and blockage of the reactive species. Bahri et. al. [72] inhibited the metal organic framework such as MIL-101, MIL-53 and CPM-5 under the dry air and relative humidity (RH = 30 %) condition. They found that complete decomposition in dry condition but having negative impact on all MOF due to presence of the 30 % RH. The presence of the water molecule restricts the toluene molecule to reach to the active centre as a result there was decrease in the adsorption capacity.

1.5.6 Effect of the flow rate

The gas flow rate is one of the main parameter to control the desorption of the toluene and oxidation time. When gas flow rate increases, the residence time of the gas stream is decreased which decreases the exposure time of plasma during the regeneration period, resulting in the decomposition efficiency being suppressed. The system has high specific input energy (SIE) when gas flow rate is low, meaning that the system required high energy for the desorption and oxidation process. On the other hand, if there is low gas flow rate, there may be insufficient oxygen species available to react with adsorbed toluene, resulting in decreasing in mineralization rate and CO_2 selectivity. Youn et. al. [66] found that the low flow rate of the gas leads to the higher production of the byproducts rather than the selective product. Therefore, the choice of gas flow rate in sequential process is depend on experiment condition.

1.5.7 Discharge power

The discharge power is the key factor for the adsorption-discharge process. The discharge power calculates by using voltage and current (V-Q) Lissajous method. The discharge power helps to calculate the specific input energy (SIE). Yao et. al. [104] studied the voltage and current lissajous method in presence and the absence of the catalyst. They vary the discharge power (16-20 W) as a function of the applied voltage for different catalysts. They found that the peak intensity decrease in the presence of catalyst and the number of the microdischarge slightly increased which did not have significant influence on the degradation of the toluene. Wu et. al. [73] have done study of the V-Q Lissajous. The toluene removal efficiency (TRE) is found on the basis of the specific input energy (SIE). Wang et. al. [105] depicted the toluene removal efficiency as a function of the SIE varies from 10-325 JL^{-1}. They found that as SIE increases the TRE is also

increased, regardless the catalyst. At 160 JL^{-1}, In absence of the catalyst it shows 32 % TRE and introduction of the catalyst in the discharge zone with plasma enhance the TRE till 78 %. Mok et. al. [65] studied the effect of the discharge power on the toluene removal by sequential manner. They found as the discharge power increases the rate of the oxidation to convert the adsorbed toluene into the CO and CO_2 is faster.

Xu et. al. [106] studied the effect of the SIE (50-300 JL^{-1}) on the different catalyst such as MCM-41, 60Co-MCM-41 impregnated and the Co (20-100 %) incorporated on the MCM-41. The toluene conversion and CO_x selectivity increases as SIE increases and for 60Co-MCM-41 incorporate they found the 100 % toluene conversion at 226 $J.L^{-1}$ further increase in the SIE leads to slightly increment for CO_x selectivity. The trend was found for all the catalyst was Co 60 % incorporated on the MCM-41 > 60Co-MCM-41impregnated > MCM-41> NTP alone. Qin et. al. [107] found the correlation of the formation of the microdischarge with dielectric constant of the adsorbent/catalyst. The trend was observed ZSM-5-$BaTiO_3$ > ZSM-5-TiO_2 > ZSM-5-γ-Al_2O_3 (Figure 1.10). Yi et. al. [67] studied the degradation of the toluene in the two different discharge zone such as ventilation and the closed discharge. They found that for the low concentration of toluene rather VOC can be degrading by using closed discharge due to the prolongation of the residence time of the toluene and the ventilation discharge is more suitable for the high concentration of the VOC or toluene because more oxygen species has been generated.

Youn et. al. [66] studied the current patterns and Lissajous plot for Fe loaded ZSM-5 and Beta. They found consumption energy is more for Fe content zeolite than individual zeolite. For Fe/ZSM-5, they observed a dense microdischarge than the Fe/Beta. This indicates that Fe/ZSM-5 have high microdischarge per pore volume as a result it has more active species than Fe/Beta. The effect of different voltage 14-20 kV was examined by Yu et.al. [76]. In this study, they carried out a comparative study of different protocol for the removal of toluene, such as CIPC, CPPP, SIPC and SPPP. Among all, SIPC is standing as an outstanding process. This is because in SIPC, most of the adsorbed toluene decomposed by electrons and active species and convert into CO_2 and H_2O. Moreover, they have measured Voltage-current waveform with and without catalyst. The packing of material leads to increasing in the current intensity and microdiscahrge.

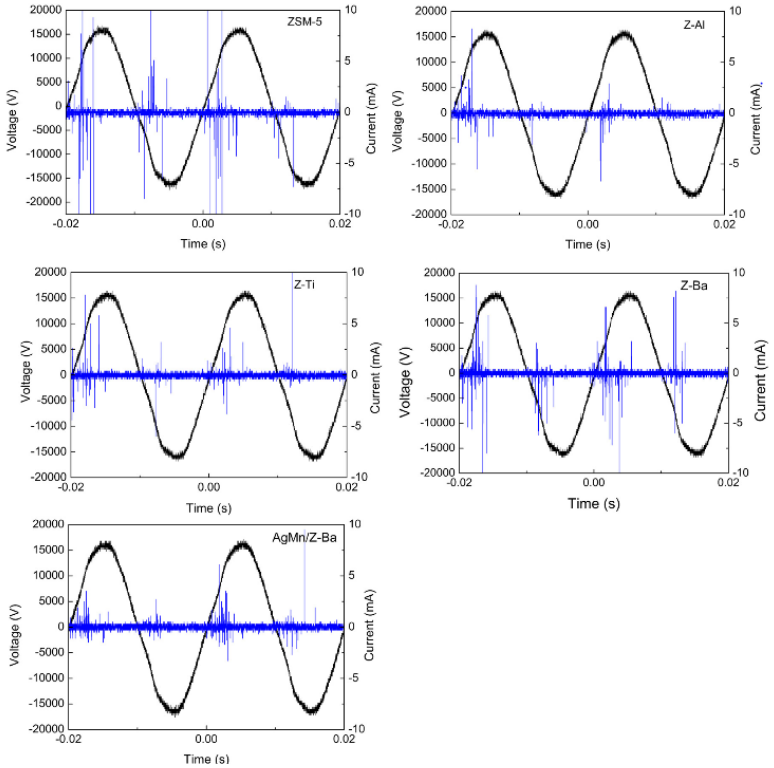

Figure 1.10. *Typical discharge voltage-current waveform of the ZSM-5, ZSM-5-γ-Al_2O_3, ZSM-5-TiO_2 , ZSM-5-$BaTiO_3$, AgMn/ZSM-5- $BaTiO_3$.*

This indicates that the introduction of Ag/ZSM-5 in the reactor changes the bulk streamers to surface streamer on catalysts surface. The choice of proper voltage and current is essential to have good mineralization rate, to avoid unwanted byproducts (O_3, N_2O) and energy efficiency [79].

1.5.8 Regeneration of the materials

The role of non-thermal plasma in the regeneration of the materials mainly takes advantage of active species like O_3, O and OH radicals in the area of the surface to modify the nature of the adsorbed toluene species. Mok et. al. [65] reported that the adsorption sites on γ-alumina are occupied with toluene when plasma is off. The adsorbed toluene is oxidized with the plasma turned on, resulting in increase in the number of vacant sites available for ozone adsorption. This phenomenon leads to ozone decomposition producing more atomic oxygen on the surface catalysts [65]. More active oxygen species further enhance the toluene oxidation; meanwhile, more toluene or organic by-products will be removed from the surface of catalysts. Therefore, the catalyst can

obtain more active sites compared to the absorption process with the help of plasma. An efficient catalyst regeneration technology can be achieved by using a sequential process of adsorption and NTP discharge. The sequential treatment, i.e. adsorption followed by NTP oxidation, is expected to treat waste streams over a wide range of VOC concentrations.

1.6 Mechanism of Toluene decomposition

1.6.1 Scheme of toluene decomposition in ATC process

It is postulated for sequential adsorption-thermal process (ATC) similar degradation pathways than those observed for catalytic toluene oxidation reaction. The models for VOC oxidation include three main mechanisms such as Mars-van Krevelen (MvK), Langmuir-Hinshelwood (L-H) and Eley-rideal (E-R) mechanisms. When regarding transition metal oxides, $CuMnO_x$ show usually high activity for toluene oxidation [108–110]. However, these catalysts are difficult to characterize when they are poorly crystallized in terms of copper and manganese speciation as well as lattice defects and oxygen vacancy concentrations which strongly depends on Cu/Mn ratio and on the mode of preparation. Due to the multivalent character of Mn and Cu, the MvK mechanism also known as redox mechanism has been invoked for the oxidation of toluene on such CuMnOx entities. Firstly, toluene molecules interact with surface lattice oxygen resulting in the formation of oxygen vacancies. In the presence of gas-phase oxygen, reduced manganese and copper ions react with gaseous O_2 refilling the oxygen vacancies.

On this purpose, Li. *et al.* [111] reported recently on Mn-Cu bimetallic oxides prepared by a one-step hydrothermal method. It is shown that the lattice defect and oxygen vacancy concentrations can be tuned by controlling the Cu/Mn molar ratio. Particularly, emphasis was put on the role of lattice oxygen and the reaction pathways of toluene oxidation based on proton transfer reaction-mass spectroscopy (PTR-MS). Owing to the PTR-MS results, it was found that toluene oxidation worked *via* the MvK mechanism. Toluene was firstly absorbed on the catalyst surface and further reacted with lattice oxygen (O_{latt}), which resulted in the reduction of the metal oxides. In the course of the reaction, adsorbed toluene was firstly oxidized to benzyl alcohol, which further reacted with O_{latt} to produce benzaldehyde and benzene. After that, the deep oxidation of benzene allowed to form phenol and benzoquinone. Subsequently, the ring of benzoquinone was easy to open and produced some by-products before total mineralization. Secondly, the consumed O_{latt} was replenished by gaseous O_2 and the reduced metal oxides were oxidized again

to regenerate O_{latt} as represented in Figure 1.11 for the catalytic oxidation of toluene over $MnCu_{0.5}$ catalyst. Based on Raman, XPS and O_2-TPD results it was shown that $MnCu_{0.5}$ catalyst exhibited larger oxygen capacity and easier oxygen species mobility. Concurrently, the homogeneous dispersion of Mn, Cu and O was beneficial to improve the redox reaction. These properties were claimed to enhance the continuous transfer of electrons from the metal oxides to the adsorbed O_2 that would contribute to form O_{latt}. The used $MnCu_{0.5}$ catalyst maintained its O_{ads}/O_{latt} ratio, indicating that $MnCu_{0.5}$ had a good stability, and the redox cycle could be continued to catalytic oxidation of toluene. As a result, all these factors promoted and determined the process of ring cleavage and deep oxidation.

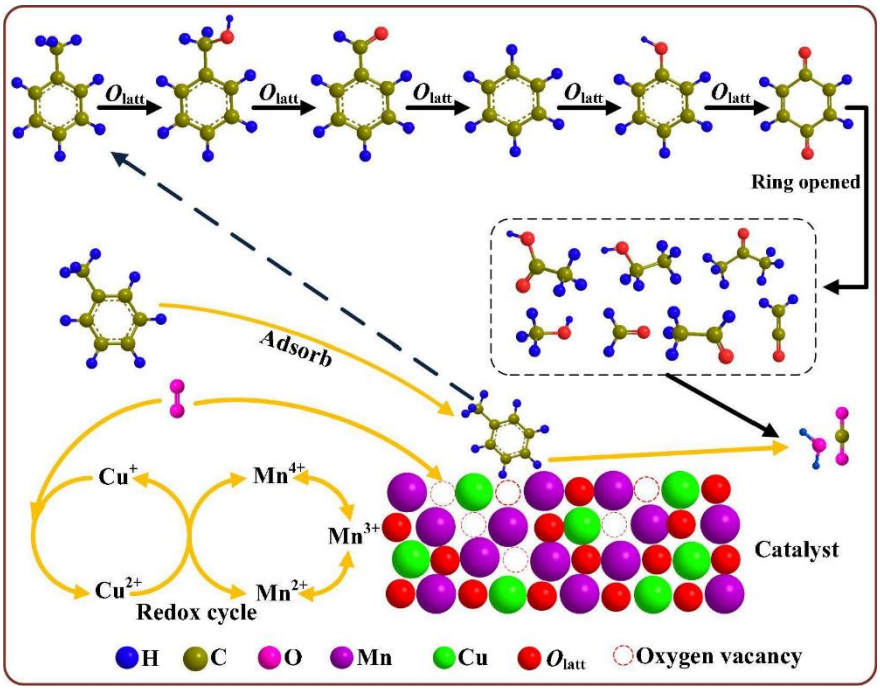

Figure 1.11. *Proposed reaction mechanism of toluene oxidation over $MnCu_{0.5}$ catalyst [111].*

Luo *et al.* [112] also proposed a Mars-van-Krevelen mechanism for the low-temperature oxidation of toluene performed on a copper-modified manganese oxide with a tunnel structure (Cu-Mn-4). Abundant oxygen species, good low temperature activity, low average manganese oxidation state and high surface area led to a remarkable catalytic performance of this catalyst. A simple cyclic redox system was postulated involving the Cu^{2+}/Cu^{+} and Mn^{4+}/Mn^{3+} redox couples with O_2 activated on Cu^{+} and toluene oxidized by Mn^{4+}.

Very recently, a series of characterizations combined with time-resolved *in situ* DRIFTS were used to apprehend the roles of Cu and Mn in CuMn oxides and density functional theory (DFT) simulations were conducted to check the experimental conclusion [113]. Time-resolved *in situ* DRIFTS showed that benzoic acid was the only intermediate which could be observed.

The oxidation process of toluene over CuO alone displayed in Figure 1.12 shows that toluene could be easily activated to benzoic acid. Toluene was first adsorbed parallel to the CuO surface with one of the H in -CH_3 bonded with the O atom in CuO (A → B).

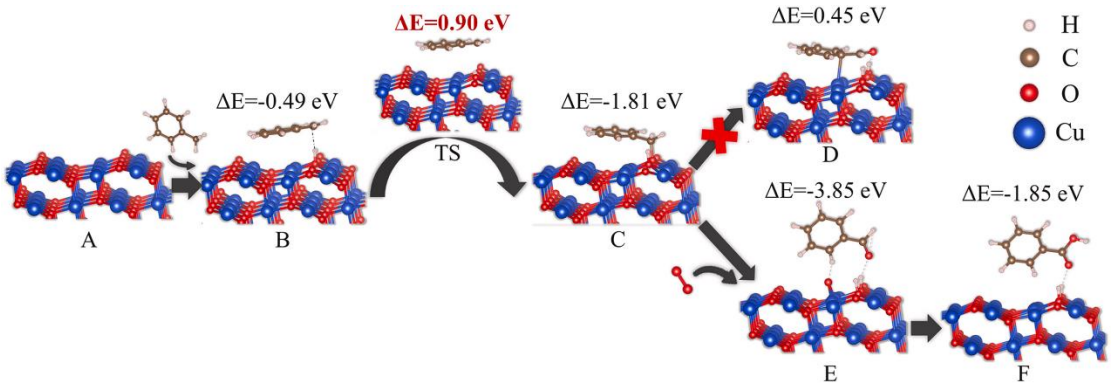

Figure 1.12. *The oxidation process of toluene over CuO [112].*

The -CH_3 in adsorbed toluene was subsequently activated by Cu-O to generate -CH_2 (B→TS→C). The generated -CH_2 could be oxidized by a lattice O atom (C→D) or gaseous/weakly adsorbed oxygen (C→E). To generate -COH and then left an oxygen vacancy or a residual O atom, respectively. However, the oxidation of -CH_2 by gaseous oxygen happened spontaneously (ΔE = - 3.85 eV), suggesting that gaseous/weakly adsorbed oxygen reacted more facilely with the adsorbed species. Finally, the -COH could be spontaneously oxidized by the residual O to generate – COOH (Δ E= - 1.85 eV). Through this reaction path, adsorbed toluene could easily be oxidized to benzoic acid on the CuO surface. The reaction energy barrier was the activation of -CH_3 to -CH_2 through transient state (B→TS, Δ E= 0.90 eV). Furthermore, the adsorption energy of benzoic acid over CuO was - 0.88 eV, which was stronger than the adsorption of toluene (-0.49 eV). Therefore, the oxidation of toluene to benzoic acid could benefit of the adsorption capacities of CuO.

The same reaction path was also simulated on the CuMn oxide catalyst (Figure 1.13).

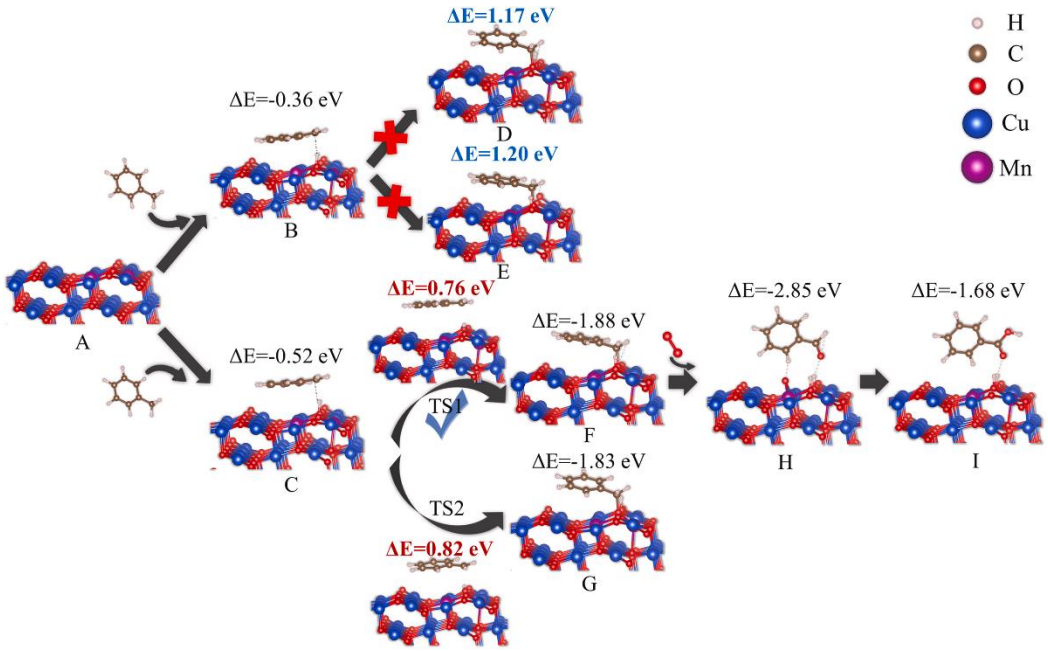

Figure 1.13. *The oxidation process of toluene over CuMn [112].*

First, the comparison of the energies of toluene adsorption of - 0.36 and - 0.52 eV on Mn-O and Cu-O sites in the O-Cu-O-Mn-O structure (A→ B, A→ C), respectively, suggested that the Cu-O site was more suitable for toluene adsorption. Moreover, the activation of adsorbed toluene at the Mn-O site was not spontaneous (B→ D ΔE =1.17 eV, B→ E ΔE =1.20 eV), further confirming that the Mn-O site in O-Cu-O-Mn-O was not suitable for toluene adsorption. However, the adsorbed toluene at the Cu-O site could be activated by the Mn-O site (C→TS1→F) or an adjacent Cu-O site (C→TS2→G) with reaction barriers of 0.76 eV (C→TS1) and 0.82 eV (C→TS2), respectively. These results suggested that the adsorbed toluene tended to be activated by the Mn-O site. Finally, the activated species could be oxidized by gaseous/weakly adsorbed oxygen to generate benzoic acid spontaneously (F→H→I). The benzoic acid adsorption energy (-0.88 eV) over CuMn was also stronger than that of toluene. Based on the above results, the reaction barriers of CuMn (0.76 eV or 0.82 eV) were lower than that of CuO (0.90 eV), proving that the oxidation of toluene on CuMn was easier than on CuO due to the formation of O-Cu-O-Mn-O structure, which was consistent with the time-resolved in situ DRIFT spectra. Meanwhile Mn-O was a more effective activation site than was Cu-O, whereas Cu-O mainly performed as an adsorption site in O-Cu-O-Mn-O structure. The synergism of the adsorption site and activation site contributed to the formation of benzoic acid on CuMn, which derived from the activation of toluene.

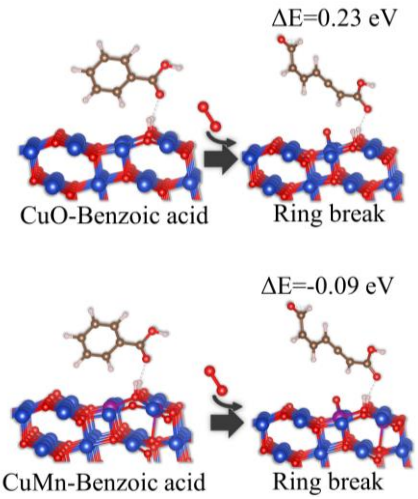

Figure 1.14. *The ring-breaking process of benzoic acid over CuO and CuMn [112].*

Furthermore, the ring-breaking processes over CuO and CuMn (Figure 1.14) were studied. The ring-breaking reaction appeared more likely to occur over CuMn than over CuO. Therefore, the oxidation rate of benzoic acid matched the activation rate of toluene to benzoic acid over CuMn. This balance contributed to the superior toluene oxidation ability of CuMn catalysts.

1.6.2 Scheme of toluene decomposition in APC process

In APC process, Veerapandian and coworkers [77] proposed that the reaction can be divided into two parts. The first in which part of toluene was desorbed and was converted through reaction in gas phase. The second concerns the toluene remained adsorbed which underwent reaction at the catalyst surface. The former involves the direct degradation of desorbed toluene by electron collision followed by the reaction with other short life active species (such as N^+, N^{2+}, O^+ and O^{2+}). The latter involved the total oxidation of adsorbed toluene by Hopcalite which was often described by MvK mechanism. A plausible degradation route for desorbed toluene in gas phase and adsorbed toluene on the catalyst surface was illustrated in Figure 1.15. Among the main gas phase decomposition by-products of toluene oxidation in glass beads DBD reactor (such as CO_2, CO, N_2O and ozone) which were already reported [114], CO_2 and N_2O are present in Hopcalite/glass beads PBDBD. However, the oxidation of CO and decomposition of ozone in the presence of Hopcalite can be elucidated by MvK mechanism.

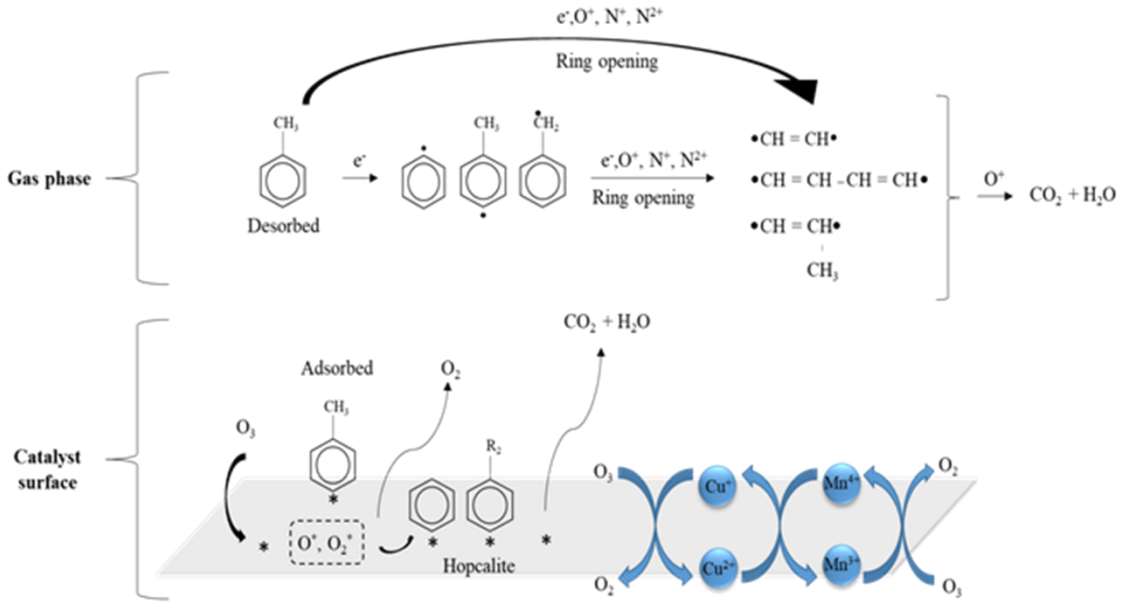

Figure 1.15. *Scheme of the adsorbed and desorbed toluene in gas phase and on the catalyst surface in APC process [77].*

For the degradation of gas phase toluene which was desorbed from Hopcalite/glass beads in PBDBD the energetic electron impact dissociations and radical impact dissociations, with radicals such as O^+, N^+ and N^{2+} breaks the ring of toluene and led to the formation of N_2O, CO_2 and H_2O. This process involved several reaction steps which were given below [115–117].

$$C_6H_5.CH_3 \rightarrow C_6H_5 + CH_3 + e^- \quad (1.3)$$

$$C_6H_5.CH_3 + e^- \rightarrow C_6H_4.CH_3 + H + e^- \quad (1.4)$$

$$C_6H_5.CH_3 + e^- \rightarrow C_5H_6 + C_2H_2 + e^- \quad (1.4)$$

$$C_6H_5.CH_3 + e^- \rightarrow C_3H_4 + C_4H_4 + e^- \quad (1.5)$$

$$C_6H_5.CH_3 + O^+, +{O_2}^+ + N^+ + {N_2}^+ \rightarrow C_6H_5.CH_3 + O_3, N, O, N_2 \quad (1.6)$$

The formation of different intermediates and toluene reacted with different radicals (O^+, N^+ and N^{2+}) which led to the formation of CO_2.

$$N_2^* + O_2 \rightarrow N_2O + O^* \quad (1.7)$$

$$N + NO_2 \rightarrow N_2O + O^* \quad (1.8)$$

According to MvK mechanism, the adsorbed organic species were oxidized by the lattice oxygen and the gas phase oxygen reoxidized the oxygen vacancy. Thus, the presence of multi-

oxidation state of metals which could be oxidized and reduced in the redox or reaction cycle was crucial. The presence of Mn and Cu in Hopcalite can form a redox cycle.

$$Cu^{2+} + Mn^{3+} \rightarrow Cu^{+} + Mn^{4+} \quad (1.9)$$

In this coupling the continuous charge transfer and the reduced metal oxide was replenished by the active oxygen formed through the decomposition of ozone. Thus, the reducibility of the metal oxide and replenishment of the oxygen vacancies were the rate determining step in the oxidation of toluene in Hopcalite PBDBD reactor.

$$O_3 + * \rightarrow O_2 + O^* \quad (1.10)$$

$$O_3 + O^* \rightarrow O_2^* + O_2 \quad (1.11)$$

$$O_2^* \rightarrow O_2 + * \quad (1.12)$$

$$O^* + CO \rightarrow CO_2 + * \quad (1.13)$$

$$18O^* + C_7H_8^* \rightarrow 7CO_2 + 4H_2O \quad (1.14)$$

Where * denotes the active sites on the surface of the catalyst.

1.7 Design of materials

1.7.1 Hopcalite

In 1920 Lamb et.al. [118] investigated the group of catalyst which are combined by metals such as Mn, Cu, Ag and Co. These catalyst is known as “Hopcalite” and its catalytic properties of has been confirmed by Jones and Taylor in 1923. As a consequence, Hopcalite is widely used for respiratory protection systems for various types of applications like military, mining and space devices, etc [119,120]. It is highly active in the amorphous state but has generally been observed to lose activity at temperatures above 773 K [121] where crystallization of the spinel, $CuMn_2O_4$, occurs. However, crystalline $CuMn_2O_4$ has also been reported to be active. It catches a lot of research attention due to its low cost, high activity, and moisture resistance. A lot of attention has paid to overcome their moisture deactivation and its lower catalytic activity. The mechanism of the deactivation of Hopcalite [122] and regeneration of Hopcalite catalyst [123] has been studied to understand closely the behavior of catalyst. It is recognized as one of the most efficient catalyst for low-temperature oxidation reactions such as CO oxidation [121,123,124] which has been

studied at the end of world war I, indoor HCHO oxidation [125], benzene oxidation [126], and toluene oxidation [127]. The high catalytic activity in CO oxidation over $CuMnO_x$ catalyst has been ascribed previously to the redox reaction $Cu^{2+} + Mn^{3+} \rightleftarrows Cu^{+} + Mn^{4+}$ and the high adsorption of CO onto Cu^{2+}/Mn^{4+} and of O_2 onto Cu^{+}/Mn^{3+} [121]. Current commercial Hopcalite catalyst has low activity towards CO oxidation at low temperature and is rapidly deactivated due to moisture and or impurities [128]. The crystal structure and interface between two mixed phases are having influence of physicochemical and catalytic properties of CuMn oxide catalysts. It is known that copper-associated oxygen species are very active in $CuMnO_x$ catalyst. The catalysts bimetallic nature helps improve catalytic activity due to the interaction of lattice oxygen, and mobility corresponds to Cu and Mn species respectively.

On the other hand, the catalytic activity of Hopcalite is depend on several factors such as: influence of different precursor, synthesis approaches, molar ratios of Cu:Mn, drying conditions, calcination, and environment intrinsic morphological. Tanaka et.al. [129] proposed improvement in catalytic activity of Hopcalite by improving their pore volume, surface area and lattice oxygen movement on the surface of it. It is worth to note that presence of lattice oxygen in Cu species and movement of lattice oxygen from Mn species leads to enhance the catalytic activity of Hopcalite [130].

Wang et.al. [131] reported the presence of Cu^{2+}-O^{2-}-Mn^{4+} leads to enhancement in the concentration of oxygen vacancy. Oxygen transfer and oxygen vacancy formation are favorable to M-V-K mechanism and toluene oxidation at low temperature. Therefore, copper-manganese oxide acquired many advantages which encourage low temperature conversion activity of toluene [119].

All of above characteristic of Hopcalite allows to stand as good candidate for catalytic oxidation. As already mentioned, it is well known for the CO oxidation, oxidation of Formaldehyde, Benzene, Toluene and so on. Our main motto to use amorphous Hopcalite for toluene oxidation and till now only few researchers devoted focus on it. The overview of Toluene oxidation by using Hopcalite has been reported in Table 1.8. All the reactions given here are conducted at different temperature. Direct comparison of Hopcalite is convoluted due to the different operating parameters (reaction temperature, gas flow rate) and Hopcalite (Cu/Mn molar ratio, synthesis method).

To sum up, we can claim that amorphous Hopcalite will be a promising candidate for storage generation process such as sequential adsorption-thermal catalytic oxidation and for sequential adsorption plasma catalysis study.

Table 1.8. *Overview of catalytic oxidation of Toluene over Hopcalite (CuMnOx).*

Catalyst	Synthesis condition	Reaction Conditions	Space velocity	T_{10} (°C)	T_{50} (°C)	T_{90} (°C)	Ref.
Purelyst MD-101	Commerical catalyst,	0.2 g, 800 ppmv/air	30000 mL.g^{-1}.h^{-1}	151	168	180	[109]
$CuMn_2O_4$-P4	Coprecipitation (P),	(100 mL.min^{-1})		185	195	200	
$CuMnO_X$-R2	Redox (R)			146	173	190	
$CuMnO_X$-R3				164	179	194	
HR-2Mn1Cu	Hydrolysis driving	0.1 g (40-60 mesh),	30000 mL.g^{-1}.h^{-1}	~ 187	228	237	[132]
CP-2Mn1Cu	redox precipitation,	1000 ppmv/air (50		~ 230	245	259	
	Coprecipitation	mL.min^{-1})					
Cu-Mn-4	Hydrothermal	(20-40 mesh), 1000	1000 h^{-1}	100	138	169	[112]
Cu-Mn-7		ppmv/air (50		~ 110	170	199	
Cu-Mn-10		mL.min^{-1})		~ 155	202	221	
$Cu_{1.5}Mn_{1.5}O_4$	Ionotropic alginate gel	0.13 g, 1000 ppmv	-	-	239	315	[124]
		(200 mL.min^{-1})					
CuMn	Coprecipitation	1000 ppmv/air	30000 h^{-1}	~ 60	245	274	[108]
		(550 ml.min^{-1})					
δ-MnO_2-T	Self-propagated	(40-60 mesh), 1000	30000 mL.g^{-1}.h^{-1}	-	252	295	[133]
Mn2Cu1-S	flaming (SPF)	ppmv/air (60		~ 215	275	-	
Mn6Cu1-S		mL.min^{-1})		~ 215	245	274	
Mn8Cu1-S				~ 215	243	265	
Mn10Cu1-S				~ 215	238	258	
Mn12Cu1-S				~ 215	246	282	
CM-300	Hydrothermal	0.3 g (40-60 mesh),	19800 mL.g^{-1}.h^{-1}	-	241	256	[119]
CM-400		600 ppmv/ /(20%			243	256	
		O_2+80%N_2) air					
		(100 mL.min^{-1})					
AT-CuMn-S AT-	Redox-precipitation	0.2 g, 800 ppm, O_2	30 L.g_{cat}^{-1}.h^{-1}	206	223	232	[127]
CuMn-B AT-Mn-B		=21% N_2 balance,		182	202	222	
AT- LaMn-P		100 mL.min^{-1}		191	224	247	
				215	230	251	

1.7.2 Ceria

Metal oxide catalysts serve as catalysts and as catalyst supports for the production of renewable energy, remediation of environmental pollutants, and synthesis of chemicals [134,135]. Rare-earth oxides have been widely used as structural and electronic promoters to improve activity, selectivity and thermal stability of catalysts [136]. Cerium is the most abundant rare-earth metal in the Earth's crust (approx. 66.5 ppm) and is more abundant than copper, cobalt and lithium

[137]. The main sources of cerium are the light rare earth element (LREE) minerals such as, bastn̈asite, allanite, cerite and monazite [138]. Cerium oxide (commonly known as ceria, CeO_2) is one of the most significant and applied rare earth oxides in industrial catalysis [136,139].

Cerium oxide (CeO_2) has a cubic fluorite structure with space group $Fm\bar{3}m$ and a cell parameter of 5.41˚ A at room temperature [140]. The CeO_2 structure consists of a cubic close-packed array with each cerium ion (white circles) coordinated by eight oxygen ions (gray circles), and, vice versa, each oxygen ion is surrounded by four cerium ions in a crystal unit as illustrated in Figure 1.16. [141].

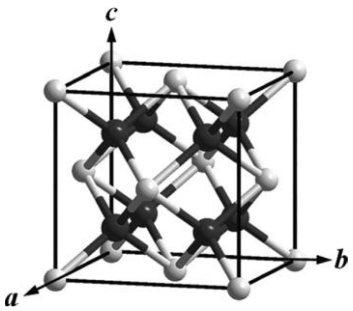

Figure 1.16. *Fluorite structure of ceria. Dark spheres represent oxygen ions, and white spheres represent cerium ions.*

Cerium oxide (CeO_2) has been extensively investigated in the field of heterogeneous catalysis both as a catalyst and as a support for noble metals. Furthermore, it is classed as a reducible metal oxide, similar to TiO_2, in that when neutral oxygen vacancies are formed, the two electrons given back to the oxide are localized on two Ce ions, reducing them from Ce^{4+} to Ce^{3+}, similar to the Ti^{4+} to Ti^{3+} reduction process in reduced TiO_2. This is due to its unique redox properties and high oxygen storage capacity (OSC), allowing it to quickly switch oxidation state between Ce^{4+} and Ce^{3+} in the stable fluorite structure [142,143]. The importance of CeO_2 originates from its unique redox properties and high OSC, allowing it to switch between Ce^{4+} and Ce^{3+} in a stable fluorite structure. In other words, CeO_2 can undergo substantial oxygen stoichiometric changes in response to change in temperature, oxygen pressure, electric field, and presence of dopants, without undergoing a change in the fluorite crystal structure [144,145]. The transport of oxygen in the ceria lattice results in the creation of intrinsic point defects. These point defects can be created by either thermal disorder or by interaction with the surrounding atmosphere. The predominant defects observed in reduced ceria are anion Frenkel pairs and anion vacancies (Figure 1.17.) [146].

In the *anion Frenkel type defect*, an oxygen ion is displaced from its lattice position to an interstitial position, hence creating a vacancy at its original position and a defect at the interstitial site [146]. In general, the formation of these defects does not influence the overall charge and stoichiometry of the lattice. The defect type is illustrated using the Kröger and Vink defect notation as

$$O_o^x \leftrightarrow O_i^{"} + V_{\ddot{o}} \qquad (1.15)$$

where, O_o^x and $O_i^{"}$ represent oxygen ions in the lattice and interstitial positions, respectively, and VÖ indicates an oxygen vacancy created at the lattice site.

In the o*xygen vacancy* defect, an oxygen ion is removed from one of the lattice positions, hence creating a vacant site [147,148]. In order to maintain the charge balance in the lattice, two Ce(IV) ions reduce to Ce(III) ions. The defect formation is represented by the following equation:

$$O_o^x + 2Ce_{Ce}^x \rightarrow V_{\ddot{o}} + 2Ce'_{Ce} + \frac{1}{2}O_{2\,(g)} \quad (1.16)$$

Ce_{Ce}^x implies a cerium ion in its lattice position, and Ce'_{Ce} denotes the reduction of cerium from Ce(IV) to Ce(III).

In the past years, several studies based on atomistic calculations have also suggested the presence of additional defects in the ceria lattice, such as interstitial and Schottky disorder [149]. An interstitial defect is the displacement of both a cerium and two oxygen ions to form interstitial sites, for example,

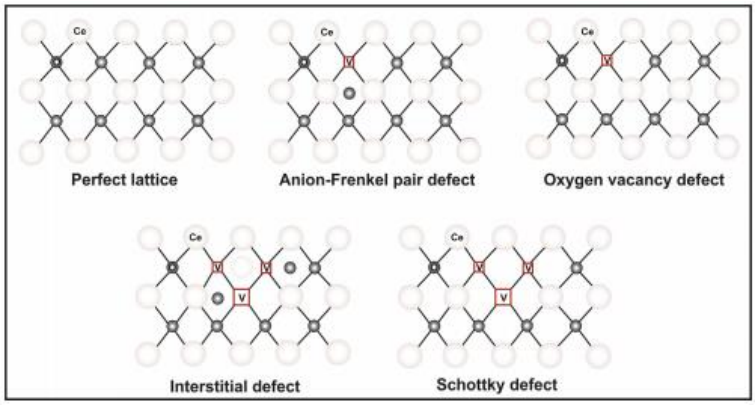

Figure 1.17. *Possible types of point defects in the CeO_2 lattice. Key: Oxygen—dark gray circles, cerium- white circles, and vacant site-red (black in print version) square with "V."*

$$2O_o^x + Ce_{Ce}^x + 2V_i^x \leftrightarrow 2O_i'' + Ce_i + 2\,V_{ö} + V_{Ce}'''' \qquad (1.18)$$

In the above equation, O_i'' and Ce_i indicate oxygen and cerium ions in their respective interstitial sites, V_i^x and V_{Ce}'''' represent the vacant interstitial site and vacant site created at the cerium lattice position, respectively. Finally, in the case of Schottky disorder, vacant sites are created by the removal of both the cations and anions from their lattice sites, while maintaining stoichiometry. The following equation illustrates the defect type:

$$2O_O^x + Ce_{Ce}^x \leftrightarrow 2\,V_{ö} + V_{Ce}'''' + CeO_{2(s)} \qquad (1.19)$$

Due to the unique oxygen transport properties and ability to accommodate large concentration of defects, ceria is an attractive material for processes that require a constant supply of oxygen in a reductive environment.

Because of these redox properties, CeO_2 is used in a wide range of applications such as an ultraviolet absorber in sun blocks, [140] O_2 sensors, [141] and antioxidant in the field of biomedicine [150]. Ceria is commercially used as a catalyst support in applications such as three-way catalysts (TWC) [151] and as solid electrolytes in low-temperature solid oxide fuel cells [152,153]. Further, the oxidation of CO [154], NO [155], hydrocarbons [156], the low-temperature water gas shift (WGS) reaction [157], and steam reforming of biooil [158] have been investigated on ceria and ceria-supported catalysts.

In recent year, researchers proposed new synthetic protocol which allowed to get ceria in different morphologies with well-defined exposed planes. For instance, ceria nanoparticles usually have an octahedral shape, mainly exposing stable (111) facets [159]. Ceria cubes preferentially expose active (100) planes, whilst ceria rods are thought to expose (100) and (110) surfaces, which are less stable and thus more reactive than the (111) surface [160]. Compared with bulk ceria, these ceria nanoshapes exhibit excellent redox properties and high specific activity/selectivity due to the exposure of active surface planes, as well as having more defects and higher surface to volume ratio [161]. Catalytic activity of different morphology based ceria has been tested for several catalytic applications. For present work, we mainly focused on catalytic oxidation of toluene and few recent results has been tabulated in Table 1.9.

Table 1.9. *Overview of catalytic oxidation of toluene over Ceria-nanorods (Ceria-NR).*

Catalyst	Synthesis condition	Reaction Conditions	Space velocity	T_{10} (°C)	T_{50} (°C)	T_{90} (°C)	Ref.
Ceria_nr_A	Hydrothermal	0.05 g, 80 ppmv/ /(20% O_2+80% Ar) synthetic air (100 $mL.min^{-1}$)	52000 h^{-1}	150	~ 200	~ 250	[162]
Ceria_nr_B				150	~ 210	~ 270	
Ceria_nr_C				200	~ 250	~ 300	
5h7M	Hydrothermal (h for synthesis hour and M for NaOH concentration)	0.3 g, 1000 ppmv /(20% O_2) dry air(150 $mL.min^{-1}$)	32000 $mL.g^{-1}.h^{-1}$	~ 160	225	280	[163]
24h10M				~ 160	240	315	
48h10M				~ 175	242	305	
24h15M				~ 175	270	330	
Ceria nanorods	Hydrothermal followed by ultrasonic without template	0.3 g (40-60 mesh), 1000 ppmv/air	20000 $mL.g^{-1}.h^{-1}$	~160	~210	~275	[164]
Ceria-r	Hydrothermal	0.2 g (40-60 mesh), 1000 ppmv/ (20%O_2/N_2)air (160 $mL.min^{-1}$)	48000 $mL.g^{-1}.h^{-1}$	~170	~220	-	[165]
CeO_2	Hydrothermal	0.3 g (40-60 mesh), 1000 ppmv/dry air	32000 $mL.g^{-1}.h^{-1}$	150	225	250	[166]
CeO_2	Hydrothermal	0.05 g, 242 ppmv/dry air	-	152	225	300	[167]

The overall review studied shows that ceria can be stand as outstanding candidates because of its redox properties. It is worth to test its potential for storage regeneration process.

1.7.3 UiO-66-SO_3H

Metal−organic frameworks (MOFs) [168,169] also known as porous coordination polymers (PCPs) [170,171] or porous coordination networks (PCNs) [172] or porous crystalline solids are organic−inorganic hybrids congregated from metal ions (or clusters or secondary building units) and bi-/multi-dentate organic linkers held by metal ions/clusters in a periodic manner.

On the bases of dimensional structures such as nanocubes, balls, metal-organic polyhedra and only made up of organic linkers then termed as Coordination Polymers and metal-organic frameworks respectively [173,174]. Chemically, thermally, and mechanically stable [175], tunability of structural and functionality of MOF allowed to have wide scope in the application due to which it is stands as a promising candidate for the scientists and engineers [176,177]. Nowadays, MOFs have been studied for the fundamental interests such as catalytic intermediate trapping and energy transfer, as well as for potential practical applications including gas storage

and separation, heterogeneous catalysis, chemical sensing, biomedical applications, and proton conduction [178–182].

MOFs have been the foremost candidates for storage and separation applications because of their large pore apertures and functionalized pore surfaces, which result in suitable interactions with incoming guest molecules. Size/shape exclusion plays a crucial role in governing the adsorption process, which is also often aided by the unique structural flexibility, resulting in an outstanding molecular sieving effect [181]. A various MOFs has been used as adsorbent to adsorb the VOCs/Toluene such as ZIF-8 [183], UiO-66 [184], UiO-66(NH_2) [184,185], ZIF-67 [184], MOF-199 [184], MOF-5 [184], MIL-101-Fe [184], MOF-177 [91] etc.

On account of these advantages, MOFs have been found to present suitability for diverse applications such as:

- Gas storage and separation
- Separation of industrially relevant liquid mixtures
- Fuel cell applications (proton/hydroxide conduction)
- Sensing of toxic and hazardous species
- Heterogeneous catalysis
- Magnetism

The facile access to structure-property correlation has resulted in rapid advancement of MOFs for the aforementioned applications. Also, the ability to tune the pore architecture and pore character results in tailoring the compounds for target-specific applications. In addition, the ability to transduce the host-guest interactions via different signals affords remarkable advantage of using MOFs or MOF-based materials for several applications. Based on these aspects, MOFs continue to progress as distinguished solid-state crystalline materials which will seek greater relevance towards practical implementation in the coming years. Among the different applications suitable using MOF-based materials, the current work focuses on development of MOFs towards environmental applications.

MOFs play a vital role in the environmental applications due to its high selectivity, sensing detection of the target molecules such as ionic species, gases, and molecules. For the Gas-

adsorption-separation application, flexible MOFs play a vital role due to variation in the pore geometry, secondary building unit, organic linker, and solvent [186]. Due to uniformity in the crystal size and size distribution of MOFs [187] promote the mass transfer phenomena. All of the above features of the MOFs suggest that it can be a promising candidate for the removal of VOCs in the plasma-catalysis system. Mitra and co-worker first time used MOFs for the removal of VOCs in presence of plasma [72]. Mitra et.al. [72] has investigated the removal of toluene by using single stage system. They found that MIL-101, MIL-53, CPM-5 has shown 90 % removal efficiency for the toluene in dry condition and it has been reduced in presence of the 30 % relative humidity.

Moreover, considering the promising adsorption capacity and stability of MOF we have chosen the UiO-66 is one of the materials.

UiO-66 (UiO = University of Oslo) that has been successfully synthesized by various group of researcher with many different functional groups. It exhibits exceptional stability, [188] and has good adsorption properties. The UiO-66 family of microporous materials is based on a 3D structure of zirconium-oxo clusters. UiO-66 is synthesized with benzene dicarboxylate (bdc−2) and many modified dicarboxylate linkers; even tetracarboxylate linkers have also been successfully used to synthesize functionalized versions of UiO-66. UiO-66 is a Zr(IV)-based MOF having exceptional hydrothermal stability and is a model compound for diverse post-synthesis organic function-alization. UiO-66 is constituted by Zr_6O_4 $(OH)_4$ nodes having the six Zr^{4+} ions in octahedral geometry and the four oxygen atoms or hydroxyl at the centers of each of the facets of the octahedra. These nodes are coordinated with twelve terephthalate (BDC) ligands in such a way that each Zr atom becomes coordinated with eight oxygen atoms in a square antiprismatic geometry. The structure is defined by two types of cages with tetrahedral (0.7 nm) and octahedral (0.9 nm) shapes that can be accessed through triangular windows of about 0.6 nm (Figure 1.18). The surface area of UiO-66 depends on the preparation method and the presence of defects.

As commented above, one of the most relevant properties of UiO-66 that explains its wide use in heterogeneous catalysis is its high structural stability. This material can be heated at temperatures about 375 °C, without collapsing the structure although some dehydration and rearrangement of the coordination around the Zr^{4+} ions can occur. This change in the coordination number of Zr^{4+} from eight to seven that take place upon dehydration at temperatures above 300 °C can be reversibly restored to the situation of the as-synthesized material by subsequent hydration.

This remarkable thermal stability is complemented with a high stability in a wide range of organic solvents and water.

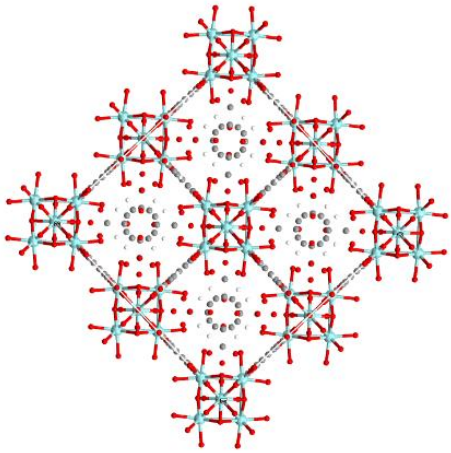

Figure 1.18. *Structure of UiO-66 framework (cyan spheres = Zr, red spheres = oxygen, grey spheres = carbon).*

Till todays date, catalytic activity of pure UiO-66 has been tested for the toluene oxidation. No catalytic activity has shown by UiO-66. Nobel metals has been used to enhanced the catalytic activity of it (Table 1.10). This work inspired that UiO-66-SO_3H can also be stand as good candidate due to its high surface area, presence mild acidic activity.

Table 1.10. *Overview of published articles for catalytic oxidation over UiO-66.*

Catalyst	Synthesis condition	Reaction Conditions	Space velocity ($mL.g^{-1}.h^{-1}$)	T_{10} (°C)	T_{50} (°C)	T_{90} (°C)	Ref.
UiO-66	Solvothermal	0.1 g (20-40 mesh), 1000 ppmv/air (50 $mL.min^{-1}$)	30000	400	-	-	[189]
Pd-U-H	Impregnation			174	232	238	
Pd-U-NH	$NaBH_4$-reduction			134	192	204	
Pd-U-EG	Ethylene glycol-reduction			131	191	198	
UiO-66	Hydrothermal	0.1 g, 1000 ppmv (40-60 mesh)/(20% O_2+80%N_2) air (100 $mL.min^{-1}$)	60000	-	-	-	[190]
0.1% Pd@UiO-66	Double solvent			200	232	238	
0.2% Pd@UiO-66				220	210	217	
1% Pd@UiO-66				222	236	246	
2% Pd@UiO-66				222	238	249	
UiO-66	Hydrothermal	0.1 g (20-40 mesh granular), 1000 ppmv/(toluene 7 $mL..min^{-1}$, 30 vol% O_2/Ar 33 $mL.min^{-1}$, Pure argon 10 $mL.min^{-1}$ (50 $mL.min^{-1}$)	30000	400	-	-	[191]
2Ag-U	Liquid phase reduction			280	332	347	
6Ag-U				281	305	318	
10Ag-U				248	277	295	
14Ag-U				285	283	298	

Considering all of the above explained properties of different materials we have proposed a novel storage regeneration process such as combination of adsorption-catalytic oxidation.

Furthermore, catalytic behaviour of different materials has been tested for the abatement of toluene via adsorption-plasma catalysis.

1.8 Strategic methodology

The aim of this section is to summarize the scope of this thesis and the strategic methodology that was implemented during Ph.D. study.

The emissions of volatile organic compounds (VOCs) threaten the environment and human health severely because most of them are highly toxic, carcinogenic, and yield even more hazardous compounds such as secondary organic aerosol particles, which lead to photochemical smog, stratospheric ozone depletion, etc. Despite that, they are intensively used in industry for different applications: surface coating, printing, adhesives, solvents.

Toluene (toluol, methylbenzene, phenylmethane) is an aromatic hydrocarbon. It is an organic solvent widely used in many industrial processes including plastic production, chemical synthesis and gasoline manufacturing. A volatile liquid (i.e., it becomes vapor at room temperature), toluene produces psychoactive effects when inhaled in pure form or from numerous commercial products, such as solvents, gasoline, paints, varnishes, paint thinner, adhesives, and inks, among other products.

During the last decades, great efforts have been made to develop effective and environmentally friendly VOC elimination techniques. Compared to common VOC control techniques such as absorption, regenerative thermal oxidation, regenerative catalytic oxidation, etc.

Adsorption is one of the most effective and cost-efficient technologies; moreover, it can realize the recovery of VOCs. The selection of a suitable adsorbent is crucial for VOC adsorption technology. Among various adsorbents, zeolites, metal oxides, carbon materials are widely used for their stable physical and chemical properties, high surface area, porosity, and regenerability. On the other hand, absorbent need to be regenerated either ex-situ or in-situ which involves interrupting the depollution process.

Catalytic oxidation is one of the most effective method for the abatement of VOCs. The addition of a catalyst accelerates the rate of oxidation by adsorbing oxygen and contaminants on the surface where they react to form oxidation products like CO_2 and H_2O which are the desired products of the total oxidation of VOCs. On the other hand, major drawbacks of this method are its cost as it involves high energy consumption and its difficulty to operate when low VOC concentration (1000 ppmv) need to be treated.

During the last decade, some studies have proposed the use of non-thermal plasma (NTP) for the degradation of diluted (>1000 ppmv) volatile organic compounds (VOCs) streams. NTP produces very reactive chemical species (active radicals, ionic and excited atomic and molecular species) to oxidize volatile organic compounds, mainly forming CO_2 and H_2O. It is a flexible, compact, quick start-up and relatively cheap technique, which can be suitable for the treatment of low pollutant concentrations. NTP is an attractive technology in such a way that the energy delivered to the plasma allows to get very energetic electrons while the temperature of the gas is kept near to ambient. These highly accelerated electrons trigger multiple chemical processes such as excitation, ionization, and dissociation of background molecules (N_2/O_2) enabling an efficient decomposition of the VOC. However, this high reactivity towards VOC removal is tempered by a low selectivity towards CO_2/H_2O and by the production of toxic by-products such as nitrogen oxides, O_3. Furthermore, formation of other gaseous harmful VOCs cannot be discarded. However, for toluene decomposition NTP produces NO_2, formic acid, benzyl alcohol, acetic acid, benzaldehyde, phenol and benzoic acid as a byproduct.

In addition, various hybrid technologies such as (adsorption+ photocatalysis, adsorption + plasma, Photocatalysis + plasma, adsorption + catalysis and so on) have emerged to complement one another cost effectively.

Inspired from these hybrid technologies, we have proposed to implement innovative sequential adsorption followed by catalytic oxidation processes differing by the nature of the activation of the catalytic steps: either by thermal activation (ATC) or through plasma activation (APC).

Furthermore, different materials can be considered for these sequential processes. Depending on its nature, the material used as adsorbent can have intrinsic catalytic properties

which can be used or optimized. Otherwise, this adsorbent material can act as support for catalytically active phases.

For this study, different materials have been considered such as Hopcalite, Ceria-NR, and UiO-66-SO_3H. Hopcalite is composed of CuO and MnO was chosen because it is well known for ozone decomposition. The presence of the different oxidation state of $Cu^{2+/+}$, $Mn^{3+/4+}$ contributes to the redox properties of this material. Thus, we hope that Hopcalite will act as dual-functional.

Ceria-nanorods (CeO_2) is well known as a catalyst and/or as support. This is due to its unique redox nature and high oxygen storage capacity (OSC), allowing it to quickly switch its oxidation state between Ce^{4+} and Ce^{3+} in the stable fluorite structure. Therefore, we are expecting that for our reaction system this material will show interesting catalytic performances.

The third choice of material is a so-called Metal-Organic-Framework (MOF), for instance UiO-66-SO_3H. Owing to its remarkable mechanical, chemical, water and thermal stability, zirconium-based MOFs become potential adsorbents and is expected to provide efficient adsorption capacity towards toluene.

The synthesized materials have been characterized by various techniques, in particular PXRD, XPS, TEM, EDS, H_2-TPR, FTIR-ATR, ToF-SIMS, and N_2 adsorption to determine their structural and textural properties.

Our aim for this study was to develop materials with long period of adsorption (t_1) through high adsorption capacity and short time of catalytic oxidation (t_2) thanks to high catalytic activity. A first approach consisted in analyzing the properties of the materials with regard to adsorption followed by thermal desorption/reaction. In parallel, the reactivity of these systems was studied in plasma conditions.

The sequential toluene adsorption and oxidation of the materials have been tested on the home-made set up using diluted toluene in inert gas for adsorption and inert of oxygen during desorption/reaction step. ATC process was studied at University of Lille while APC test were undergone at University of Ghent.

On the bases of their performance for abatement of toluene a catalytically active phase (0.5, 1, 2 and 10 wt. % Ag) was added. In spite of the more expensive cost of silver, it is the preferred one because of high specific activity, resistance to deactivation and ability to be regenerated.

Chapter 1 is dedicated to the bibliographic study of the abatement of toluene as a VOC model, their removal techniques such as adsorption, catalytic oxidation, NTP and coupling of methods.

Chapter 2 provides detailed experimental methods for materials synthesis, characterization. Experimental setups are described as well.

Chapter 3 describes the sequential adsorption and Thermal/catalytic oxidation process (ATC) for abatement of the toluene by using Hopcalite, UiO-66-SO_3H and Ceria-NR.

Chapter 4 describes effect of silver addition to Hopcalite in ATC.

Chapter 5 is dedicated to the detailed study sequential adsorption plasma catalysis (APC) process using Hopcalite for the abatement of the toluene.

Chapter 6 describes effect of silver addition to Hopcalite in APC.

Chapter 7 contain an overall discussion and conclusions of this work.

Chapter 2

Experimental Methodology

Chapter 2 Experimental methodology

2.1 Introduction

Throughout this chapter, the abatement of toluene in combination with different catalysts and/or in combination with non-thermal plasma is discussed in details. This chapter divided in three sections.

The first part is dedicated to the abatement of toluene using a sequential adsorption-thermal/catalytic (ATC) process. This section consists of set-up optimization and experimental process analysis. All experiments described in this section were conducted at Lille university.

The second section is devoted to the abatement of toluene using a sequential adsorption-plasma catalysis (APC) process. This section consists of set-up optimization and experimental process analysis. All experiments described in this section were conducted at Ghent university.

The third section depicts the synthesis of different catalysts and characterization which has been conducted in Lille and Ghent university.

2.2 Toluene abatement test

Sequential adsorption and catalytic process was performed at the University of Lille. The description of the set-up and experimental process are presented below:

2.2.1 Experimental set up

The main reaction is sequential adsorption of toluene followed by catalytic oxidation. With respect to “traditional” co-feed and stationary catalytic studies, the sequential operation involves particular technical and methodological solutions.

Schematic diagram of the setup is represented in Figure 2.1. It is based on a traditional co-feed setup which was adapted both in terms of gas feed and analysis to perform sequential operation. It consists of three main parts. Gas cylinders feed a process box section containing

switching valves and mass flow gas regulators (Bronkhorst). This allows the preparation of the polluted gas mixture containing Helium and Toluene flows or oxidant gas mixture (He and O_2). The following section consists of the reactor itself which has been placed in the furnance. Finally the last section is constituted by the gas analysis tools. A microGC is present for stationnary expeirments while for sequential operation a mass spectrometer needs to be used in order to obtain relevant time resolved data.

2.2.2 Reactant source

Toluene is provided directly in gas phase from a pre-mixed cylinder containing 0.1 vol. % Toluene in Argon. The needed working concentration is obtained by dilution of this pre-mixture in Helium in the process box.

Similarly, oxygen is provided through a pre-mixed cylinder containing 10 vol. % O_2 in Helium.

Gas flows are controlled by mass flow controllers contained in the process box while the switching between different gas mixtures is performed manually.

2.2.3 Catalytic reactor

The required amount (typically 0.3 g) of the material was placed inside the pyrex-glass reactor (inner diameter of 10 mm and a wall thickness of 1 mm) for each reaction. The reactor was then placed into the coaxial tubular furnace, which was temperature regulated (TEMPATRON, PID500, equipped with two thermocouples). Thermocouple 1 was used to monitor the temperature of the reactor surface, and Thermocouple 2 was inserted into the reactor near to the catalyst surface.

2.2.4 Analysis system

The composition of the gaseous stream flowing from the inlet (by-pass mode) and outlet or reactor were analyzed on-line by mass spectrometer (Omnistar, Pfeiffer Vacuum, Model GSD 301 O2) also used to analyze the gaseous system.

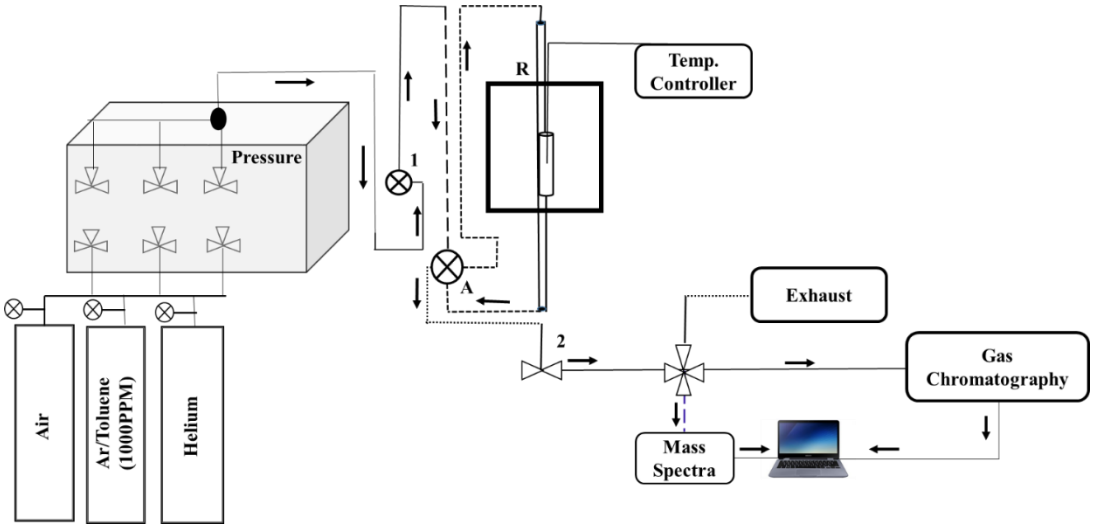

Figure 2.1. *Schematic diagram of the experimental set-up used for abatement of toluene by adsorption-thermal catalytic oxidation.*

2.2.5 Partial pressure analysis (online mass spectrometer)

In the mass analyzer (Omnistar, Pfeiffer), the gas is ionized through electron bombardment. A voltage is applied between anode and cathode, which accelerates the electrons generated by the filament. Then, the ions are separated by the m/z ratio by a quadrupole mass filter which consists of four parallel rods arranged in the square position. Every pair of opposite rods designated (+) or (-) is connected with the other. The functional quadrupole field deflects the ions in the X and Y directions, resulting in helical trajectories through the filter. The required mass range and desired resolution are governed by the dimensions of the filter and the selection of the operating frequency. This ion later goes through a detector (secondary electron multiplier) to increase the collected signal. Finally, a Faraday collector detector can also be used but with much less sensitivity.

The most significant m/z is used for each component but interference between different gasses have also to be taken into account as shown in Table 2.1.

The sensitivity of the online mass-spectrometer is determined relatively to Helium. He, Ar, Toluene and O_2 sensitivity are calculated during each experiment using the by-pass sequence at the beginning and end of each test. Mass spectrometer background signals are also determined during this sequence. Other gases are calibrated regularly using calibrated composition gas cylinders (He, Air, Toluene, O_2 …).

Table 2.1. *Ion fraction distribution for main components.*

Methane		Toluene		Cyclohexadiene		Formic Acid		Benzyl alcohol		benzoic acid							
CH_4		C_7H_8		C_6H_8		CH_2O_2		C_7H_8O		$C_7H_6O_2$		CO	CO_2		H_2O	$C_2H_4O_2$	
16	100																
15	90																
															18		
						28	17					28	28	10			
						29	100										
																43	100
						44	10						44	100			
						45	48									45	91
		46	1			46	61										
																60	75
				77	45			77	55								
				78	12					78	6						
				79	100			79	100								
				80	35												
		91	100														
		92	78														
										105	100						
								107	70								
								108	90								
										122	82						

2.2.6 Catalytic oxidation Test

Typically, 0.2 g of catalyst was placed in the reactor. Prior to each test, the sample was treated in air (100 mL.min^{-1}) at 330 °C for 30 min (2 °C·min^{-1}). 1000 ppmv of toluene was injected (Bronkhorst) in synthetic air at flow rate 100 mL.min^{-1} and passed through the reactor at 300 °C. The reaction temperature was decreased from 330 °C to 150 °C (rate - 0.5 °C·min^{-1}) to 30 °C (rate -0.2 °C·min^{-1}). Reactants and products were analyzed online by a gas chromatograph (GC, 7860A Agilent Gas Chromatograph) equipped with a thermal conductivity detector (TCD) using a Stabilwax (10 m) column. The results are expressed in terms of toluene conversion into carbon dioxide:

$$X\ (\%) = \frac{[CO_2]_{out}}{7 \times [C_7H_8]_{in}} \times 100 \qquad (2.1)$$

Where X (%) is conversion of toluene based on toluene oxidation. $[]_{in}$ and $[]_{out}$ are the species concentration measured at the inlet and outlet of the reactor respectively.

2.2.7 Sequential adsorption/thermal catalytic oxidation (ATC) Test

The objective was to evaluate the adsorption properties towards toluene and the conversion of adsorbed species in neutral or oxidant gas stream in temperature programmed conditions (Figure 2.2). The following protocol was applied unless specified differently.

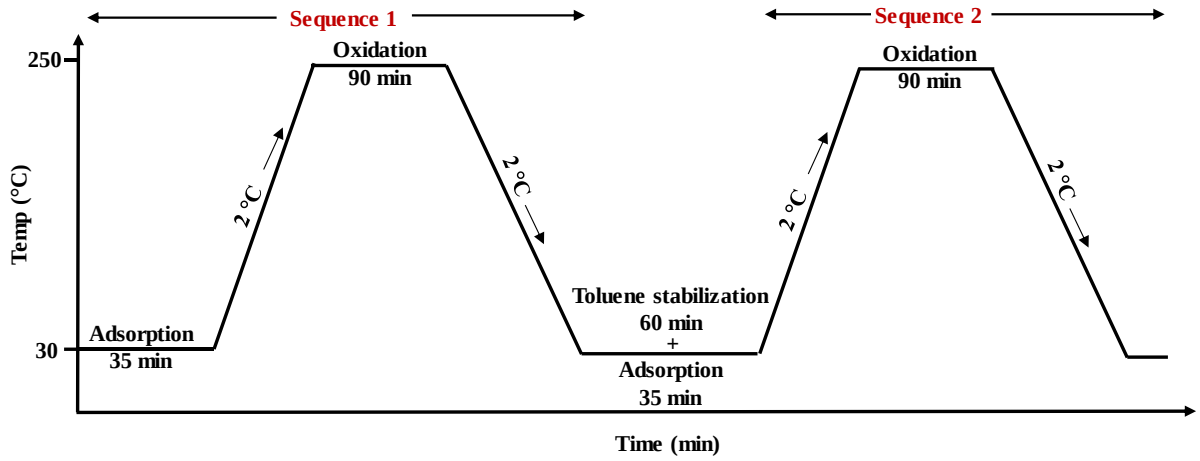

Figure 2.2. *Schematic diagram of the experimental set-up used for abatement of toluene by adsorption-thermal /catalytic oxidation.*

2.2.7.1 Pre-activation process

Before the experiment, the calcined material (0.3 g) was pre-activated at 150 °C for 4 h with heating rate 5 °C.min^{-1} in presence of air (flow rate 100 mL.min^{-1}) to avoid contamination and presence of absorbed species on the surface of the material. The calcined catalyst was then cooled to room temperature by in air.

2.2.7.2 Stabilization of Toluene flow

Simultaneously, through the process box was started and the He and toluene in Argon flow set as per the desired initial toluene concentration. For example, for 100 ppm toluene the He flow (90 mL.min^{-1}) and toluene in argon flow (10 mL.min^{-1}) was set and sent to vent.

2.2.7.3 Adsorption process at room temperature

The amount of toluene adsorbed on the material the experiments were determined out at room temperature and atmospheric pressure. The prepared the gas mixture (He/Ar + toluene) was then flown towards the analyzer by turning 1st valve from vent to setup and keeping 4-way valve A in by-pass mode. Simultaneously, the analysis was carried out by passing flow to mass spectrometer instead of exhaust by turning valve 3. At a given moment valve A was switched to allow the gas to flow through the reactor zone and catalyst bed. The mixture of He and toluene

was supplied continuously till a determined toluene concentration was reached. This could be the initial concentration to measure the adsorption up to saturation or a lower value chosen.

2.2.7.4 Desorption process at room temperature

The amount of the toluene reversibly adsorbed on the material was calculated by performing a desorption experiment at room temperature. Following the previous adsorption process, the flow of Ar + toluene was switched off and the Helium flow adjusted (e.g. to 100 $mL.min^{-1}$) in order to assess the amount of the toluene reversibly adsorbed on the sample. The toluene partial pressure resulting from desorption from the surface of material was monitored and calculated.

2.2.7.5 Thermal Desorption/Reaction process

The following step aims at determining the amount of toluene which may desorb at higher temperature or react either with the solid or with gaseous oxygen. This is realized by heating the sample in temperature programmed way (25 °C to 250 °C, heating rate 2 $°C.min^{-1}$, hold at 250 °C for 1.5 h) in pure Helium or is mixture of O_2 and Helium (50:50, 25:75). Simultaneously, the signals characteristic of toluene (m/z = 91), CO_2 (m/z = 44), possible by-products such as formic acid (m/z = 29), benzaldehyde (m/z = 77), and CO (m/z = 28) were recorded by the MS detector.

Amount of toluene adsorbed ($q(Tol)_{ads}$), desorbed at room temperature ($q(Tol)_{desRT}$) and desorbed during temperature programmed reaction ($q(Tol)_{desTPR}$) and amount of CO_2 formation ($q(CO_2)_{TPR}$) are calculated as follows:

$$q(\mathrm{Tol})_{\mathrm{desRT}}\ (\mu mol.g^{-1}) = A \times \sum_0^t \left(\frac{P(Tol)_t + P(Tol)_{t+1}}{2}\right) \times \Delta t \qquad (2.2)$$

$$q(\mathrm{Tol})_{\mathrm{desTPR}}(\mu mol.g^{-1}) = A \times \sum_0^t \left(\frac{P(Tol)_t + P(Tol)_{t+1}}{2}\right) \times \Delta t \qquad (2.3)$$

$$q(\mathrm{CO_2})_{\mathrm{TPR}}\ (\mu mol.g^{-1}) = A \times \sum_0^t \left(\frac{P(CO_2)_t + P(CO_2)_{t+1}}{2}\right) \times \Delta t \qquad (2.4)$$

$$q(\mathrm{Tol})_{\mathrm{ads}}\ (\mu mol.g^{-1}) = q(\mathrm{Tol})_{\mathrm{desRT}} + q(\mathrm{Tol})_{\mathrm{desTPR}} + \frac{q(\mathrm{CO_2})_{\mathrm{TPR}}}{7} \qquad (2.5)$$

$$CO_2\ Yield\ (\%) = \frac{q(\mathrm{CO_2})_{\mathrm{TPR}}}{7 \times q(\mathrm{Tol})_{\mathrm{ads}}} \times 100 \qquad (2.6)$$

Where $P(Tol)_t$ and $P(CO_2)_t$ are concentrations of toluene and CO_2 is at a given time expressed in atm, t is in min, $A = \frac{10^{-3}}{R \times T} \times \frac{F}{m}$ in which F is total gas flow in $mL.min^{-1}$, m is mass of the material in g, T = 293 K and R = 8.0206 $L.atm.mol^{-1}.K^{-1}$.

2.2.7.6 Stability tests in cycling sequential adsorption-thermal catalytic oxidation (ATC)

The sequential adsorption-thermal catalytic oxidation (ATC) was performed in a similar manner than before and was repeated over Hop and Hop-1 Ag three (Hop-3S) and five times (Hop-1 Ag-5S), respectively. The suffix-xS (x = 1 to 5) was added to specify the number of cycles. Between each sequence the catalyst was kept under static O_2 : He (25:75) atmosphere.

2.3 Plasma set up description

A schematic representation of the experimental setup is represented in the Figure 2.3. It is made up of three main parts: a) Reaction gas supply system, b) The Dielectric barrier discharge (DBD) packed bed reactor and c) the analytical instrumentation. Each part will be elucidated in detail in the following paragraphs.

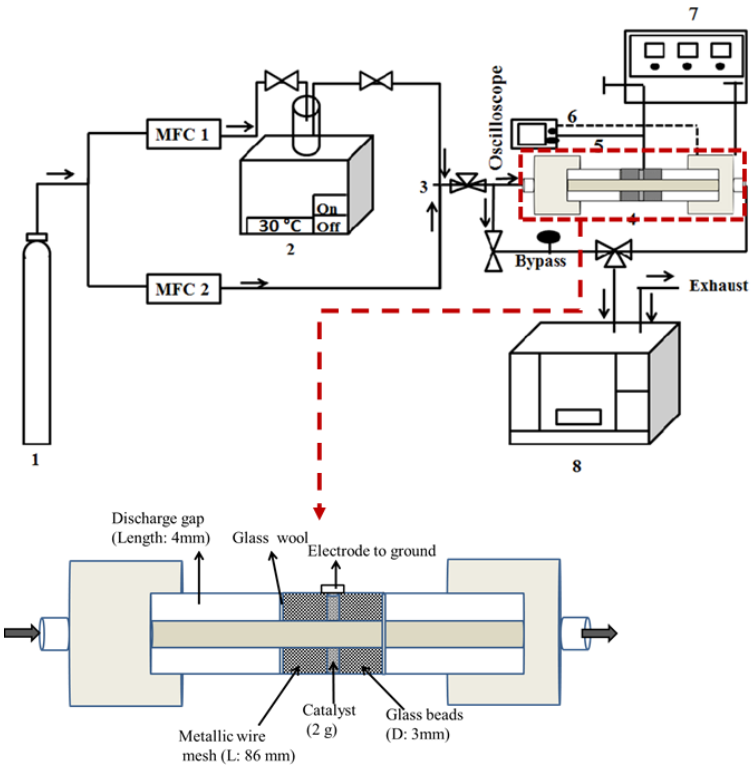

Figure 2.2. *Schematic representation of the plasma set up for toluene abatement.*

1. Dry air cylinder; 2. Toluene bubbler; 3. Mixing chamber; 4. Packed bed DBD reactor; 5. Resistor (46.4 Ω); 6. High voltage and current probe; 7. AC power source (50 kHz); 8. FTIR spectrometer.

2.3.1 Plasma Treatment procedure

Dry air (Alphagaz 1, Air Liquide) is used as the carrier gas in the experiments. Toluene (99.9 %) was acquired from Carl Roth (Belgium) and was stored in a bubbler. Toluene bath chamber temperature was maintained at 30 ± 0.5 °C, as illustrated in Figure 2.4, in order to keep toluene at a constant temperature. Two separate mass flow controller (MFC) (Bronkhorst®, El Flow®) (Figure 2.3) is used to adjust and regulate the flows of air and air through the toluene bubbler.

Figure 2.3. *Gas system with mass flow controller and water bath.*

2.3.2 DBD reactor

The DBD plasma reactor is represented in Figure 2.5. The reactor is made of a quartz cylinder with a diameter of 22 mm, a length of 250 mm and a well thickness of 3 mm. The inner electrode is of a stainless steel rod with a diameter of 4 mm. A stainless steel iron mesh is used as outer electrode which is covered on the outer surface of the DBD plasma reactor with a length of 86 mm. The distance between the inner wall of the quartz cylinder and the inner electrode which is well known as a discharge gap is filled with glass beads of 3 mm diameter. The bead is fixed in a particular position with the help of quartz wool on the both sides of reactor. The volume of the discharge is 3.83 cm^3 and the corresponding residence time of the gas in the plasma zone is 0.23 s.

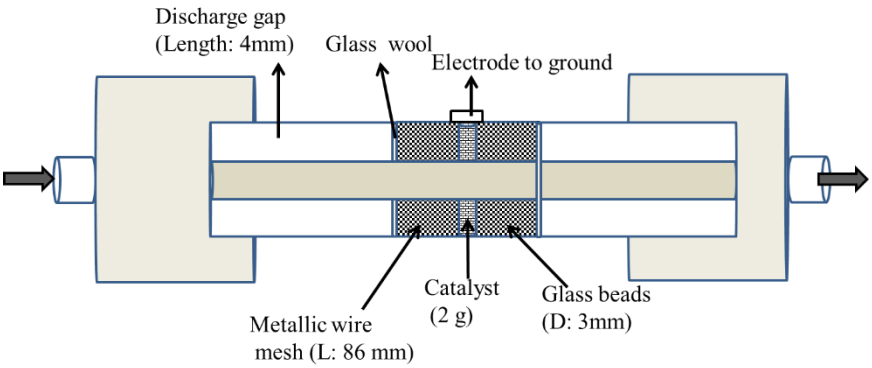

Figure 2.4. *Schematic representation of the packed bed DBD reactor.*

Figure 2.5. *AC power source.*

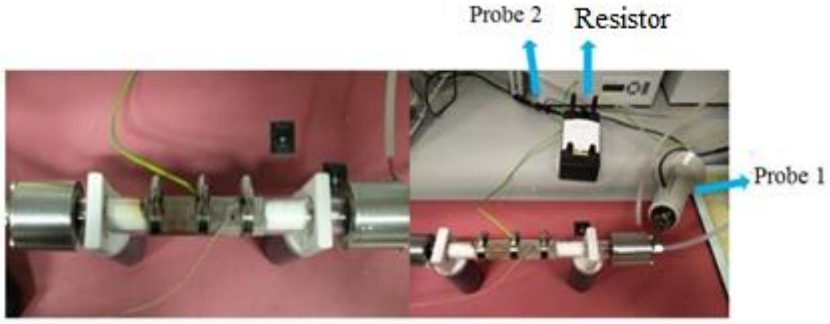

Figure 2.6. *DBD systems with (a) DBD reactor; (b) voltage-current measurement circuit.*

An AC high voltage source (Figure 2.6) with amplitude of 7.0 kV and with a fixed frequency of 50 kHz is connected to the inner electrode. The outer electrode is connected to the ground through a resistor of 46.4 Ω (Figure 2.7).

2.3.3 Energy measurement

Figure 2.8 represents the I-V graph with the help of that the discharge energy has been calculated. The oscilloscope data has been used to get the current-voltage plots. With the help of these plots the discharge power is determined. The electrical energy consumed per current discharge cycle equals the voltage multiplied by the current per discharge cycle. The discharge power P was then calculated by multiplying the electrical energy by the frequency of the feeding voltage (50 kHz).

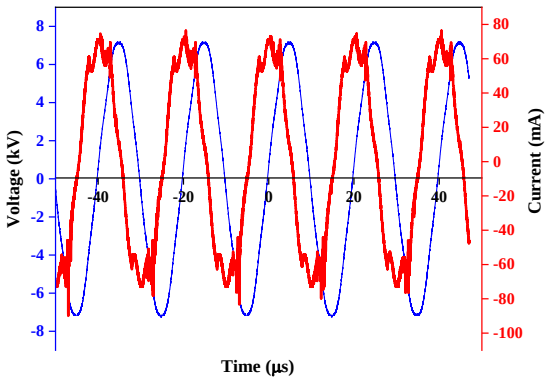

Figure 2.7. *Voltage V and current I waveforms of the packed bed DBD reactor at an applied voltage of 7.5 kV.*

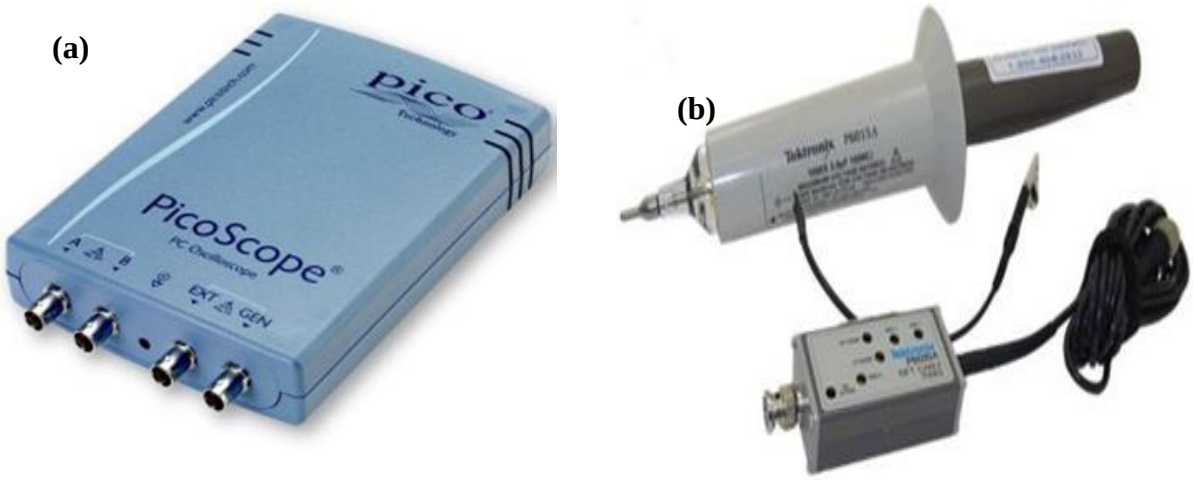

Figure 2.8. *The energy measurement device with (a) oscilloscope, (b) high voltage probe.*

The applied high voltage was measured using a 1000:1 high voltage probe (Tektronix P6015A, Figure 2.9 b). The charge stored on the electrodes was monitored by measuring the voltage across the capacitor connected in series to the ground electrode. The resulting voltage-charge waveforms were recorded via a digital oscilloscope (PicoScope 3204A, Figure 2.9 a). Total discharge energy is also correlated to the specific input energy (SIE), which can be calculated on the basis of following equation:

$$E = \frac{1}{T}\int_{t=0}^{T} VI.dt \qquad (2.7)$$

$$P = E * f \tag{2.8}$$

$$SIE\ \left(\frac{J}{l}\right) = \frac{discharge\ power\ (W)}{gas\ flow\ rate\ \left(\frac{l}{s}\right)} \tag{2.9}$$

E is the discharge energy, T is the discharge time, V is voltage across the reactor, I is current of the capacitor, P is discharge power and of the discharge frequency.

2.3.4 Gas analyzing instrumentation

The chemical composition of the gaseous stream has been analyzed by using FTIR spectroscopy (Brucker, Tensor 27) which has been displayed in the Figure 2.10. Infrared spectroscopy is of molecular vibration response. When exposed to infrared radiations, molecules will selectively absorb specific wavelength radiations which cause a change in their dipole moment. Consequently, the vibrational energy levels of the molecules will transfer from a ground state to an excited state.

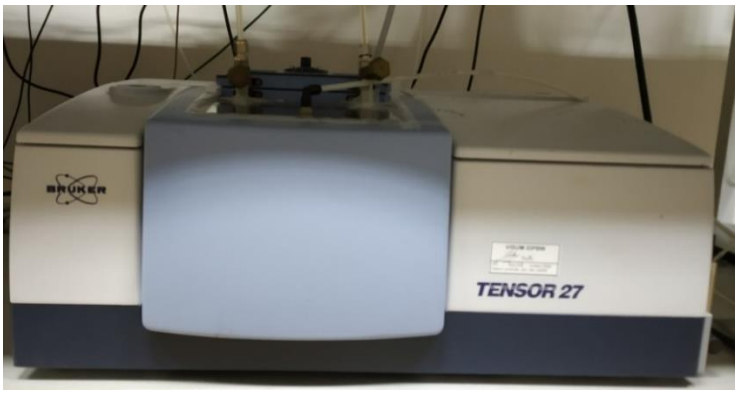

Figure 2.9. *Gas analyzing instrumentation with FTIR.*

The frequency at which the molecule will adsorb the radiation is determined by the vibrational energy gap. The number of possible absorption peaks is directly related to the number of vibrational freedoms of the molecule. The intensity of absorption peaks is related to the extent of the change in dipole moment and the possibility of the transition of energy levels. Therefore, by analyzing the infrared spectrum, one can readily obtain abundant structural information of a molecule.

The following experimental conditions were used to measure the FTIR spectra of both the background and the sample. After a steady-state was observed, the next measurement was conducted automatically.

- Instrument type: Tensor 27 Sample Compartment RT-DLa TGS
- Accessory : General Type-absorbance
- Gas cell : 20 cm optical path length
- Resolution :4 cm^{-1}
- Sample scan number 20 scans
- Background scan number: 20 scans
- Saved data from 4000 to 600 cm^{-1}

2.3.5 Calibration experiments

2.3.5.1 Toluene and COx calibration

The toluene calibration has been performed on the set up. The predefined mixture of different gas streams (toluene 500 ppm, CO_2: 250 ppm, CO: 250 ppm,) in air was connected to set up. Calibration has been performed at a flow rate of 1 $L.min^{-1}$ An FTIR spectrum of toluene in the range of 3060.2 to 3019.4 cm^{-1} which is matches with the standard spectrum of the National Institute of Standards and Technology (NIST). The different steps performed during the calibration process are described below:

Before performing any experiment, the background spectra has been recorded on the FTIR spectrometer, the calibration gas (500 ppm of toluene in air) was fed into the system.

The calibration gas (500 ppm of toluene in air) has been fed and the FTIR spectra has been recorded. Peak has been appeared in the range of 3060.2 to 3019.4 cm^{-1}. The procedure has been repeated for 60 minutes.

A linear regression was applied to the average integration area as a function of time, and the slope (K_1) was used to calculate toluene concentration.

The K_1 is expressed in the following equation (2.10):

$$K_1 = \frac{C_{toluene}}{S_{toluene}} = 1561.8 \qquad (2.10)$$

Where $C_{toulene}$ is the predefined concentration of toluene (ppm) and $S_{toulene}$ the absorbance of the integration area.

2.3.5.2 CO_2 calibration

A cylinder containing a predefined mixture of CO_x was used for CO_2 and CO calibration. The composition of the calibration gases was: CO_2: 250 ppm, CO: 250 ppm, Toluene: 500 ppm.

The cylinder of mixed gases was fed into the system at a flow rate of 1 L.min^{-1}. By comparing with standard NIST data it has been confirmed that peak corresponds to each are located at the same place as reported. After confirmation of the compounds the respective peak has been integrated. The integration process is same as explain in previous paragraph. The slope of the CO_2 (K_2) and CO (K_3) has been calculated as per the following equations:

$$K_2 = \frac{C_{CO_2}}{S_{CO_2}} = 94.6 \qquad (2.11)$$

$$K_3 = \frac{C_{CO}}{S_{CO}} = 1472.2 \qquad (2.12)$$

In summary, the calibration parameters for all compounds are listed in Table 2.2. All concentration calculations have been calculated on the basis of following table.

Table 2.2. *The summary of calibration parameters.*

Compound	Formula	Wavenumber (cm^{-1})	K
Toluene	$C_6H_5CH_3$	3060.2-3019.4	1561.8
Carbon dioxide	CO_2	2388.4-2287.2	94.6
Carbon monoxide	CO	2140.3-2071.4	1472.2

2.3.6 Plasma Experiment process

Toluene removal reactions are performed in a home-made Packed bed dielectric barrier discharge (PBDBD) reactor at atmospheric pressure. This reaction is divided into two parts (i) adsorption of toluene (for 5-40 min) (ii) NTP discharge (1 h) for total oxidation of adsorbed toluene which helps to calculate the unconverted toluene and products. Before any experiment, the calcined material is dried at 150 ºC for 4 h at ramping rate 2 ºC with 0.2 L.min^{-1} of dry air to remove the unwanted carbonaceous species and moisture. Meanwhile, the flue gas of 0.2 L.min^{-1} dry air containing 500 ± 10 ppm toluene flowed bypass the PBDBD reactor. The spectra are

recorded (after each 30 sec) for 1 h continuously to know the actual initial toluene concentration. A 2 g of catalyst is loaded into the discharge gap to comprise the plasma-catalysis hybrid system. Then, the flue gas of 0.2 L.min^{-1} dry air containing 500 ± 50 ppm toluene flowed into the PBDBD reactor to start the adsorption of toluene for 20 min. Afterwards, keep the flue gas flow in bypass and record it for half an hour to be sure the initial toluene concentration is same. Furthermore, stop the flue gas and flush the FTIR line by dry air (0.2 L.min^{-1}) to be confirm there is no traces of toluene remains and record it. Finally, air flow is passes through PBDBD reactor and switch on the plasma (44-46 W) for 1 h. The whole process (Figure 2.11) is described as sequence 1 which performed continuously until sequence 4 which helps to know the behavior of regeneration and catalytic performance. The gaseous products are online analyzed using a Fourier-transform infrared (FT-IR) spectrometer (Bruker, Tensor 27).

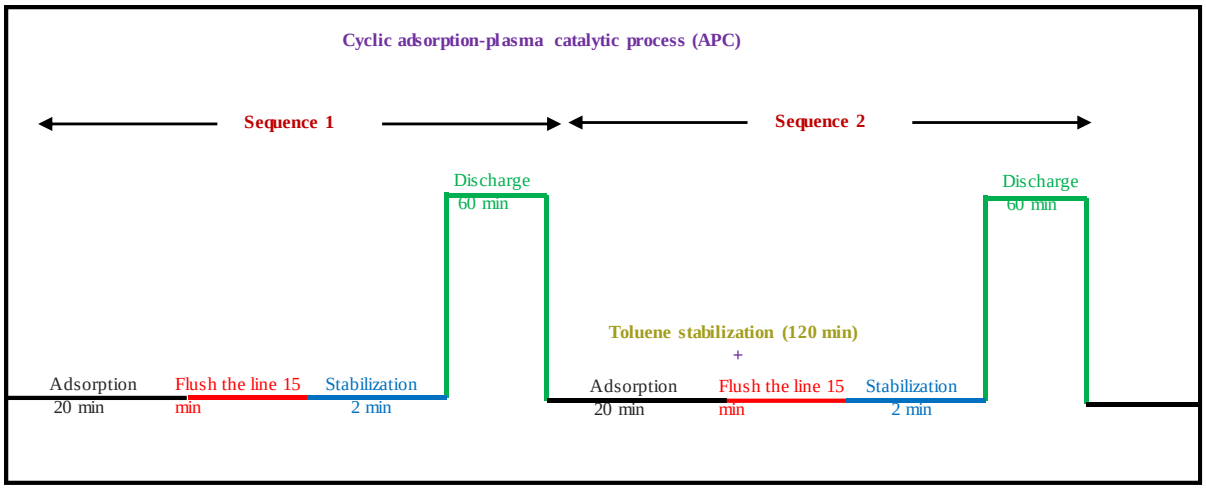

Figure 2.10. *Schematic diagram of the experimental set-up used for abatement of toluene by adsorption-plasma oxidation.*

The amount of toluene adsorbed (µmol. g^{-1}), CO_2 formation (µmol. g^{-1}), selectivity and yield of CO_2 (S_{CO2}, Y_{CO2}) and carbon balance (BC) are calculated by the following equations:

$$q_{ads,des}\ (\mu mol.g^{-1}) = \int_0^t \frac{C_{toluene\ (ppm)}\ f\ \frac{L}{min} dt_1\ (min)}{24.4 \frac{L}{mol}\ m(g)} \times 10^{-6} \qquad (2.13)$$

$$q_{CO2\ formation}\ (\mu mol.g^{-1}) = \int_0^t \frac{C_{\ CO2\ (ppm)}\ f\ \frac{L}{min} dt_2\ (min)}{24.4 \frac{L}{mol}\ m(g)} \times 10^{-6} \qquad (2.14)$$

$$S_{CO2}\ (\%) = \frac{q_{CO2}}{7 \times (q_{ads} - q_{unconv})} \times 100 \qquad (2.15)$$

$$Y_{CO2}\,(\%) = \frac{q_{CO2}}{7 \times \text{qads}} \times 100 \quad (2.16)$$

$$P = E \times F \quad (2.17)$$

$$EC\ (kW.hm^{-3}) = \frac{P \times t_2}{F_1 \times t_1} \quad (2.18)$$

$$EY_{(Tol)}\ (g.kWh^{-1}) = \frac{2 \times q_{ads} \times 92.14}{P \times t_2} \quad (2.19)$$

$$EY_{(CO2)}(g.kWh^{-1}) = \frac{2 \times q_{CO2} \times 44.01}{P \times t_2} \quad (2.20)$$

where $C_{toluene}$, C_{CO2} is the concentration of toluene and concentration of CO_2 respectively, F is the total flow rate ($L.min^{-1}$), m is the mass of material (g) and t is the total adsorption time in min. The unconverted toluene is also calculated by using equation (1). The difference of amount of toluene adsorbed and unconverted toluene denoted as $[Toluene]_{converted}$. Products Selectivity and yield are calculated by using equation (2.15) and (2.16) respectively. The power is calculated on the bases of equation (2.17); where P is discharge power, E is discharge energy which is calculated by $E = \frac{1}{T}\int_{T=0}^{T} VI.dt$ (Where V and I represent the voltage across the reactor and current of capacitor) and F is discharge frequencies. The energy cost (EC) and energy yield (EY) of toluene, CO_2 are calculated by using equations (2.18), (2.19) and (2.20); where P is discharge power (kW), t_1, t_2 are time required for adsorption and for discharge process. F_1 is total flow rate used during adsorption process.

2.4 Synthesis of different materials

2.4.1 Hopcalite

Hopcalite has been purchased form the Purelyst MD101 company, Korea. The pellets (diameter of 3 ± 0.5 mm) have been crushed with the help of molten-piston. To ensure the uniformity of the particle size, the crushed Hopcalite has been passed through the sieve (200-300 μm). The uniform fine powder has been calcined at 300 °C for 4h in air flow with ramping rate of 2 °C.min^{-1}.

2.4.2 UiO-66-SO_3H

UiO-66-SO_3H was synthesized as per the reported literature [192].Typically, a mixture of $ZrO_2Cl_2 \cdot 8H_2O$ (0.31 mmol), mono sodium 2-sulphoterethalic acid (0.31 mmol) and formic acid (3.18 mmol) in N, N Dimethyl acetamide (3 mL) is placed in a Pyrex tube (10 mL). The filled pyrex tube is sealed and heated at 150 °C for 24 h, followed by cooling to room temperature. The white precipitate is collected by filtration, washed with acetone and dried in air. Furthermore, as synthesized compound is activated as per following procedure. As synthesized UiO-66-SO_3H (0.3 g) is stirred in dimethyl formaldehyde (DMF, 20 mL) under ambient conditions for 12 h. Furthermore, this solution is filtered and activated by using methanol (30 mL) under ambient conditions for 24 h. The activation of compound is done by heated methanol exchange compound at 65 °C under dynamic vacuum for 24 h.

2.4.3 Ceria-NR

Ceria-NR (CeO_2) has been synthesized as per the procedure reported by Du et. al. [193]. Typically, 1.74 g of $Ce(NO_3)_3 \cdot 6H_2O$ and an appropriate amount of NaOH (19.2 g) were dissolved separately in 40 mL of distilled water each. The solutions were mixed together and kept stirring for 30 min. The mixture was then transferred to a stainless steel autoclave with Polytetrafluoroethylene (PTFE) lining (100 mL) and maintained at 100 °C for 24 h. Then, the autoclave was cooled to room temperature naturally. The resulting slurry was collected by centrifugation, washed with distilled water and ethanol, and then dried at 80 °C for 12 h. Finally, the resulting powder was calcined at 400 °C for 5 h in air with ramping rate 2 °C.min^{-1}.

2.4.4 Silver impregnation over different materials

Silver (X = 0.5, 1, 2, and 10 wt.%) over calcined Hopcalite was prepared by wet impregnation method [194]. Typically, in round bottom flask, 100 mL of a silver nitrate solution ($AgNO_3$, 99.5 %, Fluka) containing desire amount of silver was added to 1 g of the calcined Hopcalite (diameter of 3±0.5mm, crushed and sieved to obtained uniform particle size 200-300 μm). The required amount of silver nitrate for each silver loading catalyst is shown in Table 1. Furthermore, the resulting mixture was stirred at room temperature for 2 h at 300 rpm. Then the mixture was subjected to stirred constantly at 60 °C, using a rotary evaporator (rotational speed:20

rotations/min) at a pressure of 50 mbar (Büchi Rotavapor R-114). The obtained solid was dried overnight at 100 ºC followed by an air flow calcination (0.2 L min^{-1}) at 400 ºC (1 ºC min^{-1}) for 4 h. For UiO-66-SO_3H, sample was used as synthesized and the rest of the procedure was same as before. The catalysts were labeled Hop-X Ag, where X denotes the amount of silver impregnated.

Table 2.3 *Summary of the required amount of silver nitrate.*

Material	Wt. of $AgNO_3$ (g)
Hop-0.5 Ag	0.0078
Hop-1 Ag	0.0158
Hop-2 Ag	0.0316
Hop-10 Ag	0.0158

The amount of silver nitrate for different silver loading catalysts were calculated by following steps:

For example, for Hop-1 Ag,

Calculation: Silver source: Silver nitrate ($AgNO_3$, 99.5 % fluka) = Mol.Wt =169.872 $g.mol^{-1}$.

Ag = 107.86 $g.mol^{-1}$.

Hop-1 Ag:

Ag = $AgNO_3$

107.86 = 169.872

0.01 = ?

X = 0.01* 169.872/107.86 =0.01574 g of $AgNO_3$

Correction of 99.5 % was given

X= 0.01582 g of $AgNO_3$

2.5 Characterization methods

Materials were characterized by using different techniques like X-Ray Diffraction (XRD), N_2 physisorption (BET), X-ray photoelectron spectroscopy (XPS), Temperature programmed reduction (TPR), Thermal gravimetric analysis (TGA/DSC), Scanning electron microscopy (SEM), Transmission electron microscopy (TEM), Fourier transform Infrared Spectroscopy-

Attenuated Total Reflectance (FTIR-ATR) and Time of Flight Secondary Ion mass spectrometry (ToF-SIMS).

Detailed information of the used characterization techniques is given below.

X-ray powder diffraction (XRD)

XRD is a rapid, non-invasive analytical technique primarily used for phase identification of crystalline materials. XRD analysis was applied on the different catalysts to identify the presence of different phases in the catalysts.

The XRD patterns of the different materials were obtained using a D8 Advanced Bruker AXS diffractometer. The wavelength of CuKα1 X-ray radiation used was 1.5418 Å. The configuration for Bragg-Brentano diffractometer was theta-2 theta. The samples were immobilized on ceramic glass (Macor) holders. The angle (2θ) of XRD was varied between 0 and 80° with a step size of 0.01° and an integration time of 1 s.

Textural properties analysis via Brunauer–Emmett–Teller (BET) and Barrett-Joyner-Halenda (BJH)

The textural properties, specific surface area and pore size distribution, were studied via N_2 adsorption-desorption measurements at liquid nitrogen temperature. BET theory aims to explain the physical adsorption of gas molecules on a solid surface and serves as the basis for the measurement of the specific surface area. BJH analysis is a pore size distribution determination method, which is typically applied to nitrogen desorption data measured at 77 K on catalysts.

Two types of surface area analyzers were employed during the course of this work: the Micromeritics Flow Sorb III serial 416 and the Micromeritics TriStar-II. The first one provided the single-point surface area measurement and was capable of measuring the samples surface area from 0.01 $m^2.g^{-1}$ to over 1000 $m^2.g^{-1}$. Before the test, a continuous flow of N_2 passed over the sample at atmospheric pressure, and then the degassing process was performed on the bases of the required temperature for materials. After degassing, the samples were first cooled at liquid nitrogen temperature, and sequentially into distilled water. The surface area can be calculated based on the equation (2.20) described below:

$$S_{BET} = \frac{A * L}{m_{degassing}} \qquad (2.20)$$

Here A is molecular cross-sectional area, m is the mass of adsorbent, and L = 6.023×10^{-23} is the Avogadro constant.

The surface areas and porosity were obtained using Micromeritics TriStar-II device. The device contains two parts: one is the sample degas system, which contains a sample degasser (Micromeritics Vacprep 061) and a vacuum pump (PFEIFFER Duo 2.5). Another one is an analysis system, which contains the surface areas and porosity analysis equipment (Micromeritics TriStar-II) and a vacuum pump (PFEIFFER Duo 2.5).

Prior to the measurement, Hopcalite, Ceria and UiO-66-SO_3H were degassed at 150 °C for 5 h, 250 °C for 5 h and 100 °C for 24 h under vacuum, respectively. After the samples were placed in the test chamber; the surface area and pore size distribution were calculated automatically. The total pore volume (V_{total}) was estimated from the amount adsorbed at a relative pressure of 0.99.

X-ray photoelectron spectroscopy (XPS)

XPS is a surface-sensitive semi-quantitative spectroscopic technique that measures the elemental composition of the first few nm.

X-ray photoelectron spectroscopy (XPS) is widely used for probing the electronic structure of atoms, molecules and condensed matter. When an X-ray photon of energy hν is incident on a solid matter, the kinetic energy (EK) and the binding energy (Eb) of the ejected photoelectrons can be related as follows:

$$EK = h\nu + Eb \qquad (2.21)$$

This kinetic energy distribution of the photoelectrons is fabricated by a series of discrete bands, which symbolizes for the electronic structure of the sample. The core level binding energies of all the elements (other than H and He) in all different oxidation states are unique, which provides instant detection of the chemical composition of the sample after a full range scan. However, to account for the multiplet splitting and satellites accompanying the photoemission peaks, the photoelectron spectra should be interpreted in terms of many-electron states of the final ionized state of the sample, rather than the occupied one-electron states of the neutral species.

For XPS experiments, the analysis was performed at room temperature under ultra-vacuum conditions. Using an AXIS Ultra DLD Kratos spectrometer equipped with a monochromatized

aluminum source (Al Kα = 1486.7 eV) and a charge compensation gun. The hemispherical analyzer (ΔE / E) was constant. The power of the source was kept at 150 W, and the passing energies of the high resolution and the overview survey were 40 eV and 160 eV with step sizes of 0.1 eV and 1 eV respectively. All binding energies were referenced to the C 1s core level peak at 284.8 eV. The data has stimulated by using CasaXPS software. Quantitative analysis was accounted for a nonlinear Shirley background subtraction.

The AOS of Mn was calculated based on the binding energies of the doublet separation of Mn3s (ΔE). The equation is described as follows:

$$AOS\ Mn = 8.956 - 1.13\Delta E \qquad (2.22)$$

H_2-Temperature-programmed reduction (H_2-TPR)

TPR is a technique for the characterization of heterogeneous catalysts and the quantification of their reduction capacity.

0.050 g of catalyst samples were prepared for the TPR tests. H_2-based TPR experiments were performed using a Micromeritics Autochem catalyst analyzer equipped with a quartz U-shaped microreactor. A H_2/Ar gas mixture was sent into the reactor at 50 mL.min^{-1} while the reactor temperature was increased from room temperature to 1000 ° C at a heating rate of 10 ° C.min^{-1}.

Thermogravimetric analysis (TGA)

Thermogravimetric analysis is a technique measuring the variation in mass of a sample when it undergoes a temperature scanning in a controlled atmosphere. Thermal analysis is widely used to study the structural stability material. It also provides information about temperature required for the removal of adsorbed water and decomposition of the occluded organic species. Data obtained from TG, DTA and DTG helps in evaluating the thermal properties of materials. The shape and splitting of the endotherms (low temperature) helps to identify the location of water molecules. Phase transformations (if any) can also be understood from the exotherms obtained at higher temperatures.

The different samples thermal analysis was performed using a thermogravimetric analyzer (TA instruments SDT 2960 simultaneous DSC-TGA). Samples were heated from room temperature to 1000 °C at a ramp rate of 10 °C.min^{-1} and in an air (100 mL.min^{-1}) atmosphere.

Scanning Electron Microscopy (SEM)

The morphologies of catalysts were examined by SEM images recorded on a Hitachi S-3400N apparatus. SEM micrographs were taken with an accelerating voltage of 15 kV. Before SEM analysis, the samples were deposited on carbon tape.

Transmission Electron Microscopy (TEM)

The sample morphology was characterized by Transmission electron microscope (TEM) using a FEI Titan Themis 60-300 kV and FEI TECNAI TEM at 200 kV with LaB6 filament. For TEM analysis, the sample powders were deposited on a carbon-coated copper grid.

Fourier transform Infrared Spectroscopy-Attenuated Total Reflectance (FTIR-ATR)

Fourier transform infrared (FTIR) spectroscopy deals with the vibration of chemical bonds in a molecule at various frequencies depending on the elements and types of bonds. Attenuated Total Reflectance- Fourier transform Infrared Spectroscopy (FTIR-ATR) spectra were recorded on Thermo scientific iS50 FTIR spectrometer. For each sample 256 scan were measured with an instrument resolution 2 cm^{-1} over the spectral range 4000-200 cm^{-1}.

Time of Flight Secondary Ion mass spectrometry (ToF-SIMS)

ToF-SIMS data were acquired using a ToF-SIMS5 spectrometer (ION-TOF GmbH Germany) equipped with a bismuth liquid metal ion gun (LMIG). The crushed powder samples were bombarded with pulsed Bi_3^+ primary ion beam (25 keV, 0.25 pA) rastered over an area of 500 × 500 μm^2. With 100 scans and 128 ×128 pixels the total fluence did not amount up to 10^{12} ions/cm^2 ensuring the static condition. Charge effect were compensated by means of 20 eV pulsed electron flood gun. Under these experimental conditions, the mass resolution ($m/\Delta m$) was about 4000 at m/z=107 for Ag^+. Data were collected over a mass range m/z= 0-800 for both positive and negative ions.

Chapter 3

Abatement of Toluene Using a Sequential Adsorption-Thermal Catalytic Oxidation Process (ATC): Comparative Study of Potential Adsorbent/Catalytic Materials

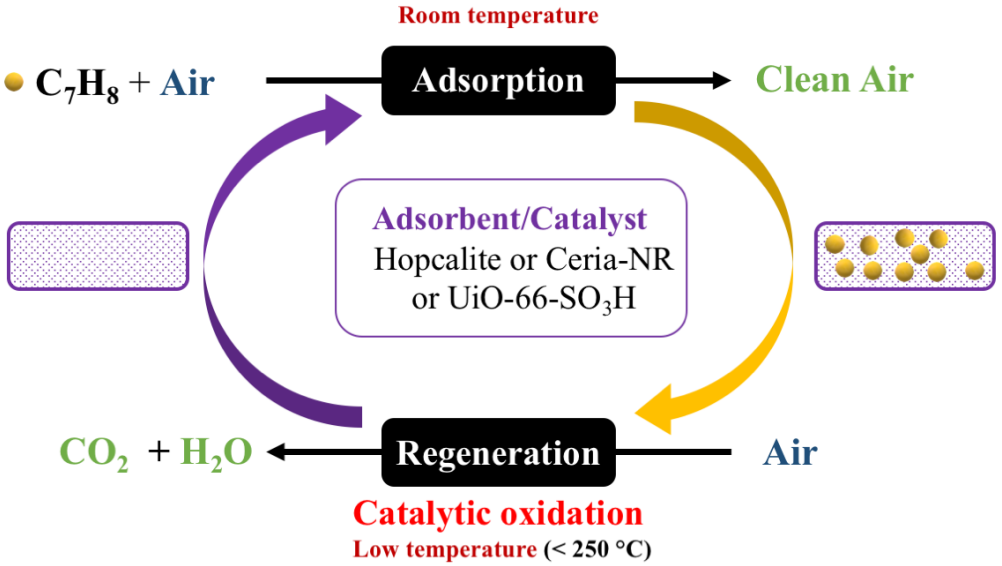

The results of chapter 3 were published in the following international peer-reviewed journal:
Shilpa Sonar, Jean-Marc Giraudon, Savita Kaliya Perumal Veerapandian, Rim Bitar, Karen Leus, Pascal Van Der Voort, Jean-François Lamonier, Rino Morent, Nathalie De Geyter and Axel Löfberg.
Abatement of Toluene Using a Sequential Adsorption-Catalytic Oxidation Process: Comparative Study of Potential Adsorbent/Catalytic Materials.
Catalysts 2020, 10 (7), 761.

Chapter 3 Abatement of Toluene Using a Sequential Adsorption-Thermal Catalytic Oxidation (ATC) Process: Comparative Study of Potential Adsorbent/Catalytic Materials

3.1 Introduction

Storage regeneration processes is novel approach to eliminate low-concentration indoor VOCs such as formaldehyde and benzene [42]. This sequential method implies two steps: (i) first, the VOC is adsorbed on a material and (ii) then a regeneration of the material through VOC oxidation into CO_2 and H_2O is performed. A key issue in this approach is the design of adsorbent/catalytic materials which should possess balanced properties between storage and regeneration. To overcome on this problem a novel strategy for toluene abatement is proposed using a sequential adsorption-regeneration process. The implementation of such process requires to identify proper materials that exhibit both sufficient adsorption capacity and good catalytic performances. This can be approached by different ways, for example by adding catalytic functions to well-known adsorbents or by developing the adsorption properties of known catalytic materials. For instance, in this exploratory work, Hopcalite (Purelyst 101MD), nanorod Ceria, and a sulfonic Zr-based metal organic framework (MOF) (UiO-66-SO_3H) have been used for the adsorption-thermal catalytic removal of toluene using a mild thermal activation from 25 °C up to 250 °C.

Toluene was first adsorbed on the material and a mild thermal activation was performed afterwards in order to oxidize toluene into CO_2 and H_2O. The materials were characterized by XRD, N_2 adsorption-desorption analysis, H_2-TPR and TGA/DSC. The performance of Hopcalite (Purelyst 101MD), nanorod Ceria, and a sulfonic Zr-based metal organic framework (MOF) (UiO-66-SO_3H) have been investigated.

3.2 Experimental conditions

Two catalysts such as Ceria-NR and UiO-66-SO_3H are prepared. The commercial catalyst Hopcalite (Purelyst MD101). It is used to compare the catalytic activity with as prepared catalysts. The characterization includes XRD, N_2 adsorption-desorption isotherms, H_2-TPR, TGA/DSC and XPS. The detail synthesis process, characterization process and experiment process can be seen in chapter 2.

3.3 Result and Discussion

3.3.1 Catalyst Characterization

3.3.1.1 Structural Properties

The X-ray diffraction (XRD) pattern (Figure 3.1) of Hopcalite shows two low intensity peaks positioned at 36.7° and 66.0° in 2θ originating from some based MnO_2 spacing in line with the amorphous character of the material [195]. The XRD pattern of the as-synthesized CeO_2-NR shows well defined diffraction peaks located at 28.5°, 33.1°, 47.5°, 56.3°, 59.1°, 69.4°, 76.7°, and 79.1° ascribed to the (111), (200), (220), (311), (222), (400), (331), and (420) planes of the face-centered cubic (fcc) CeO_2 fluorite structure (JCPDS 34−0394, space group Fm3m) [196]. Using the Scherrer formula, it was found that mean crystallite size of 8 nm from the (111) peak. The XRD pattern of UiO-66-SO_3H is in good agreement with those reported previously for a crystalline activated UiO-66-SO_3H [188,192,197,198].

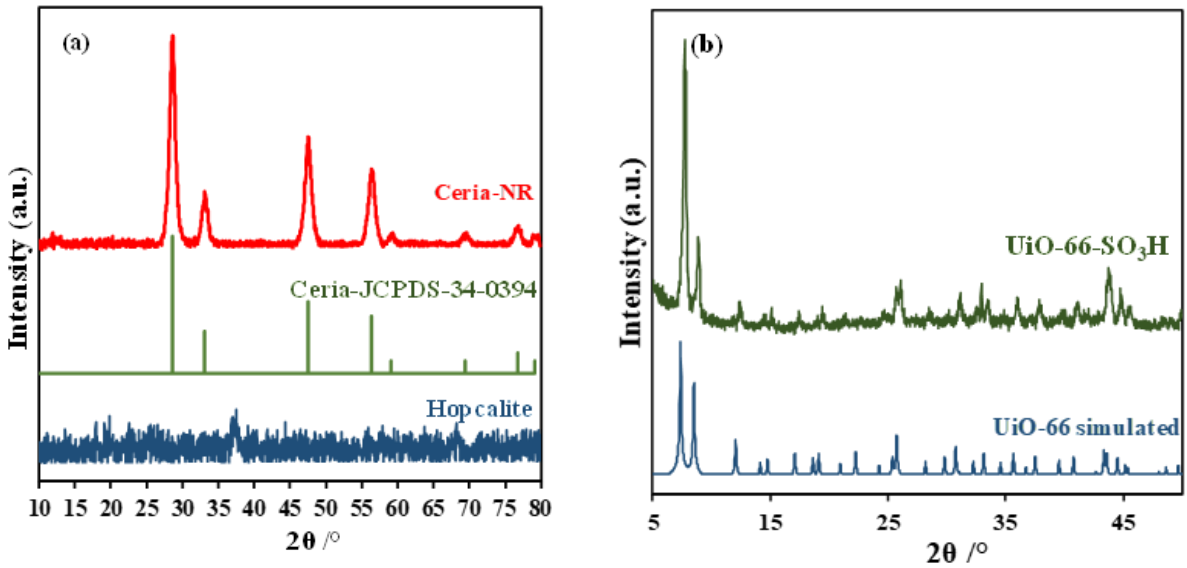

Figure 3.1. *XRD patterns of (a): Hopcalite and CeO_2-NR, (b): UiO-66-SO_3H.*

3.3.1.2. Textural Properties

The N_2 adsorption-desorption isotherms and pore size distribution (PSD; insets) of the three materials are illustrated in Figure 3.2 and the corresponding textural properties are summarized in Table 3.1. The crushed and sieved particles of commercial Hopcalite show a type IV isotherm with

an H3 hysteresis loop in the relative pressure (P/P^0) range of 0.42-1.0. The formation of two adsorption steps at relative pressures (P/P^0) 0.6-0.8 and 0.9-1.0 due to capillary condensation is indicative of a mesoporous material in line with well-distributed pore diameters at 7.8 nm followed by a broad porosity distribution displaying maximum pore diameters around 80 nm. Additionally, the vertical nitrogen uptake at P/P^0 below 0.05 is characteristic of micropore filling. The specific surface area is 229 $m^2.\ g^{-1}$ and the total pore volume V_p is 0.45 $cm^3.g^{-1}$. The S_{BET} value is less than the one reported by the supplier (> 300 $m^2.\ g^{-1}$ as pellets).

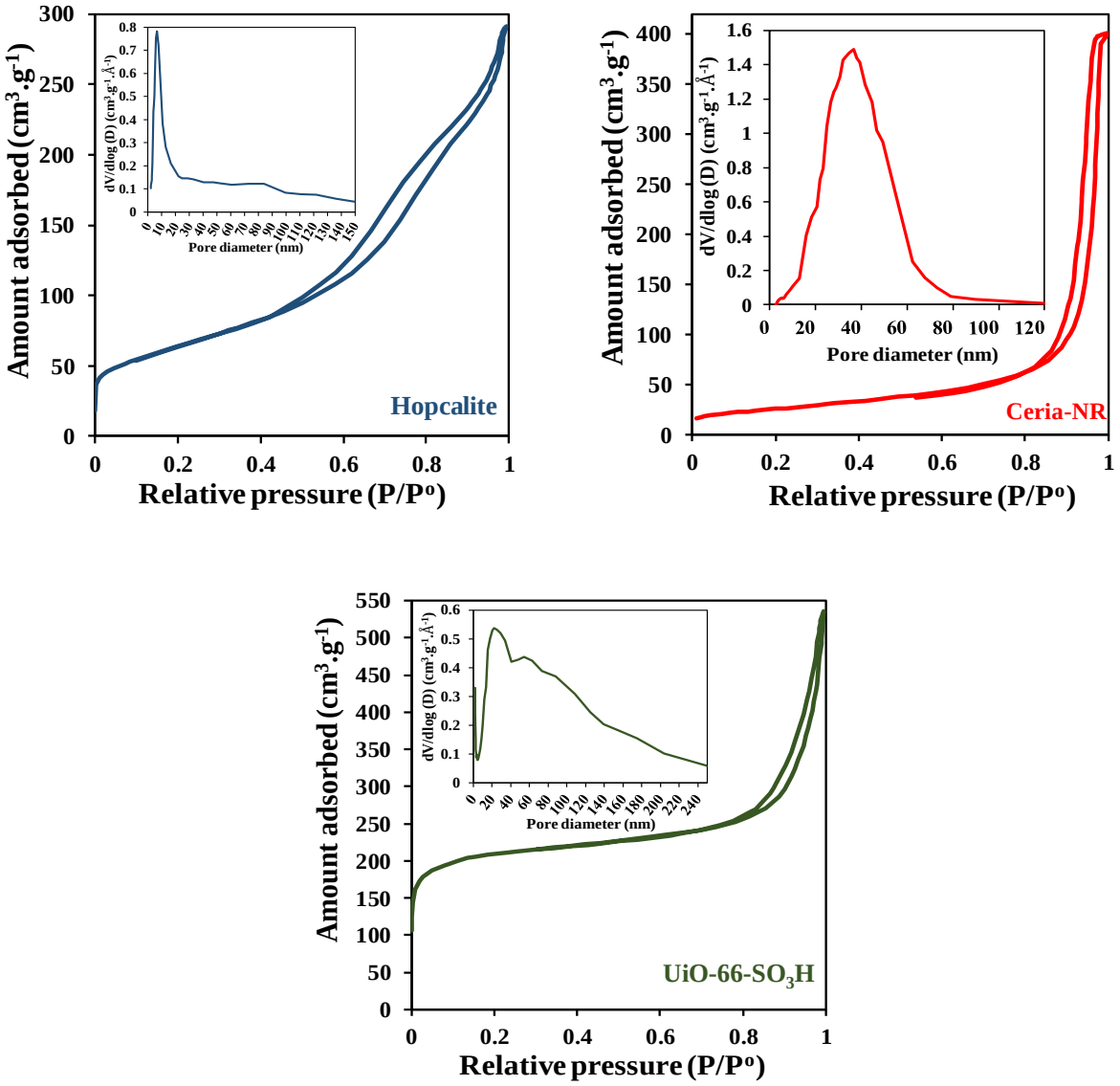

Figure 3.2. *N_2 adsorption/desorption isotherms and PSD (inserts) of Hopcalite, Ceria-NR and UiO-66-SO_3H.*

The isotherm of Ceria-NR shows a Type IV shape with a Type H1 hysteresis loop in the high relative pressure (P/P^0) range of 0.82-1.0. The PSD shows a broad peak centered at 35 nm corresponding to the inter-particle spaces in the scaffold-like assembly of nanorods [199]. The BET surface area of 91 $m^2.g^{-1}$ and V_p of 0.63 $cm^{3}.g^{-1}$ are in accordance with previous results [193,200].

The N_2 sorption isotherm of activated UiO-66-SO_3H is a somewhat mixed type I/IV, with a sharp increase of gas uptake at the low-pressure range and an observable hysteresis between adsorption and desorption branches in the high relative pressure (P/P^0) range of 0.73–1.0. UiO-66-SO_3H is a microporous metal-organic framework. The lattice capillary condensation is due to interparticle porosity. As formic acid acts primarily as a monodentate modulator to compete with bidentate bridging H_2BDC-SO_3H ligands for coordination sites on Zr-oxo clusters, the generation of missing-linker defects can be envisioned via incomplete exchange of the pre-loaded formate ligands on the $[Zr_6O_4(OH)_4]^{12+}$ secondary building units [201]. The specific surface area of 685 $m^2.g^{-1}$ is in agreement with values generally reported for a rather similar material [192,202,203] although an exceeding value of about 1180 $m^2.g^{-1}$ was reported for a sulfonic UiO-66 synthesized via a direct solvothermal approach using a mixture of organic linkers (H_2BDC-SO_3H/ H_2BDC) [204].

To sum up, the textural properties are broadly in line with those expected for commercial Hopcalite, CeO_2-NR and UiO-66-SO_3H taking into account the adopted experimental procedures. UiO-66-SO_3H shows an outstanding S_{BET} value as compared to the two other porous materials. Additionally, the three materials differ from their pore size distributions. Indeed, the functionalized UiO66-SO_3H displays a hierarchical porosity while the two other solids are mesoporous with Hopcalite developing smaller pores than CeO_2-NR.

3.3.1.3. Redox Properties

The redox properties of the samples were assessed by means of H_2-TPR experiments. H_2-consumption traces are reported in Figure 3.3 and H_2 consumption amounts are compiled in Table 3.1.

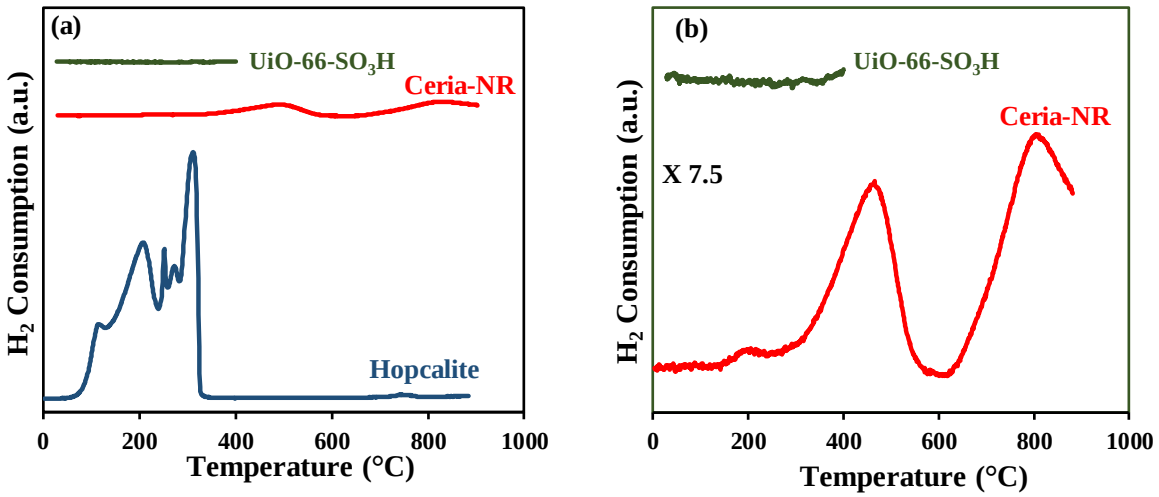

Figure 3.3. *(a) H_2-TPR curves of the samples; (b) zoom of the H_2-TPR curves.*

Table 3.1. *Textural and redox properties of the materials.*

Materials	S_{BET} ($m^2\ g^{-1}$)	V_p [a] ($cm^3\ g^{-1}$)	H_2 Consumption ($mmol\ g^{-1}$)
Hopcalite	229	0.45	11.1
Ceria-NR	91	0.63	0.65
UiO-66-SO_3H	685	0.82	0.60

[a] Total pore volume.

The H_2 consumption trace of commercial Hopcalite is complex and resembles broadly to that reported previously for a CuO-MnO_2 solid [205]. The reduction process starts at 90 °C and ends at approximately 360 °C. Five reduction peaks are observed with maxima located at 147, 209, 239, 273 and 343 °C. The first peak at 110 °C and part of the second one are assigned to the reduction of CuO_x entities into Cu(0). As soon as Cu(II) is reduced into Cu(0), a spill-over of hydrogen takes place from Cu(0) to Mn(IV) entities. As that stage, the reduction of Mn(IV) species occurs in different steps to give MnO at the end of the process. This is supported by the quantitative results of the H_2 consumption per gram of catalyst. The H_2 consumption of 11.1 $mmol.g^{-1}$ results to a Mn average oxidation state (AOS) of 3.92, a value close to 4.0, assuming the complete reduction of CuO into Cu(0).

The H_2-TPR trace is very flat for CeO_2-NR attesting of a low H_2 consumption as compared with Hopcalite. Three reduction peaks centered at 221 °C, 488 °C and 830 °C related to surface-adsorbed oxygen, sub-surface oxygen and bulk oxygen can be detected in Figure 3.3b [206]. The sub-surface oxygen species, which are generally considered as the active oxygen species in the low temperature oxidation reactions, amount to 0.65 $mmol/g_{cat}$, which is much less than the value

of 1.05 mmol.g_{cat}^{-1} obtained by Z. Hu et al. for Ceria nanorods [159]. The H_2-TPR trace for UiO-66-SO_3H is flat from 20 °C to about 400 °C in line with a non-redox active material.

XPS has been performed on Hopcalite to get information about the composition and chemical states of Cu and Mn. The atomic Cu/Mn ratio is 0.16. The Mn AOS, estimated from BE energy separation of the two Mn 3s peaks, [207] is 3.14. The BE of $Cu2p_{3/2}$ of 933.3 eV is in accordance with Cu (II) oxide related species [208]. Hence, we get a Cu(II)/Mn(III) redox system at the surface of Hopcalite in accordance with literature [122].

3.3.1.4. Thermal Stabilities Properties

The thermal stability of the solids has been assessed through TGA/DSC characterizations performed in dry air (Figure 3.4).

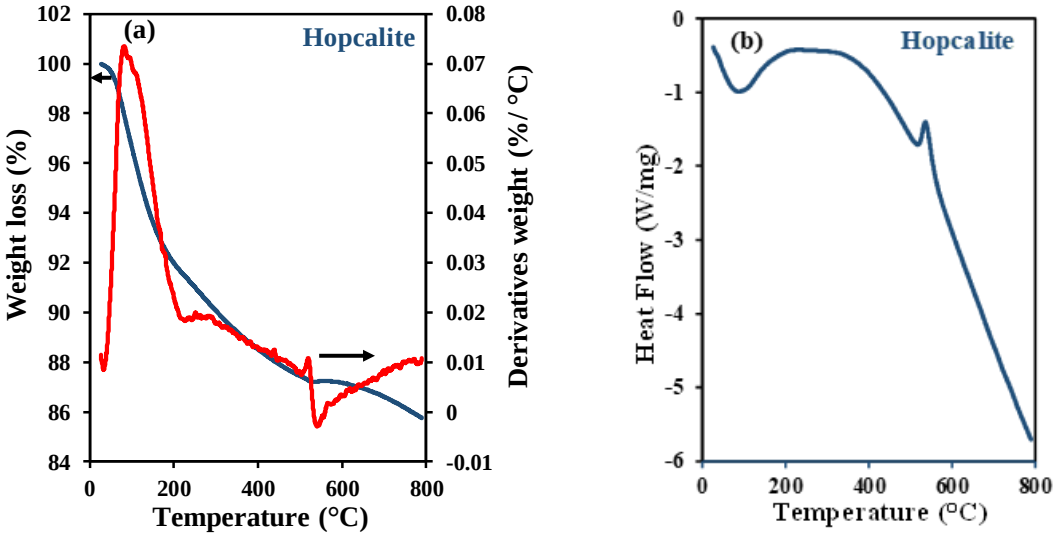

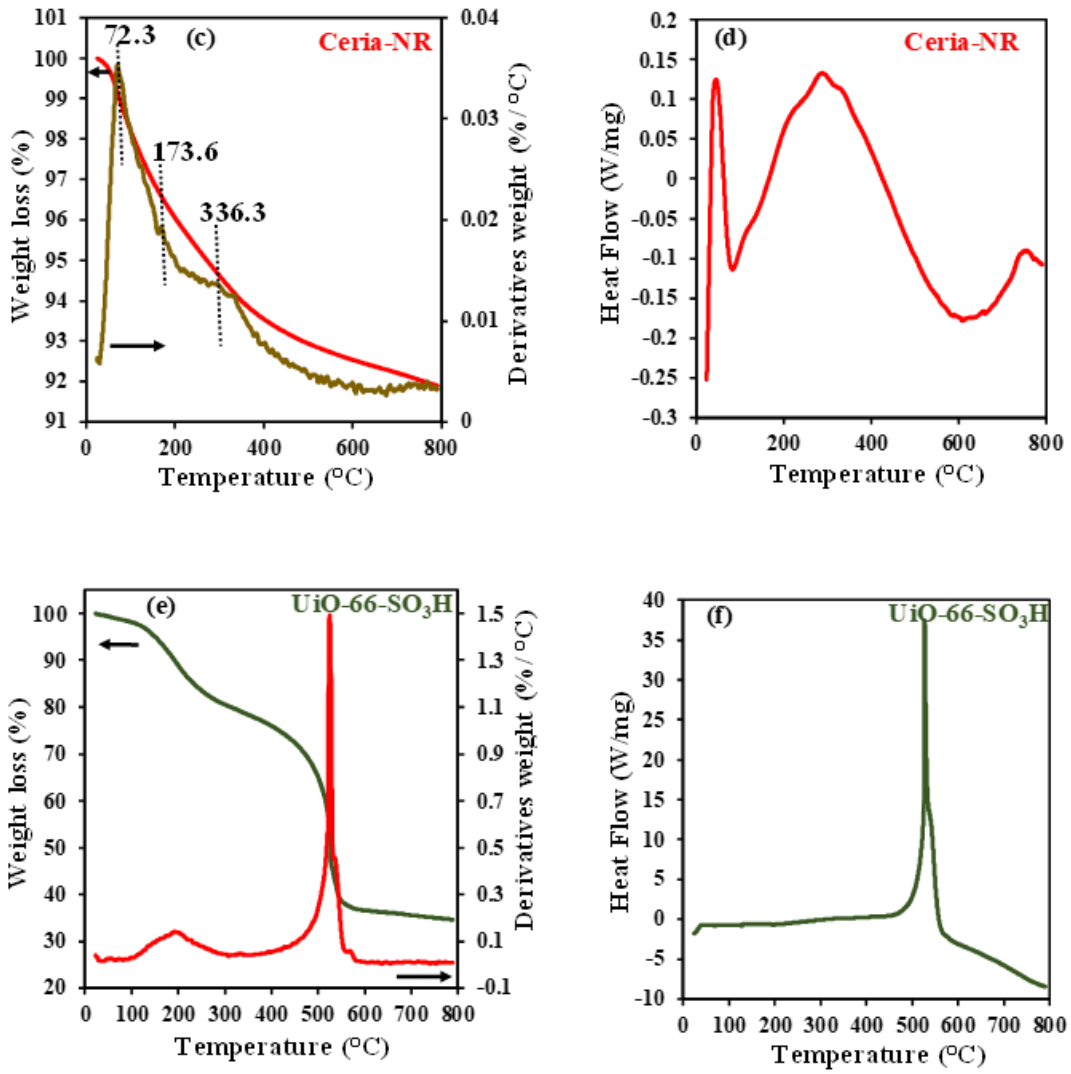

Figure 3.4. *Weight loss (a, c, d) and heat flow (b, e, f) profiles during TGA-DTG analysis of Hopcalite (a,b), CeO_2-NR (c, d) and UiO-66-SO_3H (e, f).*

TGA curve of Hopcalite shows a total weight loss of 14.2 wt.% upon heating up to 800 °C. The DTG curve shows two maxima followed by a minimum at 86.8 °C, 522.6 °C and 540 °C, respectively. The first weight loss (25 °C-150 °C, 8.5 wt.%) is assigned to the release of residual water (endothermic peak) followed by dehydroxylation up to 510 °C (4.2 wt.%) [209]. Afterwards a small gain of weight accompanied with an exothermic peak is observed (0.06 wt.%) followed by a slight weight loss (1.5 wt.%) up to 800 °C.

TGA curve of CeO_2-NR is displayed in Figure 5b. The studied sample shows overall weight loss of 8.0 wt.% upon heating up to 800 °C. A three weight loss step process can be identified

from the DTG curve giving two minima at 72.1 °C and 173.6 °C and 336.3 °C. Based on previous reports the first weight loss (25 °C-200 °C) accompanied with an endothermic peak can be attributed to the elimination of physically and chemically absorbed water as well as surface OH groups [210,211]. The second weight loss accompanied with a broad exothermic signal can be due to dehydroxylation/oxygen lattice removal. The last weight loss accompanied with an exothermic peak at 336 °C can be due to crystallization of CeO_2 [210].

For the activated UiO-66-SO_3H, the DTG curve shows minima at 185 °C and 520 °C indicative of two main weight loss steps (Figure 4). The first weight loss (≈ 20 wt.%) up to 300 °C can be attributed to the release of volatile impurities and CO_2 trapped in the porous network of the MOF [192]. This assumption is supported by the fact that UiO-66-SO_3H loses 11.6 wt.% after being heated at 100 °C under vacuum prior to the N_2 adsorption measurement and that no heat flow is detected for a temperature up to 400 °C. A small weight loss occurs between 300 and 400 °C (≈ 4 wt.%). The second main weight loss in the 400-700 °C temperature range amounting to 41 wt.% is due to the decomposition of the MOF. A strong exothermic peak at 520 °C substantiates such a thermal decomposition. The weight loss of 41 wt.% is substantially less than the expected one of 65.5 wt.% assuming total decomposition of $[Zr_6O_4(OH)_4(BDC\text{-}SO_3H)_6]$ into ZrO_2. This can be related to partial substitution of the bridging BDC-SO_3H linkers for formate ligands [212].

Hence it can be stated from TG analysis coupled with DSC that the three samples under study can accommodate a thermal activation at 250 °C without deterioration which is a prerequisite for the intended regeneration process.

3.3.2 Catalytic Oxidation of Toluene

The light-off curves for toluene oxidation are shown in Figure 3.5 and the T_{10}, T_{50}, and T_{90} (temperatures required to achieve 10 %, 50 %, and 90 % of toluene conversion into CO_2) are given in Table 3.2. During the light-off curve study, only CO_2 and H_2O products have been observed.

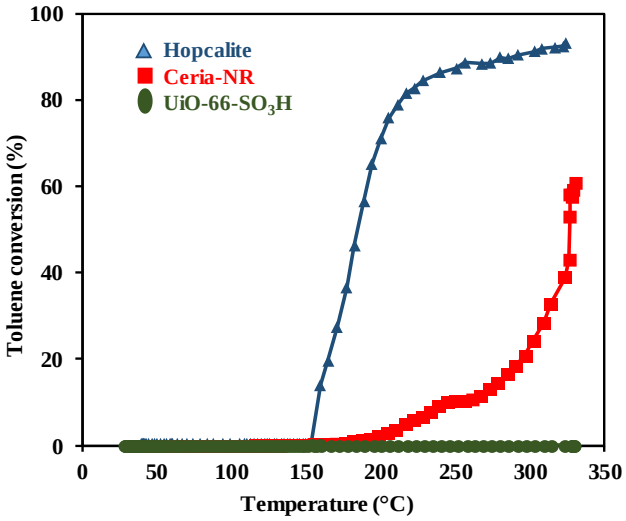

Figure 3.5. *Light-off curves obtained in the presence of Hopcalite, Ceria-NR and UiO-66-SO_3H for toluene oxidation.*

Table 3.2. *Catalytic properties of the solids in the toluene oxidation.*

Catalyst	T_{10} (°C)	T_{50} (°C)	T_{90} (°C)
Hopcalite	157	185	291
Ceria-NR	232	321	-
UiO-66-SO_3H	-	-	-

Among the different materials, Hopcalite exhibits the best specific activity in terms of T_{10}, T_{50} and T_{90}. Such results are in accordance with those reported elsewhere [109]. The textural properties (mesoporosity, amorphous state) coupled to the easy cycling between Mn and Cu different valences account for such a behavior. CeO_2-NR is significantly less active as T_{90} could not be measured (> 330 °C) and the T_{50} of 321 °C is substantially higher than that of Hopcalite. However, Ceria itself is sufficiently active to catalyze the oxidation of toluene. The numerous defects in Ceria in the form of oxygen vacancies are believed to be responsible for its unique catalytic properties. Indeed, Ceria with NR morphology is generally recognized to promote oxygen vacancies. However, the surface oxygen amount of 0.65 $mmol.g_{cat}^{-1}$ is two times less than the amount found by Hu et. al. [159]. As described by López et. al. [162], the prevalence of surface oxygen vacancies (linked to a high surface-to-bulk oxygen ratio) promotes the activity of the catalysts. Consequently, the lower amount of surface Ceria may account herein for a T_{50} value higher than reported in the literature for NR Ceria, which are typically in the order of 210-220 °C [162]. As expected, UiO-66-SO_3H does not convert toluene due to a lack of redox properties.

Taking into account the carbon balance, it is found that toluene is trapped inside the UiO-66-SO_3H structure.

3.3.3 Sequential Adsorption/Thermal Catalytic (ATC) Conversion

3.3.3.1. Effect of the Initial Toluene Concentration on Hopcalite

To investigate the dynamic adsorption behavior of toluene over Hopcalite, breakthrough adsorption tests were performed with different initial concentrations of toluene (Figure 3.6a) ranging from 50 to 500 ppm. The adsorption process consists of three steps. First, toluene is fully adsorbed by Hopcalite and very low concentrations of toluene are detected at the outlet of the reactor. This is generally called the unsaturated zone of the breakthrough curve. Second, the appearance of non-adsorbed toluene in the outlet flow, described as the breakthrough stage, is indicative of a weaker adsorption of toluene and by mass transfer limitations. Finally, the inlet toluene concentration is reached, which indicates the saturation [159] and allows for the evaluation of dynamic toluene adsorption capacity of Hopcalite in the given conditions.

At high concentrations of toluene (200 and 500 ppm), the adsorption of toluene is fast. The time during which total adsorption occurs (unsaturated zone) is very short and does not significantly depend on toluene inlet concentration. The curves mostly differentiate by the slope at which saturation is reached in the breakthrough stage. The total adsorption capacity is very similar, in the range of approximately 380-390 $\mu mol.g^{-1}$ (Table 3.3). This behavior may be due to the improvement of driving force for mass transfer across the liquid film along with increasing of the adsorption rate which leads to quick saturation of the adsorbent [213]. This is even more enhanced when 100 ppm toluene feed is used for which the unsaturated zone is less well defined and the adsorption process slower. Finally, with 50 ppm toluene feed, the process is radically different as no toluene can be detected for a long period and subsequently the saturation abruptly occurs.

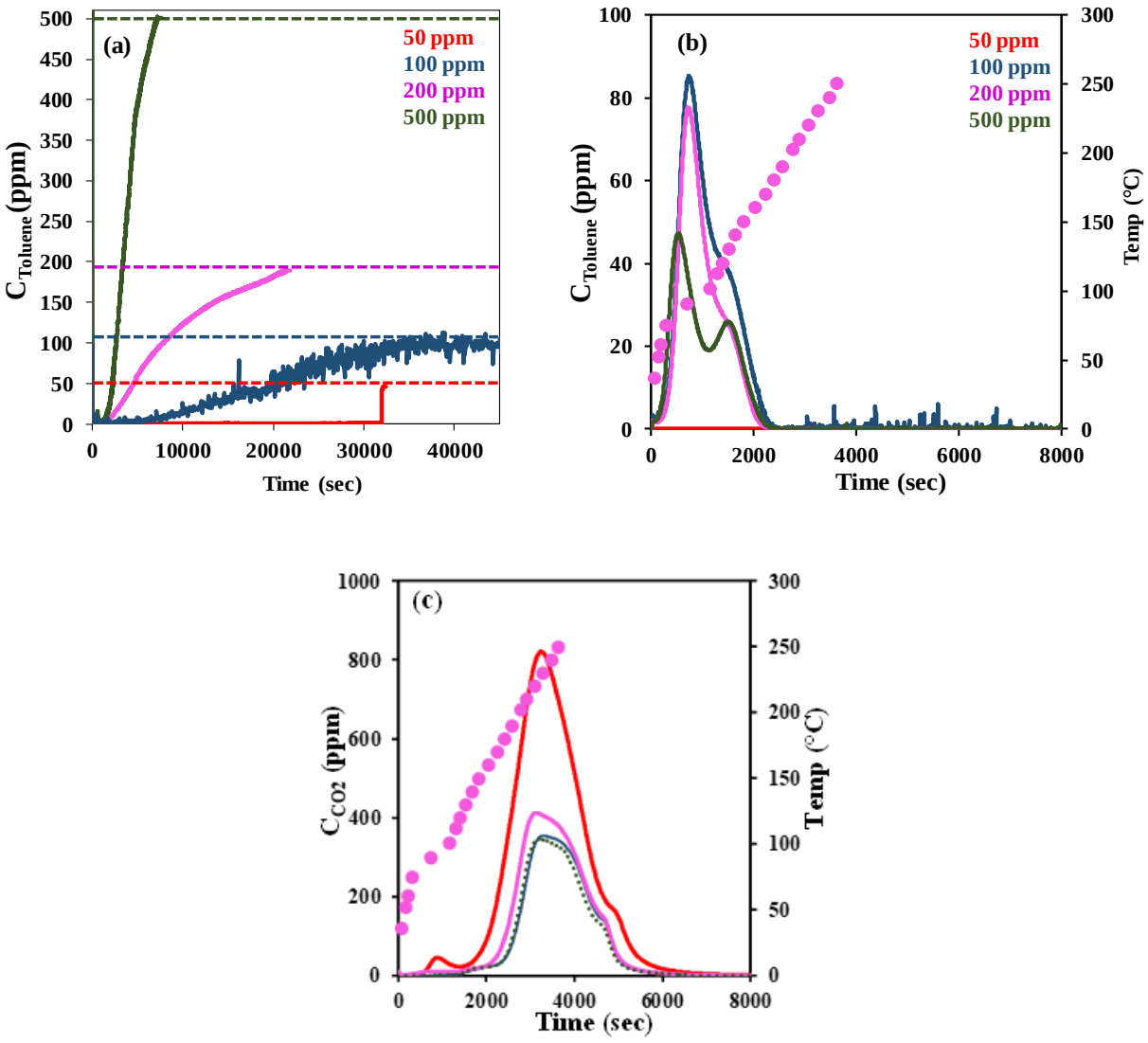

Figure 3.6. *(a) Breakthrough curves of Hopcalite at different initial toluene concentration (dotted line corresponds to the concentration of toluene) (b) TPD profile of toluene (c) TPR profile of CO_2 (circle represent the temperature).*

The different behavior during the toluene adsorption step according to inlet concentration also affects the "useful" adsorption capacity of the material. Indeed, in a real abatement process, the outlet toluene concentration would not be allowed to exceed a given threshold value, i.e., the adsorption step would need to be stopped once the threshold is reached. If one arbitrarily sets the threshold at 10 ppm, the breakthrough curves allow to determine approximately the useful adsorption capacity at 470, 230, 160 and 190 µmol.g^{-1} with initial toluene concentrations of 50, 100, 200, and 500 ppm, respectively. With the exception of 50 ppm conditions, these values are

significantly lower than those obtained when the full adsorption capacity is considered (Table 3.3). This suggests that Hopcalite materials should be used preferentially in abatement processes involving rather low toluene concentrations.

Table 3.3. *Adsorption (ADS) and desorption (DES) reaction of toluene on Hopcalite in He atmosphere.*

Toluene Initial Concentration (ppm)	Tol. ADS at RT (µmol g^{-1})	Tol. DES at RT (µmol g^{-1})	Tol. DES During TPR (µmol g^{-1})	CO_2 Formed During TPR (µmol g^{-1})	CO_2 Yield (%)
50	472	0.0	0.6	3306	99.9
100	384	38	160	1300	48.4
200	392	74	115	1421	51.8
500	379	73	107	1392	52.5

These results suggest a complex adsorption process which could involve a rapid adsorption and condensation in the macropores of Hopcalite at high toluene feed concentration followed by diffusion in the mesopores of the solid (Figure 3.6a). At lower toluene feed concentration, adsorption can occur directly inside the mesoporous structure. Differences can also be seen in the desorption of toluene both at room temperature (not represented) and during heating (Figure 3.6b) in helium. Above 200 ppm toluene concentration, considerable amounts of toluene (72–74 µmol $.g^{-1}$) desorb at room temperature, showing that adsorption is strongly reversible. Using 100 ppm, this amount reduces to approx. 38 µmol.g^{-1} but a higher amount of toluene desorbs during the heating indicating stronger interactions between the adsorbent surface and toluene.

Again, a singular behavior is observed using the lowest toluene concentration for which practically no toluene desorption is observed at room temperature. This indicates a strong interaction between toluene and Hopcalite when adsorption is conducted very slowly which is consistent with the long unsaturated time observed during the breakthrough experiment.

The gas phase analysis based on mass spectrometry reveals the formation of CO_2 (m/z = 44) during the temperature programmed desorption process (Figure 3.6c). Interestingly, no other by products such as CO and HCHO have been observed which is indicative of a high selectivity of Hopcalite towards total oxidation. It can be seen that CO_2 formation starts at 110-120 °C when the lowest toluene concentration was used (50 ppm) and at approximately 150 °C for the higher toluene concentrations. It should be noted that, in this case, CO_2 is produced by reducing the Hopcalite as no oxygen is provided by the gas flow. The highest amount of CO_2 formation is observed (Table 3.3) in the case of an initial toluene concentration of 50 ppm which is consistent with the absence of toluene desorption at room temperature or during TPR.

Therefore, it can be seen that the so-called irreversible adsorption of toluene (i.e., which does not desorb at RT or during heating) is favored when a low concentration of toluene is used in the inlet feed. This could be due to a better distribution of toluene species on the surface of Hopcalite, in particular within the mesoporous structure. Another possibility is that the irreversible adsorption is slow.

3.3.3.2. Comparative Study of the Different Materials

In the previous section, the dynamic toluene adsorption capacity of the adsorbent was determined by breakthrough curves. The breakthrough provides interesting information with regards to the adsorption properties of a solid but, as explained, cannot be reached in a real toluene abatement process because this would mean that a significant amount of toluene would still be released during the so-called breakthrough stage of the curve. In a real process, the adsorption would need to be stopped when a given threshold is reached corresponding to an acceptable level of toluene emission. For these reasons, a comparative study of the three different materials (Hopcalite, UiO-66-SO_3H and Ceria-NR) was performed using 100 ppm toluene in the feed and the process was stopped when a concentration of approximately 10 ppm was reached in the outlet flow. In this way, only the so-called "useful" adsorption capacity was taken into consideration.

To identify the catalytic properties, TPR has been performed in two different conditions: (1) in a pure inert gas, i.e., in a pure helium flow and (2) in an oxidizing atmosphere: He: O_2 = 50:50 with a total flow = 100 mL.min^{-1} in both cases. For each experiment, a fresh sample has been used.

All quantitative data obtained on the three materials in inert or oxidizing atmosphere are summarized in Table 3.4. The "useful" adsorption capacities follow this order: UiO-66-SO_3H > Hopcalite > Ceria-NR which is consistent with the surface area of the respective solids (Table 3.1). Slight differences are observed on all samples between adsorption steps followed by TPR in He or in He:O_2 even though the adsorption process in always performed in similar conditions (without O_2). This can be due to the difficulty in precisely evaluating the moment at which a 10-ppm residual toluene concentration is reached.

Table 3.4. *Comparison of materials during toluene (100 ppm) adsorption followed by temperature programmed desorption in inert and oxidizing atmosphere.*

Materials and TP Atmosphere	Tol. ADS at RT (µmol g^{-1})	Tol. DES at RT (µmol g^{-1})	Tol. DES During TPR (µmol g^{-1})	CO_2 Formed During TPR (µmol g^{-1})	YCO_2 (%)
Hopcalite-He	136	1.4	23.8	780	81.9
Hopcalite-He:O_2	108	1.8	6.8	698	92.3
Ceria-He	73	8.6	60.5	28.0	5.5
Ceria-He:O_2	51	2.6	34.8	53.8	15.1
UiO-66-SO_3H-He	339	1.6	301	258	10.9
UiO-66-SO_3H-He:O_2	315	2.3	267	315	14.3

Figure 3.7 describes the toluene and CO_2 concentration evolution during TPR which follows the adsorption sequence. First, it can be noted that on Hopcalite the overall process is much more efficient in terms of CO_2 yield when the adsorption process is effectively limited to the useful adsorption capacity. Indeed, at a similar inlet concentration of 100 ppm, the CO_2 yield reaches 81.9 % when adsorption is limited to 10 ppm max outlet concentration (Table 3.4) whereas only 48.4 % was obtained when the total adsorption capacity is reached (Table 3.3). Clearly, the amount of reversibly adsorbed toluene is strongly reduced by limiting to the useful adsorption capacity. Still on Hopcalite, in the absence of O_2, a desorption of toluene is observed from room temperature up to approximately 150 °C. This desorption process appears in the form of two peaks, but this could be due to an irregularity in the rate of temperature increase around 80-100 °C as can be seen for all experiments.

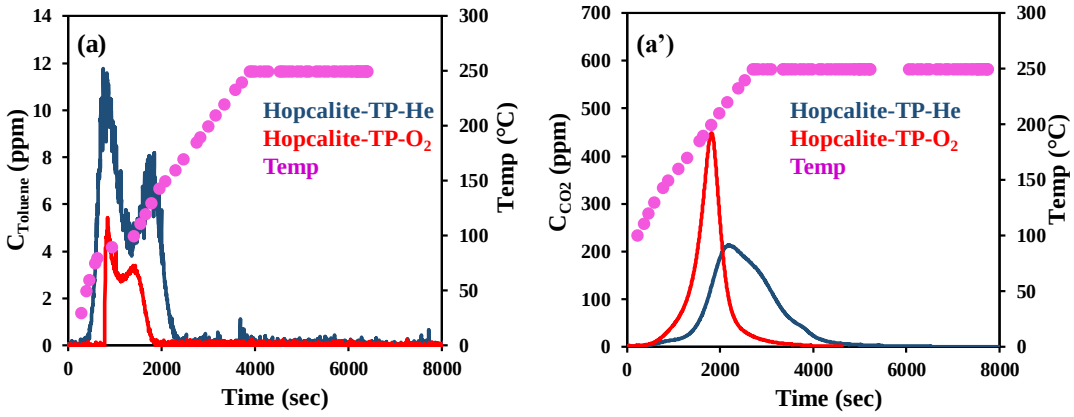

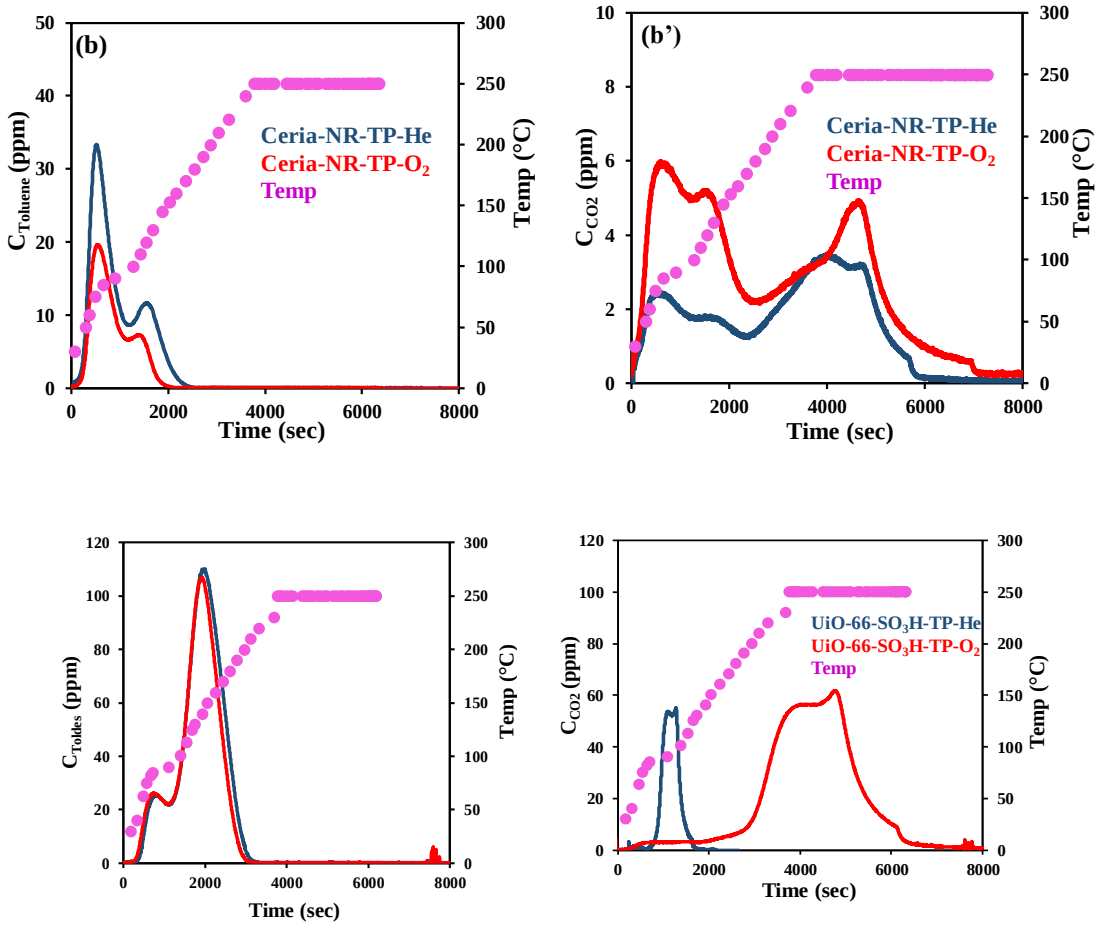

Figure 3.7. *Toluene (a, b, c) and CO_2 (a', b', c') concentration evolution during temperature programmed reaction on Hopcalite (a, a'), CeO_2-NR (b, b') and UiO-66-SO_3H (c, c').*

The decrease in toluene desorption corresponds to the appearance of CO_2 (Figure 3.7a', dark blue curve) due to the reaction between toluene and the lattice oxygen species contained in the catalyst. In the presence of oxygen (red curves), the desorption of toluene is interrupted at lower temperature (T < 100 °C) by a sharp increase of CO_2 production. The maximum CO_2 production is reached at approximately 200 °C and ends before the temperature reaches its maximum of 250 °C contrary to what is observed in the absence of a gaseous oxygen feed. These results are in good agreement with the excellent redox properties of Hopcalite for toluene oxidation as a very high conversion of toluene to CO_2 is also obtained in the absence of oxygen (81.6 vs. 92.0 % in absence or presence of O_2, respectively). The catalytic properties of Hopcalite are evidenced by the lowering of reaction temperature and by a better total conversion to CO_2. Interestingly, the maximum conversion of adsorbed toluene to CO_2 is reached at a similar temperature in sequential mode with respect to the co-feed (Figure 3.5) for which T_{50} was observed at 185 °C.

A similar behavior is observed for CeO_2-NR (Figure 3.7b, b') but with the major difference that the amounts of CO_2 produced are considerably lower than for Hopcalite. It is nevertheless interesting to observe that more CO_2 is produced in the low temperature range (< 200 °C) while practically no catalytic activity was observed at such low temperature in the co-feed (Figure 3.5). At higher temperature, the behavior of Ceria is less affected by the presence of O_2 in the gas phase confirming that mostly subsurface oxygen may be involved.

With the objective to get a more accurate view on the redox properties of the two transition metal oxides, the quantity of extracted oxygen from the solids has been estimated from the amount of CO_2 released during He-TPR after toluene adsorption (Table 3.4) to be compared with H_2 consumption and thus released oxygen in the H_2-TPR experiments (Table 3.1). For Hopcalite, the extracted oxygen to global oxygen (O_{ext}/O_{glo}) atomic ratio estimated from the He-TPR (toluene) is approximately five times lower than the ratio obtained from the H_2-TPR experiment (Table 3.5). This indicates that only the most reducible species or that a few layers of Hopcalite are involved in the reaction. Regarding CeO_2-NR, it is seen that the amount of extracted oxygen with respect to global oxygen (O_{ext}/O_{glo}) in the TPR after toluene adsorption is approximately 10 times lower than the ratio extracted during H_2-TPR. This is in good coherence with the H_2-TPR profile (Figure 3.3) which indicated only a very small hydrogen consumption below 300 °C associated with adsorbed oxygen species. This result suggests that mostly surface and eventually some subsurface oxygen species participate in this oxidation process, which is in accordance with literature [162,214].

Table 3.5. *Determination of extracted oxygen from solids in He atmosphere.*

Materials	**H_2-TPR O Consumption (mmol g^{-1})**	**O_{ext}/O_{glo} [a]**	**He-TPR (Toluene) O Consumption (mmol g^{-1})**	**O_{ext}/O_{glo} [a]**
Hopcalite	11.1	0.47	2.00	0.08
CeO_2-NR	0.65	0.056	0.07	0.006

[a] atomic ratio.

In the case of UiO-66-SO_3H, most toluene desorbs from the surface of the catalysts without transformation (Figure 3.7c) and this is unaffected by the presence of O_2 in the gas phase. Interestingly however, such desorption occurs at much higher temperature as the maximum toluene pressure is reached around 150 °C and ends around 200 °C. Indeed, for other materials, such a process would end below 150 °C. This confirms the excellent adsorption capacities of UiO-66-SO_3H. Significant amounts of CO_2 are produced on this material but these are not affected by the presence of O_2 (Figure 3.7c' and Table 3.4). This indicates that toluene reacts with oxygen species

contained in the solid. As UiO-66-SO_3H is not expected to contain such redox properties, one can suppose that the Zr species at the surface of the MOF are partially oxidized and can provide such redox functionality but no actual catalytic properties. Also, UiO-66-SO_3H MOFs contain a lot of B-OH groups, that could also be involved in the oxidation of toluene [215].

To sum up the results, during ATC Hopcalite possess high catalytic activity and high yield formation in absence and/ or presence of oxygen. Interestingly, in presence of oxygen the CO_2 formation is take place at below 200 °C. Moreover, no significant difference has been observed for Ceria-NR and UiO-66-SO_3H in absence and presence of the oxygen. Although only a single adsorption-catalytic combustion sequence was performed in each case, this study shows that the Hopcalite stands as a good candidate due to its adsorption and redox properties. As the reaction takes place at temperatures significantly below that of the calcination, good reproducible cyclic behavior can be expected but will need to be explored in future. In the case of Ceria-NR and UiO-66-SO_3H, future study should be focused on enhancing the catalytic activity by addition of an active phase.

3.4 Conclusions

The adsorption capacity and catalytic activity of three different materials have been compared for toluene oxidation in co-feed mode and in a novel sequential mode. Among all studied samples, Hopcalite shows the best toluene oxidation and sequential adsorption-thermal oxidation properties. On this material, it has been shown that the adsorption process can be efficient and that the optimal adsorption capacity can be reached at low (< 100 ppm) toluene feed. At higher toluene feed concentration, reversible adsorption takes place which is detrimental for the efficiency of the abatement process. The notion of "useful" adsorption capacity is therefore employed to describe the amount of toluene adsorbed before the residual toluene pressure reaches a given acceptable threshold. For instance, with a 10-ppm threshold, the adsorption is mostly irreversible and good toluene abatement performance is reached. Indeed, at a similar inlet concentration of toluene (100 ppm), the CO_2 yield is almost twice as large when adsorption is limited to adsorption capacity as compared to that of the obtained adsorption reaching full capacity. In the toluene oxidation step of the process, Hopcalite exhibits the best catalytic oxidation properties allowing to reach high levels of toluene conversion into CO_2 and low pollutant release by desorption.

Although the Ceria-NR possesses some catalytic properties, its reactivity at low temperature is not sufficient to convert adsorbed toluene in a useful temperature range, i.e., below 150 °C. Overall performances are thus insufficient to be considered for such a sequential process unless the catalytic performance is enhanced by the addition of an active catalytic phase. UiO-66-SO_3H on the other hand is a promising material with respect to its excellent adsorption capacities. However, its catalytic properties also need to be improved in order to be considered for a sequential process.

Generally, this exploratory study allows to identify key criteria for the selection of candidate materials for a sequential adsorption-catalysis process for toluene abatement. This study opens the path for further investigations in the search for innovative materials associating active catalytic properties and high-performance adsorption capacities. These may be constituted by well-known adsorbent materials associated with supported catalytically active phases. Alternatively, bulk materials possessing both adsorption and catalytic requirements can be considered and Hopcalite appears as a good candidate in this purpose. Deeper studies of sequential processes are nevertheless required, in particular with regard to the stability of this material in repetitive working conditions. The influence of water vapor and of other competitive pollutants will also need to be carefully investigated in order to simulate realistic pollution abatement conditions.

To optimize the sequential adsorption thermal process using different materials, two essential aspects will therefore, need to be optimized: on one hand, optimize the experiment parameter, and on the other, introduce active phase on materials.

Chapter 4

Abatement of Toluene Using a Sequential Adsorption- Thermal Catalytic Oxidation (ATC) Process over Ag/Hopcalite

Preamble

In previous chapter, the basis of a hybrid process combining adsorption of VOC pollutant followed by thermal catalytic combustion was set. The performances of three type of materials were explored. They were chosen for their known properties in catalytic oxidation of VOC (bare Hopcalite), redox capacity (Ceria) or adsorption performances (UiO-66-SO_3H) as such characteristics are expected to have major importance in one or the other steps of the process.

Results gathered in Chapter 3 indeed confirm that all three properties are needed to achieve useful performances. Actually, only Hopcalite present all necessary characteristics and, indeed, have interesting efficiency. These observations lead to the object of present chapter, i.e. to improve the catalytic properties of the materials by the addition of an active catalytic phase on Hopcalite and test the influence of silver over material.

Chapter 4 has been written as a stand-alone article to be submitted shortly.

Chapter 4 Abatement of Toluene Using a Sequential Adsorption-Thermal Catalytic Oxidation (ATC) Process over Ag/Hopcalite

4. Introduction

Volatile organic compounds (VOCs) are considered as hazardous air pollutants which can have detrimental effects on human health and environment. These negative impacts have prompted many countries to initiate air quality legislation to reduce VOC emissions. VOCs are emitted from different sources, such as outdoor sources (industrial processes and transportation) and indoor sources (household products). For gaseous effluents containing lean VOC concentrations, the catalytic oxidation which is an effective way for VOC abatement is no longer cost effective [216,217]. Recognizing this, advanced adsorption processes have been proposed as cost-effective alternatives to current VOC abatement technologies.

These advanced processes use the concept of « storage-regeneration » cycling [42]. This sequential method implies two steps: (i) first, the VOC is adsorbed on a bi-functional material which plays the role of an adsorbent followed by (ii) the regeneration of the material through VOC oxidation into CO_2 and H_2O. This regeneration step can carried out using thermal oxidation [218], non-thermal plasma destruction [77] or oxidation by ozone [219]. When using this cyclic approach, the design of a dual functionalized material which should possess balanced properties as adsorbent and oxidation catalyst is crucial. The bi-functional materials used for the storage of VOCs should have high and selective VOC storage capacity, but should also be easily regenerated without any release of the VOCs and generation of secondary pollutants.

In their search for a good combined adsorbent/catalyst dual-functional material controlling low concentrations of toluene, Baek *et al.* have carried out adsorption-catalytic regeneration over different transition metal-loaded zeolites HY [220]. Among all metal- loaded HY samples, the Ag/HY catalyst showed the lowest conversion temperature for toluene oxidation. The authors concluded that silver oxide species or partially oxidized metallic silver onto the surface of the metallic silver phase act as active redox sites during the oxidation reaction. The successful elimination of toluene by an adsorption/combustion process in humid conditions has also been reported by Wang *et al.* using Ru/hierarchical HZSM-5 zeolites as adsorbent/catalyst [221]. The good performance of these bi-functional materials was attributed to their increased external surface

and mesoporous volume, their shortened diffusion length and their enhanced low-temperature reducibility. Additionally, simultaneous adsorption and oxidation of toluene has also been recently carried out over TiO_2/SiO_2 and ZrO_2/SiO_2 mixed-metal oxides (MMOs) with varying compositions taking advantage of the fact that titanium- and zirconia-based materials are known to have an excellent affinity towards toluene during adsorption and reaction [222]. It has been shown that Ti-based MMOs are more efficient than Zr-based materials by displaying a higher dynamic capacity and toluene conversion as a result of their higher surface area and pore volume, their surface defects, and the presence of hydroxyl groups.

Inspired by these results, in a previous study, we have investigated the efficiency a calcined commercial Hopcalite material (Purelyst–MD101) among other materials for toluene abatement considering a single adsorption/thermal catalytic oxidation (ATC) [223]. The highest CO_2 yield was found to be 92 % using Hop, which was the result of the best possible compromise between the Hop textural and redox properties. In an effort to optimize the effectiveness of Hop, we propose in this work to disperse Ag on Hopcalite. Indeed, it is well known that silver can react with the aromatic ring of toluene allowing π-complexation during its storage phase. Additionally, Ag-containing mixed $CuMnO_x$ catalysts can improve the activity of carbon monoxide oxidation, which is the last step of total oxidation of toluene [224].

In this work, Ag-promoted calcined Hopcalite (Purelyst-MD101) materials are prepared by wet aqueous impregnation followed by drying at 100 °C. Adsorption-desorption/oxidation of gaseous toluene on these supported Ag materials are assessed by uncomplete breakthrough experiments (adsorption time = 35 min) followed by temperature programmed reactions (TPR) in a $He:O_2$ (75:25) gaseous mixture (regeneration process). The efficiency of the regeneration step is discussed in terms of the catalytic properties of the materials and is compared to their catalytic performances in total oxidation from light-off curves. Additionally, a study in cycling mode is performed over Hop and Hop-1 Ag to apprehend the stability of the developed dual-functional materials. Finally, the adsorbent/catalyst performances of the silver based materials are discussed in terms of Ag speciation and dispersion on the calcined Hopcalite.

4.1 Experimental Conditions

The commercial catalyst Hop (Purelyst MD101) is used as support. The silver (0-10 wt.%) is impregnated on Hop. The characterization includes XRD, N_2 adsorption-desorption isotherms, H_2-TPR, TGA/DSC and XPS. The detail synthesis process, characterization process and experiment process can be seen in Chapter 2.

4.2 Result and Discussion

4.2.1 Catalyst Characterization

4.2.2.1 Structural and morphological characterization

The elemental bulk compositions of the prepared Hop-x Ag materials are tabulated in Table 1. This table shows that the Ag/Mn atomic ratio increases globally in accordance with Ag loading, as expected. On the other hand, the Cu/Mn and K/Mn atomic ratio vary very little of 0.26 ± 0.02 and ~ 0.07, respectively. The X-ray diffraction (XRD) pattern (Figure 4.1A) of calcined commercial Hop shows two very low intensity peaks positioned at ~ 37 ° and ~ 66° in 2θ which is in line with previous observations and can be attributed to the highly disordered character of some MnO_x based materials [225]. When adding silver, no diffraction peaks related to Ag, AgO_x or other based silver oxide species are observed in the 2θ scan window 30°- 46° (Figure 4.1B) even for a silver content of 10 wt.%. These results thus indicate that Ag species are well dispersed on Hop and may be substituting the framework manganese cations of Hopcalite or/and the size of doped Ag related crystallites are too small to be detected. It is also worthy to note that the peak located at 2θ ~ 37° broadens and increases in intensity when considering the XRD pattern of Hop-x Ag with increasing Ag content. This increase may be caused by the replacement of some K^+ ion with some Ag^+ ions during the doping process. The transmission electron microscopy (TEM) images of Hop and all Hop-x Ag samples (Figure 4.2) supported the fact that metallic Ag particles are not distinguishable from the Hop material. TEM images show only the fringes of layer stacking with a layer thickness of ~7.1 Å which can be consistent with some disordered phyllomanganate material [226].

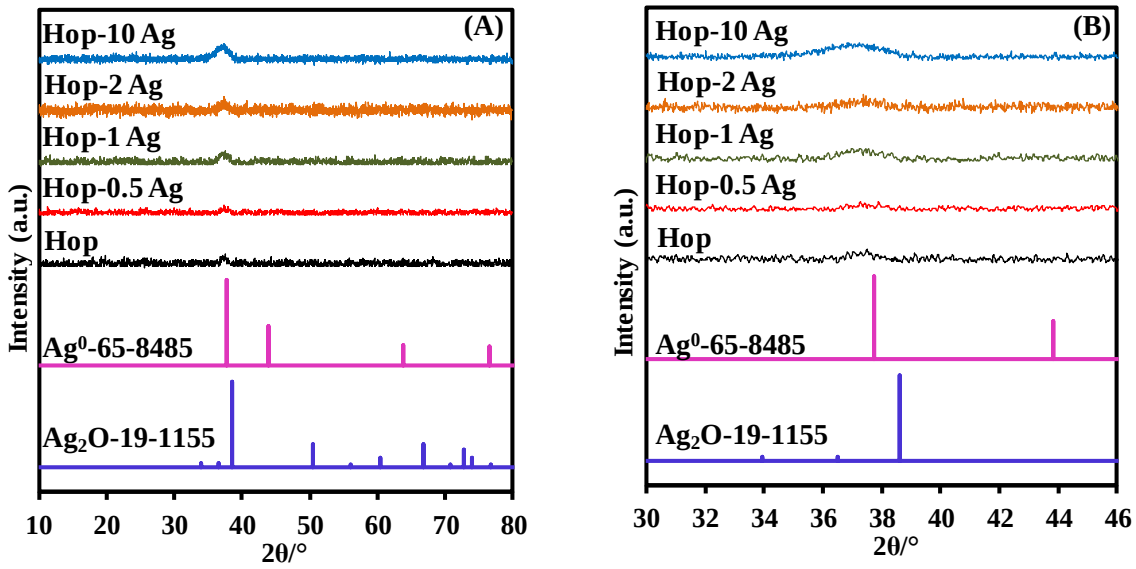

Figure 4.1. *XRD patterns of (A) fresh Hop and silver based Hop materials; (B) zoom in 30 °- 46° 2θ range.*

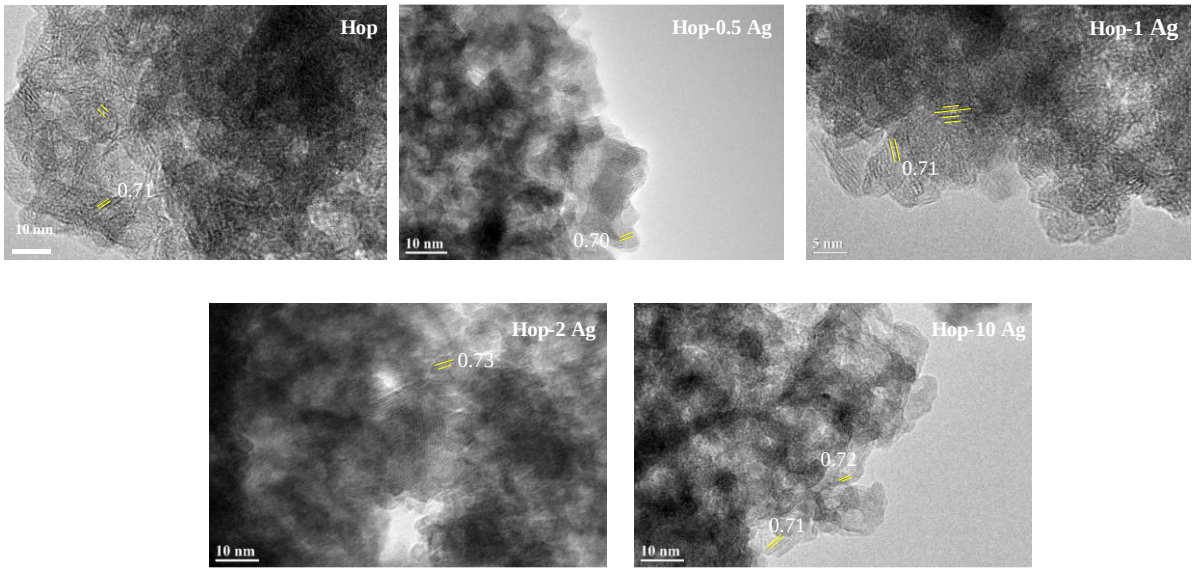

Figure 4.2. *TEM images of Hop and silver based Hop materials.*

4.2.2.2 Textural properties

The N_2 adsorption-desorption isotherms and pore size distribution (PSD; insets) of the materials are given in Figure 4.3 (A) and (B) respectively and the corresponding textural properties are summarized in Table 4.1. The crushed and sieved particles of calcined commercial Hopcalite

show a type IV isotherm with an H3 hysteresis loop showing a mesoporous structure [223]. When adding Ag, it is observed that the shape of the N_2 isotherms is preserved. Moreover, the nitrogen uptake at P/P_0 below 0.05 is reduced indicative of a partial blockage of the microporosity. This reduction in nitrogen uptake is however much less pronounced for the Hop-10 Ag sample. The latter observations are also supported by the decrease of the specific surface areas when adding Ag and the accompanying rise of the maximum pore size from ~ 7 nm to ~11-14 nm. However, for the Hop-10 Ag sample, the specific surface area increases again while the D_p value is lower (approximately 8 nm) (Figure 4.3B; Table 4.1).

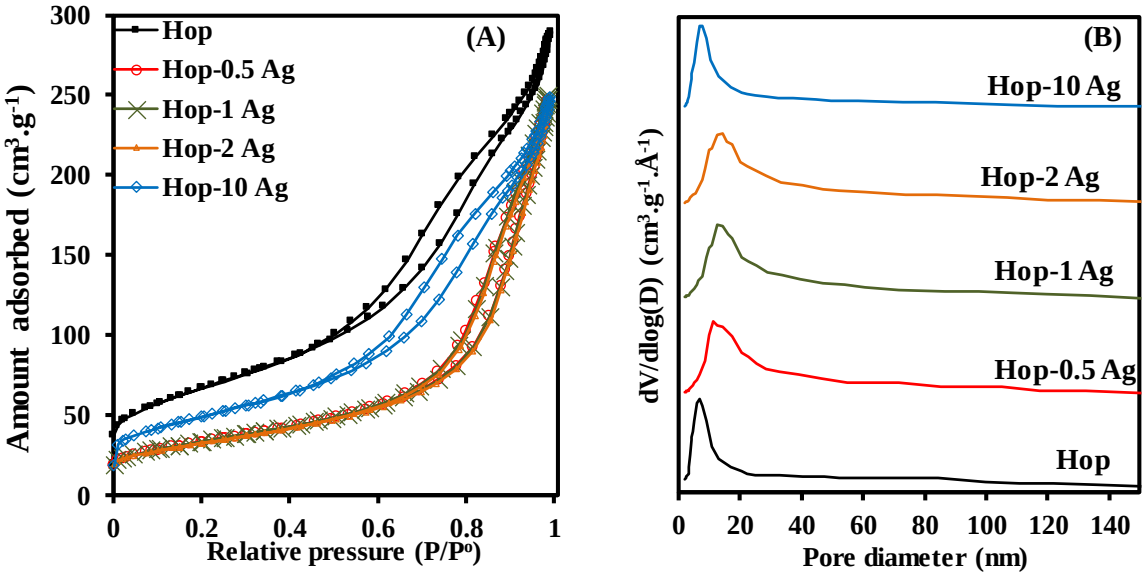

Figure 4.3. *(A) N_2 adsorption/desorption isotherm and (B) pore size distribution of Hop and silver based Hop materials.*

Table 4.1. *Physico-chemical properties for Hop and Hop-x Ag.*

Material	Ag/Mn	Cu/Mn	K/Mn	S_{BET} ($m^2.g^{-1}$)	D_p[a] (nm)	T_{max}[b] (°C)	H_2 uptake ($mmol.g^{-1}$)
Hop	-	0.28	0.078	232	7	341	11.1
Hop-0.5 Ag	0.006	0.27	0.074	118	11	314	11.1
Hop-1 Ag	0.008	0.29	0.078	118	14	311	10.9
Hop-2 Ag	0.025	0.27	0.072	115	14	307	11.2
Hop-10 Ag	0.105	028	0.074	175	8	307	11.2

[a] Maximum pore diameter, [b] H_2-TPR maximum peak temperature

4.2.2.3 Redox properties

Figure 4.4 shows the H_2-TPR profiles of the samples. For Hop, the envelope is complex and show 5 peaks in the temperature range of 100 °C to 385 °C in line with the reduction of MnO_x into MnO and of Cu^{x+} into Cu(0). When adding silver, the reduction process takes place in a narrowing window in terms of temperature (100 °C-345 °C) resulting mainly from a downward temperature shift of the most intense peak (see Table 4.1). This peak shift occurs for all Ag-loaded samples and is also accompanied by a decrease in the total number of peaks in the envelope. However, for the Hop-10 Ag sample, an additional peak is again clearly observed at 182 °C which may result from the reduction of Ag_2O clusters being present inside the channels or on the external surface of Hopcalite. It can thus be concluded that silver promotes the reduction of copper/manganese oxides. As metallic silver can enhance the reducibility of MnO_x and CuO_x through spillover of hydrogen, it is believed that silver is mostly present in an ionic form as the onset temperature of reduction is only poorly affected by the addition of silver, although the total H_2 consumption of the silver based catalysts is quite similar. However, it is noteworthy to mention that the presence of Ag(I) is also confirmed by XPS results (see below).

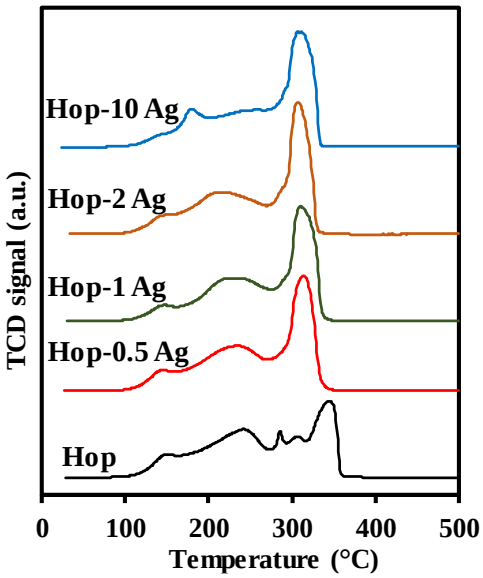

Figure 4.4. *H_2-TPR profiles of Hop and silver based Hop materials.*

4.2.2.4 Surface composition

Static ToF-SIMS has been applied to survey the very outermost surface of the pure Hop and the Ag based catalysts taking advantage of its high surface sensibility. In all samples, ToF-SIMS analysis reveals high concentrations of light elements such as K and Na on the surface. Moreover, NO_3^- is also been observed as inorganic adsorbate on the surface. Such species preclude to get significant information for secondary ion with m/z higher than 150. For the Ag based catalysts, Ag^+ is the only observed Ag related secondary ion.

To obtain more information on the surface composition, XPS has been also applied to these catalysts. Figure 4.5 and 4.6 exhibit the Ag 3d, Cu 2p, Mn $2p_{3/2}$ and Mn 3s XPS spectra of the Hop based samples and the XPS peak position and the atomic ratios are reported in Tables 4.2 and 4.3. For all samples, the Ag $3d_{5/2}$ peaks are centered at 367.6 ± 0.1 eV. This value is similar to that of Ag in Ag_2O [227] and significantly lower than the one of metallic silver, which located at 368.0 ± 0.2 eV [228] thereby indicating the presence of Ag(I) on all Ag loaded samples. The binding energy (BE) of Cu $2p_{3/2}$ at 933.0 ± 0.3 eV (Figure 4.6A) as well as the presence of satellite peaks confirm a chemical state of +2 for copper on all Hop samples [109,229]. It is also noteworthy that the BE of the Mn $2p_{3/2}$ is located at 642 ± 0.2 eV and does not significantly vary with Ag content (Figure 4.6B). This conclusion can also be seen from the data in Table 4.2 showing that the addition of silver does not induce some significant shift in BE for Mn and Cu. Furthermore, for all samples, a mean oxidation state of manganese close to 3.0 is obtained from the BE separation between the two components of the Mn 3s core level as shown in Figure 4.6C [207]. A Plot of Ag/Mn atomic ratio (Table 4.3) as a function of the bulk atomic ratio obtained from EDS (Table 4.1) presented in Figure 4.6D shows that the Ag(I) species are well dispersed at the surface of Hop and all the more that the nominal Ag content decreases. Furthermore, it should be noted that the Cu/Mn atomic ratio of 0.24 ± 0.2, K/Mn ratio of 0.11 ± 0.6 and O/Mn ratio of 2.8 ± 0.3 are not significantly affected by the presence of silver. Additionally, it is worthy to mention that a Na/Mn ratio of 0.03 ± 0.1 is obtained for any samples.

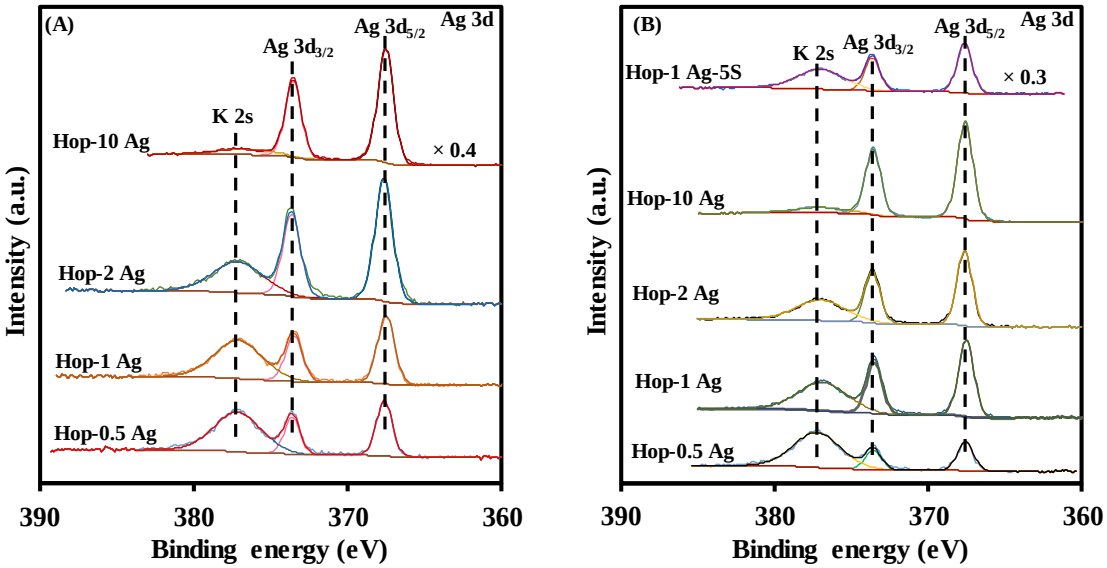

Figure 4.5. *Ag 3d core level spectra of silver based Hop materials (A) fresh, (B) after one and five storage-regeneration sequences (5S).*

Table 4.2. *XPS analysis data for Hop and Hop-x Ag.*

Material	Peak Position (eV)		
	Ag $3d_{5/2}$ (FHWM)	Cu $2p_{3/2}$	Mn $2p_{3/2}$
Hop	-	933.3	642.1
Hop-0.5 Ag	367.6 (1.19)	933.5	642.0
Hop-1 Ag	367.5 (1.29)	933.1	641.8
Hop-2 Ag	367.7 (1.35)	932.7	642.1
Hop-10 Ag	367.6 (1.22)	933.2	641.8
Hop-S	-	933.3	642.1
Hop-0.5 Ag-S	367.6 (1.21)	933.4	642.1
Hop-1 Ag-S	367.8 (1.17)	933.3	642.0
Hop-2 Ag-S	367.7 (1.15)	933.6	642.0
Hop-10 Ag-S	367.5 (1.22)	933.3	642.0
Hop-3S	-	933.5	642.2
Hop-1 Ag-5S	367.6 (1.16)	933.3	642.1

Table 4.3. *XPS atomic ratios for Hop and Hop-x Ag.*

Material	Ag/Mn	Ag/Cu	Cu/Mn	K/Mn	O/Mn
Hop	-	-	0.23	0.12	3.1
Hop-0.5 Ag	0.02	0.12	0.20	0.12	2.7
Hop-1 Ag	0.03	0.16	0.20	0.13	2.7
Hop-2 Ag	0.05	0.23	0.20	0.11	2.7
Hop-10 Ag	0.16	0.78	0.21	0.14	3.0
Hop-S	-	-	0.24	0.13	3.4
Hop-0.5 Ag-S	0.02	0.09	0.25	0.14	2.7
Hop-1 Ag-S	0.03	0.15	0.23	0.13	2.6
Hop-2 Ag-S	0.04	0.18	0.24	0.13	2.7
Hop-10 Ag-S	0.15	0.62	0.25	0.17	3.0
Hop-3S	-	-	0.23	0.13	2.6
Hop-1 Ag-5S	0.03	0.13	0.26	0.14	2.6

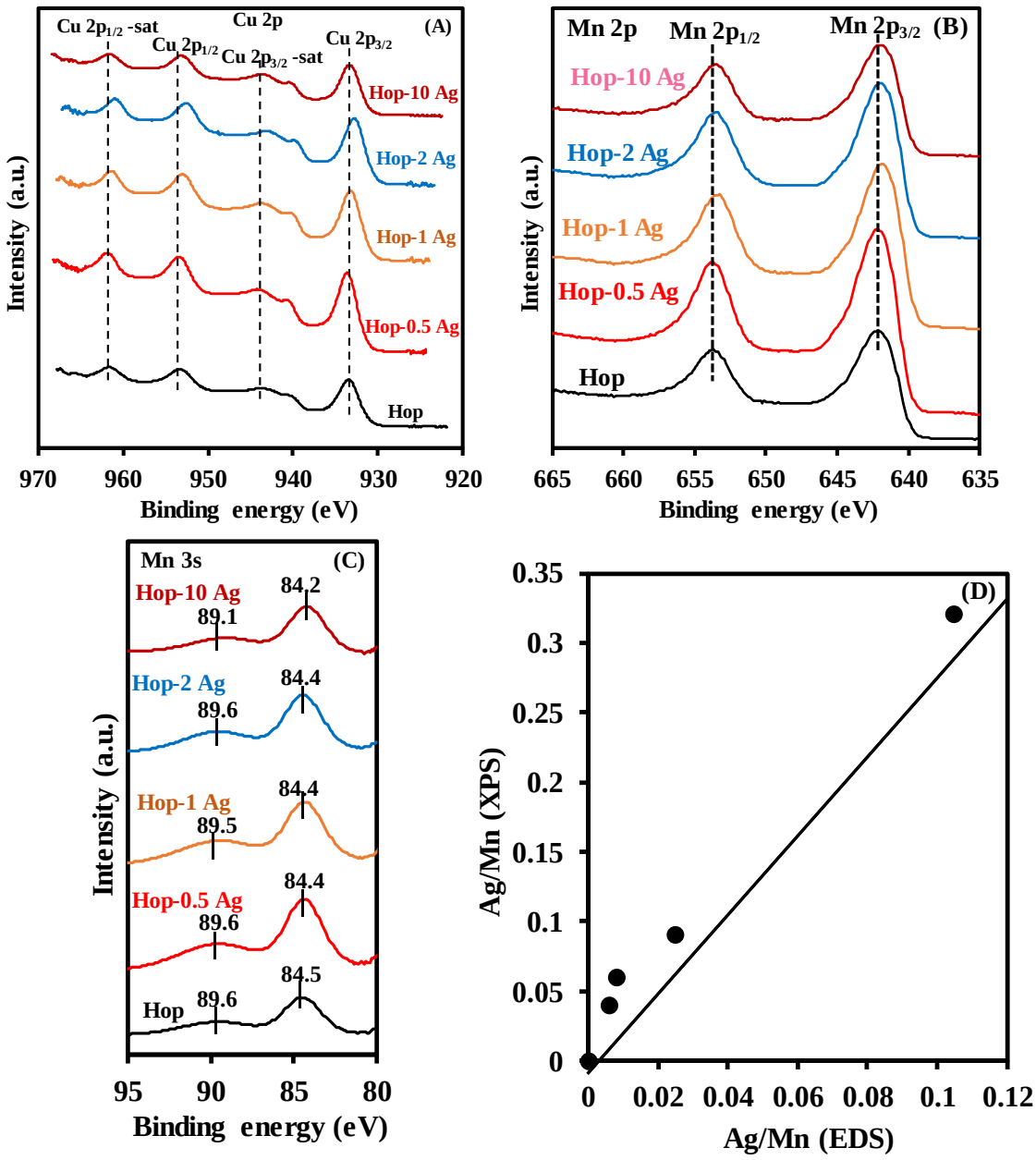

Figure 4.6. *(A) Cu 2p, (B) Mn 2p, (C) Mn 3s core level spectra of silver based Hop materials, (D) Ag/Mn (XPS) as a function of Ag/Mn (EDS).*

4.2.2 Light off curve of Hop based materials

Catalytic performances of the different Ag based catalysts have been evaluated interms of the toluene (1000 ppm) total oxidation reaction as compared to Hop. The total toluene conversion and conversion of toluene into CO_2 as a function of temperature are presented in Figure 4.7 and the

relevant temperatures are given in Table 4.4. For all catalysts, the $T_x(CO_2)$ are shifted to higher temperatures as compared to the T_x ones indicating some carbon retention as no other gaseous by-products apart CO_2 can be detected.

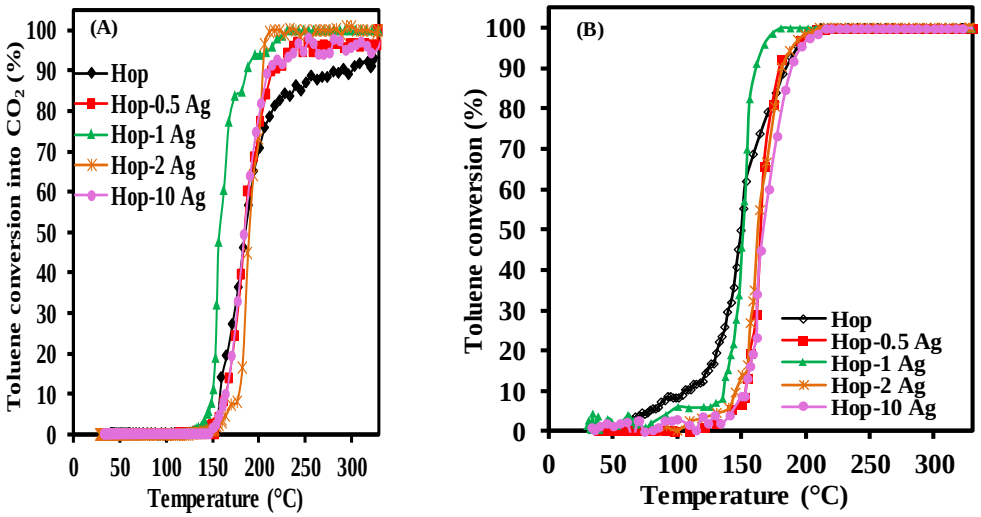

Figure 4.7. *(A) toluene conversion into CO_2 and (B) total toluene conversion as a function of temperature; inlet toluene concentration: 1000 ppm, GHSV = 30000 $mL.h^{-1}.g^{-1}$, temp: 330 °C to 150 °C (rate: -0.5 °C.min^{-1}) to 25 °C (rate: -0.2 °C.min^{-1}).*

Table 4.4. *Literature survey on Ag-based catalysts for toluene oxidation.*

Material	Concentration (ppm)	GHSV ($mL.g^{-1}h^{-1}$)	T_{10} (T_{10} CO_2) (°C)	T_{50} (T_{50} CO_2) (°C)	T_{90} (T_{90} CO_2) (°C)	Reference
Hop	1000	30,000	106 (157)	150 (185)	189 (291)	Present work
Hop-0.5 Ag	1000	30,000	154 (165)	165 (185)	178 (214)	
Hop-1 Ag	1000	30,000	138 (148)	148 (156)	155 (188)	
Hop-2 Ag	1000	30,000	145 (176)	162 (188)	182 (200)	
Hop-10 Ag	1000	30,000	152 (165)	165 (184)	192 (209)	
1% Ag/ MnO_2	1000	20,000	150	210	210	[227]
1Ag- δ-MnO_2	1000	60,000	160 (173)	182 (185)	190 (198)	[230]
0.5Ag-SDC-13 (δ-MnO_2)	1000	30,000	220	230	245	[231]
Ag/ MnO_2 wires	1000	20,000	-	196	212	[232]
7% Ag/Co_3O_4	1000	78,000	220	244	256	[233]
10% Ag/Co_3O_4			220	249	257	
1Ag- γ-Al_2O_3	1000	-	375	500	-	[234]
11Ag- γ-Al_2O_3			260	275	285	
0.81Ag/3DOM 26.9CeO_2-Al_2O_3	1000	20,000	263	308	338	[235]
Ag (12) SBA-15 O500-H300	1000	60,000	225	241	267	[236]
R-Ag/MnO_2	1000	10,000	-	190	275	[237]

In the case of Ag-containing catalysts, $T_{90}(CO_2)$ are substantially lower as compared to Hop while only Hop-1 Ag outperforms Hop in terms of $T_{50}(CO_2)$ and $T_{10}(CO_2)$ exhibiting temperatures of 156 °C and 148 °C as compared to 185 °C and 157 °C for Hop. The $T_{50}(CO_2)$ of 148 °C compares well with the most active Ag based catalysts as shown in Table 4.4.

4.2.3 Study of the adsorption/thermal oxidation sequence

To investigate the dynamic adsorption behavior of toluene over Ag-containing materials, breakthrough curves have been carried out at an inlet concentration of toluene of 100 ppm to ensure a significant duration of the unsaturated zone of the breakthrough curve as shown in Figure 4.8. It is found breakthrough times of 30-38.5 min of duration which lead to dynamic toluene adsorption capacities very similar, in the range of approximately 35.3-51.7 $\mu mol.g^{-1}$ (Table 4.5), whatever Ag loading. Based on these results, the adsorption-thermal oxidation sequence has been conducted in the following manner : a stated toluene adsorption step of 35 min to minimize the outlet toluene amount (less than 3 mol. % of the amount of toluene adsorbed) followed by sweep under He to get rid of reversibly desorbed toluene of 15 min to end up with a temperature programmed desorption/reaction process from 20 °C up to 250 °C with a heating rate of 2 $°C.min^{-1}$. The useful adsorption capacities (in $\mu mol.g^{-1}$) given in Table 4.5 increases modestly with increasing Ag loading : Hop (35.3) < Hop-0.5 Ag (35.8) < Hop-1 Ag (40.1) < Hop-2 Ag (40.5) < Hop-10 Ag (51.7). This has been attributed simultaneously to the introduction of new Ag(I) based active sites for toluene adsorption species along with a decrease of the specific surface area. Besides, the low amount of reversibly adsorbed toluene (less than 1.0 $\mu mol.g^{-1}$) attests of the beneficial role of Ag allowing better interaction between the VOC and the dual functional material.

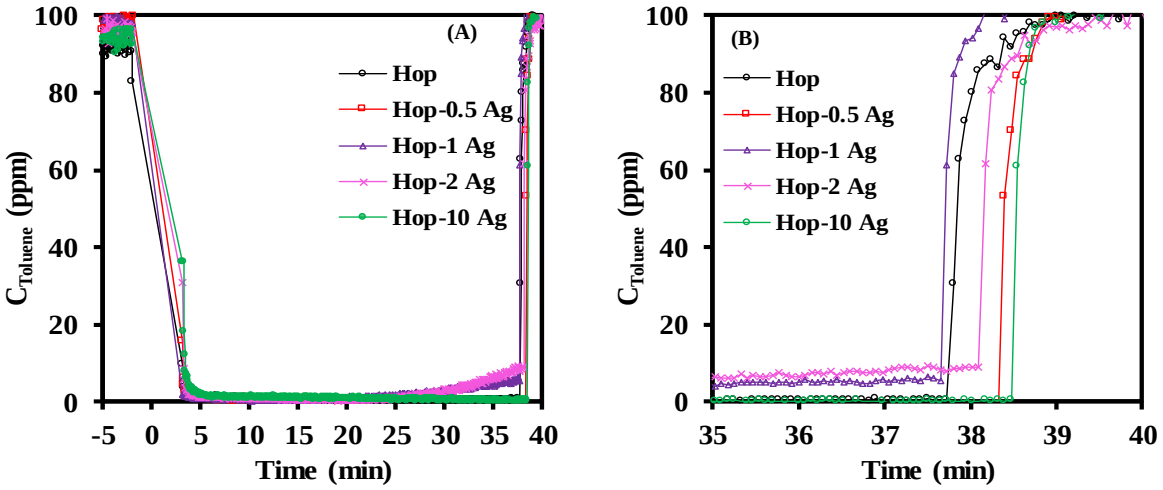

Figure 4.8. *Adsorption of Toluene (A) over Hop, Hop-0.5 Ag, Hop-1 Ag, Hop-2 Ag and Hop-10 Ag and (B) zoom in image of adsorption curve from 35-40 min.*

Table 4.5. *Comparison of Hop and Hop-x Ag during toluene (100 ppm) adsorption followed by TPR-O_2 (He: O_2 = 75:25).*

Material	$qTol_{ads}$ ($\mu mol.g^{-1}$)	$qTol_{desRT}$ ($\mu mol.g^{-1}$)	$qTol_{desTPR}$ ($\mu mol.g^{-1}$)	T_{max} CO_2 (°C)	qCO_2 ($\mu mol.g^{-1}$)	Y_{CO2} (%)
Hop	35.3	0.1	0.8	200	241.0	97.5
Hop-0.5 Ag	35.8	0.2	0.2	140	247.9	98.9
Hop-1 Ag	40.1	1.0	11.4	195	193.9	69.1
Hop-2 Ag	40.5	0.9	10.7	180	202	71.2
Hop-10 Ag	51.7	1.3	1.8	190	340.5	94.1

Figure 4.9 describes the toluene and CO_2 concentration evolution during TPR which follows the sweep under He. These are the only detected gaseous products. Clearly, the amount of desorbed toluene, less than 1 $\mu mol.g^{-1}$, is practically suppressed on Hop as on Hop-0.5 Ag. In the case of higher Ag loading, up to 2 wt.%, large quantities of toluene evolve through the detection of two peaks which could be due however to an irregularity in the rate of temperature as stated before [223]. For Ag loading of 10 wt.%, the desorption of toluene does not occur anymore. The decrease in toluene desorption corresponds to the appearance of CO_2 due to the reaction between toluene and activated oxygen of the materials. The CO_2 evolution (Figure 4.9) appears as one peak, Hop-x Ag excepted (x = 1 ; 2) for which it is found an additional small peak at very low temperature (T_{max} ~ 100 °C). It is also noteworthy that the temperature of the major peak decreases when adding Ag, a downward shift of 60 °C being observed for Hop-0.5 Ag. Additionally, on contrary to other samples, the CO_2 production ends before 250 °C which is the maximum temperature set for thermal oxidation. It should be noted that the important desorption of unreacted toluene during TPR which takes place for Hop-x Ag (x = 1; 2) occurs

when a small production of CO_2 is detected at low temperature. A possible explanation could be that these samples contain some highly active Ag related sites enabling the conversion of some toluene at very low temperature (below 100 °C). This assumption is supported from the comparison of the conversion at low temperature obtained from the light-off curves. It is strongly suggested that the heat generated by this exothermic process would provoke the unusual toluene desorption phenomenon. Also, disappearance of such sites at high 10 wt.% Ag loading can account for the disappearance of toluene desorption. Consequently, the CO_2 yields are lowest. The best CO_2 yield of 98.9 % is obtained for Hop-0.5 Ag as compared to 97.5 % for Hopcalite. It should be noted that these results encompass those reported previously for Hop amounting to a CO_2 yield of 92 % [223]. The carbon balance evaluated by using equation (2) are close to 100 % for all samples (Figure 4.10).

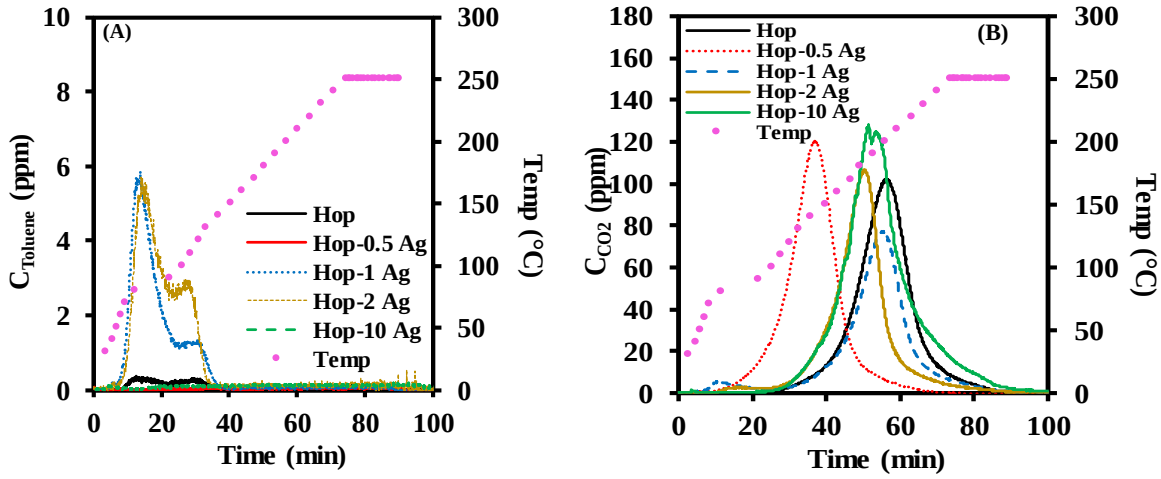

Figure 4.9. *Toluene (A) and CO_2 (B) concentration evolution during TPR in O_2 : He (25 : 75) atmosphere on Hop and silver based Hop materials.*

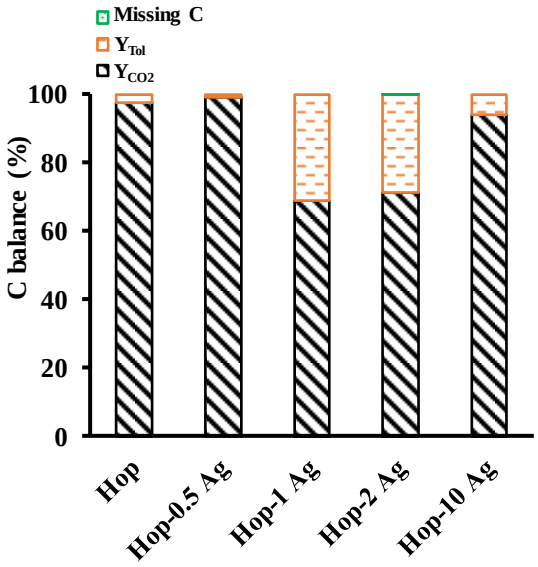

Figure 4.10. *Carbon balance of Hop and silver based Hop based materials for one storage-regeneration sequence.*

4.2.3.1 Stability of Hop and Hop-1 Ag catalyst during sequential adsorption-thermal catalytic oxidation process

The stability of Hop and Hop-1 Ag have been examined by performing three and five consecutive sequences, respectively (Figure 4.11). The amount of adsorbed toluene (Table 4.6) keeps similar considering the margin of errors. Additionally, the TPR profiles of desorbed toluene and of CO_2 superimpose indicating that the materials keep high efficiency for the toluene oxidation in cycling sequential adsorption-thermal catalytic oxidation process.

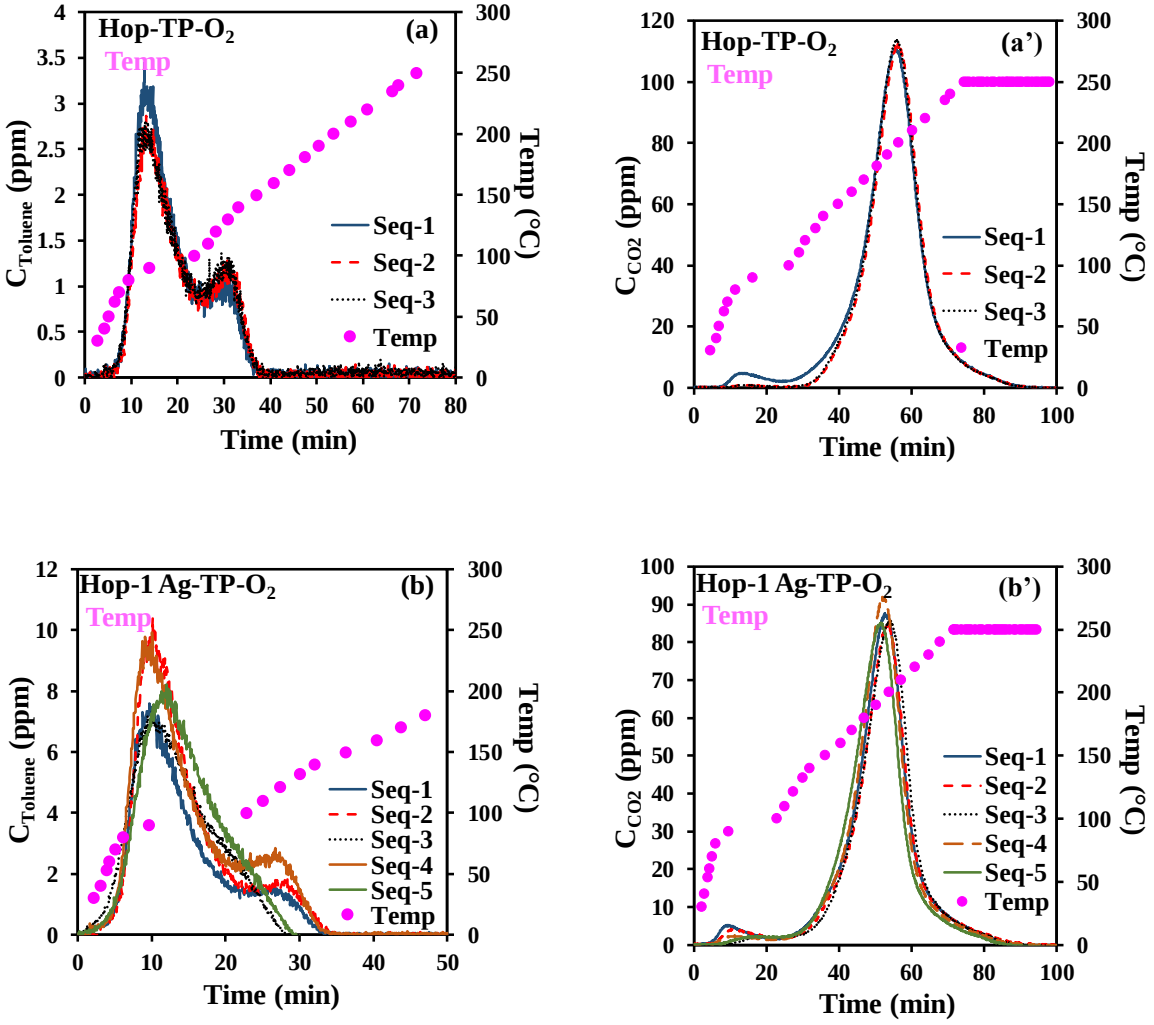

Figure 4.11. *Toluene (a, b) and CO_2 (a', b') concentration evolution during TPR in an oxidizing atmosphere over Hop (a, a'), and Hop-1 Ag (b, b').*

In each sequence, the carbon balance is close to 100 % for both samples (Figure 4.12). It should be noticed that the XPS composition and nature of the state of the main elements and in particular for Ag as seen in Figure 4.5B do not change significantly after the process.

Table 4.6. *Cycling of Hop and Hop-1 Ag during toluene (100 ppm) adsorption followed by TPR-O_2 (He: O_2 = 75:25).*

Material	$qTol_{ads}$ ($\mu mol.g^{-1}$)	$qTol_{desRT}$ ($\mu mol.g^{-1}$)	$qTol_{desTPR}$ ($\mu mol.g^{-1}$)	qCO_2 ($\mu mol.g^{-1}$)	Y_{CO2} (%)
Hop-1S	44.4	0.20	5.8	269.0	86.5
Hop-2S	42.4	0.15	6.3	251.6	84.7
Hop-3S	43.1	0.20	6.6	253.9	84.1
Hop-1 Ag-1S	40.1	1.0	11.4	193.9	69.1
Hop-1 Ag-2S	43.6	1.2	14.1	198.1	64.9
Hop-1 Ag-3S	37.4	1.3	8.5	193.3	73.8
Hop-1 Ag-4S	46.9	0.9	16.2	208.8	63.6
Hop-1 Ag-5S	35.4	1.0	8.0	184.7	74.5

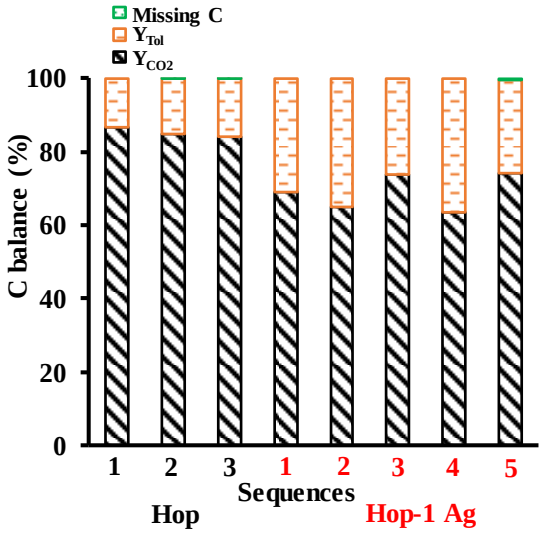

Figure 4.12. *Carbon balance of Hop and Hop-1 Ag during stability test.*

4.2.4 Effect of silver

It has been shown that the Ag content plays a critical role in the storage-regeneration process. Among other things, the nature of silver and silver content are expected to play major roles in the properties of the dual functionalized material. The existing state of silver considering the experimental procedure is Ag(I) and the dispersion of silver species is high taking into account XPS results. Considering the storage step, the beneficial effect of Ag considering the adsorption step is mitigated due to the combination of two opposite effects. The first one is the introduction of some new Ag^+ actives sites which can undergo electrostatic interactions between the aromatic ring of toluene and Ag^+ [238]. This beneficial effect is partially offset by the decrease of the specific surface area throughout some possible diffusion of related Ag(I) like clusters at the entrance of the interlayer spacing of the stacked layers of the materials in line with TEM and textural characterizations. Considering the regeneration step, the presence of some active sites for medium Ag loading provokes over-heating which allow to the desorption of unreacted toluene. This has a negative impact on the efficiency of the process. Hence, from an energy cost saving process the desorption of CO_2 at low temperature for Hop-0.5 Ag guarantees a low energy requirement for the process.

4.3 General discussion and Conclusions

Dual functional adsorbent/catalyst system with both adsorption and catalytic function was suggested as an effective control method for the removal of low concentration of toluene. From all silver supported catalysts, Hop-0.5 Ag was selected as the best candidate for the dual functional adsorbent/catalyst system as compared to Hopcalite. The low concentration of Ag allowed to get a good dispersion of Ag(I) related sites which could both act as new toluene adsorption sites and enhanced oxygen mobility allowing a low CO_2 desorption temperature.

Chapter 5

Sequential adsorption followed by plasma (APC) assisted catalytic conversion of toluene into CO_2 on Hopcalite in air stream

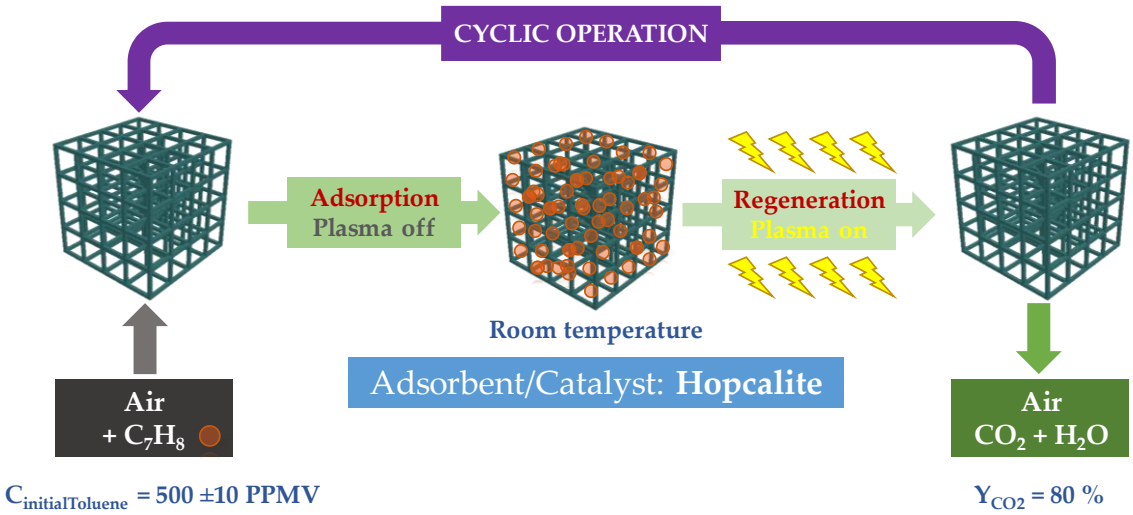

The results of chapter 5 were published in the following international peer-reviewed journal:
Shilpa Sonar, Jean-Marc Giraudon, Savita Kaliya Perumal Veerapandian, Jean-François Lamonier, Rino Morent, Axel Löfberg, and Nathalie De Geyter.
Adsorption followed by plasma assisted catalytic conversion of Toluene into CO_2 on Hopcalite in an air stream.
Catalysts 2021, 11 (7), 845.

Chapter 5 Adsorption followed by plasma (APC) assisted catalytic conversion of toluene into CO_2 on Hopcalite in air stream.

5.1 Introduction

As discussed in Chapter 3, the storage regeneration process is a novel method for the abatement of volatile organic compounds [42]. This method has previously been reported to be effective for indoor pollutants such as Formaldehyde and Benzene. A key point in this process is the design of materials with a balance of adsorption capacity and catalytic activity. To address this issue, a novel approach for toluene abatement by using a sequential adsorption-plasma catalysis process (APC) is proposed. The selection of a material with a high adsorption capacity and adequate redox properties, as well as an optimistic experiment condition is critical for this process. As a result, the main object of present chapter is to design the material; optimize the different reaction conditions and investigate the energy cost and process efficiency.

For VOC removal, there are several technologies have been reported; among which sequential adsorption-plasma catalysis process has been chosen. The details of process and reported various catalysts has been given in previous chapters. On the bases of pervious study, Hopcalite has been chosen for present study.

The main objective of the work, is to explore the performance of Hopcalite for the removal of toluene at high concentration (500 ppm) using a APC process. To reduce the VOC release at the exit of the reactor during the storage stage and to reduce the exothermicity of the NTP induced oxidation of adsorbed toluene over Hopcalite, the effect of low toluene storage stage time duration (t_1) and of the applied discharge power P on the performance of the APC process have been studied in terms of catalytic and energetic performances. Furthermore, a four sequential APC experiment has also been performed to study the stability of Hopcalite with time. Finally, different physicochemical characterizations including XRD, H_2-TPR, N_2 adsorption–desorption analysis and XPS have been conducted to detect eventual modifications of the bifunctional material.

5.2 Material and Experimental

Commercial catalyst Hopcalite details is provided in Chapter 2. The characterization includes XRD, XPS, BET, and H_2-TPR is performed on fresh and used material. The detailed preparation process and characterization process can be seen in Chapter 2. Sequential

adsorption-plasma catalysis process was performed at the University of Ghent. The description of the set-up and experimental process are given in Chapter 2 in section 2.3.

5.2.1 Experimental

The experimental set-up was decomposed into three main components: (i) flue gas preparation, (ii) adsorption and non-thermal plasma reactor, and (iii) gas analysis. The initial toluene concentration C_0 (Toluol ≥ 99.5%, Carl Roth) in dry air (Alphagaz 1, Air Liquide) and the total gas flow rate were maintained at 500 ± 10 ppm and 0.2 $L.min^{-1}$, respectively, using mass flow controllers (MFC, El-flow®, Bronkhorst). The adsorption and subsequent plasma oxidation experiments were conducted at room temperature and atmospheric pressure. The description of the PBDBD (packed bed dielectric barrier discharge; AC power supply of 50 kHz) reactor was previously given [114]. The reactor was filled with 2 g of Hopcalite trapped between two layers of borosilicate glass beads (Sigma Aldrich, 3 mm diameter). The power injected in the plasma reactor was calculated by integrating the instantaneous voltage and current waveforms averaged over four cycles. The gaseous products were analyzed using a Fourier-transform infrared (FT-IR) spectrometer (Bruker, Tensor 27). The FT-IR is equipped with a DTGS (deuterated triglycine sulfate) detector and a gas cell with a 20 cm optical path length with ZnSe windows. After reaching steady state conditions, the FT-IR spectra averaged over 20 different samples are obtained with a resolution of 4 cm^{-1} and an aperture of 6 mm. OPUS (Bruker) software is used to collect and analyze the obtained spectra.

The toluene, CO and CO_2 concentrations were estimated after calibration using standard gas mixtures.

5.2.2 Toluene abatement through APC

The basic sequence for the APC process was divided into two steps: (i) toluene adsorption (t_1: storage stage duration) at 25 °C followed by (ii) NTP exposure in dry air (t_2: discharge stage duration). In this approach, the influence of process variables such as storage stage time span t_1 and power P delivered by the plasma ignition on the efficiency of the APC process in terms of abatement performance as well as energy cost were first investigated. Finally, a four sequential APC experiment was performed using the optimized storage stage duration and NTP power to assess the stability and repeatability of the APC process with time.

As the high inlet concentration of toluene to be treated herein (500 ppm) might lead to an increase of weakly adsorbed VOC, i.e. reversibly adsorbed VOC, the t_1 time span range

relative to the adsorption storage stage investigated in this study was short (5 to 40 min). As a consequence, saturation of the Hopcalite packed bed plasma reactor was not completely achieved. Once t_1 was reached, the toluene flow was stopped and allowed to purge. Then, the non-thermal plasma was ignited on the material. The time span t_2 was set at 60 min to be sufficiently long to monitor the temporal evolution of all gaseous species at the reactor exit and to ensure a recovery of the surface of Hopcalite by NTP regeneration for another adsorption step. This procedure allowed to determine an optimized t_1 storage time span in terms of minimizing the energy consumption of the process.

Before every experiment, the calcined Hopcalite (2 g) was dried at 150 °C for 4 h (2 °C.min^{-1} ; 0.2 L.min^{-1} of dry air).

Effect of the storage stage duration t_1: In the first step, the stabilized flue gas (500 ± 10 ppm toluene/air; F_1 = 0.2 L.min^{-1}) was sent into the PBDBD reactor for a duration t_1 ranging between 5 and 40 min (5, 10, 20, 30 and 40 min). In the second step, an air flow was sent through the reactor with an operating plasma (46 W) for a t_2 of 60 min (F_2 = 0.2 L.min^{-1}).

Effect of the NTP power: After a storage duration t_1 of 20 min performed in similar conditions as mentioned above, the air flow was sent through the reactor using a NTP at four different powers (40, 46, 52 and 72 W) for a t_2 of 60 min. Intermediate experiments at a power of 46 W were performed before applying any change in applied power to validate that the characteristics of the APC process were unchanged at the start of each new sequence.

Effect of stability of the APC process: A four sequence APC experiment was performed under the same conditions as mentioned above with a storage duration t_1 of 20 min and a discharge power P of 46 W.

Considering 1g of catalyst, the amount of adsorbed toluene (q_{ads}) was estimated from the molar amount of gaseous toluene exposed to the catalyst for t_1 from which the contribution of non-adsorbed toluene was retrieved. From the integration of the temporal profiles of unconverted toluene (q_{unconv}) and CO_2 formed during NTP exposure, the amount of toluene converted q_{conv} ($q_{ads} - q_{unconv}$) and of CO_2 formed (q_{CO2}) were calculated at 25 °C. CO_2 selectivity (S_{CO2}), CO_2 yield (Y_{CO2}), energy cost (EC), and energy yield $EY_{(Tol)}$ and $EY_{(CO2)}$ were calculated by using the following equations :

The amount of toluene adsorbed (µmol. g^{-1}), CO_2 formation (µmol. g^{-1}), selectivity and yield of CO_2 (S_{CO2}, Y_{CO2}) and discharge power (P) are calculated by the equations which provided in detailed in Chapter 2 (Section 2.3.6).

5.3Result and Discussion

5.3.1 Effect of toluene exposure time on APC process performances

The effect of toluene exposure time on the amount of adsorbed toluene has been investigated using a gaseous effluent of 500 ± 10 ppmv of toluene/air (0.2 L.min^{-1}) at 25 °C. Five low-term toluene exposure times (5, 10, 20, 30 and 40 min) have been chosen allowing promotion of the amount of irreversibly adsorbed toluene. Figure 5.1(a) shows the toluene concentration profiles during the adsorption storage stage for all adsorption time spans under study. For the examined low toluene exposure times, the toluene concentration evolutions during the first 15 minutes match that of the FT-IR response observed during the purge of an empty reactor (Figure 5.1(a)). After reaching that time, the concentration of toluene increases as a function of time and the resulting curves mostly overlap. Taking into account these observations, it is considered that all introduced toluene is irreversibly adsorbed on the material until the slope of the toluene concentration becomes positive. Hence, at the beginning of the experiments, most of the toluene in the simulated exhaust gas is removed from the gas phase due to strong adsorption on the surface of Hopcalite. After ~ 15 min, the concentration of toluene at the outlet of the reactor gradually increases. This may be due to the lower availability of vacant surface sites which can get occupied by toluene which leads to the creation of repulsive forces between adsorbate present on the adsorbent surface and in the gas bulk phase. The total amount of toluene adsorbed on the Hopcalite packed bed increases quite linearly from 16.7 to 70.6 µmol.g^{-1} as a function of time (Table 5.1).

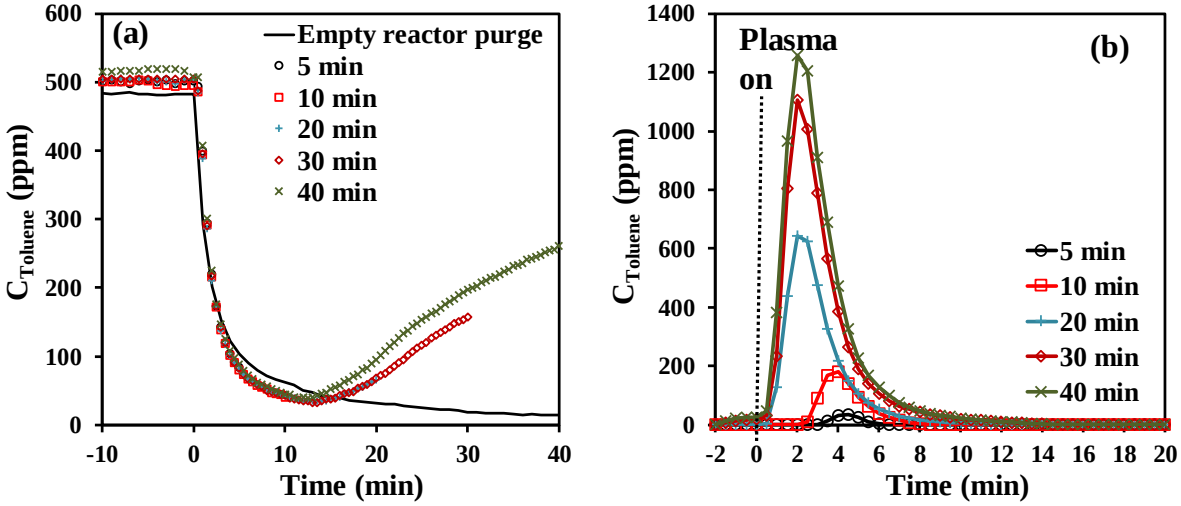

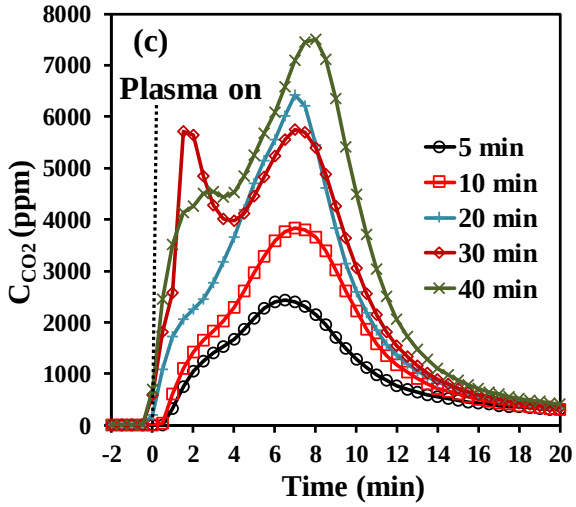

Figure 5.1. *Effect of toluene stage duration time (t_1) on the concentration profiles of (a) toluene during the adsorption step (including a blank test without catalyst), (b) toluene during NTP exposure for the first 20 min (toluene desorption), and (c) CO_2 during NTP exposure for the first 20 min (CO_2 formation).*

After the adsorption step, the NTP exposure step has been performed in dry air (0.2 $L.min^{-1}$) at a discharge power of 46 W using a time span of 60 min. During NTP exposure, toluene, CO_2, N_2O, NO_2, NO and H_2O are the only gaseous species detected at the outlet of the reactor by FT-IR, as shown in Figure 5.2. This work will only focus on the quantification of the desired end product (CO_2) as the quantification of H_2O, NO_2 and N_2O was not possible as the instrument was not calibrated for these species. Figure 5.2 (b) represents an enlargement of the FT-IR spectrum (4 min of NTP exposure) of the effluent from the DBD reactor, which revealed the desorption of toluene at the beginning of the NTP discharge stage. To summarize, during the discharge stage, in addition to the desorption of reversibly adsorbed toluene molecules, an eventual break down of irreversibly adsorbed toluene into CO_2 and H_2O is observed. Interestingly, the formation of NO_x species appears only after approx. 10 minutes of reaction and is observed continuously after 20 min. Thus, no or little NO_x is produced during the CO_2 production supposedly because the oxidation active sites are occupied by adsorbed toluene. Once toluene is fully converted, these sites become active for N_2 oxidation. This feature opens the path for a significant reduction of NO_x production by adjusting the NTP discharge time to the minimum required for the combustion of adsorbed toluene and the regeneration of the catalyst.

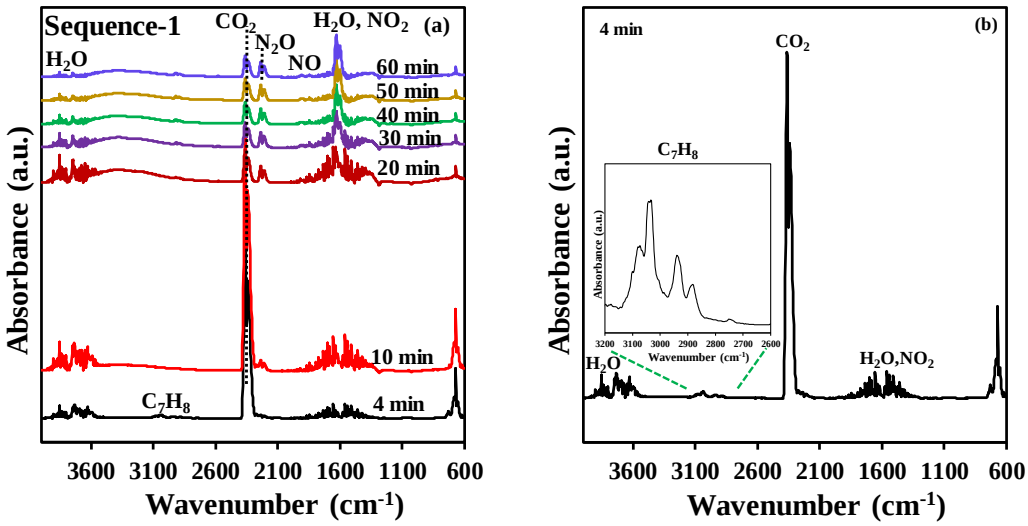

Figure 5.2. *(a) Example of FT-IR spectra of the outlet gas at various times during plasma treatment (data collected for experiment using t_1 = 20 min), (b) FT-IR spectrum at 4 min (inset: zoom within the 2600 - 3200 cm^{-1} range).*

As shown in Figure 5.1(b), during NTP exposure, toluene desorbs as one desorption peak in each experiment. The transient desorption of toluene is short in time, and the maximal desorbed toluene concentration is reached after 2 to 4.5 min of plasma exposure and returns to baseline after 12 min of plasma exposure. While the onset of the peak formation as well as the desorption peak maximum occur at the same time from a toluene exposure time above 10 min, these positions are shifted to a higher plasma exposure time when the toluene exposure time decreases below 10 min indicating that the species are more strongly bonded to the surface when the overall amount of adsorbed toluene is smaller. The amount of desorbed toluene varies from 0.2 to 15.1 µmol.g^{-1} (labelled as "$q_{toluene\ unconverted}$" in Table 5.1) to be compared to the total amount of toluene adsorbed (16.7 to 70.6 µmol.g^{-1}). The difference between the adsorbed toluene and unconverted toluene is stated as "$q_{toluene\ converted}$", which is in the range of 16.5 - 55.5 µmol.g^{-1}. It thus turns out that the toluene conversion (%) decreases from 99 % to 79 % with increasing the storage stage duration t_1.

As previously mentioned, when the NTP is ignited, CO_2 is produced. As seen in Figure 5.1(c), the CO_2 concentration profiles are characterized by intense production envelopes revealing two steps of CO_2 formation for all experiments. The transient productions reach the first maximum (shoulder) value between 1 and 3 min of plasma exposure and the second maximum value between 7 and 9 min of plasma exposure and return to baseline beyond 20 min of plasma treatment. This type of behavior has been previously observed over Hopcalite whether it is by thermal desorption [223] or NTP exposure [77]. Most of the CO_2 produced in the first minutes of NTP exposure is released in the gas phase and some surface sites are thus liberated. As a

consequence, incomplete oxidized intermediates may remain in the adsorbed phase and get further oxidized under NTP exposure. This can explain the delayed formation of CO_2 (second step).

Table 5.1. *Performances of the APC process as a function of storage time span t_1.*

Time t_1 (min)	$q_{toluene\ adsorbed}$ ($\mu mol.g^{-1}$)	$q_{toluene\ unconverted}$ ($\mu mol.g^{-1}$)	$q_{toluene\ converted}$ ($\mu mol.g^{-1}$)	q_{CO2} formation ($\mu mol.g^{-1}$)	S_{CO2} (%)	Y_{CO2} (%)	C mass balance (%)
5	16.7	0.2	16.5	127.4	110	109	110
10	26.0	1.7	24.3	165.7	97	91	98
20	43.8	7.0	36.9	230.2	89	75	91
30	60.6	12.5	48.1	260.2	77	61	82
40	70.6	15.1	55.5	315.3	81	64	85

The total carbon mass balance recovered by *in-situ* NTP treatment has been determined by considering the total amount of adsorbed toluene as 100 %. CO_2 quantified at the reactor downstream has been taken into account. The temporal profiles have been integrated and their relative contributions as Y_{CO2} in the carbon balance of the NTP regeneration have been calculated. Based on that, Y_{CO2} values have been calculated and the resulting values are reported in Table 5.1. It can be seen that these values are overestimated in the case of the first experiment due to the high uncertainty coming from the very short toluene exposure time of 5 min. Within 60 min of NTP treatment, excluding the first experiment, 98 % to 82 % of the total carbon mass balance has been recovered with the CO_2 contribution amounting from 91 % to 61 %. Anyhow, the efficiency for toluene abatement into CO_2 in terms of selectivity and yield and carbon balance (Table 5.1) increases with decreasing the toluene exposure time over Hopcalite. Similar observations have been also reported by Kim et al. [239] and Huang et al. [240]. The increasing amount of adsorbed toluene has been claimed to have negative effects on both the desorption of unconverted toluene and the efficiency of the oxidation process. Some carbon deposits on the inner walls of the plasma reactor and/or adsorbed species remaining on the packed bed material after the *in-situ* NTP treatment can account for the small carbon deficiency observed in this study, as was already previously reported in literature [24, 32] in line with the absence of other gaseous organic species in the outlet of the reactor (observed by FT-IR).

To assess the energetic performance of the sequential APC process, the energy costs for purifying $1m^3$ air (EC, $kWh.m^{-3}$) and the energy yields $EY_{(Tol)}$ and $EY_{(CO2)}$ (g. kWh^{-1}) corresponding to the amount of energy spent (i) to decompose the VOC, and (ii) to produce CO_2 (q_{CO2}), respectively, have been determined (Table 5.2). The EC values have been estimated by dividing the energy consumed in the discharge stage by the volume of polluted air fed on Hopcalite using equation (2.18). The EC values lie between 46.5 and 5.8 $kWh.m^{-3}$. As expected, the energy cost rapidly decreases with increasing storage time. $EY_{(Tol)}$ and $EY_{(CO2)}$ have been

estimated by dividing the amount of toluene adsorbed and CO_2 produced (q_{CO2}) by the energy consumed as defined in equation (2.19) and equation (2.20) respectively. When increasing the storage stage time by a factor 8, the removal of 1 g of toluene and the production of 1 g of CO_2 requires less energy when compared to a short storage time. This study thus reveals that the duration of the storage stage of the APC process strongly affects its energetic performance.

Table 5.2. *Energetic performances of the APC process as a function of storage time span t_1.*

Time t_1 (min)	**EC ($kWhm^{-3}$)**	**$EY_{(Tol)}$ ($g_{Tolads.}\ kWh^{-1}$)**	**$EY_{(CO2)}$ ($g_{CO2.}\ kWh^{-1}$)**
5	46.5	0.07	0.24
10	23.2	0.10	0.31
20	11.6	0.17	0.44
30	7.7	0.24	0.49
40	5.8	0.28	0.60

5.3.2 Effect of discharge power on APC process performances

The effect of the adsorption time reveals that short adsorption periods favor the efficiency of the abatement process in terms of selectivity and yield towards complete oxidation of toluene, while longer adsorption periods are more favorable in terms of energy cost and efficiency. Therefore, for the further study over Hopcalite in this sequential abatement of toluene, a fixed adsorption time of 20 min has been chosen. The effect of the applied discharge power on the temporal evolution of toluene and CO_2 during the NTP exposure has been investigated considering a storage time span (t_1) of 20 min followed by an NTP discharge time (t_2) of 60 min with an increased applied discharge power (40, 46, 52 and 72 W corresponding to a voltage amplitude of 6.5, 7.0, 7.5 and 8.0 kV, respectively), all other parameters being similar as before. It is noticed for all experiments that the temporal toluene profiles as shown in Figure 5.3(a) during the storage stage are quite similar to the temporal evolution of the amount of toluene adsorbed within the margin of error. Based on these temporal toluene profiles, the total amount of toluene adsorbed on the Hopcalite packed bed was determined and the results are presented in Table 5.3. The obtained q_{ads} values remain quite constant (43.8 - 45.4 $\mu mol.g^{-1}$) as can be seen in Table 5.3. This can be attributed to the good efficiency of the NTP exposure for Hopcalite regeneration allowing to get at the start of each experiment a quasi-similar material.

As shown in Figure 5.3(b), toluene desorbs again as one desorption peak in each experiment during NTP exposure. The transient desorption of toluene is however short in time: all toluene desorption profiles have a peak maximum at 2 min, except for the first desorption (40 W) whose maximum production occurs at 4 min. Consequently, the amount of toluene converted shows comparable values in the range 37 - 40 $\mu mol.g^{-1}$ (see Table 5.3).

Table 5.3. *Performances of the APC process as a function of NTP power.*

Power (W)	$q_{toluene\ adsorbed}$ ($\mu mol.g^{-1}$)	$q_{toluene\ unconverted}$ ($\mu mol.g^{-1}$)	$q_{toluene\ converted}$ ($\mu mol.g^{-1}$)	q_{CO2} formation ($\mu mol.g^{-1}$)	S_{CO2} (%)	Y_{CO2} (%)	EC ($kWhm^{-3}$)	$EY_{(Tol)}$ ($g_{Tolads.}\ kWh^{-1}$)	$EY_{(CO2)}$ ($g_{CO2.}\ kWh^{-1}$)
40	45.4	7.2	38.1	203.2	76	64	10.0	0.21	0.45
46	43.8	7.0	36.9	230.2	89	75	11.6	0.17	0.44
52	44.2	6.1	38.2	214.7	80	69	13.0	0.16	0.36
72	44.7	4.3	40.4	204.3	72	65	18.0	0.11	0.25

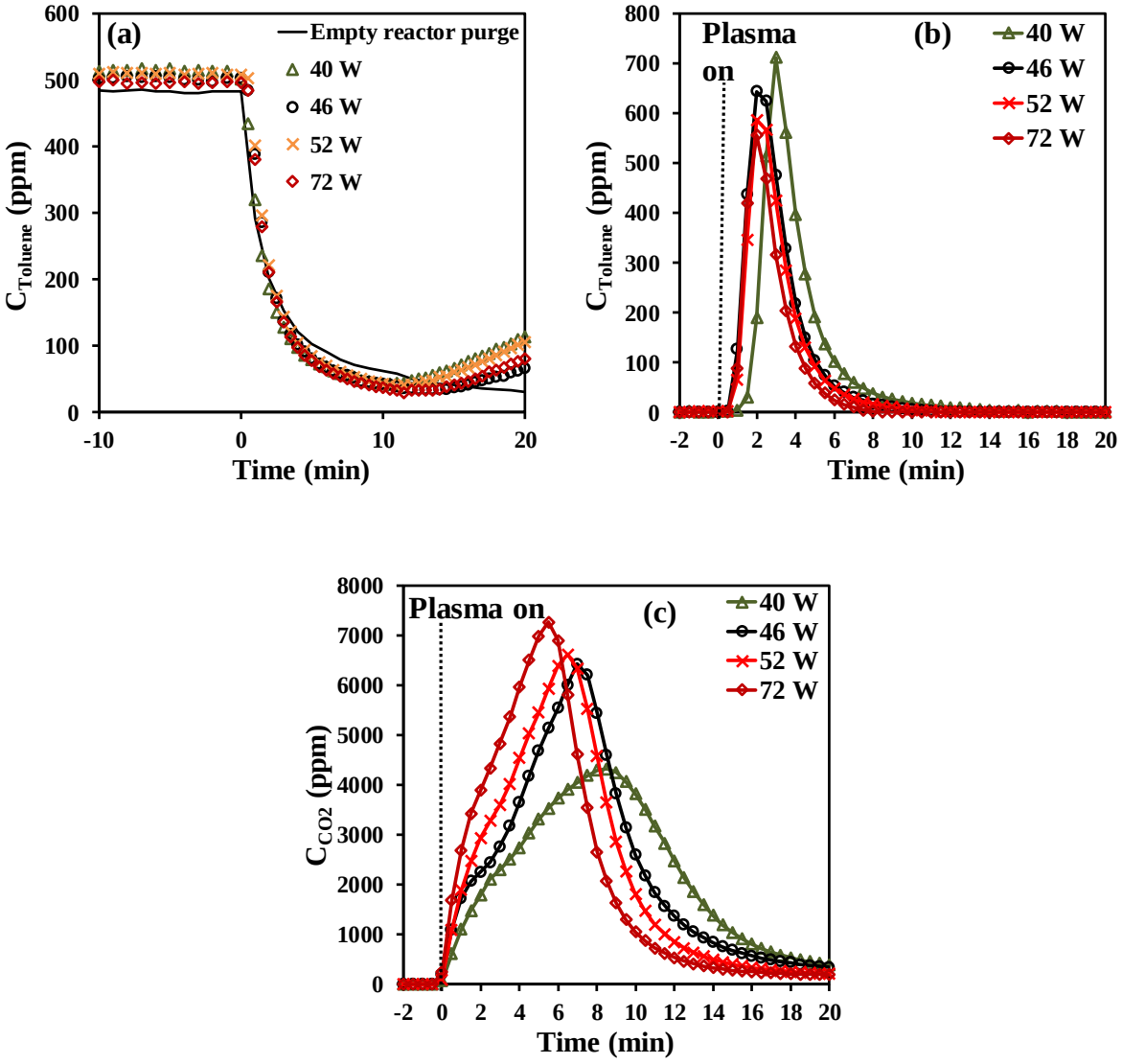

Figure 5.3. *Effect of NTP power on the concentration profiles of (a) toluene during the adsorption step (including a blank test without catalyst), (b) toluene during NTP exposure for the first 20 min (toluene desorption), and (c) CO_2 during NTP exposure for the first 20 min (CO_2 formation).*

By opposition, the temporal profiles of the CO_2 formed (q_{CO2}) are significantly affected by the applied discharge power (Figure 5.3(c)). Although the envelope reveals again the two steps

of CO_2 formation for all experiments, the rate of q_{CO2} formation is strongly accelerated by the increase of plasma power as illustrated by an increase of the maximum CO_2 concentration and the shortening of the overall oxidation process as plasma power increases. This is however accompanied by a decrease in selectivity towards CO_2 at powers above 46 W (see Table 5.3). Indeed, an optimum of selectivity and yield can be observed for a plasma power of 46 W. By using equations (2.18) to (2.20), the EC, $EY_{(Tol)}$ and $EY_{(CO2)}$ values have also been determined and are reported in Table 5.3. The EC increases from 10 to 18 $kWh.m^{-3}$ as power increases from 40 to 72 W. However, in the power range 40-52 W, there is a 25 % decrease in $EY_{(Tol)}$ and $EY_{(CO2)}$. By opposition, when comparing the range of 40-52 W to 72 W, the energy yields drop by nearly half (50 %). A low discharge power would therefore be recommended in terms of energy cost and efficiency when applying an APC abatement process.

5.3.3 Stability and repeatability of Hopcalite in adsorption-plasma catalysis

It is important that the adsorbent/catalyst performances of the bifunctional material are restored after plasma assisted regeneration. On purpose, Hopcalite for the adsorption of 500 ppm of toluene in dry air (0.2 $L.min^{-1}$) for 20 min followed by air plasma exposure (0.2 $L.min^{-1}$) for 60 min over four cycles of the APC technique has been investigated at a discharge power of 46 W. The time span of 20 min has been chosen to be a compromise between CO_2 selectivity and energy performances. Figure 5.4(a) shows the concentration profile of gaseous toluene during the storage stage monitored over the 4 sequences. The useful toluene capacity is similar for all sequences as it remains constant at 46 ± 2 $\mu mol.g^{-1}$ (Table 5.4). The lowest amounts of toluene adsorbed and toluene desorbed (Figure 5.4b) during the NTP exposure of 43.9 $\mu mol.g^{-1}$ and 3.2 $\mu mol.g^{-1}$, respectively, are observed for the first sequence. The temporal profiles of CO_2 formed (Figure 5.4c) resemble those described before. It is noticed that the first q_{CO2} production is higher than the other ones and after that the envelopes are quasi-similar. Despite some variations between the different sequences, Hopcalite exhibited a rather good stability with a mean carbon balance (excluding the first sequence due to the deposition of some intermediates on the catalyst surface from the abatement of toluene) of about 88 % and a CO_2 selectivity of about 87 %. Like previously, the EC, $EY_{(Tol)}$ and $EY_{(CO2)}$ values have been calculated by using equations (3) to (5). The EC is stable at 11.6 $kWh.m^{-3}$ for all sequences. Similarly, no significant discrepancies in $EY_{(Tol)}$ and $EY_{(CO2)}$ are found among the various sequences, with values of 0.18 (± 0.01) g. kWh^{-1} and 0.48 (± 0.06) g. kWh^{-1}, respectively.

Table 5.4. *Characteristic properties of the APC process over the 4 sequences.*

Sequences	$q_{toluene\ adsorbed}$ ($\mu mol.g^{-1}$)	$q_{toluene\ unconverted}$ ($\mu mol.g^{-1}$)	$q_{toluene\ converted}$ ($\mu mol.g^{-1}$)	q_{CO2} formation ($\mu mol.g^{-1}$)	S_{CO2} (%)	Y_{CO2} (%)	C mass balance (%)
Sequence-1	43.9	3.2	40.7	294.9	103	96	103
Sequence-2	47.7	5.3	42.4	257.2	86	77	88
Sequence-3	45.7	7.3	38.4	246.1	91	76	92
Sequence-4	44.8	5.3	39.5	223.7	80	71	83

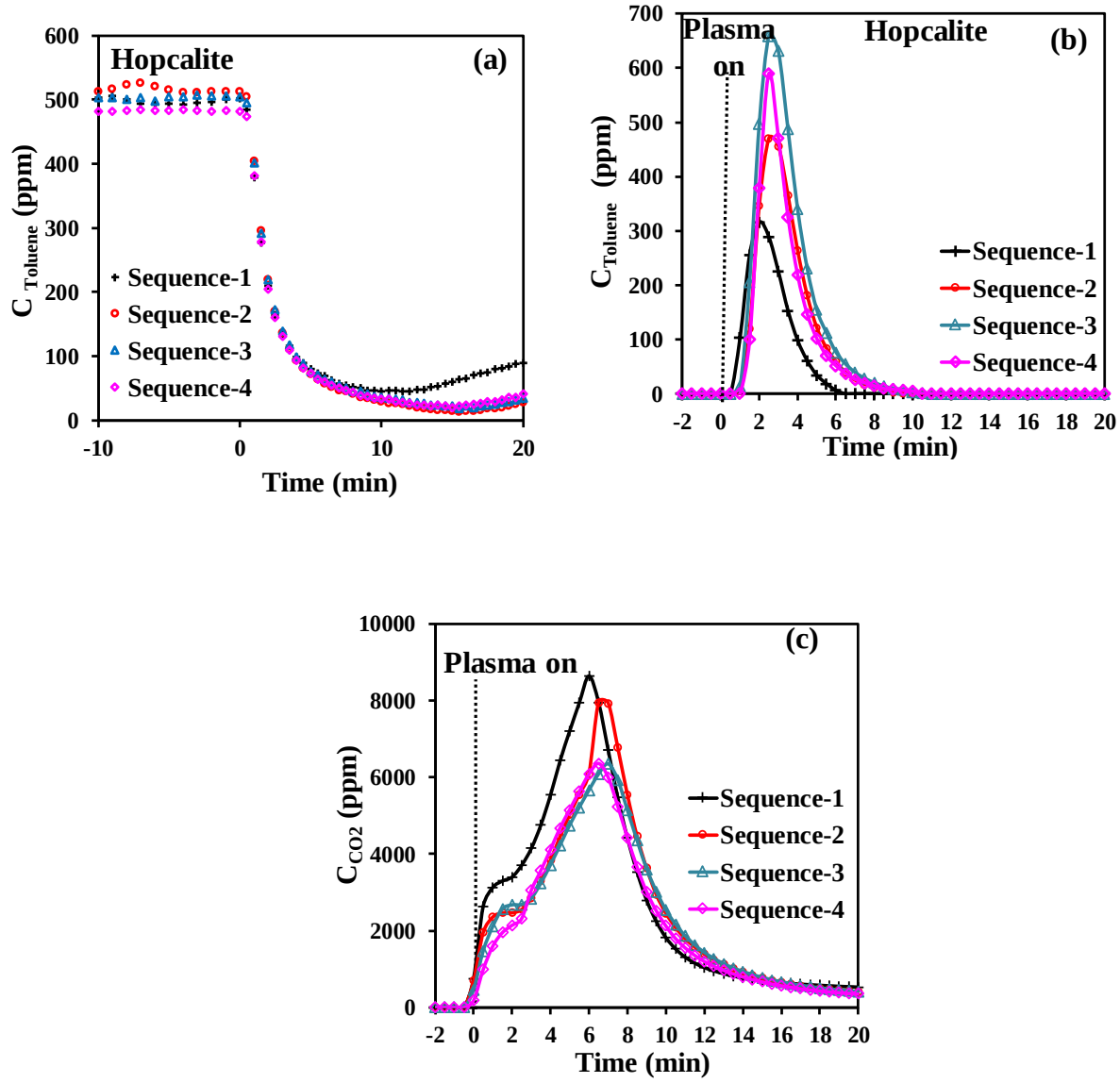

Figure 5.4. *Temporal profiles of toluene during adsorption (a), desorbed toluene during NTP exposure (b), CO_2 evolution during NTP exposure (c) over the 4 sequences.*

5.3.4 Characterization of catalyst

The X-ray diffraction patterns of Hopcalite before and after a multi-sequential APC process (after 15 NTP exposures) are shown in Figure 5.5. Two low intense peaks localized at 37.2°

and 68.2° in 2θ are shown for fresh Hopcalite indicating the presence of a mostly amorphous MnO_x phase [195,241,242]. The peak at the higher 2θ angle is still present in the XRD profile after performing the multi-sequential APC process, but shifts to a lower 2θ angle, while also becoming more intense and broader. The broadening of the peak indicates that the material possesses a poor crystallinity after the APC process performed with multiple sequences.

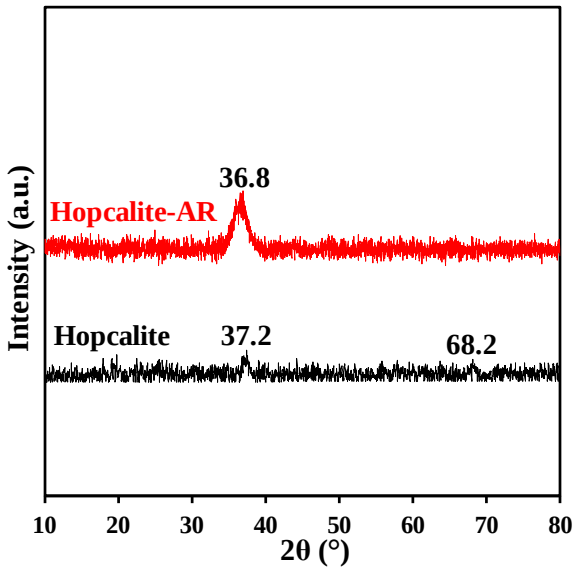

Figure 5.5. *The XRD patterns of Hopcalite before and after reaction (AR, meaning after 15 NTP exposures).*

Figure 5.6 displays the N_2 adsorption-desorption isotherms and pore size distribution (PSD) of the fresh Hopcalite and the Hopcalite after reaction (after 15 NTP exposures). A similar type IV isotherm with a hysteresis loop in the P/P_0 range of 0.42 - 1.0 showing the mesoporous character of the material is observed. A small decrease of the S_{BET} from 232 $m^2.g^{-1}$ to 195 $m^2.g^{-1}$ is noticed while the mean pore diameter and pore total volume maintain constant at 8 nm and 0.45 $cm^3.g^{-1}$ after multiple NTP exposures, respectively (c.f. Table 5.5).

Table 5.5. *Textural and redox properties of the fresh Hopcalite and Hopcalite after reaction (Hopcalite-AR).*

Materials	S_{BET}[a] ($m^2.g^{-1}$)	V_p[b] ($cm^3.g^{-1}$)	D_p [c] (nm)	H_2 Consumption ($mmol.g^{-1}$)
Hopcalite	232	0.45	7.8	11.1
Hopcalite-AR	195	0.45	8.0	10.8

a: BET specific surface area ; b: Total pore volume ; c: Pore diameter

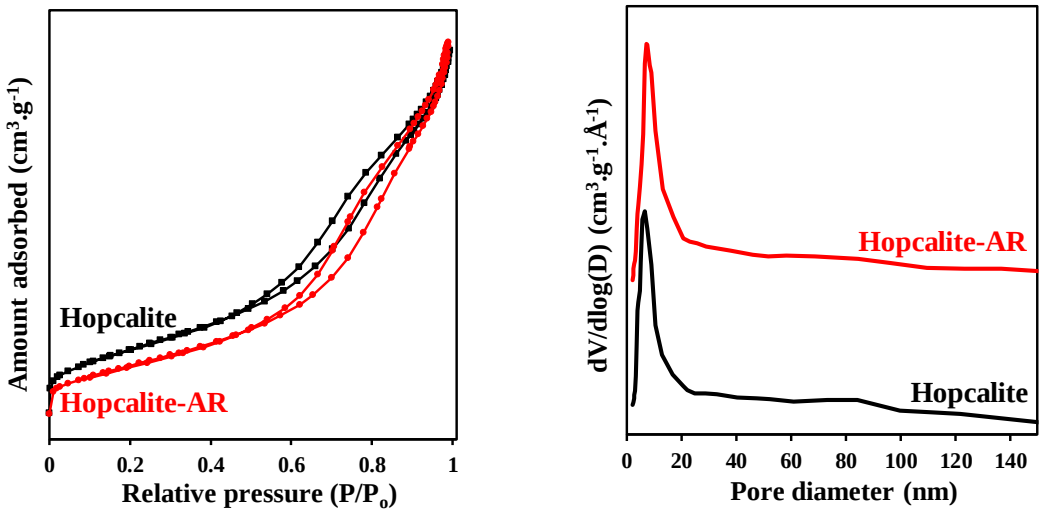

Figure 5.6. *N_2 adsorption-desorption isotherms and pore size distribution of fresh Hopcalite and Hopcalite after reaction (Hopcalite-AR).*

The surface state of Hopcalite before and after reaction was investigated by X-ray photoelectron spectroscopy (XPS) and the results are presented in Figure 5.7. The surface chemical states of the elements and the surface composition are also shown in Tables 5.6 and 5.7 respectively. The XPS survey spectra reveal the presence of Cu, Mn, C, O, K, Na and Al. The high-resolution Cu 2p envelopes are very similar before and after reaction. The Cu $2p_{3/2}$ peaks localized at binding energy of 933.4 eV ± 0.2 eV and the presence of satellites are indicative of divalent copper Cu^{2+} [109,229,243]. The Mn $2p_{3/2}$ envelopes can be successively decomposed considering a MnOOH species [244] in line with the Mn AOS (average oxidation state) of 3.1 estimated from the splitting of the two Mn 3s components [207]. The O 1s XPS spectra can be decomposed using three components: O_I = 529.6 eV, O_{II} = 531.1-531.5 eV and O_{III} = 533.4 eV. O_I, O_{II} and O_{III} have been assigned to surface lattice oxygen (O_{1att}), surface adsorbed oxygen species (such as O_2^-, O_2^{2-} O^-, OH^-/CO_3^{2-} group) denoted as O_{surf} and adsorbed H_2O on the surface, respectively [245]. It is also noteworthy to mention that the XPS composition (Table 5.7) is rather similar for Hopcalite before and after 15 NTP exposures. The O_{latt}/O_{ads} ratio of 1.17 for pristine Hopcalite also increases to 1.27 after 15 multiple NTP exposures, while also O_{III} species are absent on the latter sample (c.f. Tables 5.6 and 5.7). This suggests that the presence of a high amount of surface active oxygen species will exert a productive effect upon building the exceptional reversibility of the surface redox cycle during toluene oxidation. This explains the good catalytic activity and maintained CO_2 selectivity of several sequences performed on Hopcalite. In our previous work, Veerapandian et. al. [77] proposed a detailed mechanism of toluene abatement. It was suggested that the catalytic oxidation of toluene follows a Mars and Van Krevelen mechanism. Accordingly, adsorbed

toluene species are oxidized by the lattice oxygen and gas phased oxygen re-oxidizes the oxygen vacancy. In Hopcalite, Cu and Mn can get easily oxidized and reduced in the reaction cycle. As shown by the XPS data, Cu^{+}-Cu^{2+} and Mn^{3+}-Mn^{4+} redox couples are mostly responsible for the catalytic properties of the material.

Table 5.6. *Binding energy of the elements (eV).*

Material	Cu $2p_{3/2}$	Mn $2p_{3/2}$	O_I	O_{II}	O_{III}	K $2p_{3/2}$ (FHWM)	Na 1s
Hopcalite	933.3	641	529.6	531.0	533.4	292.5 (1.5)	1070.4
Hopcalite-AR	933.5	641	529.6	531.5	-	292.5 (1.6)	1071.1

Table 5.7. *XPS composition of the materials.*

Material	Cu/Mn	K/Mn	O/Mn	Na/Mn	O_{latt}/O_{ads}	ΔE Mn3s / eV (Mn AOS)
Hopcalite	0.26	0.11	3.1	0.06	1.17	5.14 (3.1)
Hopcalite-AR	0.29	0.12	3.5	0.07	1.27	5.20 (3.1)

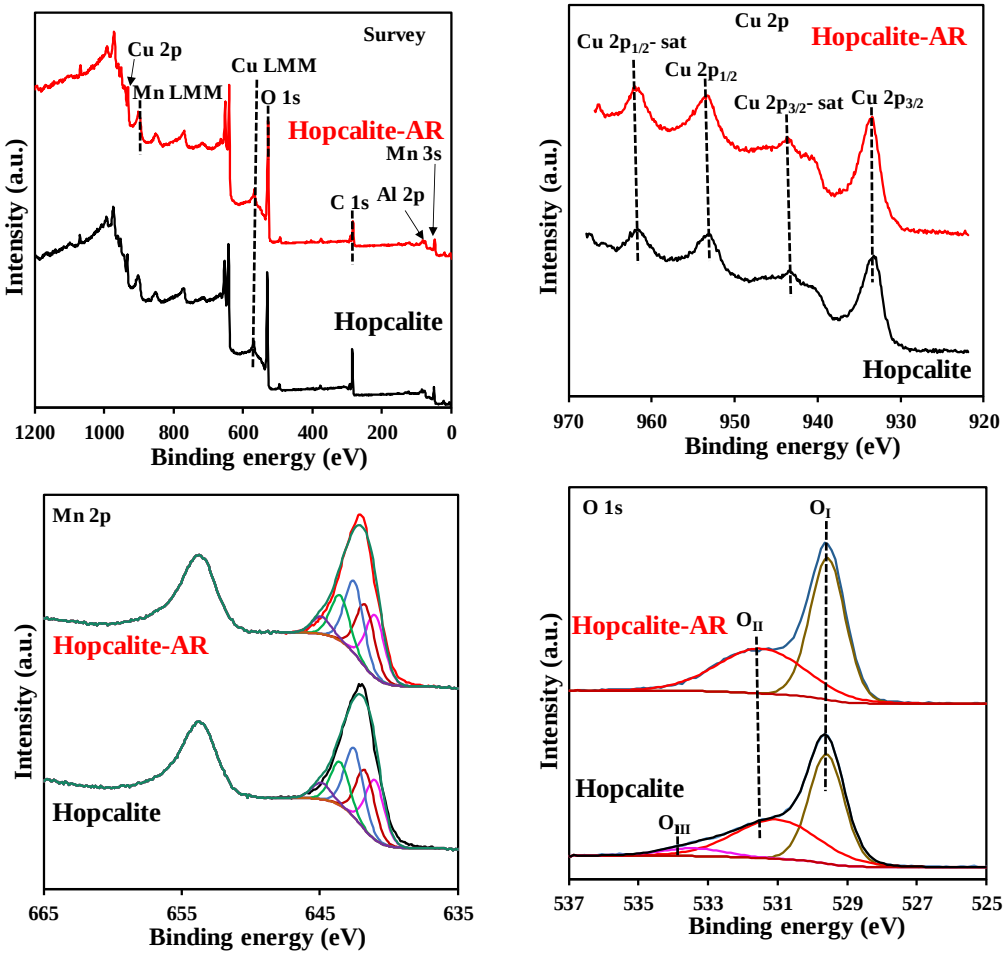

Figure 5.7. *XPS survey spectra and high resolution Cu 2p, Mn 2p, and O 1s spectra of Hopcalite and Hopcalite-AR.*

The H_2-TPR profiles of the fresh Hopcalite and the Hopcalite after reaction (thus after 15 NTP exposures) shown in Figure 8 are complex [223] and quite similar except for the absence

of the reduction peak at 149 °C for the Hopcalite after reaction. The absence of the peak at 149 °C for Hopcalite after reaction may be due to the reduction of CuO_x into Cu (0) [242]. On the other hand, in comparison to the fresh catalyst, in which XPS and H_2-TPR reveal the presence of the Cu^{2+}, this latter species is absent in the H_2 TPR profile of the used catalyst. However, the H_2 consumption values are similar for the pristine and used Hopcalite (11 ± 2 mmol.g^{-1}, c.f. Table 5.5). Moreover, the absence of the peak (at 149 °C) which corresponds to Cu^{2+} in H_2 TPR does not influence the performance of Hopcalite in APC abatement of toluene.

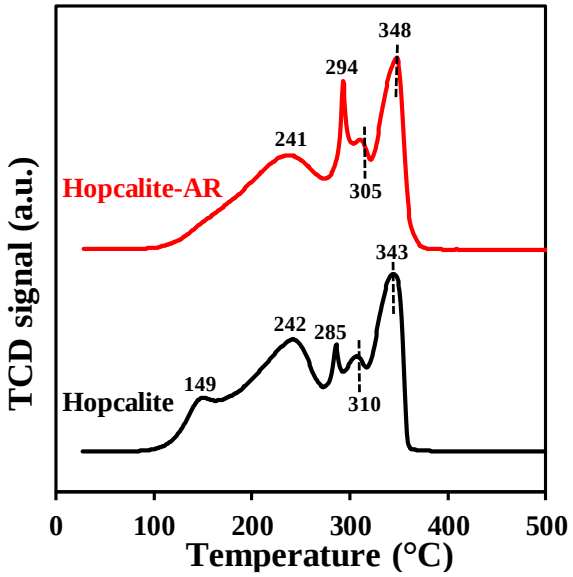

Figure 5.8. *H_2-TPR profiles of Hopcalite before and after reaction (Hopcalite-AR).*

The surface and bulk catalyst characterizations have confirmed that the structure, texture, reducibility and surface composition of Hopcalite are mostly unaffected by the repeated sequences of toluene adsorption and plasma assisted oxidation. In addition, they also confirm the efficiency of the plasma process for the regeneration of the material.

5.4 Conclusion

Hopcalite was investigated for toluene total oxidation in an APC process using a high toluene inlet concentration (500 ppm). The effect of the time span of the storage stage (t_1) as well as the effect of the delivered power (P) during the discharge stage on the efficiency of the process have been particularly studied. As expected, the energy cost rapidly decreases with an increase in the storage time t_1. Furthermore, the efficiency of the APC process in terms of $EY_{(Tol)}$ and $EY_{(CO2)}$ increases with increasing storage stage duration. Hence, limiting the amount of toluene adsorbed through a short adsorption time allows best performances in terms of CO_2 selectivity and yield, but clearly also induces the least energy efficiency and the highest energy

cost. When varying the power of the plasma, an optimum could be observed in terms of CO_2 selectivity and energy consumption for a power of 46 W. Repetition of the adsorption-oxidation process showed that the performances were not affected by subsequent plasma treatments as could be confirmed by the characterization of the material after multiple APC sequences, which revealed no significant changes in catalyst properties.

This exploratory work clearly shows the high potential of sequential processes involving toluene adsorption followed by plasma catalytic oxidation. Clearly, optimal process conditions need to be determined for each individual abatement environment (actual inlet and tolerable outlet toluene concentrations, volumes and flow rates of streams, etc.). In the present study, the only carbon containing gaseous reaction product detected was CO_2. An important aspect of such optimization process will be the determination of the nature of the by-products in order to ensure that no other toxic products are formed. However, further work has to be done to reduce the plasma on time and thus enhance the overall efficiency of the process.

Chapter 6

Abatement of toluene from air stream through a sequential adsorption-plasma catalysis (APC) system using silver impregnated Hopcalite adsorbent/catalyst materials.

Preamble

The basis of a hybrid process combining adsorption of VOC pollutant followed by plasma catalytic combustion was set in previous chapter. Hopcalite was chosen for its redox properties and its catalytic activity was investigated. Results of Chapter 5 confirmed Hopcalite as a promising candidate for such a hybrid process. Optimized experiment condition leads to full conversion of adsorbed toluene into CO_2 selectivity. Furthermore, the series of Ag impregnated Hopcalite used for the hybrid process of adsorption followed by thermal oxidation. The promising result of catalysts enhanced the interest to investigate its performance for the hybrid process (adsorption+ plasma-catalysis). The object of the presence chapter is to investigate the performance of Ag impregnated Hopcalite; compared it with parent sample (Hopcalite) and study its stability in optimized experiment condition.

Chapter 6 Abatement of toluene from air stream through a sequential adsorption-plasma catalysis (APC) system using silver impregnated Hopcalite adsorbent/catalyst materials.

6.1 Introduction

Volatile organic compounds (VOCs) emitted from various industrial and indoor activities impact greatly air quality. As a result, they provoke short- and long-term adverse health effects and affect the environment throughout the formation of tropospheric ozone, smog and acid rains [12] [246]. Among the VOC abatement technologies, Non-thermal plasma (NTP) [247] has been reported as an attractive means as it can operate at atmospheric pressure and at low operating temperatures. Indeed, the NTP generated highly reactive species such as energetic electrons and free radicals which can easily break down chemical bonds. However, NTP suffers from two main drawbacks which are (i) low mineralization of the VOC and (ii) low energy efficiency. To overcome such drawbacks, the combination of Non-thermal plasma (NTP) with catalyst systems has been assessed in last decades as an alternative technology to NTP for VOC removal. It has been shown that Non-thermal plasma catalysis can be one of the most promising technologies in the control of volatile organic compounds (VOCs) as it has the potential to combine high efficiency, high by-product selectivity and superior carbon balance than NTP [12,247] When the catalyst is integrated in the NTP reactor, NTP-plasma catalysis can be decomposed into two operational modes: continuous operation in plasma catalyst (CIPC) system and sequential operation in plasma catalyst (SIPC) system. Compared with the CIPC system, the SIPC mode consists first of VOC adsorption followed by NTP assisted oxidation processes and electrical energy is only consumed in the oxidation process, while the CIPC consumes energy all the time. In the VOC adsorption step, the VOC diluted in air is flushed on an absorbent/catalyst until the full or useful dynamic gas adsorption capacity is reached. At that stage, the plasma reactor is switched on in order to oxidize the adsorbed VOCs into harmless CO_2 and H_2O and in that way regenerate the catalyst/sorbent bed before performing another sequence. The SIPC process singles out by its cost-effective energy efficiency potential when considering low VOC concentrations (less than 1000 ppm) air streams which explained that SIPC has been particularly studied in the last decade. One of the major challenges in the design of efficient dual materials is to take account of the required supplementary properties which have to be balanced between storage (adsorption) and oxidation/regeneration [42]. This implies

to use the plasma in an effective manner by exploiting its inherent synergetic potential through combination with bi-functional materials (adsorbent/catalyst) [248,249].

Few studies have been carried out to investigate oxidative removal of toluene using SIPC. X. Xu et. al. [63] reported a comparison study between CIPC and SIPC processes using (Ag, Mn and AgMn) loaded SBA-15 catalysts. In both operating modes, toluene conversion and carbon balance decrease in the following order: AgMn/SBA-15 > Ag/SBA-15 > Mn/SBA-15 > SBA-15 which is consistent with ozone decomposition activity. Besides, SIPC outperforms CIPC regarding toluene conversion and especially carbon balance which increase from 88 to 100 % and from 38 to 78 %, respectively. As no more toluene is introduced at the discharge stage for SIPC, the contribution of the NTP induced gaseous homogeneous reactions involving toluene can be discarded to a large extent. As a consequence, minimization of the amount of carbonaceous by-products for SIPC combined with a better utilization of active oxygen species at the material surface have been invoked by the authors for the significant improved carbon balance for SIPC. Hence, integration of AgMn/SBA-15 in the NTP reactor which simultaneously possesses the highest adsorption capacity and plasma catalytic activity leads to the most efficient SIPC process for toluene abatement.

As the dual material must have among other things a high toluene adsorption capacity to applied in SIPC, zeolites which have unique micropores, cavities and channels in their frame structure can be considered as suitable adsorbents. Indeed, the micropore sizes of the zeolite which range from 3 to 20 Å are comparable to the kinetic diameters of some organic molecules such as toluene (5.85 Å). Taking these special properties into account, various types of zeolites such as 5A, HY, Hβ, HZMS-5 have been tested in SIPC [62]. Toluene removal efficiency values ≥ 80 % have been found in line to strong collisions of electrons and radicals in the micropores. Besides, the carbon balance and CO_2 selectivity decrease as follow: HY > Hβ (HZSM-5) > 5A in agreement with toluene adsorption ability and ozone adsorption ability during the plasma discharge. The better toluene adsorption capacity of HY has been attributed to high internal surface and surface acidic properties (low Si/Al). In order to promote the performances of the hybrid system, Ag has been loaded on HY and toluene removal efficiency, carbon balance and CO_2 selectivity increase from 85.2 %, 83.0 % and 69.0 % to 97.0 %, 98.1 % and 93.3 %, respectively which show that more adsorbed toluene has been completely oxidized through a better decomposition of the organic intermediates. However, significant amounts of O_3 and traces of N_2O detected at the outlet.

A comparative approach has been reported recently in the literature by X. Yu et. al. [76] in which Ag/ZSM-5 has been used as dual material based on previous studies performed by W. Wang et. al. [71]. The IPC and PPC processes have been studied both in continuous and sequential modes for toluene abatement. As support, ZSM-5 has been widely used due to its superior and tunable surface properties, hydrophobicity, metal load ability and inhibition of carbon deposition [250]. The Ag-based catalyst has been used due to its superior adsorption capacity and catalytic activity [224]. It has been observed that IPC has a higher mineralization rate than PPC systems both in continuous and sequential processes. At 20 kV a CO_2 yield (Y_{CO2}) of ~ 90 % has been achieved in SIPC which drops to a value of ~ 65 % in CIPC. However, the concentrations of O_3 and N_2O at the outlet of the reactor have always been found higher in SIPC than in PPC systems. The different nature of the contributors to the toluene degradation, namely short-lived species in ICP and O_3 in PPC, has been invoked to explain the higher concentrations of O_3 and N_2O. Additionally, it should be noted that Ag-Mn/ ZSM-5 has been shown to deactivate upon time after 10 cycles of adsorption/plasma treatment due to the accumulation of accumulated organic intermediates [71].

Besides, Veerapandian et.al. [77] investigated the performances of a DBD reactor packed calcined commercial Hopcalite (Purelyst MD-101) with glass beads as a bi-functional material in SIPC for the removal of toluene (~ 500 ppm) in air with low water content (RH ~ 3 %). Indeed, Hopcalite which is a porous material consisting of a mixture of manganese and copper oxides has been recognized for a long time to be an efficient catalyst in toluene [77,251], carbon monoxide [224] oxidation reactions and ozone decomposition [219]. It has been found that the CO_2 yield and CO_2 selectivity (based on the amount of irreversibly adsorbed toluene) have been improved, when considering the second sequence of adsorption-plasma oxidation, increasing from 60 % and 86 % to 62 % and 93 % respectively. Although the NTP treatment induces partial transformation of Hopcalite into Mn_3O_4 and a two-fold decrease of the specific surface area, it is noted that the toluene adsorption remains less affected. The increase of adsorbed oxygen species in a more defective surface of the dual material seems in line with the promotion of toluene oxidation through active oxygen coming from ozone decomposition.

In a complementary work, Sonar et al. [251] the effects of process variables such as the duration of the adsorption step (t_1) and of the delivered power P during the discharge stage have been investigated on the performances of the process for toluene total oxidation (~ 500 ppm). A short adsorption time allows best performances in terms of CO_2 selectivity and yield, but clearly also induces the least energy efficiency and the highest energy cost. When varying the

power of the plasma, an optimum could be observed in terms of CO_2 selectivity and energy consumption for a power of 46 W. Repetition of the adsorption–oxidation process (APC) showed that the performances were not affected by subsequent plasma treatments as could be confirmed by the characterization of the material after multiple APC sequences, which revealed no significant changes in catalyst properties.

In this study, the total oxidation of toluene at high concentration (500 ppm) using a four sequential APC experiment has been investigated over Hopcalite supported Ag catalysts (Hop-x Ag-S4; x = Ag wt.% : 0.5; 1; 2; 10). A low storage stage time (t_1) has been fixed in order to reduce the toluene release at the exit of the reactor during the storage stage and to reduce the release of heat of the NTP induced oxidation of adsorbed toluene over Hopcalite.

Furthermore, a nine sequential APC experiment has also been performed to study the stability of Hopcalite (Hop) and Hop-x Ag with time. Finally, different physicochemical characterizations including XRD, H_2-TPR, N_2 adsorption–desorption analysis and XPS have been performed to detect eventual modifications of the bi-functional material.

6.2 Experimental

Commercial catalyst Hopcalite is used and different weight % of silver impregnation on Hopcalite have been synthesized such as Hop-0.5 Ag, Hop-1 Ag, Hop-2 Ag and Hop-10. The characterization includes XRD, XPS, BET, EDS, TEM, TPR, TGA/DTA, FTIR and Raman, which give in detailed in Chapter 4. After sequential adsorption-plasma catalysis (APC) reaction, XRD, XPS and Raman is performed. The detailed preparation process and characterization process can be seen in Chapter 2. Sequential adsorption-plasma catalysis (APC) process was performed at the University of Ghent. The description of the set-up and experimental process are given in Chapter 2 in section 2.3. The four steps involved in each experiment such as: (i) adsorption (t_1) for 20 min, (ii) flushed the line by dry air. During this time the reactor was in the static atmosphere i.e. in the toluene gas phase, (iii) pass the dry air through reactor for 2 min to stabilize the flow, then (iv) switched on the NTP discharge (t_2 = 60 min) for oxidation of adsorbed toluene and regeneration of the material for next adsorption step.

Prior to any experiment, the calcined material was activated at 150 ºC for 4 h at ramping rate 2 ºC with 0.2 $L.min^{-1}$ of dry air to remove the unwanted adsorbed species. Typically, 2 g of activated material was packed in the DBD reactor. Simultaneously, the 0.2 $L.min^{-1}$ dry air flue gas containing 500 ± 50 ppm of toluene was prepared in by-passed of the reactor. The FT-

IR spectra were continuously recorded every 30 sec for 1 h to assess the actual initial concentration of toluene. Then, the toluene containing gas flow was switched into the DBD reactor to start the adsorption of toluene (t_1) for 20 min. Then the toluene containing flue gas was switched back to by-pass 5 min and record the toluene flow to confirmed the before and after adsorption study the toluene concentration is the same and then shut down toluene flow. During this period of time DBD reactor was in the static atmosphere i.e. toluene gas atmosphere. Then, the line was flushed with dry air (0.2 $L.min^{-1}$) for 15 min to ensure the absence of toluene species as monitored by FTIR spectra. Finally, dry air flow (0.2 $L.min^{-1}$) was passed through reactor for 2 min and then plasma (44-46 W) was turned on (t_2 =1 h). All of these steps (adsorption followed by plasma assisted catalytic conversion) were described as one "sequence".

A four sequence (Hop-x Ag-4S) APC experiment was performed under the same conditions as mentioned above with a storage duration t_1 of 20 min and a discharge power P of 46 W in order to assess the regeneration behavior and catalytic performance. In similar experimental condition as of the above was repeated over Hop-1 Ag nine times (Hop-1 Ag-9S).

The amount of toluene adsorbed (µmol. g^{-1}), discharge power (P), CO_2 formation (µmol. g^{-1}), selectivity and yield of CO_2 (S_{CO2}, Y_{CO2}), energy cost (EC), and energy yield $EY_{(Tol)}$ and $EY_{(CO2)}$ are calculated by the equations which provided in detailed in Chapter 2 (Section 2.3.6).

6.3 Result and Discussion

6.3.1 Performance for the removal of Toluene

6.3.1.1 Effect of silver content on useful adsorption of toluene

The dynamic adsorption of toluene over Hop and Hop-x Ag dual materials have been examined using a gaseous effluent of ~ 500 ± 10 ppmv of toluene/air (0.2 $L.min^{-1}$) at 25 °C for a fixed exposure time of about 20 min with a relative humidity (RH) of about 3 %. The performances of the materials have been assessed considering a breakthrough time, which is the period from the start to the time when toluene is detected in the output gas, close to 20 min. Figure 6.1 (a, b, c, d, e) shows the breakthrough curves during the adsorption storage stage for the 4 first successive adsorptions of the cycling storage-regeneration process. It is worthy to note that the profiles of concentration as a function of toluene exposure time during the first minutes, determined from the analysis of FT-IR spectra, match the one obtained during the purge of the empty reactor which lasts for about 15 min [251]. The observance of a total

adsorption of toluene is never observed for any dual functionalized materials due to the combined opposite effects resulting from (i) the purge of the PBDBD reactor and (ii) the rapid appearance of the breakthrough time. Based on these observations, it is considered that all introduced toluene is irreversibly adsorbed on the material until the slope of toluene concentration becomes positive. Taking into account of the purging profile of the reactor the useful dynamic toluene adsorption capacities have been reported in Table 6.1. The toluene adsorption capacity determined from the first sequence amounts to 44 $\mu mol.g^{-1}$ for Hop. Apart Hop-10 Ag which shows a low adsorption capacity of 32 $\mu mol.g^{-1}$ as compared to Hop, the other Ag-containing materials display rather similar values (42 $\mu mol.g^{-1} \pm 4 \mu mol.g^{-1}$) than the referenced one for Hop despite a S_{BET} decreased by two. As already outlined, doping Hop with silver allow to introduce new Ag(I) sites for toluene adsorption. Such adsorption sites have been previously invoked to interact via π interaction [76] or via electrostatic interaction with the aromatic ring [238]. However, the expected enhancement in adsorption capacity is offset by the S_{BET} decrease. Furthermore, it has to be mentioned that the useful toluene adsorption capacities are lower than expected as regard to those obtained previously of the same order of magnitude by our team in an adsorption/thermal regeneration process taking into account the initial toluene concentration which is herein higher by a factor 5 (~500 ppm as compared to ~100 ppm). This is in line with previous reports showing that, in APC mode, the adsorption efficiency is all the more important that the initial concentration is low [223]. Such lower values can be also explained in part by the competitive adsorption of water and toluene for adsorption sites as the previous study has been performed in dry air. After the second adsorption, it is observed an increase of the adsorption capacity for any materials to different extent, Hop-1 Ag excepted, with an increase up to ~ 20 % for Hop-0.5 Ag. This shows the efficiency of using NTP oxidation as regeneration process to get rid of adsorbed impurities. For the two other remaining adsorption stages, the values of the adsorption capacities although less than those of the second one are very close for all materials indicating some stability in the process.

Table 6.1. *Comparison of Hop and Hop-x Ag during toluene (500 ppm, dry air flow =0.2 L.min^{-1}, t_1 = ~ 20 min) adsorption followed by plasma discharge (P = 46 W, dry air flow =0.2 L.min^{-1}, t_2 = 1h).*

Material	$q_{Tol.ads}$ (µmol.g^{-1})	$q_{unconverted}$ (µmol.g^{-1})	$q_{converted}$ (µmol.g^{-1})	q_{CO2} (µmol.g^{-1})	S_{CO2} (%)	Y_{CO2} (%)	t_1 (min)	EC (kWhm^{-3})	EY_{Tol} ($g_{Tol.ads}$.kW^{-1}h^{-1})	EY_{CO2} (g_{CO2}.kW^{-1}h^{-1})
Hop										
Hop-1S	43.9	3.2	40.7	294.9	103	96	20	11.61	0.17	0.56
Hop-2S	47.7	5.3	42.4	257.2	87	77	20	11.61	0.19	0.49
Hop-3S	45.7	7.3	38.4	246.1	92	77	20	11.61	0.18	0.47
Hop-4S	44.8	5.3	39.5	223.7	81	71	20	11.61	0.18	0.42
Hop-0.5 Ag										
Hop-0.5 Ag-1S	46.1	21.3	24.8	317.6	183	98	20	11.61	0.18	0.60
Hop-0.5 Ag-2S	60.0	9.9	50.1	318.9	91	76	25.5	9.11	0.24	0.60
Hop-0.5 Ag-3S	52.5	8.9	43.6	281.7	93	77	22	10.56	0.21	0.53
Hop-0.5 Ag-4S	51.7	5.4	46.3	275.1	85	76	21	11.06	0.21	0.52
Hop-1 Ag										
Hop-1 Ag-1S	38.2	4.3	33.9	209.3	88	78	20	11.61	0.15	0.40
Hop-1 Ag-2S	36.8	6.1	30.7	194.9	91	76	20	11.61	0.15	0.37
Hop-1 Ag-3S	35.7	5.4	30.3	192.1	90	77	20	11.61	0.14	0.36
Hop-1 Ag-4S	37.0	6.5	30.5	181.6	85	70	20	11.61	0.15	0.34
Hop-2 Ag										
Hop-2 Ag -1S	42.6	4.3	38.3	279.8	104	94	20	11.61	0.17	0.53
Hop-2 Ag -2S	67.2	8.2	59. 4	360.3	87	76	20	11.61	0.27	0.68
Hop-2 Ag -3S	41.2	5.9	35.3	244.4	99	85	20	11.61	0.16	0.46
Hop-2 Ag -4S	40.5	6.6	33.93	240.7	101	85	20	11.61	0.16	0.46
Hop-10 Ag										
Hop-10 Ag-1S	31.6	6.3	25.3	214.2	121	97	20	11.61	0.13	0.41
Hop-10 Ag-2S	36.9	5.3	31.6	207.1	94	80	20	11.61	0.15	0.39
Hop-10 Ag-3S	38.6	6.5	32.1	214.0	95	79	20	11.61	0.15	0.41
Hop-10 Ag-4S	39.3	6.3	33.0	209.7	91	76	20	11.61	0.16	0.40

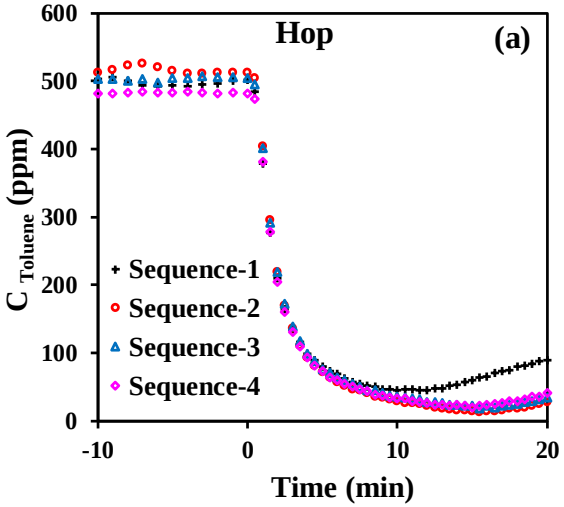
Hop
(a)
C Toluene (ppm)
Time (min)
Sequence-1
Sequence-2
Sequence-3
Sequence-4

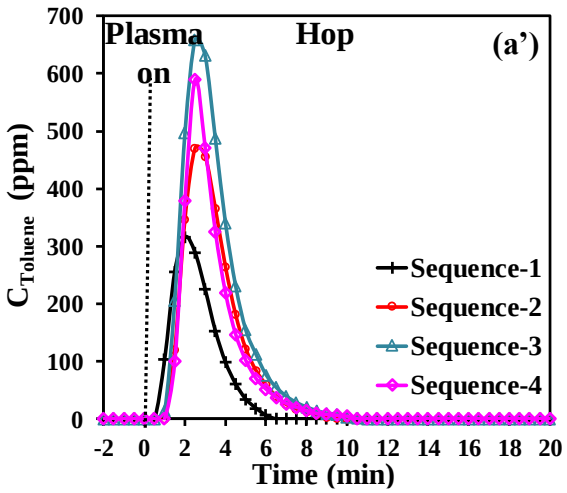
Plasma on
Hop
(a')
C Toluene (ppm)
Time (min)
Sequence-1
Sequence-2
Sequence-3
Sequence-4

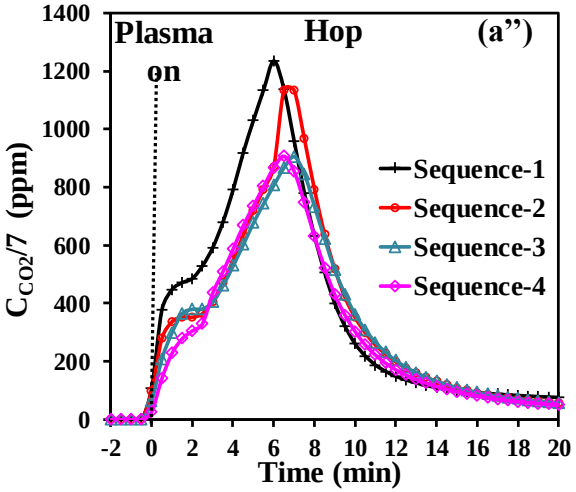
Plasma on
Hop
(a")
C CO2/7 (ppm)
Time (min)
Sequence-1
Sequence-2
Sequence-3
Sequence-4

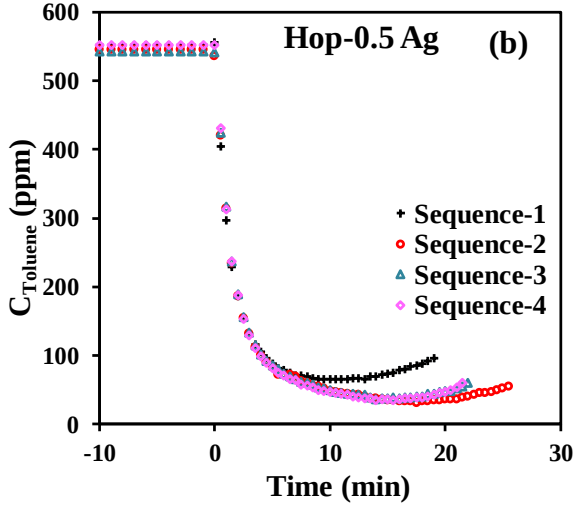
Hop-0.5 Ag
(b)
C Toluene (ppm)
Time (min)
Sequence-1
Sequence-2
Sequence-3
Sequence-4

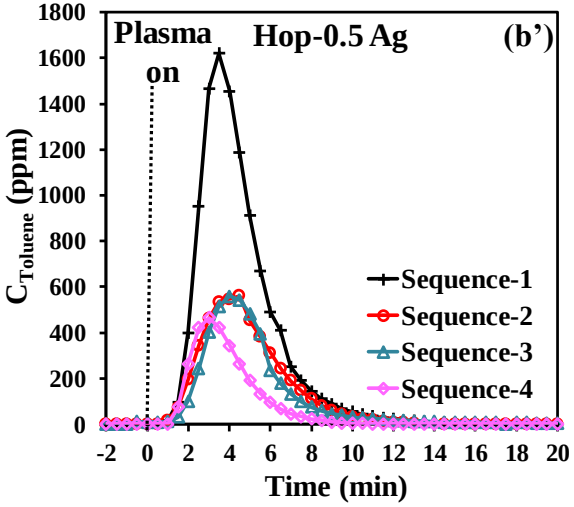
Plasma on
Hop-0.5 Ag
(b')
C Toluene (ppm)
Time (min)
Sequence-1
Sequence-2
Sequence-3
Sequence-4

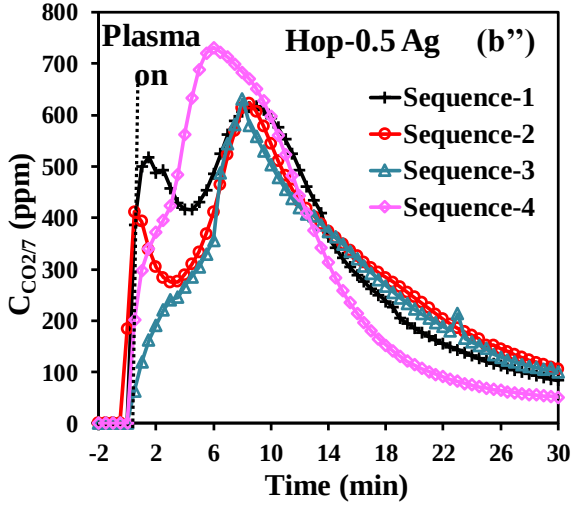
Plasma on
Hop-0.5 Ag
(b")
C CO2/7 (ppm)
Time (min)
Sequence-1
Sequence-2
Sequence-3
Sequence-4

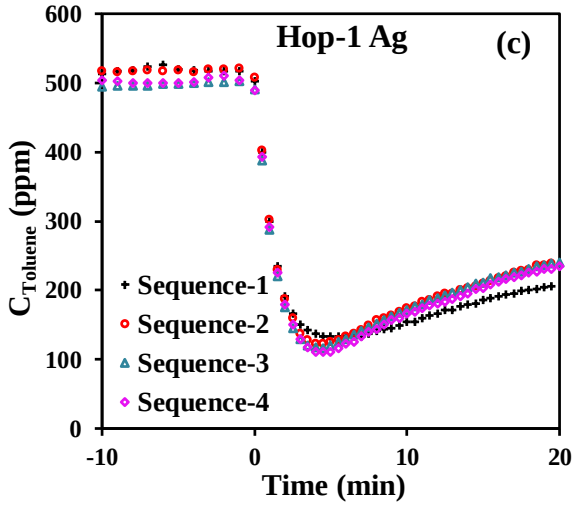
Hop-1 Ag
(c)
$C_{Toluene}$ (ppm)
Time (min)
Sequence-1
Sequence-2
Sequence-3
Sequence-4

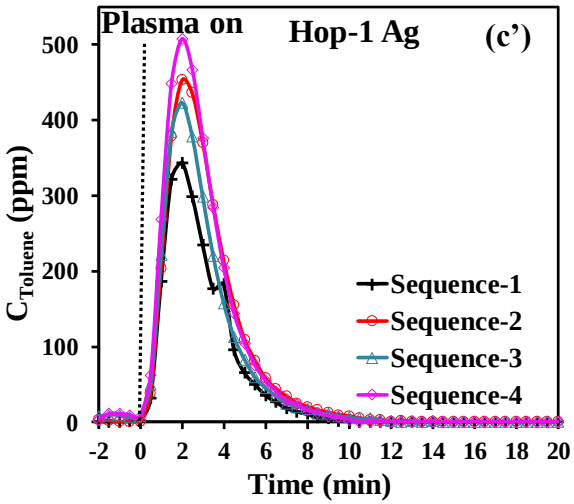
Plasma on
Hop-1 Ag
(c')
$C_{Toluene}$ (ppm)
Time (min)
Sequence-1
Sequence-2
Sequence-3
Sequence-4

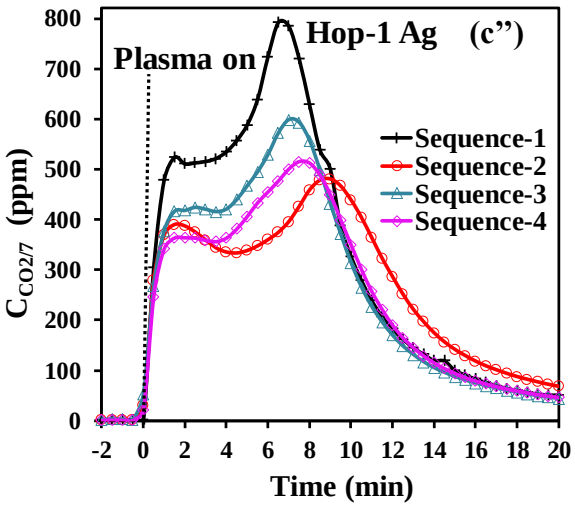
Plasma on
Hop-1 Ag
(c")
$C_{CO2/7}$ (ppm)
Time (min)
Sequence-1
Sequence-2
Sequence-3
Sequence-4

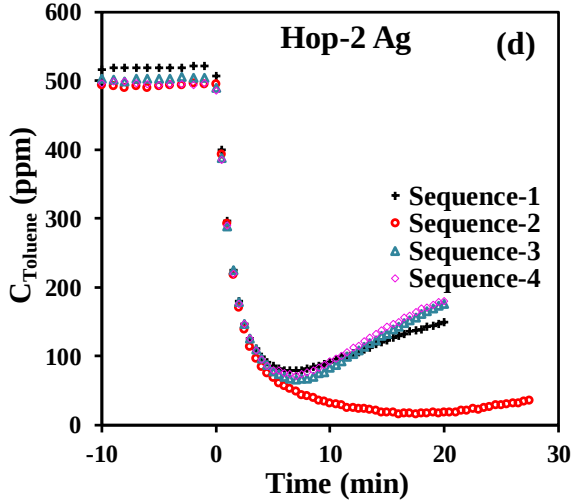
Hop-2 Ag
(d)
$C_{Toluene}$ (ppm)
Time (min)
Sequence-1
Sequence-2
Sequence-3
Sequence-4

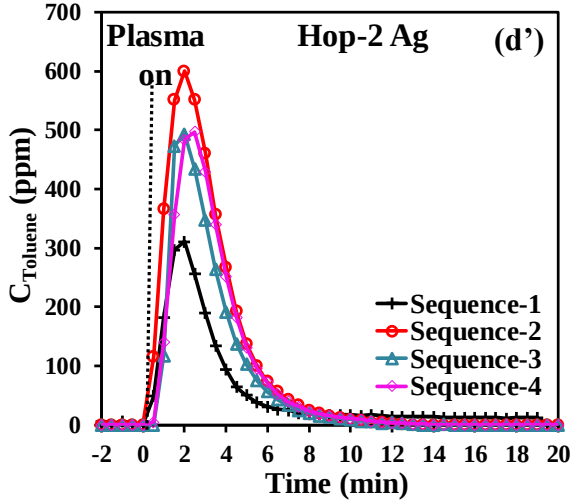
Plasma on
Hop-2 Ag
(d')
$C_{Toluene}$ (ppm)
Time (min)
Sequence-1
Sequence-2
Sequence-3
Sequence-4

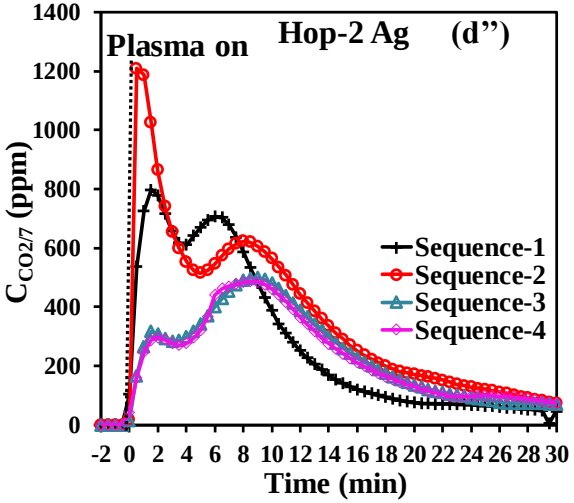
Plasma on
Hop-2 Ag
(d")
$C_{CO2/7}$ (ppm)
Time (min)
Sequence-1
Sequence-2
Sequence-3
Sequence-4

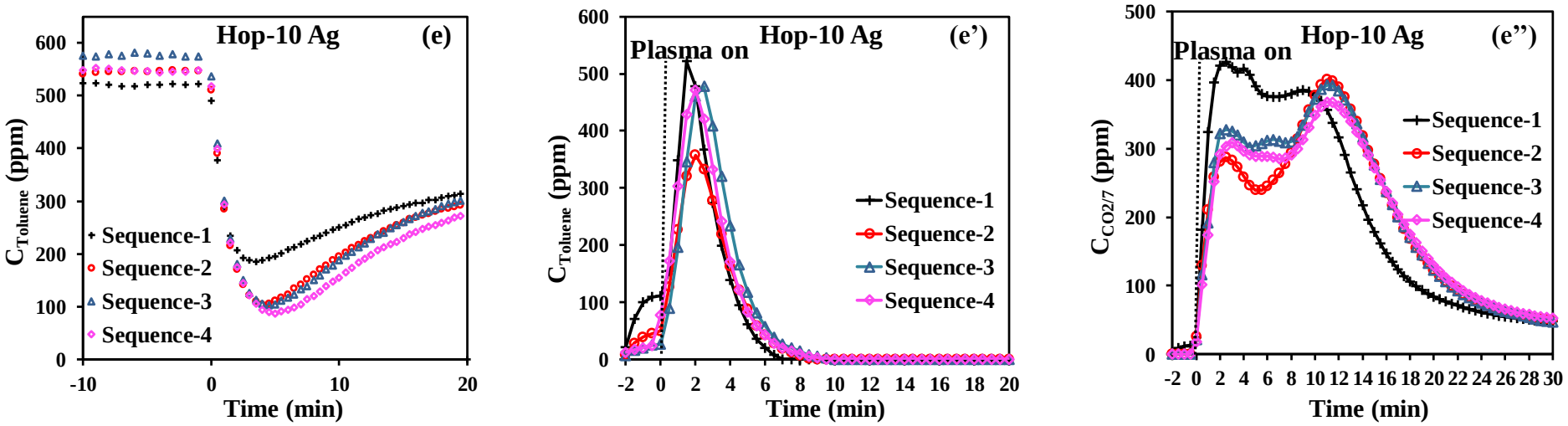

Figure 6.1. *Amount of toluene, desorbed Toluene (') and CO_2 evolution ('') profiles of (a) Hop, (b) Hop-0.5 Ag, (c) Hop-1 Ag, (d) Hop-2 Ag and (d) Hop-10 Ag.*

6.3.1.2 Effect of silver content on NTP oxidation

After the adsorption step, the NTP exposure step has been performed in air (RH ~ 3 %; 0.2 $L.min^{-1}$) at a discharge power of 46 W using a time span of 60 min. During NTP exposure, toluene, CO_2, N_2O, NO_2, NO, and H_2O are the only gaseous species detected for all materials at the outlet of the reactor by FT-IR, as shown in Figure 6.2. This work will only focus on the quantification of the desired end product (CO_2) as the quantification of H_2O, NO_2, and N_2O was not possible as the instrument was not calibrated for these species. Figure 6.2b represents an enlargement of the FT-IR spectrum (4 min of NTP exposure) of the effluent from the DBD reactor, which revealed the desorption of toluene at the beginning of the NTP discharge stage. To summarize, during the discharge stage, in addition to the desorption of reversibly adsorbed toluene molecules, an eventual break down of irreversibly adsorbed toluene into CO_2 and H_2O is observed. Interestingly, the formation of NOx species appears only after approx. 10 min of reaction and is observed continuously after 20 min. Thus, no or little NOx is produced during the CO_2 production supposedly because the oxidation active sites are occupied by adsorbed toluene. Once toluene is fully converted, these sites become active for N_2 oxidation. This feature opens the path for a significant reduction of NO_x production by adjusting the NTP discharge time to the minimum required for the combustion of adsorbed toluene and the regeneration of the catalyst.

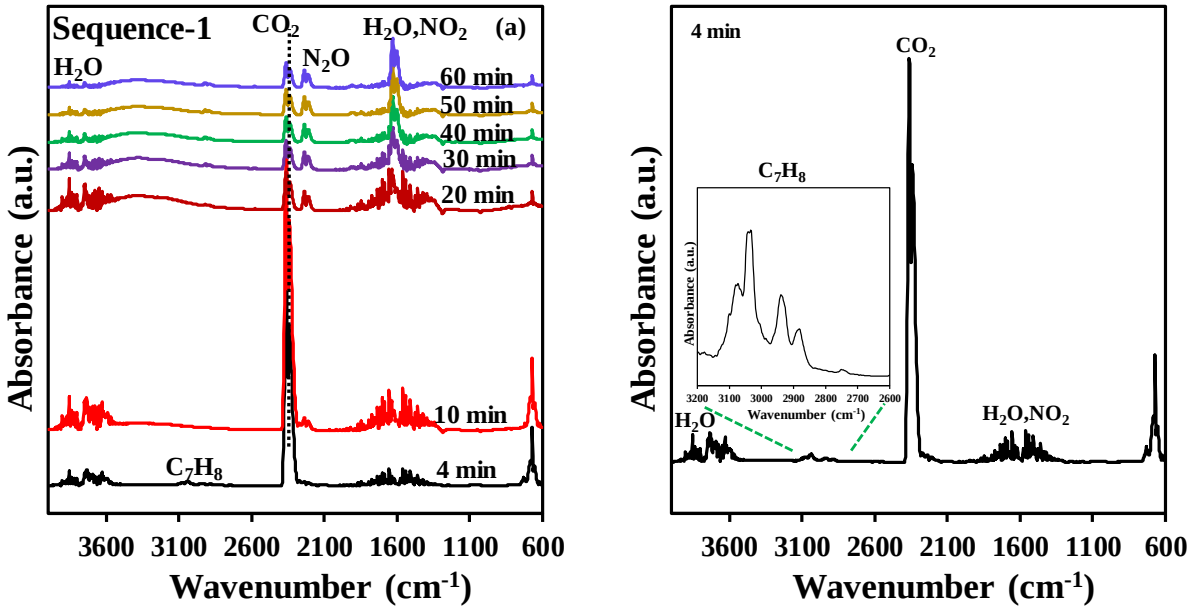

Figure 6.2. *Example of FT-IR spectra of the outlet gas at various times during plasma treatment (data collected for experiment using t1 = 20 min), (b) FT-IR spectrum at 4 min (inset: zoom within the 2600–3200 cm−1 range).*

Figures 6.1 display time evolution of the desorbed toluene (a', b', c', d', e') and produced CO_2 (a'', b'', c'', d'', e'') concentrations for all materials and the evolution of the pertinent parameters is given in Table 1. As shown in Figure 6.1, during NTP exposure, toluene desorbs as one desorption peak **for Hop** in each sequence. The transient desorption of toluene is short in time, and toluene maxima desorption are reached within 2 to 4.5 min of plasma exposure and gradually decreased to vanished after 12 min of plasma exposure. For all silver-containing materials, although the amount of the toluene desorbed is different from one another, a quite similar behavior of the toluene trace as a function of time is observed. For all materials, the desorbed amount of toluene varies from 3 to 10 µmol.g^{-1} whatever the sequence under concern (labelled as a "$q_{toluene\ unconverted}$", Table 6.1) with the exception for sequence 1 on sample Hop-0.5 Ag. Indeed, for this experiment, an unusual value of 21.3 µmol.g^{-1} of toluene is noticed. The difference between adsorbed toluene and unconverted toluene which is stated as "$q_{toluene\ converted}$" is in the range of 25 to 60 µmol.g^{-1}. The highest $q_{toluene\ converted}$ values of 50.1 and 59.4 for Hop 0.5 Ag and Hop 2 Ag resulting from the second adsorption are related to the high efficiency of the NTP regeneration to remove the adsorbed impurities presented at the surface of the material as already stated above.

By opposition, the transient production of CO_2 which is larger in time, takes place in two steps. The first maximum of CO_2 production is reached within 1.0 to 2.0 min and the second within 6.0 to 9.5 min of plasma exposure. After that, the CO_2 production gradually decreases to mostly disappears after 20-30 min of plasma exposure. The two-step CO_2 production can be related to the presence of **two different active sites on the surface** as postulated previously for the storage/thermal regeneration process. The first CO_2 production, more visible on Ag-loaded samples, which appears maximal for the first sequence could result from the efficient conversion of adsorbed toluene into CO_2 and from reactive desorption of some (hydrogeno)carbonates absorbed during air exposure of the samples prior to toluene abatement reactions into CO_2. In contrast, the CO_2 produced during the second step (slow step) seems less affected by the presence of Ag. From Table 6.1, it is shown that the CO_2 selectivity and CO_2 yields range between 85 % - 100 % and 70 % - 97 % during the cycling process. The CO_2 selectivity higher than 100 % observed at the end of the first sequence has been attributed to the decomposition of some adsorbed related (hydrogeno)carbonates at the surface of the materials as stated above. The slight SCO_2 decrease observed in the course of the following sequences may be due to the accumulation of some partially oxidized organic intermediates on the catalyst surface [239]. It is observed that at the end of the cycling process, taking into account the four sequences, that the CO_2 selectivity and CO_2 yields are always improved when adding silver. Among the silver containing materials, Hop-2 Ag exhibits the best CO_2 selectivity and CO_2 yield of ~ 100 % and 85 %, respectively, as compared to 81 % and 71 % for Hop. Figure 6.3 shows the carbon balances of the different catalysts after the different sequences. Regarding the last two sequences, the catalyst with the best carbon balance is Hop-2 Ag. For the last sequence, ~ 100 % of the total carbon balance is recovered with 85 % z

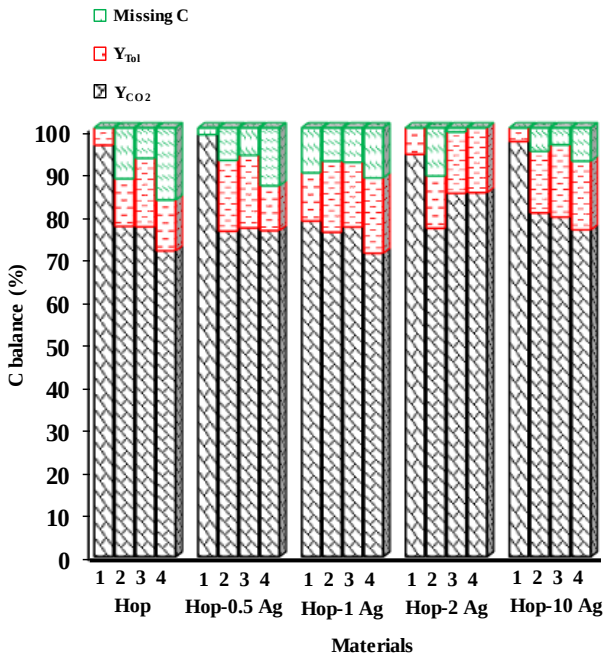

Figure 6.3. *Carbon balance of Hop and silver based Hop based materials for four APC sequences.*

The energetic performances of the APC process over Ag-based materials have been estimated (Table 6.1) for an EC (energy cost for purifying 1 m^3 of air) close to 11.6 $kWh \cdot m^{-3}$ in terms of $EY_{(Tol)}$ and $EY_{(CO2)}$ ($g \cdot kWh^{-1}$) which are the energy yields corresponding to the amount of energy spent (i) to decompose toluene, and (ii) to produce CO_2 (q_{CO2}), respectively.

After four sequences, the evolution of EY_{Tol} ($g_{Tol}.kW^{-1}h^{-1}$) is as follows : Hop-0.5 Ag (0.21) > **Hop** (0.18) > Hop-2 Ag (0.16) ~ Hop-10 Ag (0.16) ~ Hop-1 Ag (0.15) while the EY_{CO2} ($g_{CO2}.kW^{-1}h^{-1}$) decreases as follow : Hop-0.5 Ag (0.52) > Hop-2 Ag (0.46) > **Hop** (0.42) > Hop-10 Ag (0.40) > Hop-1 Ag (0.34) while. Overall, the removal of 1 g of toluene and the production of 1 g of CO_2 require less energy on Hop-0.5 Ag than on Hop. These results reveal that the introduction of low amount of Ag is beneficial in terms of energetic performances of the process.

6.3.2 Stability of Hop-1 Ag catalyst during plasma catalytic process

In APC process, it is very important to study the durability of material. For this, the behavior of Hop-1 Ag in APC has been investigated throughout nine sequences in the same conditions than reported above and the results are displayed in Figure 6.4. The amount of toluene

adsorption capacity is very similar at 38.2 ± 3 µmol·g^{-1} in the course of the sequence. During NTP exposure the amount of reversible adsorbed toluene is 6.5 ± 3 µmol·g^{-1} while that of CO_2 produced is 182.5 ± 14.5 µmol·g^{-1}. The NTP-assisted Hop-1 Ag material displays a SCO_2 and YCO_2 of 84 and 71 %.

Figure 6.5 shows the carbon balance after the different sequences for Hop-1 Ag. Regarding the last four sequences, 100 % of the total carbon balance recovered with 67 % from CO_2 and 15 % from desorbed toluene. It has to be noted that the FT-IR spectra show the characteristic bands corresponding to unconverted toluene, CO_2, H_2O, N_2O and NO_2. Taking into account the nine sequences it is found for an EC of 11.6 k.Wh.m^{-3} values of EY_{Tol} and EY_{CO2} in the range 0.14 (± 0.003) g_{Tolads}.kW^{-1}h^{-1} and 0.35 (±0.03) g_{CO2}.kW^{-1}.h^{-1}.

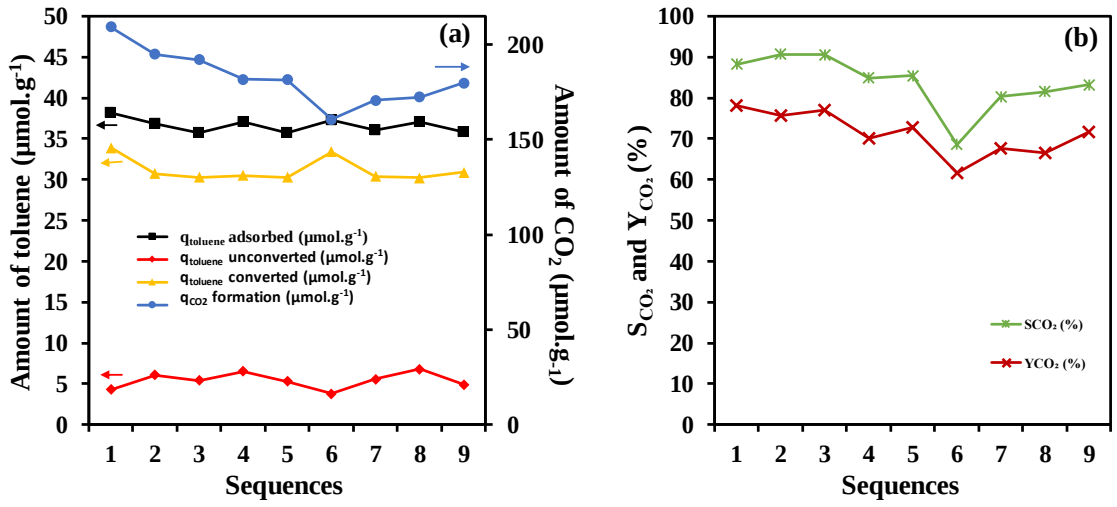

Figure 6.4. *Effect of adsorption-plasma cycle over Hop-1 Ag: (a) amount of toluene adsorbed, amount of toluene unconverted, amount of toluene converted and (b) selectivity and yield of CO_2.*

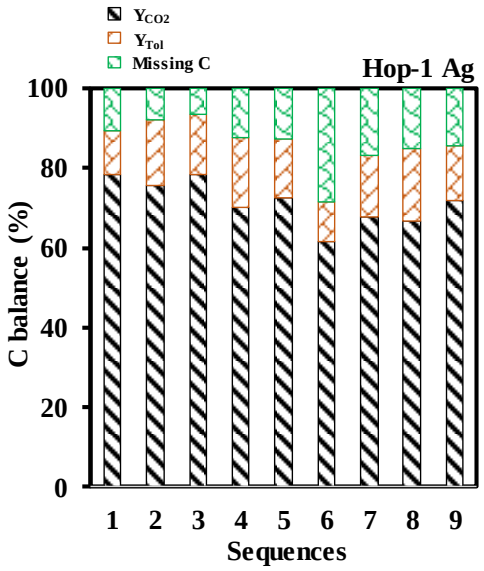

Figure 6.5. *Carbon balance of Hop-1 Ag during stability test.*

6.3.3 Characterization of the bi-functional materials after reaction

Figure 6.6 shows the XRD patterns of the used materials after APC which are characterized by a broad peak at 2θ of about 37°. It has to be noted that no crystallized phase appears in contrast to the previous study revealing the characteristic peaks of Mn_3O_4 in APC mode using Hopcalite [77]. The short duration of the storage stage adopted in this work as compared with those given in ref. [77] allows to minimize the release of heat which can induce phase transformation in the bulk material.

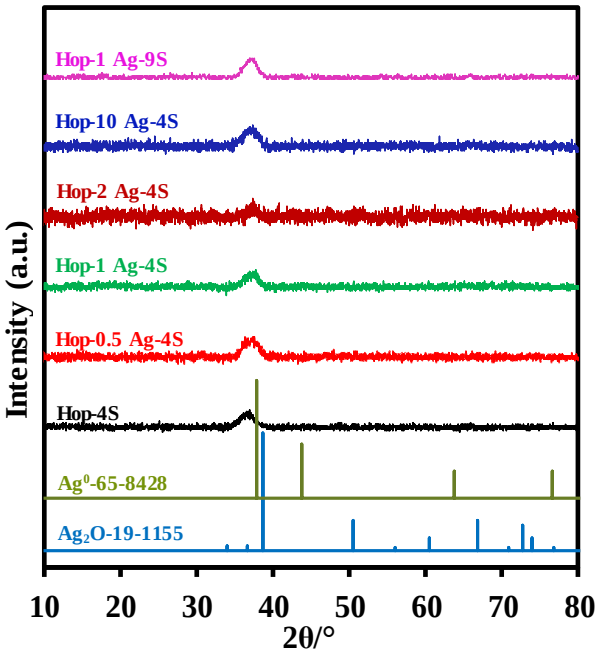

Figure 6.6. *XRD patterns of Hop and Hop-x Ag materials after four (4S) and nine (9S) adsorption-plasma sequences.*

The surface compositions of used materials were characterized by XPS (Figure 6.7 and Tables 6.2 and Table 6.3). Furthermore, no significant surface modifications in terms of the state and relative percentages of the different constitutive elements such as Ag, Cu, Mn, K and O have been observed. However, it should be noticed a significant increase of the S_{BET} for Hop-1 Ag after 9 sequences from 118 to 158 $m^2.g^{-1}$ indicating that the NTP treatment induces textural modifications allowing a partial recovery of the micropores which play an important role in the adsorption of toluene.

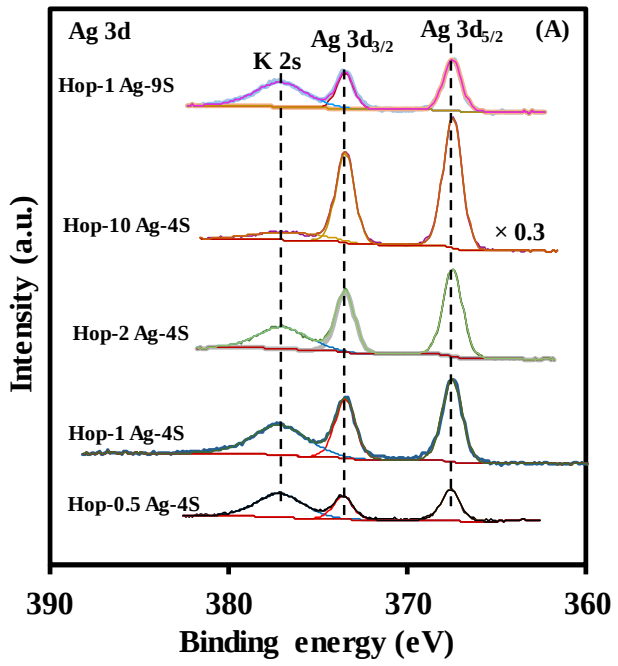
Ag 3d
K 2s
Ag 3d3/2
Ag 3d5/2
(A)
Hop-1 Ag-9S
Hop-10 Ag-4S
× 0.3
Hop-2 Ag-4S
Hop-1 Ag-4S
Hop-0.5 Ag-4S
Intensity (a.u.)
390
380
370
360
Binding energy (eV)

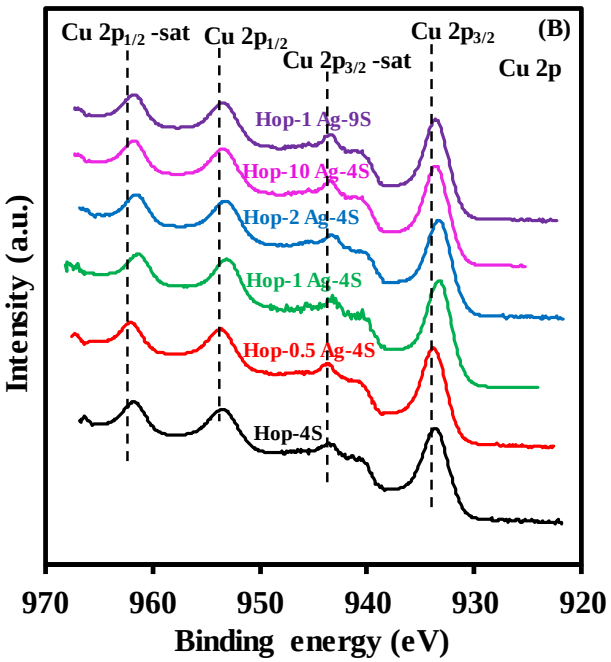
Cu 2p1/2 -sat
Cu 2p1/2
Cu 2p3/2 -sat
Cu 2p3/2
(B)
Cu 2p
Hop-1 Ag-9S
Hop-10 Ag-4S
Hop-2 Ag-4S
Hop-1 Ag-4S
Hop-0.5 Ag-4S
Hop-4S
Intensity (a.u.)
970
960
950
940
930
920
Binding energy (eV)

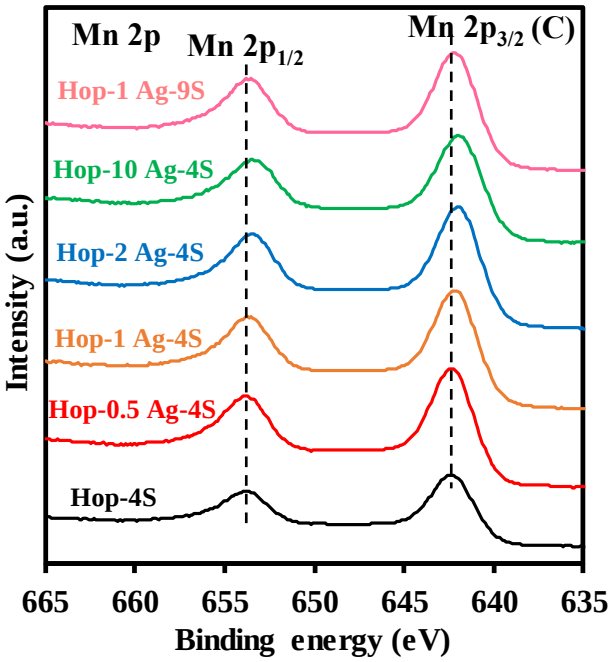
Mn 2p
Mn 2p1/2
Mn 2p3/2 (C)
Hop-1 Ag-9S
Hop-10 Ag-4S
Hop-2 Ag-4S
Hop-1 Ag-4S
Hop-0.5 Ag-4S
Hop-4S
Intensity (a.u.)
665
660
655
650
645
640
635
Binding energy (eV)

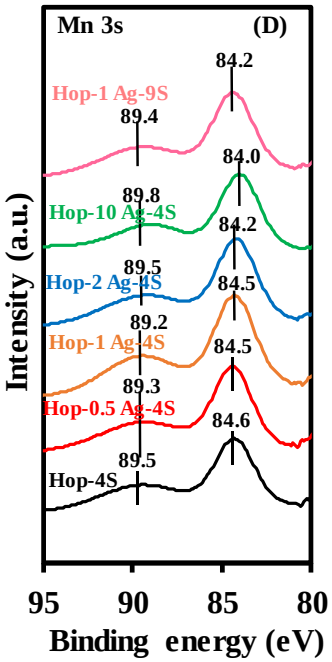
Mn 3s
(D)
Hop-1 Ag-9S
84.2
89.4
Hop-10 Ag-4S
84.0
89.8
Hop-2 Ag-4S
84.2
89.5
Hop-1 Ag-4S
84.5
89.2
Hop-0.5 Ag-4S
84.5
89.3
Hop-4S
84.6
89.5
Intensity (a.u.)
95
90
85
80
Binding energy (eV)

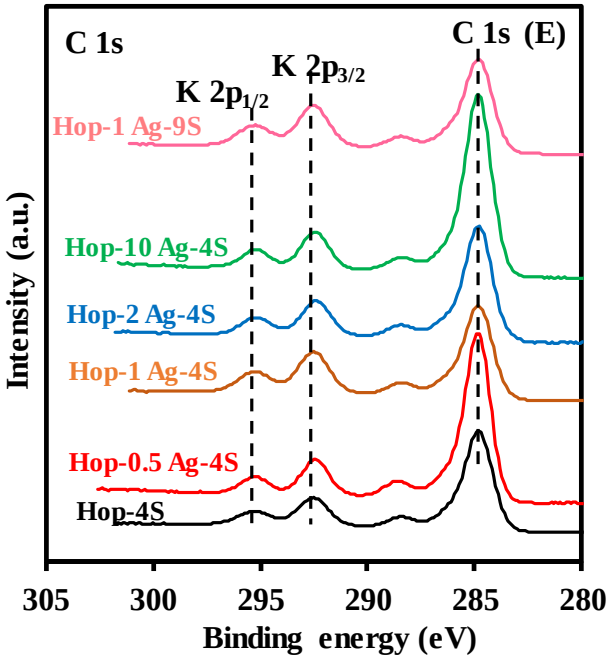

Figure 6.7. (A) Ag 3d, (B) Cu 2p, (C) Mn 2p, and (D) Mn 3s (E) C 1s core level spectra of Hop and Hop-x Ag materials after four (4S) and nine (9S) adsorption-plasma sequences.

Table 6.2. *XPS atomic ratios for Hop and Hop-x Ag after four (4S) and nine (9S) adsorption-plasma sequences.*

Material	Ag/Mn	Ag/Cu	Cu/Mn	K/Mn	O/Mn	ΔE (Mn AOS)
Hop	-	-	0.23	0.12	3.1	5.1 (3.1)
Hop-4S	-	-	0.29	0.13	3.7	5.2 (3.0)
Hop-0.5 Ag	0.02	0.12	0.20	0.12	2.7	5.3 (3.0)
Hop-0.5 Ag-4S	0.025	0.12	0.22	0.12	2.9	5.0 (3.3)
Hop-1 Ag	0.03	0.16	0.20	0.13	2.7	5.2 (3.1)
Hop-1 Ag-4S	0.032	0.14	0.23	0.14	3.0	5.1 (3.2)
Hop-1 Ag-9S	0.032	0.14	0.23	0.14	3.2	5.0 (3.2)
Hop-2 Ag	0.05	0.23	0.20	0.11	2.7	5.2 (3.1)
Hop-2 Ag-4S	0.043	0.19	0.22	0.13	3.0	5.1 (3.2)
Hop-10 Ag	0.16	0.78	0.21	0.14	3.0	4.9 (3.4)
Hop-10 Ag-4S	0.171	0.75	0.23	0.14	2.9	5.0 (3.3)

Table 6.3. *XPS analysis data for Hop and Hop-x Ag after four (4S) and nine (9S) adsorption-plasma sequences.*

Material	Peak position (eV)		
	Ag $3d_{5/2}$	**Cu $2p_{3/2}$**	**Mn $2p_{3/2}$**
Hop-4S	-	933.5	642.1
Hop-0.5 Ag-4S	367.6	933.7	642.2
Hop-1 Ag-4S	367.5	933.4	642.0
Hop-2 Ag-4S	367.5	933.3	642.1
Hop-10 Ag-4S	367.5	933.0	642.0
Hop-1 Ag-9S	367.5	933.4	642.0

6.4 Conclusion

Silver-containing Hopcalite bi-functional materials were investigated in APC mode (4 or 9 sequences) for the oxidation of high input concentration of toluene (~ 500 ppm) in the presence of moist air (RH ~ 3 %) using a PBDBD reactor filled with glass beads. APC experiments were carried out with a time span of about 20 min for the storage stage (t_1) and a delivered power (P) of 46 W. This procedure allows to get best performances in terms of CO_2 selectivity and yield, but also induces the least energy efficiency and the highest energy cost. Among the silver containing materials, Hop-2 Ag exhibits the best CO_2 selectivity and CO_2 yield of ~ 100 % and 85 %, respectively with ~ 100 % carbon recovery. By opposition, the removal of 1 g of toluene and the production of 1 g of CO_2 require less energy on Hop-0.5 Ag. Additionally, the repetition of the adsorption–oxidation process show that the performances are not affected by subsequent plasma treatments as could be confirmed by the characterization of the material after multiple APC sequences, which revealed no significant changes in catalyst properties. An important aspect of such optimization process will be the determination of the nature of the by-products in order to ensure that no other toxic products are formed. However, further work has to be done to reduce the plasma on time and thus enhance the overall efficiency of the process.

Chapter 7

General discussions, Conclusion and Perspectives

Chapter 7 General discussions, Conclusions and perspectives

7.1 General discussion

Last decades, several efficient volatile organic compounds (VOCs) removal technologies have been reported such as adsorption, absorption, condensation, catalytic oxidation, non-thermal plasma, biodegradation, photocatalysis and membrane separation. There are several reviews which highlight the advantages and drawbacks of these VOCs removal techniques [5]. The adsorption process is a simple passive method carried out at room temperature. Its performance depends on the nature of material but the main drawback is that the saturated adsorbents need to be regularly replaced and regenerated. Thus, the VOC pollution is essentially displaced from the air stream to subsequent processing. Similarly, catalytic oxidation has been demonstrated to be complete destruction of VOCs (low concentration) into CO_2 and H_2O [217]. This process has high removal efficiency but incomplete destruction may lead to formation of toxic by-products and consumes high energy by continuous heating of a large amount of gas containing only a small fraction of VOCs. On the other hand, non-thermal plasma (NTP) decomposition of VOC is deemed due to advantages such as operation at atmospheric pressure and room temperature and easy switch on/off [12]. Its main drawback is the lack of control on the selectivity of the process. The plasma-catalyst hybrid process features low-temperature operation and self-regeneration of catalysts. In this process plasma, plasma discharge occurs on the surface of catalyst surface can contribute to the activation of the catalyst. Such hybrid process can occur either in plasma catalysis and/or a post-plasma catalysis according to the position of the catalyst (in the plasma reactor or in series after the plasma reactor). In the in-plasma process, the catalyst can potentially influence the strength of discharge and enhances the oxidation of VOCs by offering extra adsorption sites which increases the residence time of VOCs in the discharge region and active sites for short-lived active species formed in the discharge region. These processes are generally continuous with a high energy cost.

The introduction of various hybrid technologies (such as adsorption+photocatalysis, adsorption+thermal/catalytic oxidation, adsorption+plasma, and photocatalysis+plasma) have emerged to complement one another.

The present thesis proposed to explore hybrid technologies such as sequential adsorption followed by thermal catalytic oxidation (ATC) and sequential adsorption followed plasma catalysis (APC) as an effective and promising method for toluene abatement. Such processes are indeed expected to combine the effectiveness of passive adsorption at low temperature and the efficiency of catalytic oxidation towards CO_2. It would also allow to regenerate the adsorbent in situ without need of discharging the system. Sequential and repetitive operation would allow to reduce the operating costs by tuning the regeneration duration with respect to the adsorption/storage step.

Both ATC and APC rely on the combination of adsorption and catalytic oxidation. Selection of the material depends strongly on the requirement of each step of the processes. For adsorption, materials (adsorbents) can possess a large surface area and a well-developed pore structure, such as active carbon, zeolite (HZSM-5, SBA-15, SBA-16), metal oxides, spinal, MOFs (Zr-MOF, Al-MIL-5, Al-MIL-53), and mesoporous silica. The adsorption performances also depend on surface chemical properties (surface of functional group). Although physical adsorption is simple, easily applicable, and economical, the regeneration remains challenging. Indeed, during regeneration process the pollutant may be released resulting in the production of harmful secondary pollution. Moreover, poor adsorption capacity is often observed due to presence of water who shows strong competitive adsorption properties. This is due to the physical nature of adsorption which is mostly unselective for abatement of VOCs. Therefore, the key requirement for this process is good adsorbent, regenerable, cost effective and elimination of secondary pollution particularly with cheap adsorbent such as activated carbon and concentrated regeneration technology, which is currently being used in various industries. In the perspective of sequential processes involving subsequent conversion of adsorbed species, strong and possibly irreversible adsorption of the pollutant is required.

For the catalytic oxidation step, the key requirement is catalyst efficiency in terms of pollutant conversion and selectivity to total oxidation. Stability, cost and environmental sustainability are other important criteria.

Combining adsorption and catalytic oxidation in a sequential process involves that the materials involved should possess optimal properties for both steps and support multiple repetitive

operations. The materials can therefore be defined as “bifunctional” and combine passive adsorption and active conversion properties.

In this research, Hopcalite (Purelyst 101MD), nanorod Ceria, and a sulfonic Zr-based metal organic framework (UiO-66-SO_3H) were chosen because of their unique characteristics that are potentially interesting for ATC and APC processes. The choice of these three materials was justified by the following reasons: Hopcalite ($CuMnO_x$), a cost-effective catalyst, consists of a mixture copper and manganese oxides. It is well known as an oxidation catalyst due to the formation of redox reaction such as reaction $Cu^{2+} + Mn^{3+} \rightleftarrows Cu^{+} + Mn^{4+}$ and the high adsorption of CO onto Cu^{2+}/Mn^{4+} and of O_2 onto Cu^{+}/Mn^{3+} [121]. Notably, it is highly active in the amorphous state, but losses its catalytic activity at high temperature (> 500°C) owing to the generation of crystallized phase [121]. Cerium oxide (CeO_2) is a catalyst or catalyst support in the field of three-way catalysis. It has unique redox properties of easy cycling between the Ce^{4+} and Ce^{3+} oxidation state. Provided high oxygen storage capacity is reached ceria a promising candidate for the catalytic oxidation reactions. The change in the morphology, size and shape of cerium oxide is known to promote catalytic activity. For example, ceria nanorods (CeO_2-NR) exposing surface (110) and (100) planes exhibit enhanced catalytic properties in CO oxidation [161]. On the other hand, the metal organic frameworks (MOF) such as UiO-66-SO_3H was selected due to its tunable structures, large surface areas and multifunctional properties for various applications such as adsorption, catalytic oxidation, and photocatalysis. It is a good alternative to zeolite and active carbons in adsorption technologies.

At initial state of study, the materials have been tested for the conventional catalytic oxidation of toluene. Among them, Hopcalite exhibits the best specific activity in terms of temperature required to achieve 10 %, 50 % and 90 % of toluene conversion into CO_2. The mesoporosity, amorphous state and easy cycling between Mn and Cu different oxidation states leads to this finding. Ceria is significantly less active as T_{50} of 321°C is higher than that of Hopcalite (185 °C). The lower amount of the surface to bulk oxygen vacancy ratio led to the poor performance as compared to the literature. Moreover, no catalytic activity of UiO-66-SO_3H has been observed due to lack of redox properties. The carbon balance confirms that toluene is trapped inside the UiO-66-SO_3H structure (Chapter 3). This finding reveals that Hopcalite stand as an outstanding candidate among three of catalysts.

Furthermore, Hopcalite has been chosen for the investigation of the dynamic behavior during adsorption of toluene. Breakthrough adsorption tests were performed with different initial concentrations of toluene ranging from 50-500 ppm (Chapter 3). At high concentration of toluene, the adsorption of toluene is fast. The time during which total adsorption occurs (full breakthrough curve) is very short and does not significantly depend on toluene inlet concentration. A similar total adsorption capacity is found (379-392 $\mu mol.g^{-1}$). This finding may be due to the enhancement of driving force for mass transfer along with the increasing adsorption rate which helps to reach fast saturation of the adsorbent [213]. This result is consistent with Veerapandian et al. finding of total toluene adsorption (Toluene initial concentration = 500 ppm) on Hopcalite [77]. In case of 100 ppm, adsorption process is much slower and for 50 ppm toluene feed, no toluene was detected for a long period and after that saturation occurred suddenly (Chapter 3). At lower toluene feed concertation, adsorption can occur directly inside the mesoporous structure. Such difference is also observed during desorption at room temperature and during heating in helium. For 100 ppm, low amount of toluene desorbed as compared to high concentration toluene study. But high amount of toluene desorbed during the heating, thus indicating stronger interaction between the adsorbent and toluene. Only CO_2 formation took place during the ATC process which proved that selectivity of Hopcalite towards total oxidation is high. In case of lower toluene concentration study the CO_2 formation take place at low temperature (110-120 °C) and for high toluene concentration 150 °C temperature is needed. This suggest that irreversible adsorption of toluene (no desorption at room temperature or during heating) is favorized by low concentration of toluene. This is due to a well distribution of toluene molecules on the surface of Hopcalite and also due to slower irreversible adsorption.

The full breakthrough study detailed above is useful in determining the adsorption properties of this material. However, adsorption capacities determined through this method are not directly useful for the abatement of pollutants. In real process, the concentration of toluene at the outlet of the system need to remain under acceptable limits meaning that the adsorption process would need to be stopped when a given threshold is reached as illustrated in Figure 7.1. The amount of toluene adsorbed when this limit is reached has been defined as a “useful adsorption capacity”. In the case of Hopcalite, this resulted in a useful adsorption capacity approximately 3 to 4 times lower than the total adsorption capacity determined considering the full breakthrough curve. This illustrates

the difficulty in determining optimal adsorption conditions and limits as these will depend considerably on the actual threshold that will be imposed e.g., by environmental regulations.

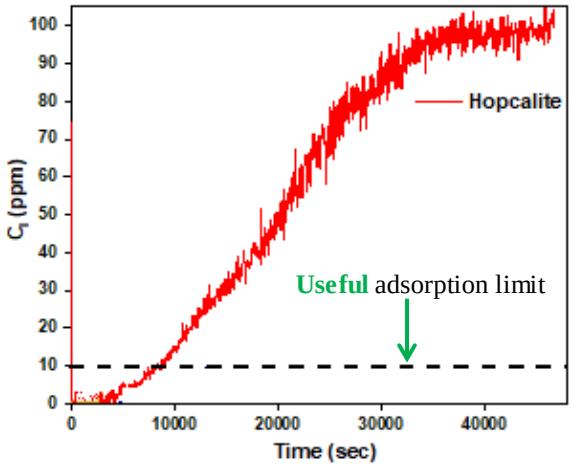

Figure 7.1. *Adsorption behaviour of Hopcalite at different conditions.*

MOF material (UiO-66-SO_3H) proved to have the highest useful adsorption capacity (315 µmol.g^{-1}), as could be expected considering its high specific surface area, followed by Hopcalite (108 µmol.g^{-1}) and Ceria (51 µmol.g^{-1}). The efficiency towards oxidation of adsorbed toluene did, however, follow a very different order. In this overall process, Hopcalite stands out as the best candidate in terms of CO_2 yield which reaches to 92.3 %. Surprisingly, CeO_2-NR produced significantly lower yield in CO_2 than Hopcalite. UiO-66-SO_3H also showed very scares efficiency in conversion of adsorbed toluene in CO_2 (< 15 %) as most desorbed during the thermal treatment. This clearly illustrates the importance of the quality of adsorption with respect to its amount.

Limiting the amount of toluene adsorbed to the so-called "useful capacity" will have a negative impact on the economic aspects of this process as it forces to reduce the adsorption time and increase the frequency of regeneration steps. On the other hand, the efficiency of the process is improved in term of yield towards CO_2 production as large amount of toluene desorption (at room temperature of during regeneration) can be avoided. Indeed, the negative effect of increasing amount of adsorbed toluene on the efficiency of oxidation to CO_2 on Hopcalite could be observed in both ATC and APC as illustrated in Figure 7.2.

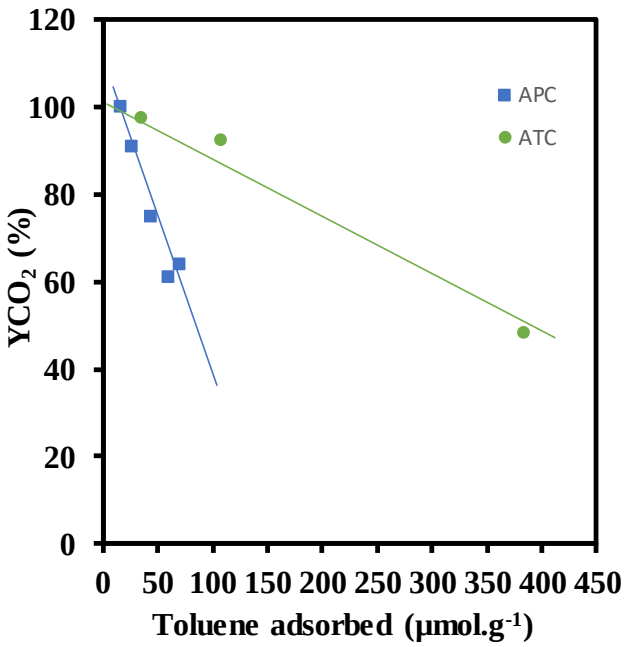

Figure 7.2. *Comparison of CO_2 yield as a function of amount of toluene adsorbed resulting from experiments with various adsorption durations during ATC (initial toluene concentration = 100 ppm, flow rate = 0.1 L.min^{-1}) and APC (initial toluene concentration = 500 ppm) processes.*

One can observe from Figure 7.2 that the negative effect of the increase of amount of adsorbed toluene on the efficiency of the process is more important in the case of APC. This is mostly due to the very rapid desorption of toluene which occur when the plasma is switched on. Although the time on stream is longer, the progressive heating process used in ATC seems more favorable to avoid massive desorption of toluene. This is an important aspect which need to be considered in the development of a process based on this concept. A rapid heating process would certainly be more favorable on economic point of view but could constitute a drawback in terms of depollution efficiency.

Based on literature, for the improvement of catalytic activity, various catalyst system based on noble metals (Ag, Au, Pd and Pt) have been intensively studied for the removal of toluene. It is well known that noble metal catalysts, have relatively high catalytic activity but their use is limited by their high cost. Silver is the less expensive noble metal and a highly active component, especially for toluene oxidation. According to the London Metal Exchange as of May 2021, the costs of palladium and platinum are respectively 100 and 41 times higher than of silver. By considering the known properties of silver in oxidation, it was chosen in order to enhance the

catalytic properties of Hopcalite. Samples with varying amount of silver (0.5, 1, 2 and 10 wt.%) were prepared by wet aqueous impregnation method and tested both in ATC (Chapter 4) and APC (Chapter 6).

It was found that except Hop-10 Ag, other Ag-containing materials display similar adsorption capacity than that of Hop.This could be explained by the Ag^+ active sites can undergo electrostatic interaction between aromatic ring (toluene) and Ag^+.

From the increase of interactions between adsorbed toluene and the surface due to Ag addition, one could have expected better performances in the subsequent oxidation process. On the contrary, slight diminution of the yield in CO_2 was observed both in ATC and APC according to the amount of Ag introduced. This is illustrated in Figure 7.3.

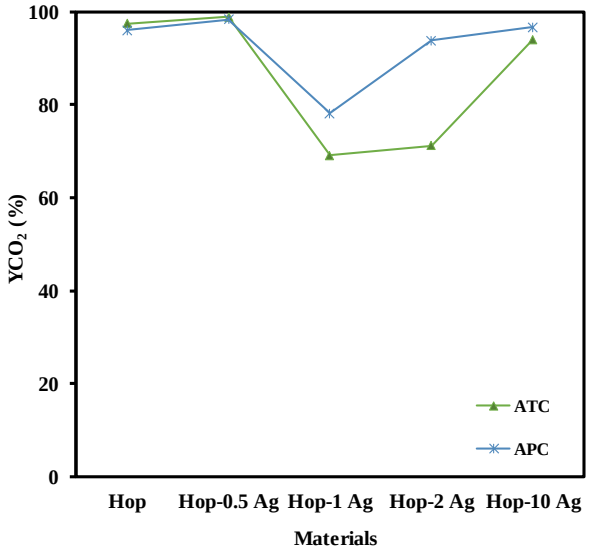

Figure 7.3. *Comparison of CO_2 yield over silver based Hopcalite materials in ATC (initial toluene concentration = 100 ppm, adsorption duration = 35 min, flow rate = 0.1 L.min^{-1}) and APC (initial toluene concentration = 500 ppm, adsorption duration = 20 min, flow rate = 0.1 L.min^{-1} in sequence 1) processes.*

The loss in CO_2 yield in 1 wt.% and 2 wt. % loading of silver was correlated to the appearance of CO_2 at low temperature (in ATC) or its increase at very short time after plasma ignition (in APC). This could be due to the presence of highly active surface species. This low temperature/rapid reactivity may generate supplementary heat in the system through the

exothermic combustion of toluene which in turn provokes the desorption of significantly higher amounts of toluene. Thus, instead of being favorable to the overall process, this increased reactivity results to be detrimental.

This constitutes an important learning from this work and illustrates the difficult balance that needs to be found between high adsorption capacity and reactivity of the materials.

However, a positive aspect however is that Hopcalite and silver based Hopcalite has proved to be very stable in such sequential processes, both ATC and APC. Indeed, repetitive operations have been performed and thorough characterizations have confirmed the robustness of these materials.

One of the objectives of sequential processes in place of continuous ones, is to avoid constant energy supply to the system. Major economic benefit would be obtained by increasing the adsorption step duration and reducing that of the regeneration one. Furthermore, the energy input during the regeneration step can also be optimized.

In this work, the thermal oxidation was explored using temperature programmed heating of the reactor. This heating mode is necessary to well understand the influence of experimental parameters or material composition but is not adequate for an industrial process. In a more realistic approach, rapid heating towards the optimal regeneration temperature will need to be obtained. This optimal temperature will be strongly dependent on the nature of the material and eventual promotion. This could be seen through the addition of silver on Hopcalite which indeed allow to significantly lower the peak of toluene oxidation to around 150 °C instead of approx. 200 °C for bare Hopcalite when 0.5 wt.% silver is introduced. One should however underline than such benefit is rapidly lost by increasing the amount of silver due to very low temperature reactivity which can cause the desorption of some toluene and thus reduce the efficiency of the system. This demonstrates the very delicate balance that needs to be found in such intrinsically transient process.

In the case of the use of plasma to activate and regenerate the materials, the energy saving can be obtained by fine tuning the power and duration of the regeneration step. Interestingly, high power input does not improve the overall efficiency of the conversion of toluene. Even considering the more rapid combustion of adsorbed toluene (Chapter 5) this does not counterbalance the lesser CO_2 production making the process less energy efficient. This opens the path to further optimization of this important step.

7.2 Conclusions and Perspectives

The concept of "storage-regeneration" cycling is proposed in this research study as an effective and promising way to eliminate low-concentration toluene when compared to other approaches for toluene removal. A key point in this approach is the design and/ or choice of material which should possess balanced properties between storage and regeneration. If the material plays individual role in both hybrid process, then another property can be generated by introducing an active phase. Mainly, the material should not only possess high and selective toluene storage capacity but also be easily regenerated without any release of the toluene or generation of hazardous secondary pollutants. For the regeneration of material, two process have been proposed such as thermal oxidation and plasma oxidation.

Initially, three materials have been considered to be integrated in sequential processes: Hopcalite, Ceria-NR and UiO-66-SO_3H. The properties of these solids have indeed been studied for the sequential adsorption followed by thermal activation giving important inputs of the requirements of materials for such process. Unfortunately, due to the fine powder structure of Ceria-NR and UiO-66-SO_3H, it was not possible to generate a stable plasma using these materials when using plasma assisted regeneration instead of thermal. For this reason, the APC study focused essentially on Hopcalite.

The study of toluene adsorption on these materials has been performed in different condition such as full breakthrough study or by performing adsorption considering a threshold value (e.g. 10 ppm) for toluene outlet concentration. This allowed to introduce the concept of useful adsorption capacity which is more in line with realistic depollution conditions.

For the regeneration through thermal oxidation, temperature programmed heating was used which permitted to study the behavior and characteristic of materials. The results demonstrated the need for highly active materials showing strong redox properties. However, they also underline the delicate balance that needs to be found to avoid toluene desorption at low temperature which undermine the overall efficiency of the process. Further work is necessary in this field and should focus on the dynamics of the heating process. Clearly, temperature programmed heating is not feasible in a real depollution system due to its duration. Rapid heating solutions, e.g. by induction, should be explored.

The regeneration through plasma activation is very promising in this respect. Low temperature and rapid regeneration are clearly the advantages of this activation process with respect to thermal oxidation. Hopcalite resulted to be a very good candidate for this purpose by showing remarkable efficiency in toluene adsorption and combustion but also in term of stability and repeatability. Other materials could not be explored due to the fine nature of the powders underlining an important drawback of plasma activation in DBD systems i.e. the necessary shaping of the materials. Although this is a difficult task, shaping of powders, or eventual coating on shaped materials offer a great opportunity to further optimize the performances of such adsorption/plasma catalytic sequential process.

This pioneering study of toluene abatement in sequential processes (adsorption-thermal oxidation and adsorption-plasma catalysis) concludes that the process is technically feasible at the laboratory scale and that a potential catalyst for this process could be proposed. Obviously, more detailed investigation is required for further optimization of these hybrid processes. Other materials may be considered such as zeolites, monoliths, mixed oxides, MOFs. In depth analysis of the dynamic behavior, including transient kinetic approach should also be investigated to optimize the combustion reaction versus desorption process and/or oxidation to undesired by products. Also, to better consider real depollution conditions, the presence of humidity should be considered as it can be expected that water vapor may influence both the adsorption step (competitive adsorption) and the selectivity of the oxidation step, both in thermal or plasma oxidation.

One of the most important challenge will then remain the upscaling of these sequential processes towards real depollution systems. In thermal oxidation this will involve innovative rapid heating systems such as inductive heating. In both cases, thermal and plasma catalysis, materials shaping will be essential as it will impact the efficiency of the heating process and that of the plasma generation.

References

[1] H.A. E.Gakidou, A. Afshin, A.A. Abajobir, K.H. Abate, C. Abbafati, K.M. Abbas, F. Abd-Allah, A.M. Abdulle, S.F. Abera, V. Aboyans, L.J. Abu-Raddad, N.M.E. Abu-Rmeileh, G.Y. Abyu, I.A. Adedeji, O. Adetokunboh, M. Afarideh, A. Agrawal, S. Agrawal, Lancet 386 (2015) 2287–2323.

[2] T.V. Dinh, I.Y. Choi, Y.S. Son, K.Y. Song, Y. Sunwoo, J.C. Kim, J. Environ. Manage. 168 (2016) 157–164.

[3] G. Liu, J. Ji, H. Huang, R. Xie, Q. Feng, Y. Shu, Y. Zhan, R. Fang, M. He, S. Liu, X. Ye, D.Y.C. Leung, Chem. Eng. J. 324 (2017) 44–50.

[4] L. Zhu, D. Shen, K.H. Luo, J. Hazard. Mater. 389 (2020) 122102.

[5] X. Li, L. Zhang, Z. Yang, P. Wang, Y. Yan, J. Ran, Sep. Purif. Technol. 235 (2020) 116213.

[6] C. Yang, G. Miao, Y. Pi, Q. Xia, J. Wu, Z. Li, J. Xiao, Chem. Eng. J. 370 (2019) 1128–1153.

[7] S. Alejandro-Martín, H. Valdés, M.H. Manero, C.A. Zaror, Catalysts 8 (2018).

[8] J. Kim, B.K. Lee, Process Saf. Environ. Prot. 119 (2018) 164–171.

[9] W.K. Jo, C.H. Yang, Sep. Purif. Technol. 66 (2009) 438–442.

[10] E.F. Mohamed, G. Awad, C. Andriantsiferana, A.I. El-Diwany, Environ. Technol. (United Kingdom) 37 (2016) 1197–1207.

[11] Y. Lu, J. Liu, B. Lu, A. Jiang, C. Wan, J. Hazard. Mater. 182 (2010) 204–209.

[12] S. Sultana, A. Vandenbroucke, C. Leys, N. De Geyter, R. Morent, Catalysts 5 (2015) 718–746.

[13] A. Luengas, A. Barona, C. Hort, G. Gallastegui, V. Platel, A. Elias, Rev. Environ. Sci. Biotechnol. 14 (2015) 499–522.

[14] F. Heymes, P. Manno-Demoustier, F. Charbit, J.L. Fanlo, P. Moulin, Chem. Eng. J. 115 (2006) 225–231.

[15] Y. hsin Shih, M. syue Li, J. Hazard. Mater. 154 (2008) 21–28.

[16] B. Belaissaoui, Y. Le Moullec, E. Favre, Energy 95 (2016) 291–302.

[17] H. Zhen, S.M.J. Jang, W.K. Teo, K. Li, J. Appl. Polym. Sci. 99 (2006) 2497–2503.

[18] X. Zhang, B. Gao, A.E. Creamer, C. Cao, Y. Li, J. Hazard. Mater. 338 (2017) 102–123.

[19] N. Jiang, R. Shang, S.G.J. Heijman, L.C. Rietveld, Water Res. 144 (2018) 145–161.

[20] V. Demidiouk, S.I. Moon, J.O. Chae, 4 (2003) 51–56.

[21] Y. Guo, X. Liao, J. He, W. Ou, D. Ye, Catal. Today 153 (2010) 176–183.

[22] M. Bahri, F. Haghighat, Clean-Soil Air Water 42 (2014) 1667–1680.

[23] A.H. Khoshakhlagh, M. Beygzadeh, F. Golbabaei, Z. Saadati, Env. Sci Pollut Res Mater. (2020).

[24] H.L. Jiang, Q. Xu, Chem. Commun. 47 (2011) 3351–3370.

[25] M. Seredych, E. Deliyanni, T.J. Bandosz, Fuel 89 (2010) 1499–1507.

[26] C.O. Ania, T.J. Bandosz, Langmuir 21 (2005) 7752–7759.

[27] A. Samokhvalov, B.J. Tatarchuk, Catal. Rev. - Sci. Eng. 52 (2010) 381–410.

[28] Y. Shu, Y. Xu, H. Huang, J. Ji, S. Liang, M. Wu, D.Y.C. Leung, Chemosphere 208 (2018) 550–558.

[29] J. Eun, Y. Sik, D.C.W. Tsang, J. Song, S. Jung, Y. Park, Sci. Total Environ. 719 (2020) 137405.

[30] P. Papaefthimiou, T. Ioannides, X.E. Verykios, Appl. Therm. Eng. 18 (1998) 1005–1012.

[31] P.O. Larsson, A. Andersson, J. Catal. 179 (1998) 72–89.
[32] S.A.C. Carabineiro, X. Chen, O. Martynyuk, N. Bogdanchikova, M. Avalos-Borja, A. Pestryakov, P.B. Tavares, J.J.M. Órfão, M.F.R. Pereira, J.L. Figueiredo, Catal. Today 244 (2015) 103–114.
[33] J.J. Spivey, Ind. Eng. Chem. Res. 26 (1987) 2165–2180.
[34] Y. Lyu, C. Li, L.S. Du Xueyu, Zhu Youcai, Zhang Yindi, Environ. Sci. Pollut. Res. 27 (2020) 2482–2501.
[35] M. Schiavon, V. Torretta, A. Casazza, M. Ragazzi, Water. Air. Soil Pollut. 228 (2017).
[36] M. Ragazzi, P. Tosi, E.C. Rada, V. Torretta, M. Schiavon, Waste Manag. 34 (2014) 2400–2406.
[37] A.M. Vandenbroucke, M. Mora, C. Jiménez-Sanchidrián, F.J. Romero-Salguero, N. De Geyter, C. Leys, R. Morent, Appl. Catal. B Environ. 156–157 (2014) 94–100.
[38] M.T.N. Dinh, J.M. Giraudon, J.F. Lamonier, A. Vandenbroucke, N. De Geyter, C. Leys, R. Morent, Appl. Catal. B Environ. 147 (2014) 904–911.
[39] A.A. Assadi, J. Palau, A. Bouzaza, J. Penya-Roja, V. Martinez-Soriac, D. Wolbert, J. Photochem. Photobiol. A Chem. 282 (2014) 1–8.
[40] T. Ohshima, T. Kondo, N. Kitajima, M. Sato, IEEE Trans. Ind. Appl. 46 (2010) 23–28.
[41] Z. Ye, Z. Ye, A. Nikiforov, J. Chen, W. Zhou, J. Chen, G. Wang, Y. Zhang, Chem. Eng. J. 407 (2021) 126280.
[42] B. Chen, L. Wu, B. Wu, Z. Wang, L. Yu, M. Crocker, A. Zhu, C. Shi, ChemCatChem 11 (2019) 3646–3661.
[43] W. Xu, X. Xu, J. Wu, M. Fu, L. Chen, N. Wang, H. Xiao, X. Chen, D. Ye, RSC Adv. 6 (2016) 104104–104111.
[44] J. Reungoat, J.S. Pic, M.H. Manro, H. Debellefontaine, Sep. Sci. Technol. 42 (2007) 1447–1463.
[45] M. Guillemot, J. Mijoin, S. Mignard, P. Magnoux, Appl. Catal. B Environ. 75 (2007) 249–255.
[46] H.H. Kim, Y. Teramoto, N. Negishi, A. Ogata, Catal. Today 256 (2015) 13–22.
[47] F. Holzer, U. Roland, F.D. Kopinke, Appl. Catal. B Environ. 38 (2002) 163–181.
[48] X. Feng, H. Liu, C. He, Z. Shen, T. Wang, Catal. Sci. Technol. 8 (2018) 936–954.
[49] T. Zhu, J. Li, W. Liang, Y. Jin, J. Hazard. Mater. 165 (2009) 1258–1260.
[50] E.C. Neyts, A. Bogaerts, J. Phys. D. Appl. Phys. 47 (2014) 224010.
[51] E.C. Neyts, K. Ostrikov, M.K. Sunkara, A. Bogaerts, Chem. Rev. 115 (2015) 13408–13446.
[52] A. Bogaerts, X. Tu, J.C. Whitehead, G. Centi, L. Lefferts, O. Guaitella, F. Azzolina-Jury, H.H. Kim, A.B. Murphy, W.F. Schneider, T. Nozaki, J.C. Hicks, A. Rousseau, F. Thevenet, A. Khacef, M. Carreon, J. Phys. D. Appl. Phys. 53 (2020) 443001.
[53] A. Ogata, N. Shintani, K. Mizuno, S. Kushiyama, T. Yamamoto, 35 (1999) 753–759.
[54] A. Ogata, K. Yamanouchi, K. Mizuno, S. Kushiyama, T. Yamamoto, Plasma Chem Plasma Process 19 (1999) 383–394.
[55] B.S. Furniss, a J. Hannaford, P.W.G. Smith, a R. Tatchell, J. Polym. Sci. Part A Polym. Chem. 29 (1989) 1223–1223.
[56] H.C. Genuino, S. Dharmarathna, E.C. Njagi, M.C. Mei, S.L. Suib, J. Phys. Chem. C 116 (2012) 12066–12078.
[57] (n.d.).
[58] H.R. Omran, S.M. EL-Marsafy, F.H. Ashour, E.F. Abadir, Egypt. J. Pet. 26 (2017) 855–

863.
[59] Z. Abbas, W. Qamar, Z. Muhammad, D. Ali, Res. Chem. Intermed. (2021).
[60] Agency for Toxic Substances and Disease Registry (ATSDR), U.S. Public Heal. Serv. U.S. Dep. Heal. Hum. Serv. (2000) 357.
[61] T. Hobara, M. Okuda, M. Gotoh, K. Oki, H. Segawa, I. Kunitsugu, Ind. Health 38 (2000) 228–231.
[62] R. Huang, M. Lu, P. Wang, Y. Chen, J. Wu, M. Fu, L. Chen, D. Ye, RSC Adv. 5 (2015) 72113–72120.
[63] X. Xu, P. Wang, W. Xu, J. Wu, L. Chen, M. Fu, D. Ye, Chem. Eng. J. 283 (2016) 276–284.
[64] H. Yi, X. Yang, X. Tang, S. Zhao, J. Wang, X. Cui, T. Feng, Y. Ma, J. Chem. Technol. Biotechnol. 92 (2017) 2276–2286.
[65] Y.S. Mok, D.H. Kim, Curr. Appl. Phys. 11 (2011) S58–S62.
[66] J.S. Youn, J. Bae, S. Park, Y.K. Park, Catal. Commun. 113 (2018) 36–40.
[67] H. Yi, X. Yang, X. Tang, S. Zhao, Plasma Chem. Plasma Process. 38 (2018) 331–345.
[68] X. Dang, C. Qin, J. Huang, J. Teng, X. Huang, J. Ind. Eng. Chem. 37 (2016) 366–371.
[69] C. Qin, X. Huang, J. Zhao, J. Huang, Z. Kang, X. Dang, J. Hazard. Mater. 334 (2017) 29–38.
[70] C. Qin, X. Huang, X. Dang, J. Huang, J. Teng, Z. Kang, Chemosphere 162 (2016) 125–130.
[71] W. Wang, H. Wang, T. Zhu, X. Fan, J. Hazard. Mater. 292 (2015) 70–78.
[72] M. Bahri, F. Haghighat, S. Rohani, H. Kazemian, Chem. Eng. J. 320 (2017) 308–318.
[73] J. Wu, Q. Xia, J. Xiao, Z. Li, J. Phys. D. Appl. Phys. 50 (2017) 475202.
[74] W. Xu, X. Jiang, H. Chen, X. Chen, L. Chen, J. Wu, M. Fu, D. Ye, Chem. Eng. J. 382 (2020) 122950.
[75] W. Xu, B. Chen, X. Jiang, F. Xu, X. Chen, L. Chen, J. Wu, M. Fu, D. Ye, J. Hazard. Mater. 387 (2020) 122004.
[76] X. Yu, X. Dang, S. Li, J. Zhang, Q. Zhang, L. Cao, J. Clean. Prod. 276 (2020) 124251.
[77] Veerapandian SKP, Giraudon J-Marc, De Geyter N, Onyshchenko Y, Krishnaraj C, Sonar S, L¨ofberg A, Leus K, Van Der Voort P, Lamonier J-Franc¸ois, Morent R, J Hazard. Mater. (2020) 123877.
[78] U. Kogelschatz, Plasma Chem. Plasma Process. 23 (2003) 1–46.
[79] S. Li, X. Dang, X. Yu, G. Abbas, Q. Zhang, L. Cao, Chem. Eng. J. 388 (2020) 124275.
[80] M. Osada, T. Sasaki, Adv. Mater. 24 (2012) 210–228.
[81] A.A. Zuhairi, M.A.B. Zailani, S. Bhatia, React.Kinet.Catal.Lett. 79 (2003) 143–148.
[82] M. Lu, R. Huang, J. Wu, M. Fu, L. Chen, D. Ye, Catal. Today 242 (2015) 274–286.
[83] Z. Qu, Y. Bu, Y. Qin, Y. Wang, Q. Fu, Chem. Eng. J. 209 (2012) 163–169.
[84] W. Zhang, Z. Qu, X. Li, Y. Wang, D. Ma, J. Wu, J. Environ. Sci. 24 (2012) 520–528.
[85] K. Kosuge, S. Kubo, N. Kikukawa, M. Takemori, Langmuir (2007) 3095–3102.
[86] H. Zaitan, M.H. Manero, H. Valdés, L. De Chimie, D. Matière, C. Lcmc, U. Sidi, M. Ben, J. Environ. Sci. 41 (2016) 59–68.
[87] R.M. Serra, E.E. Miró, P. Bolcatto, A. V Boix, Microporous Mesoporous Mater. 147 (2012) 17–29.
[88] B.W. Jin, S. Zhu, Chem.Eng.Technol 23 (2000) 151–156.
[89] S. Agnihotri, M.J. Rood, Carbon N. Y. 43 (2005) 2379–2388.
[90] C. Ma, R. Ruan, Appl. Clay Sci. 80–81 (2013) 196–201.
[91] K. Yang, F. Xue, Q. Sun, R. Yue, D. Lin, J. Environ. Chem. Eng. 1 (2013) 713–718.

[92] W. Geun, J. Wook, H. Moon, Microporous Mesoporous Mater. 88 (2006) 112–125.
[93] S. Lee, H. Park, S. Lee, M. Lee, J. Ind. Eng. Chem. 14 (2008) 10–17.
[94] D. Lee, J. Kim, C. Lee, Sep. Purif. Technol. 77 (2011) 312–324.
[95] M. Takeuchi, M. Hidaka, M. Anpo, J. Hazard. Mater. 237–238 (2012) 133–139.
[96] X. Dang, J. Huang, L. Cao, Y. Zhou, Catal. Commun. 40 (2013) 116–119.
[97] X. Fan, T.L. Zhu, M.Y. Wang, X.M. Li, Chemosphere 75 (2009) 1301–1306.
[98] F. Thevenet, L. Sivachandiran, O. Guaitella, C. Barakat, A. Rousseau, J. Phys. D. Appl. Phys. 47 (2014) 224011.
[99] H.-H. Kim, A. Ogata, Eur. Phys. J. Appl. Phys. 55 (2011) 13806.
[100] A. Mizuno, H. Ito, J. Electrostat. 25 (1990) 97–107.
[101] T. Zhu, J. Li, Y. Jin, Y. Liang, G. Ma, Int. J. Environ. Sci. Technol. 5 (2008) 375–384.
[102] H. Huang, D. Ye, D.Y.C. Leung, IEEE Trans. Plasma Sci. 39 (2011) 576–580.
[103] J. Wu, Q. Xia, H. Wang, Z. Li, Appl. Catal. B Environ. 156–157 (2014) 265–272.
[104] X. Yao, J. Zhang, X. Liang, C. Long, Chemosphere 208 (2018) 922–930.
[105] T. Wang, S. Chen, H. Wang, Z. Liu, Z. Wu, Cuihua Xuebao/Chinese J. Catal. 38 (2017) 793–804.
[106] X. Xu, J. Wu, W. Xu, M. He, M. Fu, L. Chen, A. Zhu, D. Ye, Catal. Today 281 (2017) 527–533.
[107] C. Qin, H. Guo, P. Liu, W. Bai, J. Huang, X. Huang, X. Dang, D. Yan, J. Ind. Eng. Chem. (2018).
[108] J. Pan, W. Du, Y. Liu, Y. Cheng, S. Yuan, J. Rare Earths 37 (2019) 602–608.
[109] Z. Ye, J.M. Giraudon, N. Nuns, P. Simon, N. De Geyter, R. Morent, J.F. Lamonier, Appl. Catal. B Environ. 223 (2018) 154–166.
[110] S. Behar, N.A. Gómez-Mendoza, M.Á. Gómez-García, D. ̄wierczyński, F. Quignard, N. Tanchoux, Appl. Catal. A Gen. 504 (2015) 203–210.
[111] J.R. Li, W.P. Zhang, C. Li, C. He, J. Colloid Interface Sci. 591 (2021) 396–408.
[112] M. Luo, Y. Cheng, X. Peng, W. Pan, Chem. Eng. J. 369 (2019) 758–765.
[113] S. Xiong, N. Huang, Y. Peng, J. Chen, J. Li, J. Hazard. Mater. 415 (2021) 125637.
[114] Z. Ye, S.K.P. Veerapandian, I. Onyshchenko, A. Nikiforov, N. De Geyter, J.M. Giraudon, J.F. Lamonier, R. Morent, Ind. Eng. Chem. Res. 56 (2017) 10215–10226.
[115] C.W. Kwong, C.Y.H. Chao, K.S. Hui, M.P. Wan, Atmos. Environ. 42 (2008) 2300–2311.
[116] Y. Xi, C. Reed, Y.K. Lee, S.T. Oyama, J. Phys. Chem. B 109 (2005) 17587–17596.
[117] E. Rezaei, J. Soltan, Chem. Eng. J. 198–199 (2012) 482–490.
[118] A. B. Lamb, W.C.Bray, J.C.W.Frazer,.J.Ind.Eng.Chem 12 (1920) 213-221.
[119] G. Wei, Q. Zhang, D. Zhang, J. Wang, T. Tang, H. Wang, X. Liu, Z. Song, P. Ning, Appl. Surf. Sci. 497 (2019) 143777-143785.
[120] A, Mele, I.Mele, A,Mele, A. Journal, App. Sciences, 9 (2012) 265-270.
[121] S. Dey, G.C. Dhal, A Review of Synthesis , Structure and Applications in Hopcalite Catalysts for Carbon Monoxide Oxidation, Aerosol. Sci. Eng. 3 (2019) 97-131.
[122] S. Vepřek, D.L. Cocke, S. Kehl, H.R. Oswald, J. Catal. 100 (1986) 250-263.
[123] S. Dey, G.C. Dhal, Mater. Today Chem. 14 (2019) 100180-100194.
[124] S. Behar, P. Gonzalez, P. Agulhon, F. Quignard, D. Świerczyński, Catal. Today 189 (2012) 35-41.
[125] J. Pei, X. Han, Y. Lu, Build. Environ. 84 (2015) 134-141.
[126] H.J. Lee, J.H. Yang, J.H. You, B.Y. Yoon, J. Ind. Eng. Chem. 89 (2020) 156-165.

[127] Z. Ye, J. -M, Giraudon, N. Nuns, G. Abdallah, A. Addad, R. Morent, N. De Geyter, J. -F.Lamonier, Appl. Surf. Sci. 537 (2021) 147993-148000.
[128] C. Yoon, D.L. Cocke, J. Catal. 113 (1988) 267-280.
[129] Y. Tanaka, T. Utaka, R. Kikuchi, T. Takeguchi, K. Sasaki, K. Eguchi, J. Catal. 215 (2003) 271-278.
[130] C. -T. Peng, H. -K. Lia, B. -J. Liaw, Y. -Z. Chen, Chem Eng J. 172 (2011) 452-458.
[131] Y. Wang, D. Yang, S. Li, L. Zhang, G. Zheng, L. Guo, Chem. Eng. J. 357 (2019) 258-268.
[132] Z. Xiao, J. Yang, R. Ren, J. Li, N. Wang, W. Chu, Chemosphere 247 (2020) 125812.-125822.
[133] L. Li, J. Luo, Y. Liu, F. Jing, D. Su, W. Chu, ACS Appl. Mater. Interfaces 9 (2017) 21798-21808.
[134] M. V. Ganduglia-Pirovaom A. Hofmann, J. Sauer, Surf. Sci.Rep.62 (2007) 219-270.
[135] H. Idriss, M.A. Barteau, Adv. Catal.45 (2000) 261-331.
[136] G.A.M. Hussein, J. Anal. Appl. Pyrolysis 37 (1996) 111-149.
[137] C. Sun, H. Li, L. Chen, Energy Environ. Sci. 5 (2012) 8475-8505.
[138] K. Schermanz, Catalysis by Ceria and Related Materials 2 (2002) 1-528.
[139] D. Zhang, X. Du, L. Shi, R. Gao, Dalton. Trans. 41 (2012) 14455-14475.
[140] J.F. De Lima, R.F. Martins, C. R. Neri, O.A. Serra, App.Surf.Sci 255 (2009) 9006-9009.
[141] N. Izu, W. Shin, N. Murayama, S. Kanzaki, Sens. Act. Chem. 87 (2002) 95-98.
[142] K.G. Azzam, I. V Babich, K. Seshan, L. Lefferts, App. Catal. B. Envir. 80 (2008) 129–140.
[143] Tana, M. Zhang, J. Li, H. Li, Y. Li, W. Shen, Catal. Today 148 (2009) 179-183.
[144] G.S. Herman, Surf. Sci. 437 (1999) 207-214.
[145] T. Taniguchi, T. Watanabe, N. Sugiyama, A.K. Subramani, H. Wagata, N. Matsushita, M. Yoshimura, J. Phys. Chem. C 113 (2009) 19789-19793.
[146] E. Mamontov, T. Egami, J. Phys. Chem. Solids 61 (2000) 1345-1356.
[147] B. Choudhury, A. Choudhury, Mater. Chem. Phys. 131 (2012) 666-671.
[148] P.L. Land, J. Phys. Chem. Solids 34 (1973) 1839-1845.
[149] A. Walsh, S.M. Woodley, C.R.A. Catlow, A.A. Sokol, Solid State Ionics 184 (2011) 52-56.
[150] A.S. Karakoti, N. A. Monteria-Riviere, R. Aggarwal, J.P. Davis, R.J. Narayan, W.T. Self, J. Mcginnis, S. Seal, Bio. Mater. Sci. 1, (2008) 33-37.
[151] A.F.Diwell, R.R.Rajaram, H.A.Shaw, T. J. Truex, Stud. Surf. Sci. Catal. 71 (1991) 139-152.
[152] C. Xia, M.Liu, Solid State Ionics 152–153 (2002) 423-430.
[153] B.C.H. Steele, J. Power Sources 49 (1994) 1-14.
[154] X. Liu, K. Zhou, L. Wang, B. Wang, Y. Li, J. Am. Chem. Soc. 131 (2009) 3140-3141.
[155] L. Liu, Y. Cao, W. Sun, Z. Yao, B. Liu, F. Gao, L. Dong, Catal. Today 175 (2011) 48-54.
[156] A. Trovarelli, C. De Leitenburg, M. Boaro, G. Dolcetti, Catal. Today 50 (1999) 353-367.
[157] R.J. Gorte, React. Kinet. Catal. 56 (2010) 1126-1135.
[158] S. Agarwal, B.L. Mojet, L. Lefferts, A.K. Datye, Catalysis by Materials with Well-Defined Structures, (2015) 31-70.
[159] Z. Hu, X. Liu, D. Meng, Y. Guo, Y. Guo, G. Lu, ACS Catal. 6 (2016) 2265-2279.
[160] S. Liu, R. Zhang, P. Li, H. Chen, Y. Wei, X. Liang, Catal. Today 339 (2020) 241-253.
[161] Z. Wu, M. Li, J. Howe, H.M.Meyer, III, S.H. Overbury, Langmuir 104 (2010) 16595-16606.
[162] J. M. López, A. L.Gilbank, T. García, B. Solsona S. Agouram, L. Torrente-Murciano, Appl. Catal. B, Environ. 174-175 (2015) 403-412.

[163] Y. Liao, L. He, C. Man, L. Chen, M. Fu, J. Wu, D. Ye, B. Huang, Chem. Eng. J. 256 (2014) 439-447.
[164] Y. Liao, L. He, M. Zhao, D. Ye, J. Environ. Chem. Eng. 5 (2017) 5054-5060.
[165] R. Peng, X. Sun, S. Li, L. Chen, M. Fu, J. Wu, D. Ye, Chem. Eng. J. 306 (2016) 1234-1246.
[166] Y. Liao, M. Fu, L. Chen, J. Wu, B. Huang, D. Ye, Catal. Today 216 (2013) 220-228.
[167] S. Kurajica, K. Mužina, G. Dražić, G. Matijašić, M. Duplančić, V. Mandić, M. Župančić, I.K. Munda, Mater. Chem. Phys. 244 (2020) 122689-122698.
[168] S. Lee, E.A. Kapustin, O.M. Yaghi, Science, 353 (2016) 808–811.
[169] H. Li, M. Eddaoudi, M. O'Keeffe, O.M. Yaghi, Nature 402 (1999) 276-279.
[170] J. Reboul, S. Furukawa, N. Horike, M. Tsotsalas, K. Hirai, H. Uehara, M. Kondo, N. Louvain, O. Sakata, S. Kitagawa, Nat. Mater. 11 (2012) 717-723.
[171] T. Kajiwara, M. Fujii, M. Tsujimoto, K. Kobayashi, M. Higuchi, K. Tanaka, S. Kitagawa, Angew. Chemie 128 (2016) 2747-2750.
[172] J. Park, D. Feng, H. -C. Zhou, J. Am. Chem. Soc. 137 (2015) 11801-11809.
[173] C. Janiak, Dalton. Trans. (2003) 2781-2804.
[174] M. Sindoro, N. Yanai, Ah-Y. Jee, S. Granick, Acc. Chem. Res. 47 (2014) 459-469.
[175] A.J. Howarth, Y. Liu, P. Li, Z. Li, T.C. Wang, J.T. Hupp, O.K. Farha, Nat. Rev. Mater. 1 (2016) 1-15.
[176] M. Li, D. Li, M. O'Keeffe, O.M. Yaghi, Chem. Rev. 114 (2014) 1343-1370.
[177] N. Stock, S. Biswas, Chem. Rev. 112 (2012) 933-969.
[178] H. B. Wu, X.W. Lou, Sci. Adv. 3 (2017) eaap9252.
[179] K. Sumida, D.L. Rogow, J.A. Mason, T.M. McDonald, E.D. Bloch, Z.R. Herm, T.-H. Bae, J.R. Long, Chem. Rev. 112 (2012) 724-781.
[180] L. Zhu, X.-Q. Liu, H.-L. Jiang, L.-B. Sun, Chem. Rev. 117 (2017) 8129-8176.
[181] A. Karmakar, P. Samanta, A. V. Desai, S.K. Ghosh, Acc. Chem. Res. 50 (2017) 2457-2469.
[182] Y. Zhang, S.N. Riduan, J. Wang, Chem. - A Eur. J. 23 (2017) 16419-16431.
[183] F. Chu, Y. Zheng, B. Wen, L. Zhou, J. Yan, Y. Chen, RSC Adv. 8 (2018) 2426-2432.
[184] K. Vellingiri, P. Kumar, A. Deep, K.-H. Kim, Chem. Eng. J. 307 (2017) 1116-1126.
[185] J. Chun, S. Kang, N. Park, E.J. Park, X. Jin, K.-D. Kim, H.O. Seo, S.M. Lee, H.J. Kim, W.H. Kwon, Y.-K. Park, J.M. Kim, Y.D. Kim, S.U. Son, J. Am. Chem. Soc. 136 (2014) 6786-6789.
[186] S.K. Elsaidi, M.H. Mohamed, D. Banerjee, P.K. Thallapally, Coord. Chem. Rev. 358 (2018) 125-152.
[187] A.U. Czaja, N. Trukhan, U. Müller, Chem. Soc. Rev. 38 (2009) 1284-1293.
[188] J.H. Cavka, S. Jakobsen, U. Olsbye, N. Guillou, C. Lamberti, S. Bordiga, K.P. Lillerud, J. A,. Chem. Soc. 130 (2008) 13850-13851.
[189] F. Bi, X. Zhang, J. Chen, Y. Yang, Y. Wang, Appl. Catal. B Environ. 269 (2020) 118767-118781.
[190] C. Wei, H. Hou, E. Wang, M. Lu, Materials , 13 (2020) 88-98.
[191] X. Zhang, L. Song, F. Bi, D. Zhang, Y. Wang, L. Cui, J. Colloid Interface Sci. 571 (2020) 38-47.
[192] S. Biswas, P. Van Der Voort, Eur. J. Inorg. Chem (2013) 2154-2160.
[193] X. Du, D. Zhang, L. Shi, R. Gao, J. Zhang, J.Phys.Chem.C. 116 (2012) 10009-10016.
[194] M. Skaf, S. Aouad, S. Hany, R. Cousin, E. Abi-aad, A. Aboukaïs, J Catal. 320 (2014) 137-146.

[195] E.C. Njagi, C. -H. Chen, H. Genuino, H. Galindo, H. Huang, S.L. Suib, Appl. Catal. B, Environ. 99 (2010) 103-110.
[196] T. Désaunay, G. Bonura, V. Chiodo, S. Freni, J. -P. Couzinié, J. Bourgon, A. Ringuedé, F. Labat, C. Adamo, M. Cassir, J. Catal. 297 (2013) 193-201.
[197] C.G. Silva, I. Luz, F.X. Llabrés i Xamena, A. Corma, H. García, Chem. Eur. J. 16 (2010) 11133-11138.
[198] S. Øien, D. Wragg, H. Reinsch, S. Svelle, S. Bordiga, C. Lamberti, K.P. Lillerud, Cryst. Growth Des. 14 (2014) 5370-5372.
[199] Z. -Y. Yuan, V. Idakiev, A. Vantomme, T. Tabakova, T. -Z. Ren, B. -L. Su, Catal. Today 131 (2008) 203-210.
[200] Z. Xiao, S. Ji, Y. Li, F. Hou, H. Zhang, X. Zhang, L. Wang, G. Li, Appl. Surf. Sci. 455 (2018) 1037-1044.
[201] W. Liang, C. J. Coghlan, F. Ragon, M. Rubio-Martinez, D. M. D'Alessandro, R. Babarao, Dalton. Trans. 45 (2016) 4496-4500.
[202] F. Yang, H. Huang, X. Wang, F. Li, Y. Gong, C. Zhong, J.-R. Li, Cryst. Growth Des. 15 (2015) 5827-5833.
[203] A. Donnadio, R. Narducci, M. Casciola, F. Marmottini, R. D'Amato, M. Jazestani, H. Chiniforoshan, F. Costantino, ACS Appl. Mater. Interfaces 9 (2017) 42239-42246.
[204] Z. Lin, X. Cai, Y. Fu, W. Zhu, F. Zhang, RSC Adv. 7 (2017) 44082-44088.
[205] J. Kim, Y.H. Min, N. Lee, E. Cho, K.Y. Kim, G. Jeong, S.K. Moon, M. Joo, D.B. Kim, J. Kim, S.-Y. Kim, Y. Kim, J. Oh, S. Sato, ACS Omega 2 (2017) 7424-7432.
[206] V. Perrichon, A. Laachir, G. Bergeret, R. Frety, L. Tournayan, O. Touret, J Chem. Soc. Faraday Trans. 90 (1994) 773-781.
[207] V.P. Santos, M.F.R. Pereira, J. J. M. Órfão, J.F. Figueiredo, Appl. Catal. B Environ. 88 (2009) 550-556.
[208] Wagner, C.D.; Naumkin, A.V.; Kraut-Vass, A.; Allison, J.W.; Powell, C.J.; Rumble, J.R., Jr. NIST Standard Reference Database 20. NIST XPS Database Version 2003, 3, 251–252.
[209] A. Marinoiu, M. Raceanu, C. Cobzaru, C. Teodorescu, D. Marinescu, A. Soare, M. Varlam, React. Kinet. Mech. Catal. 112 (2014) 37-50.
[210] C.G. Rotaru, G. Postole, M. Florea, F. Matei-Rutkovska, V.I. Pârvulescu, P. Gelin, Appl. Catal. A. General 494 (2015) 29-40.
[211] K.M.S. Khalil, L.A. Elkabee, B. Murphy, Microporous Mesoporous Mater. 78 (2005) 83-89.
[212] G.C. Shearer, S. Chavan, S. Bordiga, S. Svelle, U. Olsbye, K.P. Lillerud, Chem. Mater 28 (2016) 3749-3761.
[213] D.M. Ruthven, (1984) 1-464.
[214] S. Dey, G.C. Dhal, Mater. Sci. Energy Technol. 3 (2020) 377-389.
[215] X. Feng, J. Hajek, H.S. Jena, G. Wang, S.K.P. Veerapandian, R. Morent, N. De Geyter, K. Leyssens, A.E.J. Hoffman, V. Meynen, C. Marquez, D.E. De Vos, V. Van Speybroeck, K. Leus, P. Van Der Voort, J. Am. Chem. Soc. 2020, 142 (2020) 3174-3183.
[216] Y. Guo, M. Wen, G. Li, T. An, Appl. Catal. B Environ. 281 (2021) 119447-119466.
[217] C. Yang, G. Miao, Y. Pi, Q. Xia, J. Wu, Z. Li, J. Xiao, Chem. Eng. J. 370 (2019) 1128-1153.
[218] C. Shi, B. -B. Chen, X. -S. Li, M. Crocker, Y. Wang, A. -M. Zhu, Chem. Eng. J. 200-202 (2012) 729-737.

[219] Z. Ye, G. Wang, J. -M. Giraudon, A. Nikiforov, J. Chen, L. Zhao, X. Zhang, J. Wang, J. Hazard. Mater. 424C (2022) 127321-127330.
[220] S.-W. Baek, J. -R. Kim, S. -K. Ihm, Catal. Today 93-95 (2004) 575-581.
[221] Y. Wang, D. Yang, S. Li, M. Chen, L. Guo, J. Zhou, Microporous Mesoporous Mater. 258 (2018) 17-25.
[222] B.O. Adebayo, A. Krishnamurthy, A.A. Rownaghi, F. Rezaei, Ind. Eng. Chem. Res. 59 (2020) 13762-13772.
[223] S. Sonar, J. Giraudon, S. K. P. Veerapandian, R. Bitar, K. Leus, P. Van Der Voort, J. Lamonier, R. Morent, N. De Geyter, A. Löfberg, Catalysts 10 (2020) 761-781.
[224] S. Dey, G. Dhal, D. Mohan, R. Prasad, J. Sci. Adv. Mater. Devices 4 (2019) 47-56.
[225] E. C. Njagi, C. H. Chen, H. Genuino, H. Galindo, H. Huang, S. Suib, Appl. Catal. B Environ. 99 (2010) 103-110.
[226] S. Grangeon, A. Fernandez-Martinez, F. Warmont, A. Gloter, N. Marty, A. Poulain, B. Lanson, Geochem Trans 16 (2015) 1-16.
[227] Y. Qin, Y. Wang, J. Li, Z. Qu, Surfaces and Interfaces 21 (2020) 100657-100664.
[228] Q. Ye, J. Zhao, F. Huo, J. Wang, S. Cheng, T. Kang, H. Dai, Catal. Today 175 (2011) 603-609.
[229] A. S. Reddy, C. S. Gopinath, S. Chilukuri, J. Catal. 243 (2006) 278-291.
[230] L. Zhang, S. Zhu, R. Li, W. Deng, C. Hong, D. Liu, L. Guo, ACS Appl. Nano Mater. 3 (2020) 11869-11880.
[231] X. Zhai, F. Jing, L. Li, X. Jiang, J. Zhang, J. Ma, W. Chu, Fuel 283 (2021) 118888-1188900.
[232] J. Li, Z. Qu, Y. Qin, H. Wang, Appl. Surf. Sci. 385 (2016) 234-240.
[233] T. Li, J. Zhao, Y. Quan, D. Luo, C. Miao, J. Ren, Environ. Sci. Pollut. Res. Int. 28 (2021) 37592-37602.
[234] S. C. Kim, J.Y. Ryu, Environ. Technol. 32 (2011) 561-568.
[235] H. Yang, J. Deng, Y.Liu, S. Xie, Z. Wu, H. Dai, J. Mol. Catal. 414 (2016) 9-18.
[236] Y. Qin, Z. Qu. C.Dong, N. Hunag, Chinese J. Of. Catal. 38 (2017) 1603-1612.
[237] J. Zhu, W.Zhang, Q. Qi, H.Zhang, Y.Zhang, D. Sun, P. Liang, Sci. Rep. 9 (2019) 12162-12171.
[238] T. Dargel, R. Hertwig, W. Koch, Mol. Phy. 96 (1999) 583-591.
[239] H.-H. Kim, A. Ogata, S. Futamura, J. Phys. D. Appl. Phys. 38 (2005) 1292-1300.
[240] H. Huang, D. Ye, D.Y.C. Leung, F. Feng, X. Guan, J. Mol. Catal. A Chem. 336 (2011) 87-93.
[241] C. Xu, B. Li, H. Du, F. Kang, Y. Zeng, J. Power Sources 184 (2008) 691-694.
[242] M. Yang, J. He, RSC Adv. 8 (2018) 22-27.
[243] G. Fierro, S. Morpurgo, M. Lo Jacono, M. Inversi, I. Pettiti, Appl. Catal. A, Gen. 166 (1998) 407-417.
[244] M.C. Biesinger, B.P. Payne, A.P. Grosvenor, L.W.M. Lau, A.R. Gerson, R.S.C. Smart, Appl. Surf. Sci. 257 (2011) 2717-2730.
[245] F. Wang, H. Dai, J. Deng, G. Bai, K. Ji, Y. Liu, Environ. Sci. Technol.2012, 46 (2012) 4034-4041.
[246] M. Plata-gryl, M. Momotko, S. Makowiec, G. Boczkaj, Sep. Purif. Technol. 224 (2019) 315-321.
[247] A.M. Vandenbroucke, R. Morent, N. De Geyter, C. Leys, J. Hazard. Mater. 195 (2011) 30- 54.

[248] Y.-F. Guo, D.-Q. Ye, K.-F. Chen, J.-C. He, W.-L. Chen, J. Mol. Catal. A Chem. 245 (2006) 93-100
[249] V. Demidyuk, J.C. Whitehead, Plasma Chem Plasma Process. 27 (2007) 85-94.
[250] S.K.P. Veerapandian, C. Leys, N. De Geyter, R. Morent, 7 (2017) 113-146.
[251] S. Sonar, J. -M. Giraudon, S. K. P. Veerapandian, J. -F. Lamonier, R. Morent, A. Löfberg, N. De Geyter, Catalysts. 11 (2021) 845-863.